

A DYNAMICAL AND STATISTICAL  
UNDERSTANDING OF THE NORTH ATLANTIC  
OSCILLATION AND ANNULAR MODES

EDWIN PAUL GERBER

A DISSERTATION  
PRESENTED TO THE FACULTY  
OF PRINCETON UNIVERSITY  
IN CANDIDACY FOR THE DEGREE  
OF DOCTOR OF PHILOSOPHY

RECOMMENDED FOR ACCEPTANCE  
BY THE PROGRAM IN  
APPLIED AND COMPUTATIONAL MATHEMATICS

JANUARY, 2006

© Copyright by Edwin Paul Gerber, 2005.

All Rights Reserved

# Abstract

We present a hierarchy of idealized models of the North Atlantic Oscillation (NAO) and Annular Modes, the dominant patterns of intraseasonal variability in the extratropical atmosphere. The models isolate the dynamics governing the spatial and temporal structure of the patterns, and provide a framework for interpreting measures of the variability produced by Empirical Orthogonal Function and teleconnection analysis.

A barotropic model on the sphere indicates that the patterns are a consequence of the chaotic “stirring” of the atmosphere by baroclinic eddies. Such stirring, represented by a simple random forcing, leads to variability of the zonal flow via variability in the eddy momentum flux convergence. Zonal structure of the forcing dictates zonal structure of the variability, suggesting that the NAO follows from the localized synoptic variability of the North Atlantic storm track. Intraseasonal variability is more persistent than the eddies that force it, as integration of eddy fluxes by the equations of motion strengthens power at lower frequencies.

The patterns’ spatial structure is investigated with analytic, purely stochastic models of the zonally averaged zonal wind and surface pressure. The meridional structure stems from geometric constraints and the conservation of mass and zonal momentum. A two-dimensional extension of the model reveals that symmetry of the statistics, not necessarily the motions, is sufficient for the existence of an annular pattern, explaining the presence of annular modes in systems lacking hemispherically coherent motions.

Conclusions from the simpler models are verified with a dry, primitive equation general circulation model. Annular mode and NAO-like patterns are found by varying the zonal structure of synoptic variability with idealized topography and heating anomalies approximating land-sea contrast. The NAO arises from the confluence of topographic and thermal forcing, and is best understood in terms of the eddy

life cycle. A parameter sensitive coupling between eddies and the large-scale flow extends the persistence and zonal coherence of the intraseasonal variability. The mainly barotropic circulation anomalies influence the baroclinicity by shifting the critical latitudes, thus shaping the eddy momentum fluxes. Sensitivity of the coupling to asymmetric forcing suggest that localized NAO-like variability is more dominant when eddy-mean flow interactions are weakened.

## Acknowledgements

It was not easy for me to transition from the role of the student to that of the research scientist. After so many years of schooling I was quite adept at completing homework sets and answering test problems, but to become a scientist, I had to learn to formulate my own questions and investigate problems where the existence of “an answer” was not necessarily given. I am most indebted to my advisor, Geoff Vallis, for getting me through the process. His ability to isolate the essence of complex systems in simpler models has shaped my approach to understanding the Earth’s climate. From his example and pragmatic advice I have learned to become a more effective researcher, writer, and teacher.

I have benefited greatly from the research environment at Princeton and GFDL, learning much from superb teachers and mentors in both applied mathematics and atmospheric and oceanic science. In addition to Geoff, Robert Calderbank, Ingrid Daubechies, Weinan E, Steve Garner, Isaac Held, Phil Holmes, Paul Kushner, Gabriel Lau, and Isadoro Orlanski have shaped my understanding of both disciplines. Post-docs Jian Lu, Gwendal Riviere, and Pablo Zurita-Gotor, and students Dargan Frierson, Shree Khare, Gang Chen, and Neven Fuckar have also provided helpful criticism and suggestions on my research at many stages in its development.

I owe much to my fellow students in PACM and AOS for creating an energetic learning and social environment. In particular, I feel extremely privileged to have worked alongside Dargan, the “other half” of applied mathematics in my class at Princeton. He was always there to hear out new ideas or give a second opinion on a talk or paper – and also to play a little bluegrass music or watch an art film over a glass of wine and mysterious cheese. I also would like to thank the administrative staff in both departments for ensuring a smooth transition through Princeton, allowing me to concentrate on my research: Howard Bergman, Cheryl Cantore, and Valerie Marino in PACM, and Johann Callan, Laura Rossi, and Anna Valerio in AOS.

I would like to give special thanks to the Fannie and John Hertz Foundation for providing generous financial support throughout my graduate education at Princeton. The foundation also allowed for periodic checkups by Lowell Wood, whose candid academic advice helped me mature as an independent researcher. Support for my education was also provided by a generous gift from William Bowen, the Princeton Materials Institute, and the National Science Foundation.

As Dickens might have put it, graduate school was the best of times, graduate school was the worst of times. I am thankful for the people who carried me through the dark hours and brought such joy to my life in the brightest. It would take another volume, likely thicker than this one, to recount all the incredible memories I've shared during my time at Princeton. My wife Nona, my family, and my friends, especially Dargan, Dave, and Rich, have made such a difference in my experience here.

I have dedicated this thesis to my grandmother. In our frequent phone conversations and time spent together during the summers and at Christmas, she always made sure to keep tabs on my research. I had to be ready to tell her (if not my advisor) what I'd accomplished that week. She was a loving example of how to live a meaningful life, and I know she would be extremely satisfied that I have successfully completed my dissertation.

For Grammy

Ruth Clifford Rosenthaler, March 24, 1922 - November 6, 2005

# Contents

Abstract . . . . .	iii
Acknowledgements . . . . .	v
<b>1 Introduction</b>	<b>1</b>
1.1 The NAO and Annular Modes . . . . .	5
1.2 Research Overview: A Tale of Three Models . . . . .	13
<b>2 The Barotropic Model: A Dynamical Null Hypothesis</b>	<b>17</b>
2.1 Introduction . . . . .	17
2.2 The Basic Model . . . . .	19
2.2.1 Jets on a $\beta$ -plane . . . . .	19
2.2.2 Source of stirring in a baroclinic atmosphere . . . . .	22
2.2.3 Patterns of variability . . . . .	23
2.3 Numerical model . . . . .	25
2.4 Results with Zonally Symmetric Stirring . . . . .	30
2.4.1 Mean state for zonally symmetric model . . . . .	30
2.4.2 Variability . . . . .	32
2.4.3 Two-dimensional patterns . . . . .	36
2.4.4 Low and high index states . . . . .	44
2.5 Results from Zonally Asymmetric Model . . . . .	44
2.6 Temporal Structure . . . . .	50

2.7	Summary and Conclusions . . . . .	52
<b>3</b>	<b>The Stochastic Model: Constraints on the Circulation</b>	<b>59</b>
3.1	Introduction . . . . .	59
3.2	A One-Dimensional Model . . . . .	62
3.2.1	Theory . . . . .	62
3.2.2	Results . . . . .	70
3.2.3	Comparison with Observations . . . . .	76
3.3	A Two-Dimensional Model . . . . .	79
3.3.1	Theory . . . . .	79
3.3.2	The Model . . . . .	80
3.3.3	Analytic Solutions . . . . .	86
3.4	An NAO-like Pattern . . . . .	88
3.5	Pressure Models . . . . .	91
3.5.1	Model $P_1$ . . . . .	91
3.5.2	Model $P_2$ . . . . .	93
3.5.3	Comparison with observations . . . . .	96
3.6	Summary and Conclusions . . . . .	98
<b>4</b>	<b>The Dry Dynamical Core I: The NAO and Annular Modes</b>	<b>102</b>
4.1	Introduction . . . . .	102
4.2	Experimental Setup . . . . .	105
4.2.1	Zonally Asymmetric Forcing . . . . .	107
4.2.2	Simulation Specifications . . . . .	110
4.3	Simulation Results . . . . .	111
4.3.1	The Baroclinic Storm Track: Simulation LSC . . . . .	111
4.3.2	Topography Alone: Simulation RM . . . . .	117
4.3.3	Confluence of Topographic and Thermal Forcing: the NAO . .	121

4.3.4	A Comparison with Observations . . . . .	123
4.4	Intraseasonal Variability . . . . .	124
4.4.1	Spatial Structure . . . . .	126
4.4.2	Temporal Structure . . . . .	135
4.5	Local and Global Patterns of Variability: NAO or Annular mode? . .	139
4.6	A More Physical Interpretation . . . . .	146
4.7	Summary and Conclusions . . . . .	150
<b>5</b>	<b>The Dry Dynamical Core II: Timescales of Variability</b>	<b>156</b>
5.1	Introduction . . . . .	156
5.2	Background . . . . .	158
5.3	Experimental Setup . . . . .	163
5.4	Sensitivities of the Model to Resolution . . . . .	169
5.5	Parameter Sensitivities . . . . .	175
5.5.1	A Remarkable Consistency in the Response . . . . .	175
5.5.2	Important Differences in the Response . . . . .	182
5.6	Zonal Asymmetries and Timescales of Variability . . . . .	185
5.7	Enhanced Persistence: Potential for Interaction Between the Large-scale Flow and Eddies . . . . .	187
5.8	A Mechanism for Enhanced Persistence . . . . .	199
5.9	On the Structure of the Annular Mode . . . . .	204
5.10	A Simple Model of the Feedback . . . . .	214
5.11	Wave Breaking and Poleward Propagation . . . . .	219
5.12	Summary and Conclusions . . . . .	224
<b>6</b>	<b>Conclusions</b>	<b>230</b>

# Chapter 1

## Introduction

*It has been many times remarked, that the weather in Greenland is just the reverfe to that in Europe; fo that when the temperate climates are incommoded with a very hard winter, it is here uncommonly mild, and vice verfa.*

So states the first known written record of what we today call the North Atlantic Oscillation (van Loon and Rogers 1978). The excerpt comes from a 1767 translation of David Crantz's *The History of Greenland*. The text, first published in Dutch in 1765, came at a time when Europe's interest in Greenland was growing for the second time. The island had been successfully settled by the Norse under Eric the Red some seven centuries earlier, circa A.D. 982, but contact between the colonies and the Europe had broken off by the fifteenth century. Inspired in part by the fact that these lost colonists would have no knowledge of the Reformation, the Norwegian Hans Egede launched a mission to the island with the support of the Danish in 1721. He found no trace of the Viking colonists, but none-the-less began a mission with the native Inuit, who had subsumed the settlements.

More important for our story, Hans and his son Paul, who accompanied his father and mother to the island in 1721, kept detailed records of the weather and climate.

Crantz includes one of the first<sup>1</sup> in situ observations of the NAO, taken from Paul's journal where he noted "that in the well known cold winter [in Europe] between 1739 and 1740 it was so mild in Difko-creek [on the west coast of Greenland], that the wild geese fled from the temperate to this frigid zone to seek warmth in January. There was no ice in the bay till far in March, even though in most winters it is covered from October to May" Situated a few degrees above the Arctic circle, the thought of any creature seeking warmth in Disco Bay in January would appear worthy of note.

Just how cold was the "well known" winter of 1739-40? Paleoreanalysis by Wanner and Luterbacher (2002) suggest that the average temperature was over 5° C below normal for much of central and Eastern Europe that season, but perhaps the most colorful descriptions are to be found in England. There the Thames froze at London, one of only 20 such occurrences since Roman times (Drower 1989). It remained solid from Boxing day to February 17th, providing grounds for an extensive "Frost Fair" through the heart of the city, as depicted in Figure 1.1. Booths set up on the ice provided popular attractions such as the "Lapland Mutton," a sheep roasted over a coal fire on the ice, drawing large crowds from the city and surrounding countryside. Despite the levity of the fair, the cold brought much suffering to London's poor. Snow fell 39 times in the London area through the winter,<sup>2</sup> and the ice and gales wrought havoc on shipping, leading to scarcity of food and fuel.

It was a particularly cold winter in the American colonies as well. From the *History of Delaware County, Pennsylvania* by Henry Graham Ashmead, published in Philadelphia in 1884, we find:

In the winter of 1739-40, when the cold was so intense in Europe, snow fell to a depth of three feet; the tops of the fences were covered, and sleds passed over them in every direction on the hard crust. The Delaware was

---

<sup>1</sup>In a study completed in 1811, Gronau noted one earlier mild winter in Greenland associated with extreme cold in Germany in 1709 (van Loon and Rogers 1978).

<sup>2</sup>From <http://www.metoffice.com/education/secondary/students/winter.html> on 7/19/2005



Figure 1.1: An illustration of the 1739-40 Frost Fair, “printed upon the ice on the River Thames, January 23rd, 1740.”

frozen over until the 15th of March.

The suffering among the exposed settlers in Lancaster County, then on the borders of civilization, was extreme, the Pennsylvania Gazette recording that they were compelled to subsist on the deer which had died, and it was no unusual event to find ten or twelve of those creatures lying within a comparatively short distance of a spring, while great numbers of squirrels and birds were frozen to death. The horses, cows, and other domestic animals exposed in the woods without shelter perished. In many instances the stags and does fed at the hay-risks with the cattle and became domesticated.

The text notes that the freezing of the Delaware River at Philadelphia, though not as unheard of as the Thames in London, was of particular note to colonist and Native Americans.

Piecing together records from Greenland, Europe, and the East Coast of America, we begin to see the full extent of the North Atlantic Oscillation, a “teleconnection” pattern linking opposing shifts in the local weather over *planetary spatial scales*. Also implied is a *seasonal timescale* – a cold winter – a timescale longer than that associated with synoptic variability. Such vacillations of the earth’s climate system have (rather confusingly) been termed “low frequency variability.” Here the intent is to stress timescales longer than those associated with the chaotic limit of typical weather prediction, say, 10-15 days, but not so low as to allow significant changes in the boundary conditions, e.g. changes in solar forcing or shifts in ocean circulation. These intraseasonal variations appear to arise naturally from the internal dynamics of the atmosphere.

Why does the winter-time weather in Greenland often deviate in the opposite direction from Europe and the East Coast of America, and why do these shifts often last on seasonal timescales? The aim of this thesis is to answer these questions through

a study of three idealized atmospheric models. But before turning to the science, we leave a few recommendations for those who curiosity was sparked by the interaction of climate discovery and history. *The Little Ice Age: How Climate Made History 1300-1850* by Brian Fagan, and *Collapse: How Societies Choose to Fail or Succeed*, by Jared Diamond, provide two different views on the ill fated Viking settlements on Greenland. The former suggest that a shift in climate over Europe and related shift in the NAO may have played a role in their extinction. For those interested in the scientific history, van Loon and Rogers (1978) provides a good background on the discovery and characterization of the NAO.

## 1.1 The NAO and Annular Modes

The large-scale atmospheric circulation displays variability on multiple timescales. The most prominent variability in the extratropics is that due to baroclinic eddies, or midlatitude weather systems, which typically have a timescale of a few days. On timescales of a season or longer atmospheric variability may be influenced by interactions at its boundaries (e.g., by the sea-surface temperature) and by other slow changes in forcing. The variability on intermediate timescales, say between 10 days and a season has a less obvious cause. The direct effect of the ocean or other changing boundary seems unlikely to be important, both because large-scale sea-surface temperatures tend to change primarily on still longer timescales and because their effect is unlikely to be strong enough to produce large changes in the atmospheric circulation on the 10–100 day timescale. Rather, we expect this variability to have a primarily atmospheric origin, ultimately arising from baroclinic activity and weather systems and reddened by the dynamics of the equations of motion. The mechanisms of such variability, however, are not fully understood.

If the atmospheric fields are appropriately filtered in time to select intraseasonal

timescales, then fairly well-defined spatial patterns of variability emerge. The patterns robustly show up in correlation maps or teleconnection patterns (Wallace and Gutzler 1981), and in the Empirical Orthogonal Functions (EOF) of the low-passed fields (e.g., Ambaum et al. 2001), and a host of such patterns have been identified by these and other scientists – the North Atlantic Oscillation (NAO), the Northern and Southern Annular Modes (NAM, SAM), the Pacific North American pattern (PNA) and so on. Of these the North Atlantic Oscillation, characterized in Figure 1.2, is probably the most well known and this, and the annular modes illustrated in Figure 1.3, will concern us. The scale of these patterns is significantly larger than that typically associated with a single baroclinic eddy, ranging from a few thousand kilometers of the NAO to the hemispheric scale of the annular modes. Three other aspects of their structure stand out: (i) They are barotropic, or at least equivalent barotropic, with little phase shift in the vertical, (ii) there is a strong dipolar component in the horizontal structure of the pressure field, and (iii) they are characterized by a red spectrum in time, with no pronounced spectral peak at any given frequency.

## Spatial Structure

The horizontal structure of the NAO is illustrated in Figure 1.2, a reproduction of Figure 4 from Ambaum et al. (2001). Panel (d), the first EOF of surface temperature, confirms the NAO’s relationship with the climate in Greenland, Europe and the East Coast of North America as suggested by the winter of 1739-40. A positive NAO is associated with anomalously cold temperature in Greenland and warmer than average temperatures in Europe and the Eastern United States. The pattern is reverse in the negative phase, as in 1739-40. Panels (a) through (c), illustrate the dynamical signature of the oscillation. The strong dipole signatures in the surface pressure, stream function, and zonal winds, respectively, chiefly characterize a movement of the extratropical jet. In the positive phase, the jet is further poleward than

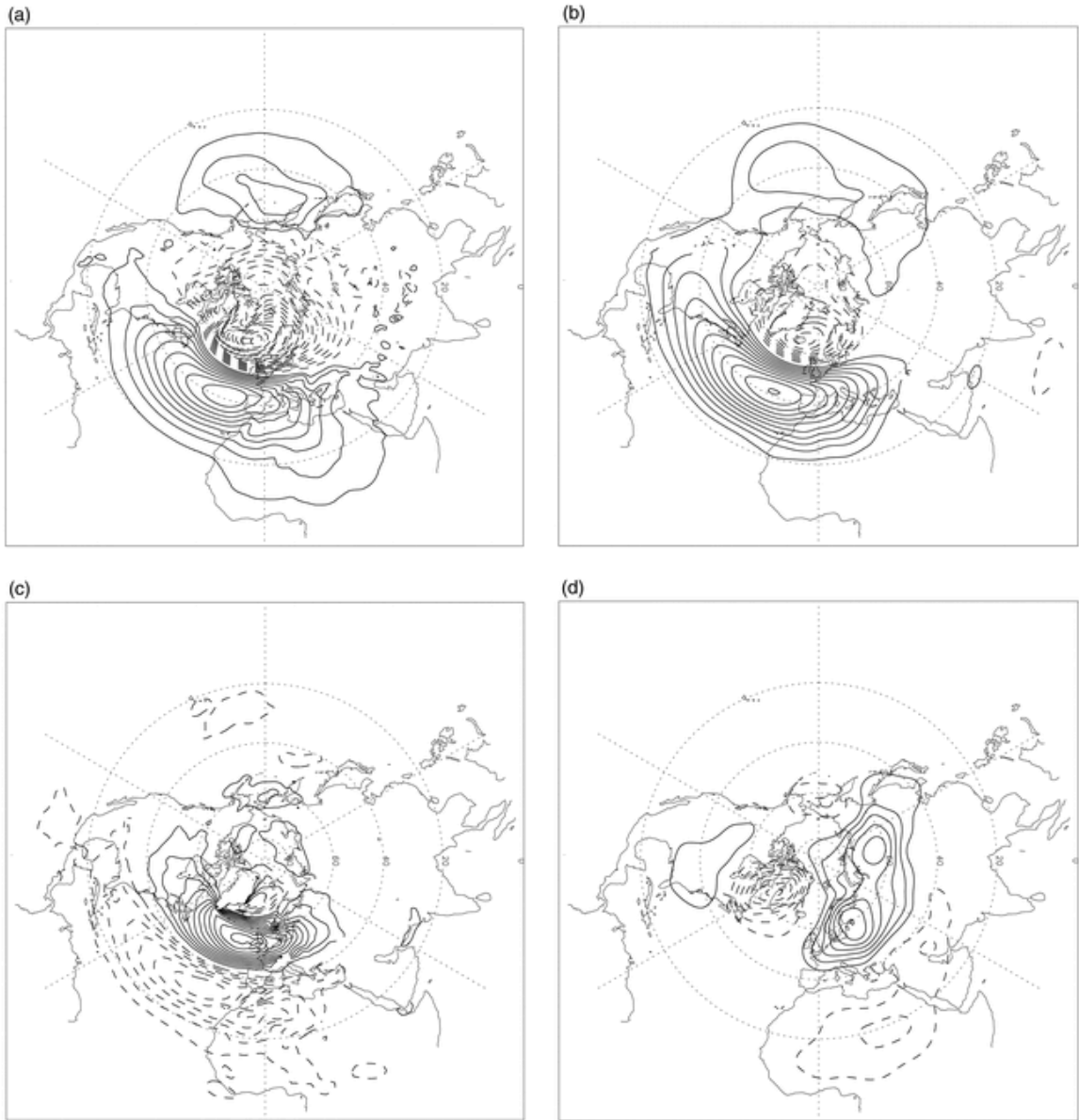


Figure 1.2: The NAO from Ambaum et al. (2001). Leading EOFs based on variability in the Euro-Atlantic sector only for the DJFM (a) mean sea level pressure (contour interval: 0.5 hPa, explaining 47.7%), (b) streamfunction at 850 hPa ( $5 \times 10^5 \text{ m}^2\text{s}^{-1}$ , 40.3%), (c) zonal wind at 850 hPa ( $0.5 \text{ ms}^{-1}$ , 44.2%), and (d) temperature at 2 m (0.5 K, 33.5%). The temperature EOF has been smoothed with a Gaussian kernel of  $3^\circ$  width.

normal, bringing increased advection of warm air from the ocean to Europe, and to a lesser extent, to the Eastern US. Greenland, on the other hand is isolated by this circulation, receiving cold air advected from the Arctic and Canadian shield. In the negative phase, the jet is shifted equatorward of climatology. Europe observes a reduction in moderating ocean breezes, which now bath Greenland, and the Eastern US experiences anomalous Northerly winds bringing colder air.

A scientific classification of the NAO pattern dates back at least to Walker and Bliss (1932), who noted “the tendency for pressure to be low near Iceland in winter when it is high near the Azores and south-west Europe,” and the relationship between the pressure changes and temperature fields. This characterization remained largely unchanged until Thompson and Wallace (1998) suggested that the NAO was part of a larger, hemispheric pattern of variability, the Northern Annular Mode (NAM), or “Arctic Oscillation.” The horizontal signature of the NAM (expressed in terms of the 1000 hPa geopotential height) is illustrated in Figure 1.3d. The pattern is similar to the NAO in the North Atlantic region, but associates this signal with a similar dipole in pressure over the North Pacific. Further evidence in support of a hemispheric mode of variability was presented by Thompson and Wallace (2000), who found a similar pattern of variability in the Southern Hemisphere. The first figure from their paper is reproduced in Figure 1.3. Panels (a) and (b) reveal the equivalent barotropic structure of the patterns. As noted above, the NAO shares this simple equivalent barotropic vertical structure. Panels (c) and (d) reveals the marked similarity of the horizontal structure in both hemispheres. The see-saw in geopotential height characterizes a hemispheric movement of the extratropical jets.

It is of considerable interest to properly characterize intraseasonal variability in the extratropics, even though by many measures the NAO and NAM contain the same information, given the similarity in the their spatial structure. As Wallace (2000) points out, the “paradigm” for classifying intraseasonal variability - be it the annular

Regressions on the annular modes

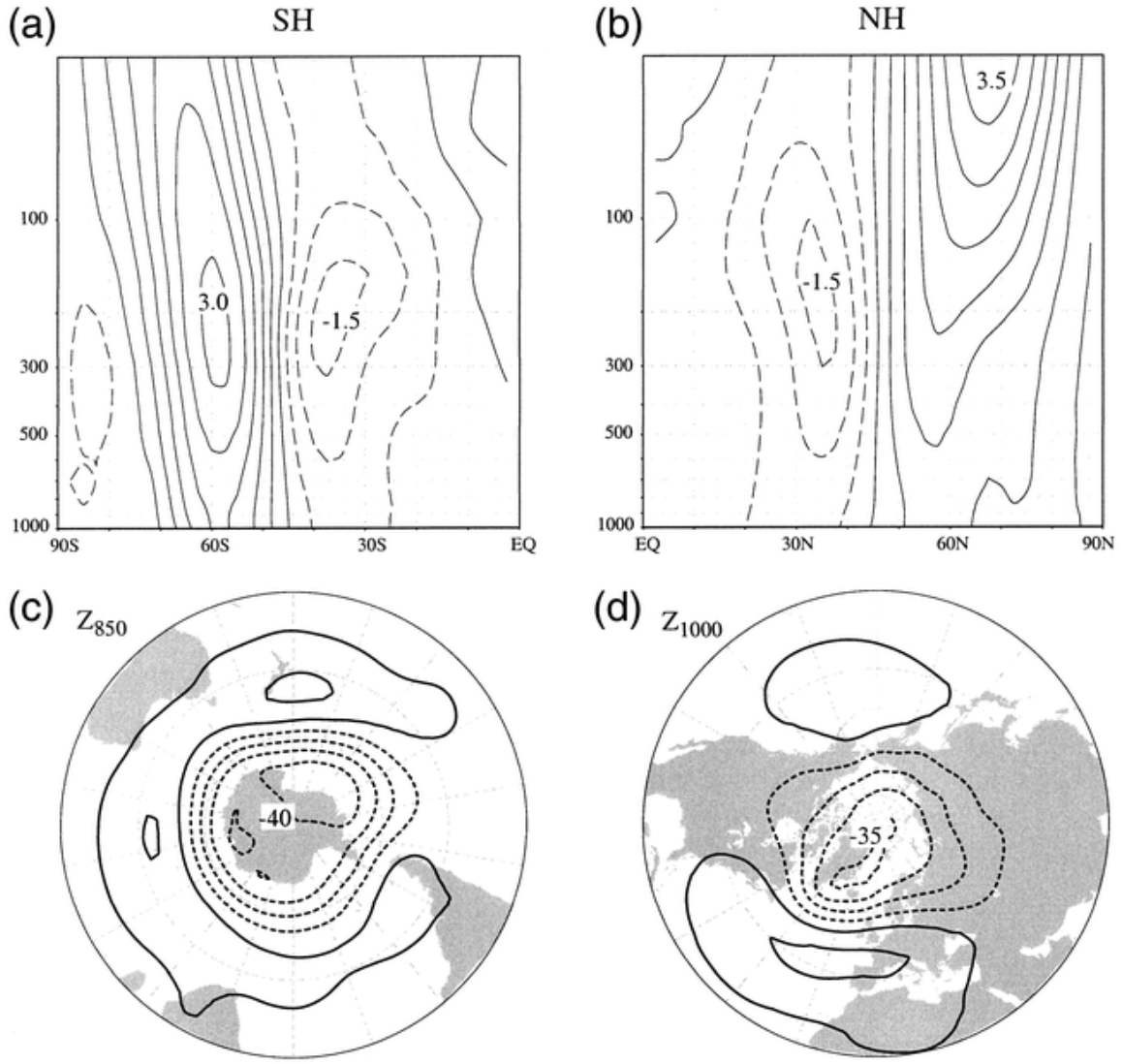


Figure 1.3: The annular modes, from Thompson and Wallace (2000). (top) Zonal-mean geostrophic wind and (bottom) lower-tropospheric geopotential height regressed on the standardized indices of the annular modes (the AO and its SH counterpart) based upon monthly data, Jan 1958-Dec 1997. Left panels are for the Southern Hemisphere, right panels are for the Northern Hemisphere. Units are  $\text{ms}^{-1}$  (top) and  $\text{m per std dev}$  of the respective index time series (bottom). Contour intervals are 10 m (-15, -5, 5, ...) for geopotential height and 0.5  $\text{ms}^{-1}$  (-0.75, -0.25, 0.25) for zonal wind.

mode, or NAO, makes a difference in how we interpret and understand such modes. The name “North Atlantic” Oscillation itself implies regional dynamics, perhaps even a role for the ocean, whereas the annular mode or Arctic Oscillation implies a more hemispheric dynamics, and perhaps a more significant role for the stratosphere. An aim in this study is to develop a better mechanistic and statistical understanding of the two modes of variability, to determine the context(s) in which the two modes are appropriate.

## Temporal Structure

The temporal structure of the NAO on interannual and on daily timescales is illustrated in Figure 1.4. Given the large overlap in the spatial structure of the NAO and NAM, the temporal evolution of the latter is quite similar, particularly at lower frequencies. The patterns clearly have power at very low frequencies – even decadal timescales – as suggested by positive phase trend over the 1980s and ’90s. The winter average variability, however, can be misleading. The extratropical jet is intimately connected with the midlatitude storm tracks, and shifts in the phase of NAO/NAM are associated with shifts in the storm track. A positive (negative) phase winter is better characterized as a string of positive or negative phase “events,” storms involving shorter timescales, from weeks to days, as seen in the lower panel of Figure 1.4.

Both the NAO and annular modes have a red spectrum, with more power on timescales of 10 days or more than on synoptic timescales. There is, however, no pronounced peak at any particular timescale. Given such a white spectrum at lower frequencies, it is possible that the decadal trends in the top panel of Figure 1.4 may be attributable to climate noise, that is, the tail of the spectrum whose dynamics are set exclusively by intraseasonal interactions.

To make this point more clear, consider a thought experiment where the NAO

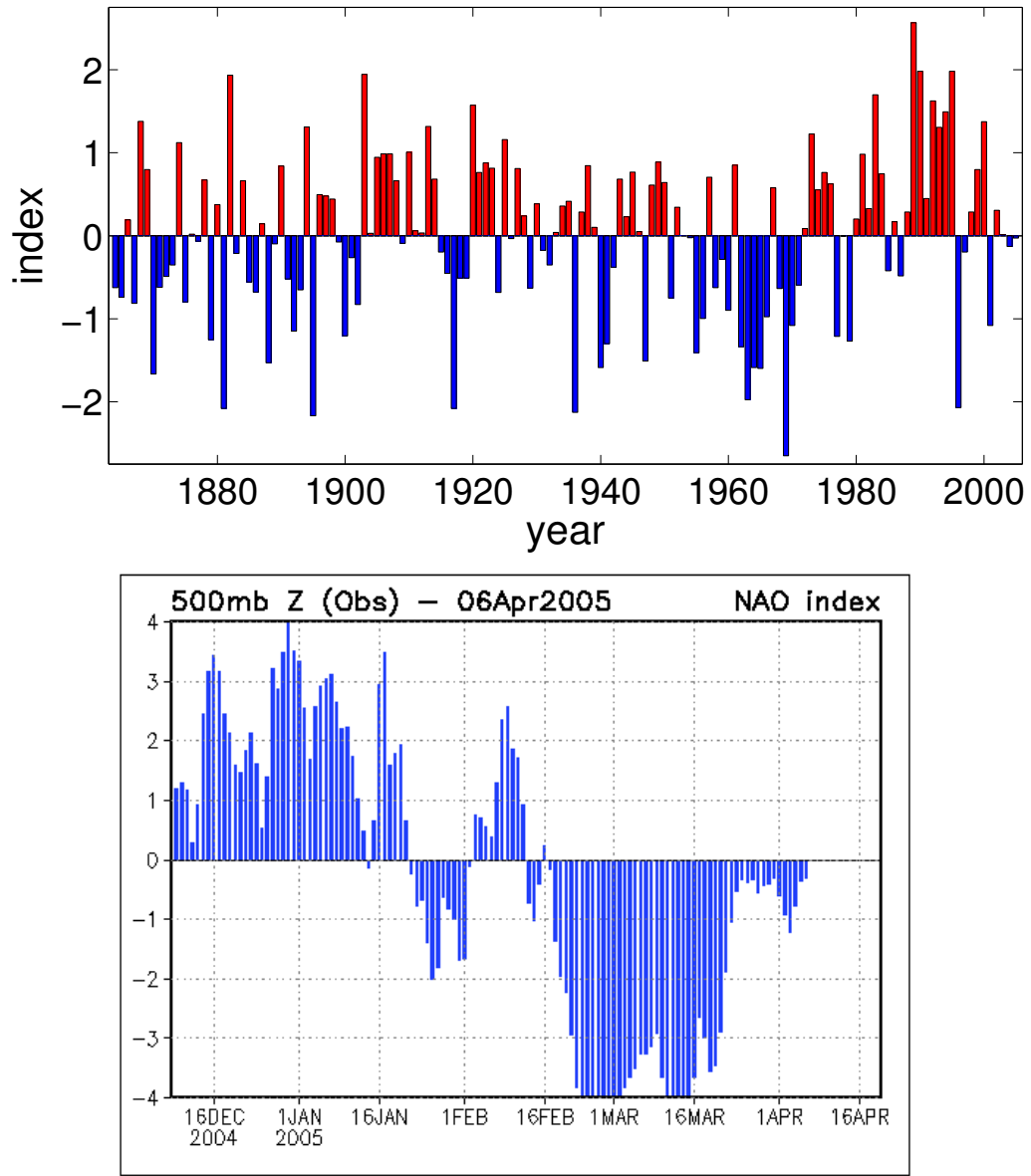


Figure 1.4: The variability of the NAO on interannual and daily timescales. (top) A long term reconstruction of the DJFM average NAO index from 1864-2005, by Jim Hurrell. The index was formed by differencing the surface pressure in Lisbon, Portugal and Stykkisholmur, Iceland. The pressures were normalized by their standard deviation to prevent bias toward the more variable northern center of action. The index was normalized to have unit variance. (bottom) The daily NAO index of the 2004-5 winter, from the Climate Prediction Center, <http://www.cpc.ncep.noaa.gov/products/precip/CWlink/pna/nao.shtml>. The index was formed by projecting the daily average 500 hPa geopotential surface onto the NAO loading pattern, and normalized so that the monthly average index has unit variance.

index is determined by a coin flip; if heads, the extratropical jet moves poleward for a month, if tails, equatorward. If one continues the experiment long enough, streaks will occur where a season's worth – or even decades worth – of heads or tails will dominate, despite the fact that such events are random at timescales longer than a month. The timescale at which independent events are selected, however, makes a critical difference to the likelihood of sustained events at lower frequencies. If the coin is flipped once a month, the probability of positive phase dominating a season, three heads in a row, is  $2^{-3} = 0.125$ . If the flip takes place every week, the chance of a consistently cold winter, 13 heads in a row,  $2^{-13}$  is significantly smaller, and with a daily coin flip, the chances become minuscule,  $2^{-90}$ . Hence, understanding the processes that control the decorrelation time (that is the time between independent events) on intraseasonal timescales can account for a large degree of the variability of the patterns at lower frequencies.

Feldstein (2000a) addresses this question for the variability of the zonal index, the first EOF of the zonally average angular momentum. Within a given season, the zonal index behaves much as a first order Markov (red noise) process with an e-folding time scale of 18, 8, 10, and 14 days in the Northern Hemisphere winter and summer, and the Southern Hemisphere winter and summer, respectively. By comparing the expected power at low frequencies for such a Markov process with the observed power on the zonal index, he concludes that interannual variability of the zonal index can be attributed to the tail of the intraseasonal distribution. In other words, there is no need for a mechanism to explain the variability of the zonal index on timescales beyond 10-20 days because it can be attributed to randomness.

Feldstein (2000b) applied the same analysis to the NAO, as defined by rotated component analysis in Barnston and Livezey (1987). Here, the evidence was not conclusive whether the variability of the NAO on interannual timescales could or could not be accounted for by randomness in the tail of the intraseasonal NAO distribution.

The statistical test came up in between this null hypothesis and the 95% certainty level that there is additional variation of the NAO on interannual timescales. [It is interesting to note that there was statistical evidence that the PNA has enhanced variability at interannual timescales that cannot be attributed to intraseasonal noise. This is not to say that there is less energy in the interannual NAO; rather, the PNA is not as persistent as the NAO on intraseasonal timescales, and so one would expect dramatically less power on interannual timescales.] Stephenson et al. (2000) also address the question of interannual variability of the NAO, focusing on the potential for multi-year predictability of the index. Their analysis was also limited by the relative shortness of the accurate records, which prevented them from making statistically rigorous conclusions.

In this study we are interested in understanding the intraseasonal variability of the NAO and annular modes, and thus focusing on atmospheric processes alone. Explaining the persistence of the modes on intraseasonal timescales – even if it is only 10 days – accounts for a substantial portion of the interannual variability. It is also likely that processes giving rise to persistence on longer timescales, such as interactions with sea surface temperatures, would not affect our conclusions regarding the internal variability of the atmosphere.

## 1.2 Research Overview: A Tale of Three Models

We have constructed a hierarchy of simple models to help us understand the spatial and temporal structure of the NAO and annular modes. The aim is to bracket the essential dynamics of the patterns; by adding and subtracting different elements of the dynamics, we isolate the essential processes that govern them. The simpler models clarify which dynamics are necessary for the existence of the NAO and annular modes. The more complex model provides insight into how the persistence of the patterns

can be extended when interactions between the large scale patterns and eddy forcing are permitted.

A barotropic model of the atmosphere on the sphere in Chapter 2 serves as a launch point for our research. With it we suggest that both the NAO and annular modes are a direct consequence of the “stirring” of the large scale flow by baroclinic eddies. The model shows how such stirring, as represented by a simple random forcing, leads to a variability in the zonal flow via a variability in the eddy momentum flux convergence. If the stochastic forcing is statistically zonally uniform, then the resulting patterns of variability (i.e., the EOFs) are zonally uniform and the pressure pattern is dipolar in the meridional direction: an annular mode. If the forcing is enhanced in a zonally localized region, thus mimicking the effects of a storm track over the ocean, then the resulting variability pattern is zonally localized, resembling the NAO. This suggests that the NAO and annular modes are produced by the same mechanism, and are manifestations of the same phenomenon.

The timescale of variability in the model is longer than the decorrelation timescale of the stochastic forcing. This is a consequence of the fact that these patterns characterize the zonal momentum in the atmosphere, the integral of the eddy momentum fluxes. Integration strengthens the power of low frequencies, which are ultimately truncated by nonlinear dynamics and friction to produce a red spectrum similar to that observed. The content of Chapter 2 appeared previously as “A Mechanism and Simple Dynamical Model of the North Atlantic Oscillation and Annular Modes,” in the *Journal of the Atmospheric Sciences*, **61**, pp 264-280, ©Copyright 2004 American Meteorological Society (AMS), a paper prepared with Geoffrey Vallis, Paul Kushner, and Benjamin Cash.

Results from the study of the barotropic model suggest that the basic spatial structure of the patterns, in particular the meridional dipole of geopotential height and zonal velocity, can be explained in a more idealized context. In Chapter 3,

we develop a series of analytic, purely stochastic models that show that the spatial structure of the NAO and annular modes is a natural consequence of the conservation of mass and zonal momentum and the geometric constraints of the extratropical circulation. The purely stochastic models also help us understand the nature of EOF analysis, and the criterion for a “statistical” annular mode – zonal symmetry of the statistics, as opposed to a “physical” annular mode – where there is zonal symmetry of the motions. The content of Chapter 3 appeared in “A Stochastic Model for the Spatial Structure of Annular Patterns of Variability and the NAO,” in the *Journal of Climate*, **18**, pp 2102-2118, ©Copyright 2005 AMS, a paper written with Geoffrey Vallis.

We verify the conclusions of the simpler models in a dry primitive equation general circulation model (GCM). In Chapter 4, NAO-like patterns are found by varying the degree of zonal asymmetry of the model’s synoptic variability (that is, the model’s storm track) with idealized topography and heating anomalies designed to approximate land-sea contrast. Only with the confluence of thermal and topographic forcing does a truly localized NAO-like pattern appear. The NAO can be better appreciated in the context of the eddy life cycle; maximum variability of the zonal flow is found in the exit region of the storm track, where eddy decay (and hence eddy momentum fluxes) dominates. In this region the extratropical, eddy driven jet is strongest, given the abundance of decaying eddies, while the subtropical, thermally maintained jet is weakest. This allows us to view the jets as two like signed vortices of approximately equal strength, and the variability can be viewed in terms of vortex-vortex interaction. Their separation and merger is, in essence, the NAO.

Lastly, we probe the temporal structure of the model in Chapter 5. The structure here is much richer than the barotropic model, as the dynamical core is “self stirring,” producing its own baroclinic instability which interacts with the large scale variability. This interaction can extend the persistence of the annular modes and

NAO through a feedback between the eddies and large scale flow. The feedback, however, is quite sensitive to resolution, model parameters, and to zonally asymmetries in the forcing, particularly topography. A thorough investigation of the model suggests that zonal asymmetries can disrupt the feedback mechanism, but fully understanding the sensitivity to model parameters and resolution has remained more elusive.

We summarize and conclude the thesis in Chapter 6. Here we present our impressions on the nomenclature and characterization of intraseasonal variability in the extratropics based on intuition gained from the three studies. And so, as Hans Egede and family set forth in 1721, we sail into unfamiliar waters, beginning our search for understanding with the barotropic model.

# Chapter 2

## The Barotropic Model: A Dynamical Null Hypothesis

### 2.1 Introduction

Although we may sometimes refer to intraseasonal variability as if there were a distinct timescale and a distinct phenomenon, there is no pronounced peak in the power spectrum of the atmospheric fields on the weeks-to-months timescale, nor is there a dip in the spectrum at timescales longer than that associated with baroclinic eddies. This suggests that the variability at intraseasonal timescales may be, at leading order, caused by a reddening of the power spectrum of the known forcing (i.e., baroclinic instability). That is, if we consider baroclinic instability to provide a nearly white stochastic forcing, then the barotropic response to such forcing will generally have a red spectrum. Both friction and nonlinear processes (i.e., chaos) tend to inhibit very long-term correlations and put a cap on the spectral reddening at some timescale, whitening the spectrum at long timescales and leading to decorrelation timescales potentially of about 10 days.

Although the NAO and annular modes are of larger scale than baroclinic eddies,

there is much to suggest that it is such eddy activity (i.e., weather systems) that is largely responsible for producing them, even though the patterns are fairly barotropic. On the theoretical side, large-scale eddy-driven structures often tend to be barotropic because the life-cycle of baroclinic eddies is characterized by a barotropic decay and a cascade to larger horizontal *and vertical* scales (Rhines 1977; Simmons and Hoskins 1978; Salmon 1980). Idealized model simulations (e.g., Orlanski 1998) have also shown the important role of baroclinic eddies in producing the quasi-stationary circulation. On the observational side, analysis of annular modes and the NAO indicates that transient, high frequency (i.e., 1–10 days) activity plays an important role in maintaining their variability (e.g., Lau 1988; Limpasuvan and Hartmann 2000; DeWeaver and Nigam 2000). Consistently, the midlatitude jet in the Atlantic sector is stronger during periods of high NAO index [Amabaum et al. (2001), their figures 6 and 7], and this jet is fairly barotropic, indicating an eddy-driven origin. Finally, recent experiments with a GCM (Cash et al. 2005) have shown a strong correlation between the location and strength of the dipole with the location and strength of the baroclinic eddy activity.

Assuming, then, that the relevant large-scale dynamics are indeed barotropic, but that that eddy activity is important as the ultimate source of the variability, our goal now is to understand how such higher-frequency (1–10 day timescale) eddy dynamics can produce the characteristic spatial patterns seen on longer (10–50 day) timescales. Specifically, we seek to present a simple dynamical model, perhaps the simplest possible dynamical model, of the NAO and annular modes in order to shed insight on the dynamics of such structures. We shall not present a complete model or a complete theory. Rather, our model might be considered as a ‘dynamical null-hypothesis’ that will be built upon in subsequent chapters to form a more complete theory. As noted in the introduction, the content of this chapter was published previously in Vallis et al. (2004).

## 2.2 The Basic Model

### 2.2.1 Jets on a $\beta$ -plane

Consider first the maintenance of the extratropical jet. This has a different dynamical origin from the highly baroclinic subtropical jet: the latter arises from a thermal wind balance with the strong meridional temperature gradients at the edge of the Hadley Cell, whereas the former is driven by eddy momentum flux convergence in midlatitude weather systems and, because these largely occur in the mature phase of the baroclinic life cycle, they act to produce a predominantly barotropic jet. In reality the subtropical and midlatitude jet are often not geographically distinct because the polar limit of the Hadley cell overlaps the equatorial limit of the midlatitude baroclinic zone, and the jets may appear as one.

A simple barotropic model illustrates the mechanisms of the eddy driven jet (e.g., Held 2000). For two-dimensional incompressible flow the barotropic zonal momentum equation is

$$\frac{\partial u}{\partial t} + u \frac{\partial u}{\partial x} + v \frac{\partial u}{\partial y} - fv = -\frac{\partial \phi}{\partial x} + F_u - D_u \quad (2.2.1)$$

where  $F_u$  and  $D_u$  represent the effects of any forcing and dissipation and the other notation is standard. The meridional momentum and vorticity fluxes are related by the identity

$$v\zeta = \frac{1}{2} \frac{\partial}{\partial x} (v^2 - u^2) - \frac{\partial}{\partial y} (uv) \quad (2.2.2)$$

so that with cyclic boundary conditions

$$\overline{v'\zeta'} = -\frac{\partial \overline{u'v'}}{\partial y}. \quad (2.2.3)$$

where the overbar denotes a zonal average, and  $\overline{v} = 0$ . (Equation (2.2.3) also holds, locally in  $x$ , if the average is a time or ensemble average provided that the eddy

statistics are zonally uniform.) Averaging (2.2.1) thus gives

$$\frac{\partial \bar{u}}{\partial t} = \overline{v' \zeta'} + \overline{F_u} - \overline{D_u} \quad (2.2.4)$$

again using that  $\bar{v} = 0$ , a result that again also holds in a time or ensemble average if the eddy statistics are zonally uniform.

Typically, there will be little direct forcing of the mean momentum, and if friction is parameterized by a linear drag then

$$\frac{\partial \bar{u}}{\partial t} = \overline{v' \zeta'} - r\bar{u} \quad (2.2.5)$$

where  $r$  is an inverse frictional timescale. Now consider the maintenance of this vorticity flux. The barotropic vorticity equation is

$$\frac{\partial \zeta}{\partial t} + \mathbf{u} \cdot \nabla \zeta + v\beta = F_\zeta - D_\zeta \quad (2.2.6)$$

where  $F_\zeta$  parameterizes the stirring of barotropic vorticity and  $D_\zeta$  represents dissipation. Linearize about a mean zonal flow to give

$$\frac{\partial \zeta'}{\partial t} + \bar{u} \frac{\partial \zeta'}{\partial x} + \gamma v = F'_\zeta - D'_\zeta \quad (2.2.7)$$

where  $\gamma = \beta - \partial \bar{u} / \partial y$  is the meridional gradient of absolute vorticity. From (2.2.7) form the pseudo-momentum equation by multiplying by  $-\zeta'/\gamma$  and zonally averaging, whence

$$\frac{\partial M}{\partial t} - \overline{v' \zeta'} = -\frac{1}{\gamma} (\overline{\zeta' F'_\zeta} - \overline{\zeta' D'_\zeta}) \quad (2.2.8)$$

where  $M = -\overline{\zeta'^2}/2\gamma$  is the pseudomomentum. From (2.2.5) and (2.2.8) we obtain

$$\frac{\partial \bar{u}}{\partial t} - \frac{\partial M}{\partial t} = -r\bar{u} + \frac{1}{\gamma} (\overline{\zeta' F'_\zeta} - \overline{\zeta' D'_\zeta}), \quad (2.2.9)$$

and in a statistically steady state

$$r\bar{u} = \frac{1}{\gamma}(\overline{\zeta' F'_\zeta} - \overline{\zeta' D'_\zeta}). \quad (2.2.10)$$

The terms on the right-hand-side represent the stirring and dissipation of pseudomomentum and in steady state their sum must integrate to zero. In a meridionally localized stirring region the first term can be expected to be positive; thus, meridionally localized but otherwise relatively unstructured vorticity stirring will give rise (for  $\gamma > 0$ ) to an eastward mean zonal flow in the region of the stirring, with a westward flow north and south of the stirring region. These equations represent the well-known physical argument that stirring gives rise to Rossby wave generation, and that momentum will converge in the region of stirring as the Rossby waves propagate away and dissipate.

If the stirred region is sufficiently broad then multiple jets may form within the stirring region (e.g., Vallis and Maltrud 1993; Lee 1997). In that case the mechanism of jet formation is often expressed in terms of an inverse energy cascade to larger scales, inhibited by the formation of Rossby waves, leading to the preferential formation of zonal flow. However, such jets may still be thought of as being maintained by the stirring of pseudomomentum, but the pseudomomentum stirring and dissipation are organized by the jet structure itself even though the vorticity stirring,  $F_\zeta$ , may be homogeneous. In the earth's atmosphere the stirring region (i.e., the midlatitude baroclinic zone) is relatively narrow in the sense that there is normally only one region of eddy driven eastward flow in the mean; however, the baroclinic zone is typically wider than the instantaneous jet itself, and the jet may thus meander within the baroclinic zone.

## 2.2.2 Source of stirring in a baroclinic atmosphere

The stirring that might generate such jets arises from baroclinic instability or, more precisely, from the transfer of energy from baroclinic to barotropic modes. To see this, consider the two-layer quasi-geostrophic equations

$$\frac{\partial q_i}{\partial t} + J(\psi_i, q_i) = 0, \quad i = 1, 2 \quad (2.2.11)$$

where

$$q_i = \nabla^2 \psi_i + F(\psi_j - \psi_i) + \beta y, \quad j = 3 - i. \quad (2.2.12)$$

and  $F$  is the inverse square deformation radius. If this is decomposed into barotropic and baroclinic modes in the standard way, the evolution equation for the barotropic mode becomes

$$\frac{\partial}{\partial t} \nabla^2 \psi + J(\psi, \nabla^2 \psi + \beta y) = -J(\tau, \nabla^2 \tau) \quad (2.2.13)$$

where  $\psi = (\psi_1 + \psi_2)/2$  and  $\tau = (\psi_1 - \psi_2)/2$ . The term on the right-hand-side is just the forcing of the barotropic mode by the baroclinic mode and although not sign definite, it generally leads to a transfer of energy into the barotropic mode as part of the baroclinic life cycle. Such stirring by baroclinic eddies thus gives rise to momentum convergence and is the ultimate cause of the surface westerly winds in midlatitudes. The vorticity flux producing the zonal jet will, of course, fluctuate simply because baroclinic activity fluctuates, partly in response to variations in the zonal shear itself and partly because it is a turbulent, chaotic system, and these fluctuations will give rise to variations in the zonal index (e.g., Feldstein and Lee 1998; Lorenz and Hartmann 2001). Although such variations will be largely barotropic, the stirring will be dependent in part on the barotropic flow, because the evolution equation of  $\tau$  involves  $\psi$ , and this may lead to feedbacks between the jets and the stirring. For example, the presence of surface drag may generate a shear from the

barotropic flow, and this in turn may produce baroclinic activity and enhanced stirring (Robinson 2000). In our numerical simulations, we will restrict ourselves to the simpler barotropic case and will model the stirring simply by a random process with time and space scales chosen to roughly mimic those of baroclinic instability, with no direct dependence on the jet itself.

### 2.2.3 Patterns of variability

Because the stirring is produced by a chaotic process it will fluctuate, and this will produce a response in the zonal wind field and the associated circulation. In particular, a fluctuation in the vorticity flux that has a simple meridional structure will produce a dipolar structure in the pressure or streamfunction field. To illustrate this, Figure 2.1 shows an idealized localized northward eddy flux of vorticity (light arrows). Two circuits are shown as solid contours with circulation  $\Gamma = \oint u_t ds$ , where  $u_t$  is the velocity component tangential to the circuit. With the mechanical damping, we have

$$\frac{d\Gamma}{dt} = \oint u_n \zeta ds - r\Gamma \quad (2.2.14)$$

where  $u_n$  is the velocity component normal to the (right-hand oriented) circuit. Because the flow is incompressible,  $\oint u_n ds = \oint (\partial\psi/\partial s) ds = 0$ , where  $\psi$  is the streamfunction. Thus, if an overbar (e.g.,  $\bar{u}$ ) denotes the average along the circuit, and a prime ( $u'$ ) the departure from this average, then

$$\frac{\partial \bar{u}_t}{\partial t} = \overline{u'_n \zeta'} - r\bar{u}_t, \quad (2.2.15)$$

and for the time average in addition to the circuit average

$$\bar{u}_t = \overline{u'_n \zeta'}/r. \quad (2.2.16)$$

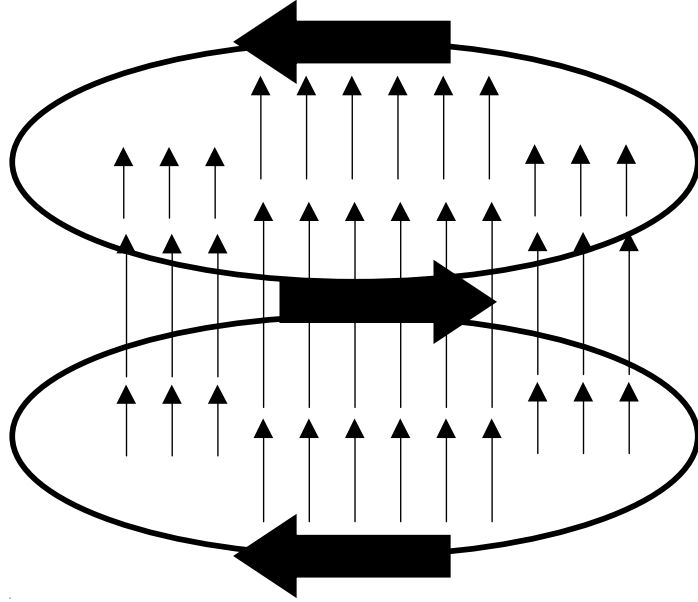


Figure 2.1: Circulation pattern induced by anomalous vorticity fluxes, in longitude (horizontal axis) and latitude (vertical axis). The light arrows represent time- or ensemble-mean fluxes of eddy vorticity. The contours represent circuits for the calculation of circulation. The heavy arrows on the circuits represent the circulation that results from the eddy vorticity flux.

Thus, a time-mean eddy flux of vorticity out of the circuit will give rise to a mean circulation. In Figure 2.1, to the north of the maximum vorticity flux, a cyclonic circulation will result, and to the south an anticyclonic circulation. This change in sign of the circulation corresponds to a change in sign of the streamfunction; if the pattern of vorticity flux is interpreted as an anomaly from climatology, the eddy vorticity flux then produces a dipolar circulation anomaly. If the fluctuation is zonally symmetric, then the circulation anomaly will extend around the hemisphere. If the fluctuation is confined to some region of longitude as in Figure 2.1, then the fluctuation will be a zonally localized dipole, rather like the NAO.

The argument above provides information about the circulation around a closed loop and, formally, says nothing about the zonal velocity itself. (Of course the loop may extend around a latitude circle, in which case  $u_t$  is the zonal velocity and we recover (2.2.5).) However, we may also expect that locally stronger stirring will give

rise to a locally stronger and more variable zonal jet: if the zonal scale over which the eddy statistics vary is longer than the meridional scale, then the first term on the right-hand-side of (2.2.2) will be smaller than the second term, after time averaging, and (2.2.3) will *approximately* hold. Similarly, the zonal advection of momentum in (2.2.1) will be smaller than that of meridional momentum, and the upshot is that (2.2.5) will approximately hold, with the overbar representing an average over a zonal sector without the need for complete zonal averaging.

Thus, in regions where stirring is enhanced over a reasonably broad zonal extent — e.g., the storm track regions — we expect to observe two related phenomena: (i) A stronger and more variable zonal jet; (ii) streamfunction or pressure anomalies that have the dipolar structure noted above. Furthermore, because these are anomaly fields, any diagnostic that seeks to economically represent the patterns of pressure or streamfunction variability, for example the EOFs, will also have a dipolar structure, and this is of course the characteristic pattern of the NAO. The latitude of the node of the mean streamfunction dipole will be that at which the mean vorticity flux is largest, and this is latitude of the mean jet itself. However, the distribution of the anomalous fluxes need not coincide with that of the mean fluxes, and we will see in Section 2.4 that the node of the EOF of the streamfunction, representing the variability of the pattern, is often poleward of the jet and associated with a change in the position of the jet.

### 2.3 Numerical model

To see whether eddy stirring can indeed produce the characteristic spatial patterns and temporal variability of annular modes and the NAO, we integrate the barotropic

vorticity equation on the sphere, namely

$$\frac{\partial \zeta}{\partial t} + J(\psi, \zeta + f) = S - r\zeta + \kappa \nabla^4 \zeta. \quad (2.3.1)$$

The notation is standard, with  $f = 2\Omega \sin \vartheta$ , where  $\vartheta$  is latitude,  $\zeta$  is vorticity and  $\psi$  streamfunction. The model is spectral with the nonlinear term evaluated without aliasing using a spectral transform method. Typically, the model is run at a resolution of T42 with test integrations at T84; this is more than adequate resolution because our concern is large-scale patterns. The last two terms on the right hand side of (2.3.1) are a linear drag and a term to remove the enstrophy that cascades to small scales, these being the simplest parameterizations of those processes that remove momentum and enstrophy from the flow. The coefficient  $\kappa$  depends on the model resolution, for that term is a subgridscale closure. The linear drag has some physical grounding in Ekman layer theory, and for a barotropic representation of the atmosphere reasonable values of  $r$  are of order  $1/5 - 1/10$  days $^{-1}$ .

The term  $S$  represents stirring of the barotropic flow by baroclinic eddies, and we represent this by a Markov process, similar to that employed in Maltrud and Vallis (1991). Typically, we choose to excite a small range of wavenumbers,  $n_{\min} < n < n_{\max}$  where  $n$  is the total wavenumber and  $n_{\min} = 8$  and  $n_{\max} = 12$ , except that small zonal wavenumbers, including the zonal flow, are excluded from the forcing. (Specifically we exclude modes with  $m = 0$  to  $m = 3$ .) Ideally, we might prefer to not impose any particular timescale on the variability of the model fields, but a white noise forcing (which has equal amplitudes at all timescales) is not particularly realistic or appropriate, because the highest realizable frequencies would be time step dependent and would not generate much response in the vorticity field, leading to a very noisy solution. Rather, we choose the random forcing to have a decorrelation timescale of about two days, similar to that of baroclinic instability. We satisfy this by making the

forcing in each wavenumber,  $S_{mn}$  to be itself the outcome of the stochastic process

$$\frac{dS_{mn}}{dt} = \dot{W}_{mn} - S_{mn}/\tau \quad (2.3.2)$$

where  $\dot{W}$  is a white noise process (a different realization for each wavenumber) and the parameter  $\tau$  determines the decorrelation time of the forcing. To implement (2.3.2), we use the related finite difference equation,

$$S_{mn}^i = (1 - e^{-2dt/\tau})^{1/2} Q^i + e^{-dt/\tau} S_{mn}^{i-1} \quad (2.3.3)$$

where  $Q^i$  is chosen randomly and uniformly  $\in (-A, A)$  where  $A$  determines the overall forcing amplitude,  $dt$  is the model time step, the superscript  $i$  is the time step index, and  $\tau$  is the prescribed decorrelation time of the forcing, which we choose to be two days.

To understand (2.3.3), we first characterize the behavior of  $S_{mn}$  in (2.3.2), which is known in the Stochastic Calculus literature as an Ornstein-Uhlenbeck process. For simplicity we drop the subscripts  $m$  and  $n$  and consider the generic process  $S$ ,

$$\frac{dS}{dt} = \frac{\sigma\sqrt{2}}{\sqrt{\tau}} \dot{W} - \frac{S}{\tau} \quad (2.3.4)$$

$$S(0) = S_0 \quad (2.3.5)$$

where  $S_0$  is the initial condition and  $W$  is the Wiener Process. As will be seen shortly, the coefficient  $\sigma(2/\tau)^{1/2}$  was chosen to control the variance of  $S$ .  $W$  has the special property that the joint distribution of  $\{W(t_i)\}$  on any set of times  $\{t_i\}$  is Gaussian. Stochastic processes with this property are known as Gaussian processes, and are wholly characterized by their mean and covariance functions.  $S$  inherits this property from  $W$ . Thus, to build a finite difference approximation to  $S$ , we need only

worry about matching its mean and covariance functions,

$$E[S(t)] = e^{-t/\tau} E[S_0] \quad (2.3.6)$$

$$\begin{aligned} \text{cov}(S(s), S(t)) &= e^{-(s+t)/\tau} \text{var}(S_0) + \sigma^2 e^{-(t-s)/\tau} \\ &\quad - \sigma^2 e^{-(s+t)/\tau} \end{aligned} \quad (2.3.7)$$

where  $s \leq t$ . When  $s, t \gg 0$ , the mean and covariance functions approach

$$E[S(t)] \rightarrow 0 \quad (2.3.8)$$

$$\text{cov}(S(s), S(t)) \rightarrow \sigma^2 e^{-(t-s)/\tau} \quad (2.3.9)$$

regardless of the initial distribution of  $S_0$ . In our model we are interested in the long term statistical behavior of the system and so lose nothing by taking the initial distribution of  $S_0$  to be the asymptotic distribution,  $N(0, \sigma^2)$ . In this case, (2.3.6) and (2.3.7) become (2.3.8) and (2.3.9).

We next consider properties of (2.3.3) by analyzing the similar finite difference equation,

$$S^i = (1 - e^{-2dt/\tau})^{1/2} \phi^i + e^{-dt/\tau} S^{i-1} \quad (2.3.10)$$

where  $dt$  is our time step and the  $\phi^i$  and  $S^0$  are random variables taken from the Gaussian distribution  $N(0, \sigma^2)$ . As a series of sums of Gaussian variables,  $\{S^i\}$  is also a Gaussian process. Its mean and covariance functions are given by

$$E[S^i] = 0 \quad (2.3.11)$$

$$\text{cov}(S^i, S^j) = \sigma^2 e^{-(j-i)dt/\tau} \quad (2.3.12)$$

for  $i \leq j$ , which match the properties of the continuous process  $S$ . As both  $S(t)$  and  $S^i$  are Gaussian Processes, the paths  $S^0, S^1, S^2, \dots$  are then equivalent to paths

Experiment	Meridional half-width of stirring region	Damping timescale	Zonally symmetric
Z1	12°	6 days	Yes
A1	12°	6 days	No

Table 2.1: Parameters for the baseline numerical experiments. Experiments with varying parameters are branches off these with a single parameter varied, unless noted. The decorrelation timescale of the forcing is always 2 days. The stirring region has a Gaussian distribution in latitude,  $\exp[(\vartheta - \vartheta_0)^2 / 2\sigma_\vartheta^2]$ , and the 'half-width' is actually the standard deviation,  $\sigma_\vartheta$ , of this. The zonally asymmetric forcing for A1 is described by (2.5.1), with  $B = 1$  and  $\sigma_x$  corresponding to 45°.

of  $S(t)$  sampled at increments of  $dt$ , and the result is time step independent.

In (2.3.3), we sample the  $\phi^i$  from a uniform distribution centered about zero, rather than a Gaussian. The modified process is not precisely an Ornstein-Uhlenbeck process: it has the same mean and covariance structure of  $S$ , but slightly different higher moments. It proved advantageous in avoiding occasional large (and unrealistic) spikes in a single wavenumber. For a small time step, the simpler algorithm presented in Maltrud and Vallis (1991) becomes equivalent to this one.

This spectral forcing is then transformed to physical space, where it is masked such that it has a non-negligible amplitude only in a midlatitude band, centered at 45° with about a 25° width. For some experiments it is also made statistically zonally nonuniform; that is, it is enhanced in a longitudinally confined region to mimic the effects of enhanced stirring in storm tracks. As for the symmetric case it is constructed to have zero projection on the zonally symmetric flow (modes with  $m = 0$ ) at all times.

Apart from this meridional masking and the choice of the scale of the stirring, the stochastic forcing is relatively unstructured, and the resulting momentum flux convergences result from the nonlinear dynamics of the model. This type of stochastic model differs from that used in, for example, Branstator (1990) or Whitaker and Sardeshmukh (1998), in which the model is linear and the mean flow is taken from observations or a GCM. Here the model is nonlinear, and it is the stochastic forcing

in conjunction with nonlinear dynamics that generates the mean flow, and that is important for its pattern of variability.

Given the general form described above, for a given set of parameters the model is first spun up, and the integration continued for a period of order 10000 days over which diagnostics are obtained. The main parameters we have varied are: (i) The strength of the forcing and its degree of zonal asymmetry, i.e. the strength of the storm track. (ii) The meridional width of the forcing region; (iii) The strength of the friction (the surface drag). Regarding (i), the overall strength of the forcing is tuned to produce a zonal jet of reasonable strength. Note that the forcing is meant to produce an eddy momentum flux convergence which is responsible for producing non-zero *surface* winds in the mid-latitude atmosphere. However, a barotropic model is often thought of as a representation of the *vertically integrated* flow. Such an ambiguity is unavoidable in a model with only one degree of freedom in the vertical; our control integration uses a forcing that produces a zonally averaged wind of about  $10 \text{ m s}^{-1}$ . Regarding (ii), in our control integration our forcing strength has Gaussian distribution in latitude, centered at  $45^\circ$ , with a meridional half-width of  $12^\circ$ . This is varied from  $3^\circ$  to being as wide as the hemisphere. Regarding (iii), the results are not sensitive to the strength of the friction when this is in the range  $1/5 - 1/10 \text{ days}^{-1}$ , and most of the simulations presented here use  $1/6 \text{ days}^{-1}$ . The parameter values for the primary simulations in the study are listed in Table 2.1.

## 2.4 Results with Zonally Symmetric Stirring

### 2.4.1 Mean state for zonally symmetric model

A typical time and zonally averaged zonal wind, and the rms (i.e., eddy) velocity are illustrated in Figure 2.2 for the pivot experiment Z1. A strong westward jet emerges in the region of the forcing, flanked by two eastward jets, rather stronger on the

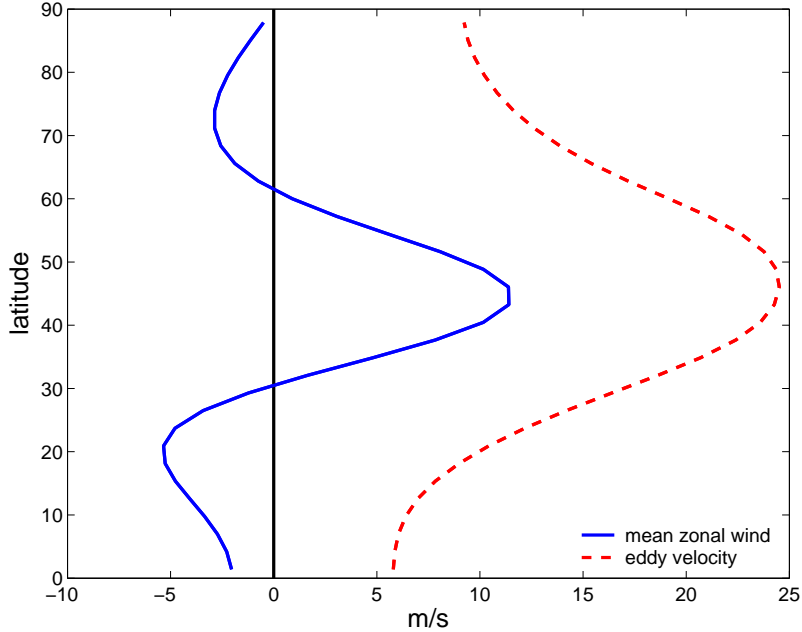


Figure 2.2: The time and zonally averaged zonal wind (solid line) from the zonally symmetric numerical model Z1 (see Table 2.1). The dashed line is the rms (i.e., eddy) velocity. The stochastic forcing is zonally uniform, and is a Gaussian distribution in the meridional direction, centered at  $45^\circ$  with  $12^\circ$  half-width.

equatorial side. Consistently, the mean position of the jet is somewhat poleward of the center of the stirring, and this poleward offset increases slightly as the forcing strength increases. The eddy velocities are of the same order of magnitude, albeit a little larger than, the zonally averaged velocity, a characteristic also of the flow in the earth's atmosphere. The pseudomomentum stirring and dissipation responsible for the mean jet are illustrated in Figure 2.3. The pseudomomentum forcing is large and positive in the jet center, with a fairly narrow distribution. The distribution of the pseudomomentum dissipation is broader, reflecting the meridional propagation of Rossby waves away from the stirring region

The natural meridional scale of a jet in homogeneous barotropic turbulence is determined by the eddy kinetic energy, and the value of  $\beta$  and friction (e.g., Maltrud and Vallis 1991; Smith et al. 2002). As noted above, if the meridional extent of the forcing region is allowed to become larger than that jet scale, alternating jets may

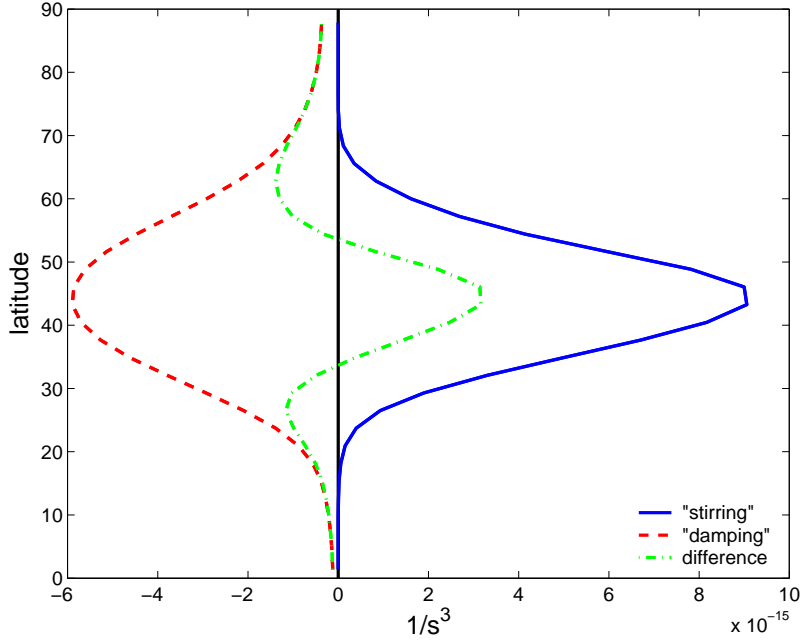


Figure 2.3: The pseudomomentum stirring  $\overline{F'_\zeta \zeta'}$  and dissipation  $\overline{D'_\zeta \zeta'}$  and their sum [see equation (2.2.10)] for Z1. The distribution of dissipation is broader than the forcing, resulting in an eastward jet where the stirring is centered, with westward flow on the flanks.

form within the forcing region. This phenomena is illustrated in Figure 2.4 when the forcing has no meridional localization, although the forcing and resulting eddies are too strong for multiple jets to be produced.

### 2.4.2 Variability

Now consider the variability of a single, eddy-driven zonal jet. Consider the momentum equation (2.2.5) and suppose that the vorticity flux is such as to produce an eastward jet in midlatitudes, and that its magnitude fluctuates temporally but that its meridional structure remains fixed. Then the zonally averaged zonal wind will fluctuate in place — it will pulse — and the associated EOF of the zonal wind will be similar to that of the mean wind (Figure 2.5a). Since at each instant the pressure field (the streamfunction) and the velocity are linearly related the associated variability in the pressure field can be expected to be a dipole. If the zonal wind fluctuates in

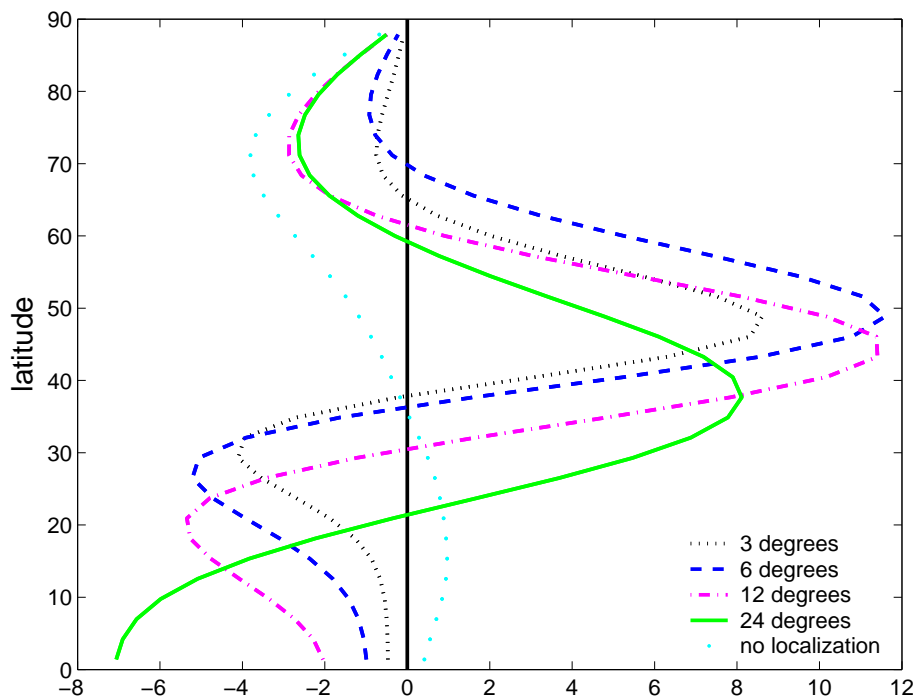


Figure 2.4: Time and zonally averaged zonal flow in experiments with varying half-widths of the forcing zone. If the forcing zone is narrow, then a single eastward jet forms in the region of the forcing.

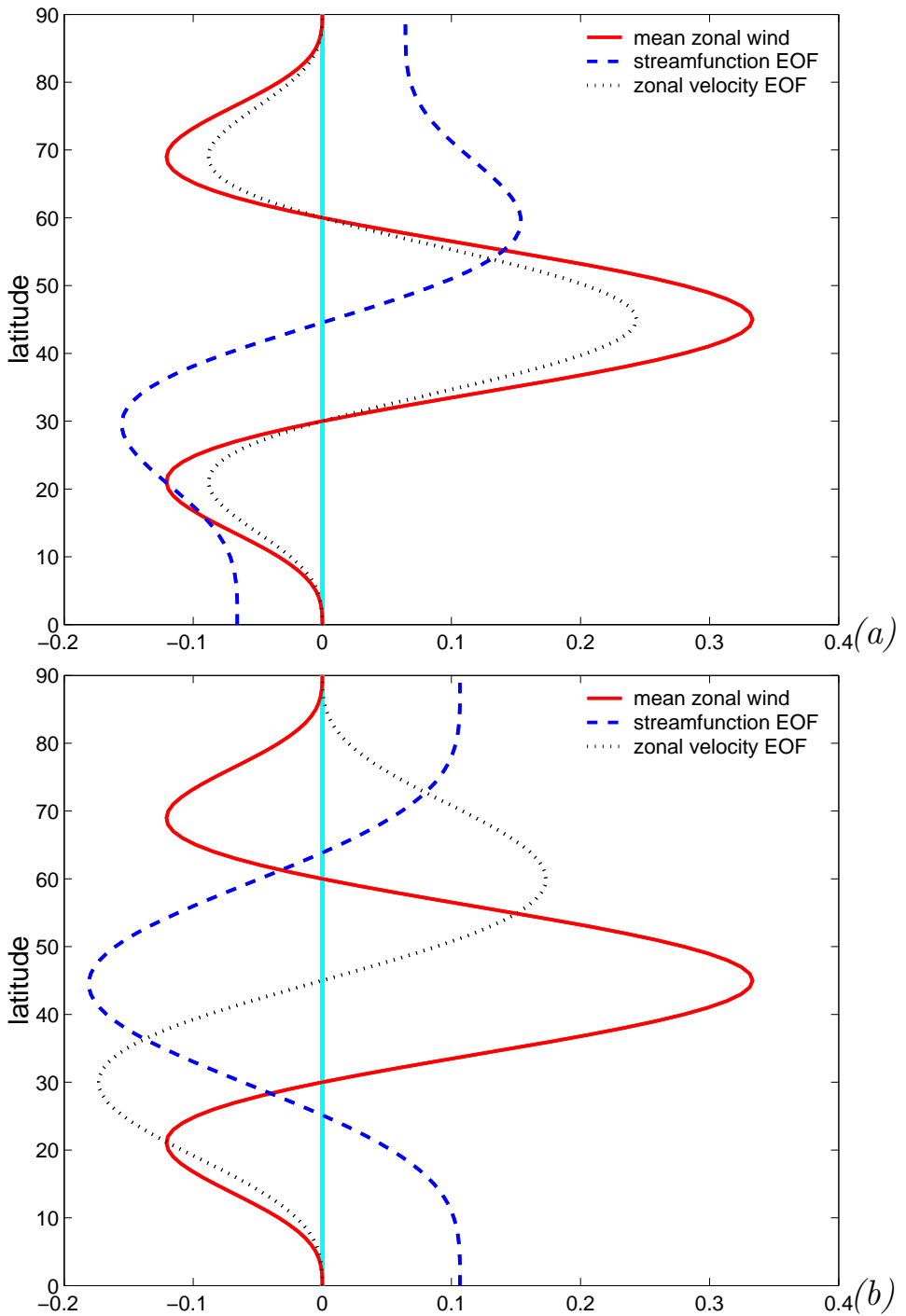


Figure 2.5: (a) Schematic of the leading EOFs associated with a pulsing jet. Solid line is the mean zonal wind itself, the dotted line is the EOF of the zonal velocity and the dashed line the EOF of the pressure or streamfunction field. (b) As for (a) but for the leading EOF associated with a wobbling or oscillating jet.

this way, the node of the pressure EOF will coincide with the maximum of the jet, which in turn occurs where the stirring is strongest. The other dominant mode of variability might be termed a wobbling of the zonal jet, that is an oscillation in its latitude without necessarily any change in amplitude (Figure 2.5b).

Both pulsing and wobbling behavior frequently occur in our numerical simulations, and one factor determining which is dominant is the width of the stirring region. If the stirring region is narrow (narrower than the resulting jet) then the jet position is effectively fixed and the first EOF resembles the jet itself. If the stirring region is wider than the natural width of a single jet, but not sufficiently wide to support two jets, the jet's position can vary within the stirred region. The behavior in these two cases is illustrated in Figure 2.6. (Here and elsewhere two-dimensional EOFs are constructed from the fields after applying a ten-day running average.)

With a stirred region of similar meridional extent to that of the baroclinic zone on earth a wobbling or a ‘mixed’ mode tends to prevail (Figure 2.7), with the second EOF looking more like a pulse. The first EOF of the streamfunction is dipolar, with a node somewhat poleward of the mean position of the jet and the lower band more or less coincident with the mean position of the jet. These structures are apparent in both the EOF of the zonally averaged fields, and in the zonally averaged EOF of the two dimensional fields (not shown). The first EOFs are typically well separated from the other EOFs. Similar structures are seen in the observations (Feldstein and Lee 1998; Lorenz and Hartmann 2001) and in simulations with a general circulation model (Cash et al. 2002). Indeed Feldstein and Lee (1998) characterize the EOFs of the northern and southern hemispheres as being either a strengthening and weakening of the jet, or a latitudinal movement of the jet, although the interpretation is complicated by additional variations in the subtropical jet.

Although useful as descriptive phrases, the pulsing and wobbling modes are not necessarily distinct physical modes. Recall that the mean wind is somewhat poleward

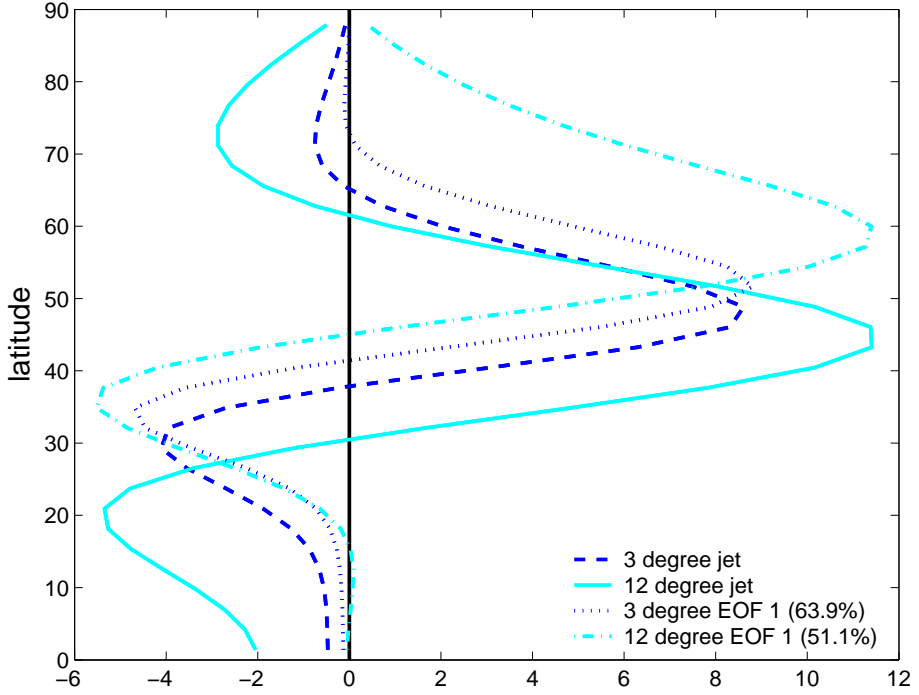


Figure 2.6: The mean value and the first EOF of the zonally averaged zonal wind simulations with a narrow stirring region (approximately  $3^\circ$  half-width) and a broader stirring region (approximately  $12^\circ$  half-width). For the narrow forcing region, the first EOF is almost a ‘pulse’, with a structure similar to that of the jet itself. For a wider forcing region, the first EOF is closer to a ‘wobble’. Figures in parentheses indicate variance accounted for.

of the center of the stirring, because of predominantly equatorward breaking of the Rossby waves. If the stirring is stronger, the jet is not only stronger but is pushed slightly poleward, and the pulse and the wobble are synchronized. The EOFs are describing this in the most economical way possible, subject to their orthogonality.

### 2.4.3 Two-dimensional patterns

When one looks at the EOF of the two-dimensional fields, the zonal average of the first EOF (of either velocity or streamfunction) is usually very similar to the EOF of the zonally average field. The same does not hold for subsequent EOFs. The first EOF normally is well separated from the others, although the variance accounted for is typically less than 20%. The first EOF of the two-dimensional streamfunction is

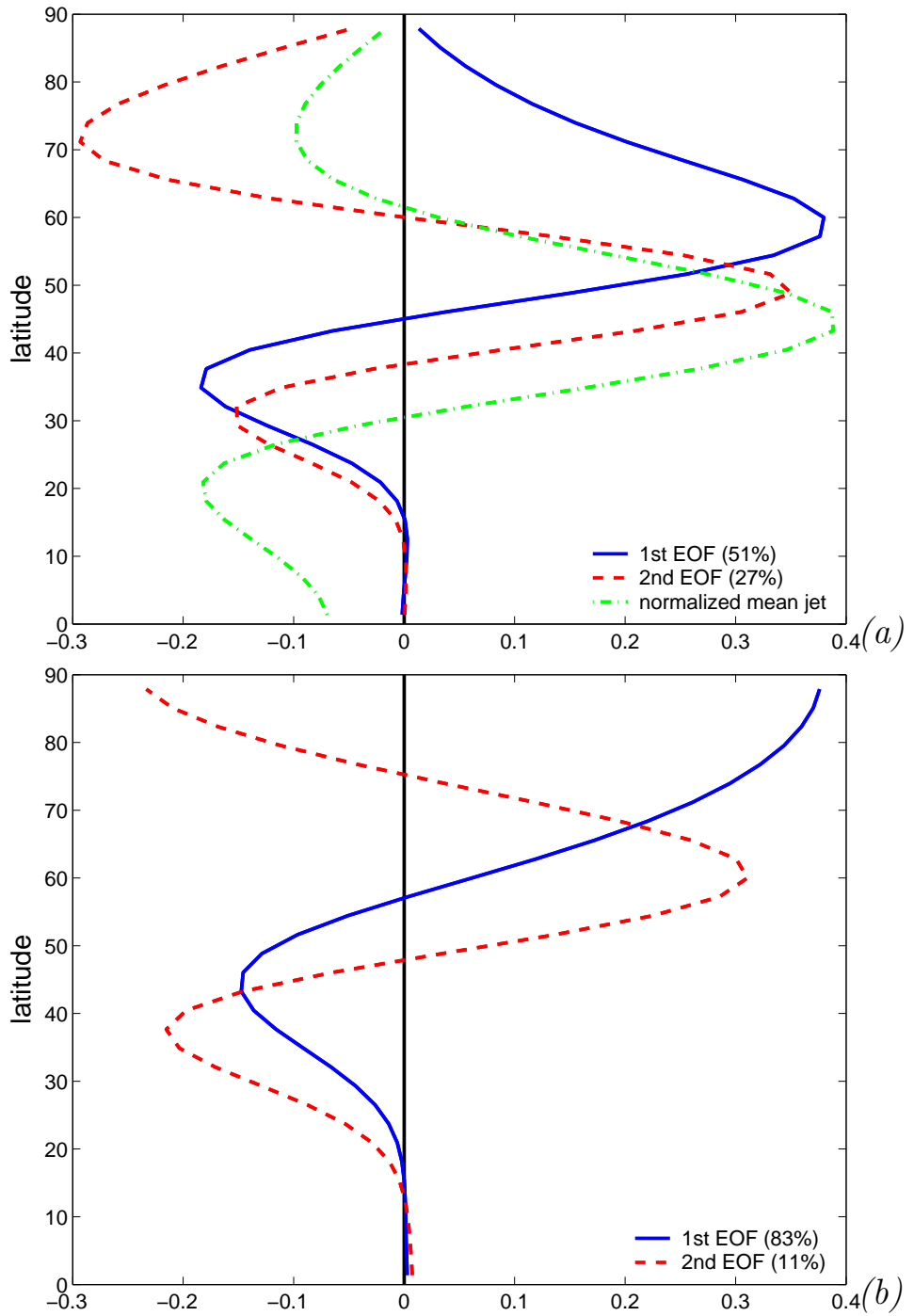


Figure 2.7: (a) The first two EOFs (solid and dashed, respectively) of the zonally averaged zonal wind forced in the zonally symmetric configuration, Z1. The solid line corresponds to a ‘wobbling’ zonal wind, the dashed to a ‘pulsing’ zonal wind. The light dotted line is the mean zonal wind. (b) Corresponding EOFs of the zonally averaged streamfunction.

illustrated in Figure 2.8. It is nearly zonally symmetric and may be taken as a definition of the annular mode of this model. Now, even though the time averaged flow is zonally symmetric, the leading EOF itself is not guaranteed to be zonally symmetric. (Suppose, for example, that all the model variability occurred at zonal wavenumber 5, then the first two EOFs would show wavenumber 5 patterns, in quadrature with each other.)

Nevertheless, the presence of a zonally symmetric first EOF should not lead one to conclude that there is a necessarily strong mode of hemispheric-wide variability in the model: the EOF analysis is merely seeking the most economical description of model variability. In particular, in most of the integrations we have examined the zonal flow does not vary synchronously across the hemisphere. The one-point correlation function shows this quantitatively (Figure 2.9). In the meridional direction, the dipolar structure of the EOF can be seen in the correlation function, especially the one centered at the pole. The zonal scale of the correlation is related to the scale of the energy containing eddies, as one might expect given that the spatial correlation function is essentially the Fourier transform of the variance of that variable (so the velocity correlation function is the Fourier transform of the energy spectrum). Thus, large-scale hemispheric-wide correlations are associated with variance in the  $m = 0$  mode and, even though zonal jets are naturally produced by eddies on the sphere or  $\beta$ -plane, the covariability of flow around a circle of latitude may be relatively weak. Ultimately, the importance or meaningfulness of an annular mode is related to how much eddy energy is in the zonal modes, and this is a quantitative issue that can ultimately be settled only by an appeal to observations (see also Cohen and Saito. 2002). The spatial structure of these correlations are in fact very similar to those found in various simulations with a general circulation model (Cash et al. 2002). There too the first EOF is almost zonally symmetric and meridionally dipolar, but there is little hemispheric-wide correlation.

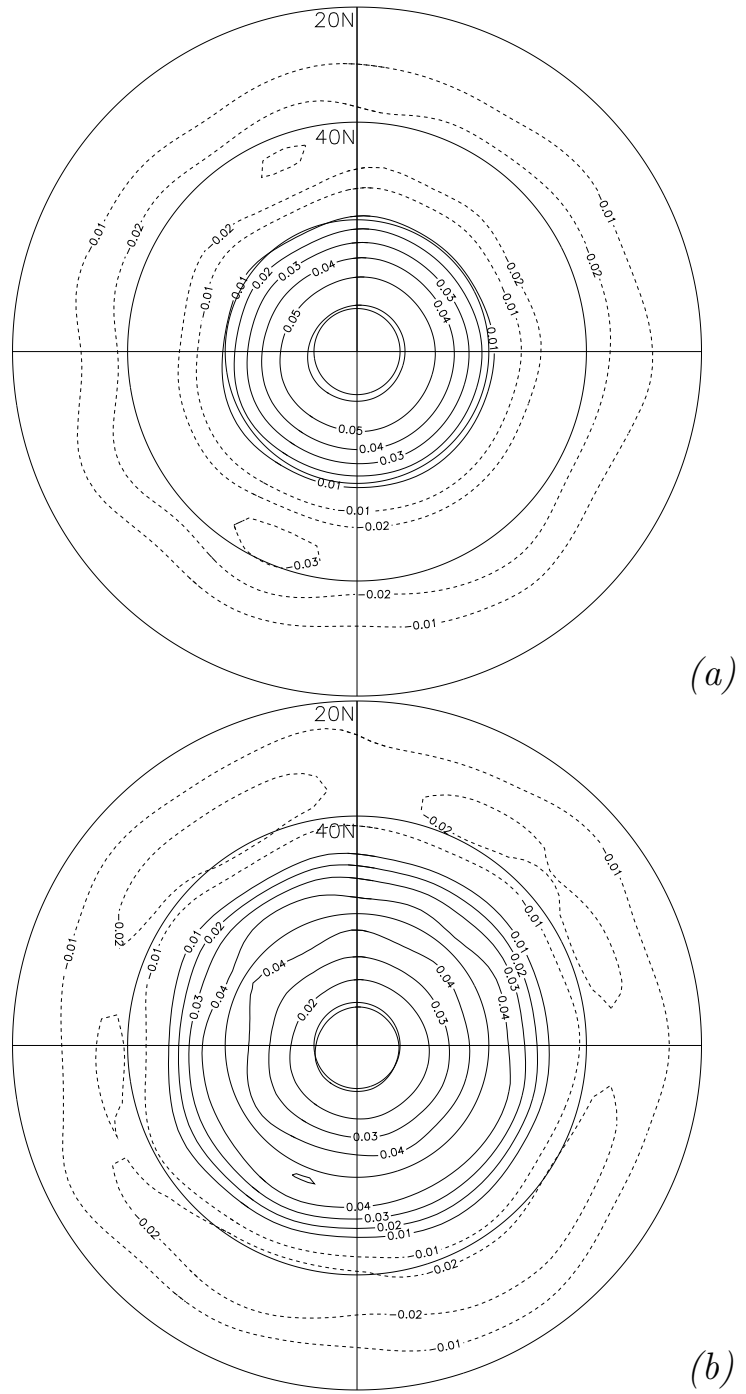


Figure 2.8: (a) The leading EOF of the streamfunction (with a 10 day running average) when the model is forced in the zonally symmetric configuration, Z1. The first and second EOFS account for 15% and 5% of the variance, respectively. (b) Leading EOF of the (10-day averaged) zonal wind. The first two EOFS account for 11% and 5% of the variance. The zero contours are omitted.

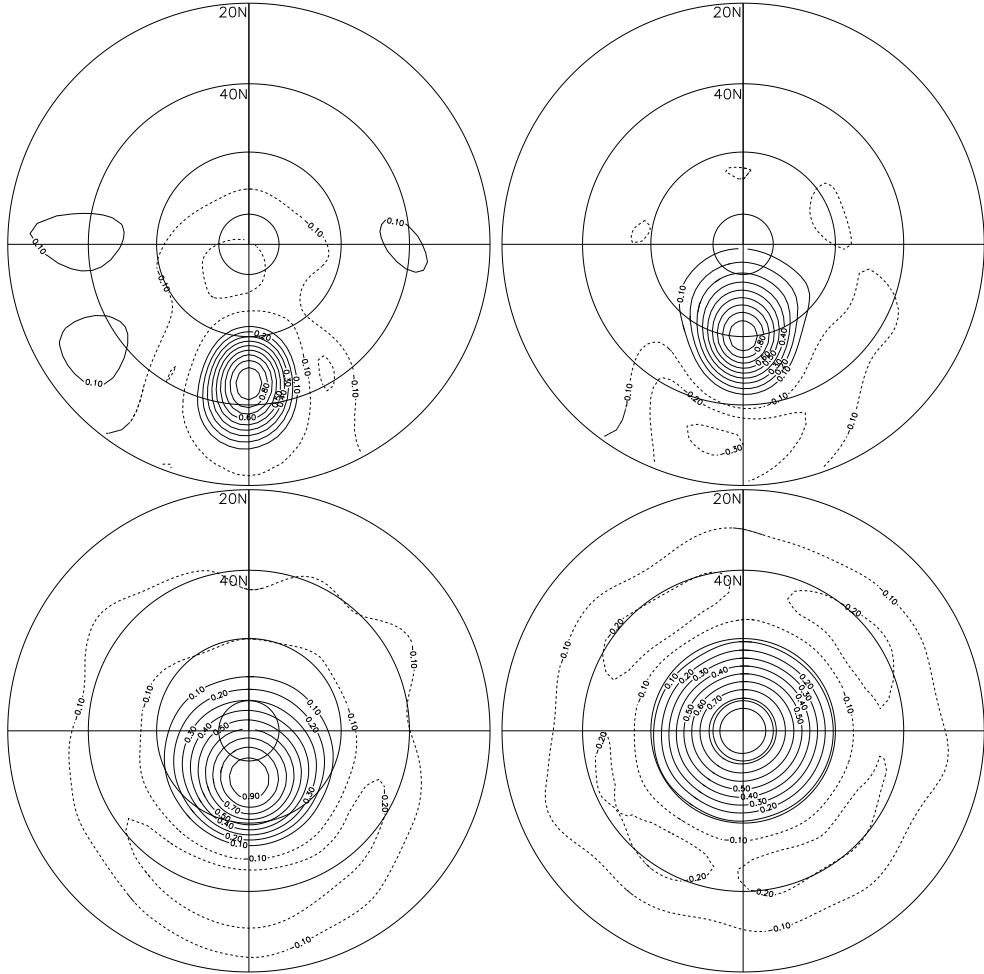


Figure 2.9: The one-point auto-correlation of the streamfunction for the same integration as Figure 2.8, for four different base points (which can be identified as the points where the correlation is one). Because the statistics are zonally symmetric, the longitude of the base points is unimportant. The zero contours are omitted.

We can obtain another sense of the hemispheric vs local nature of the variability by constructing the EOFs from a quadrant (i.e., regions  $90^\circ$  wide) rather than the full hemisphere. In both cases the fields are put through a 10-day running average before computing the EOFs, and these are illustrated in Figure 2.10. The first EOF of the regional field is quite similar with that constructed from the full hemispheric field, consistent with the notion that it is the same mechanism producing the variations in the zonal velocity on a hemispheric and on a regional scale. (In fact, if the EOF computed from the zonally averaged flow is regressed onto the sector-averaged flow, the correlation of this time-series with the time-series of the principal component in the sector is almost always over 95%.)

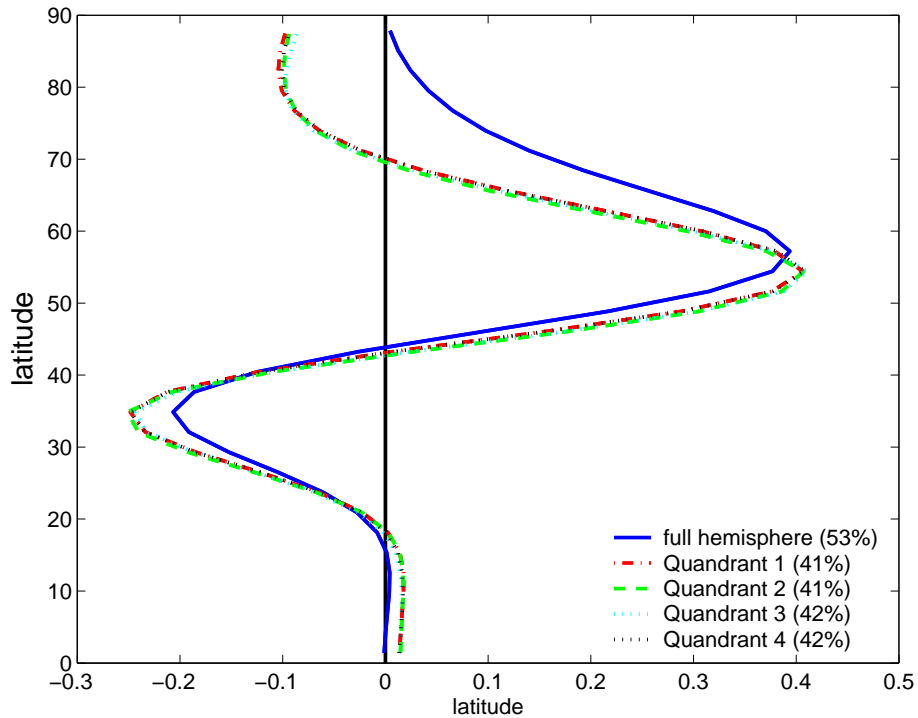


Figure 2.10: The EOF calculated from the zonal averaged flow in the entire hemisphere and from the zonally averaged flow in four quadrants (various dashed lines, on top of each other) for Z1. If the hemispheric EOF is regressed onto data in any one quadrant, then its time series has a correlation of approximately 0.97 with that of the principal component in the quadrant.

However, the variations in the various quadrants are not always in concert. To quantify this, we compute the correlations between the daily time series of the principal components (PCs) corresponding to the regional and hemispheric EOFs, and between two opposing quadrants. The values of these are:

$$C(Z, Q1) = 0.61 \quad (2.4.1a)$$

$$C(Z, Q2) = 0.63 \quad (2.4.1b)$$

$$C(Q1, Q2) = 0.06. \quad (2.4.1c)$$

Here  $C(Z, Q1)$  is the temporal correlation between the PCs of the first EOF from the zonally averaged flow and that of flow in a quadrant (and similarly for  $C(Z, Q2)$ ), and  $C(Q1, Q2)$  is the correlation between the flow in the two quadrants. The difference between  $C(Z, Q1)$  and  $C(Z, Q2)$  is solely due to the finite length of the time series, and so is a measure of the error due to that.

If there were a pure annular mode in the sense that the zonal velocity varied in unison on a hemispheric scale the correlations would all be unity. If the quadrants were completely independent we would have

$$C(Z, Q1) = 0.5 \quad (2.4.2a)$$

$$C(Z, Q2) = 0.5 \quad (2.4.2b)$$

$$C(Q1, Q2) = 0. \quad (2.4.2c)$$

Clearly the flow here is something in between these extremes. One may conclude that although similar dynamics is acting on both the regional and hemispheric scale (because the meridional structure of the respective EOFs are so similar) this dynamics does not necessarily act in unison. We cannot expect the real atmosphere to have quantitatively the same values as (2.4.1), but the qualitative picture is likely similar.

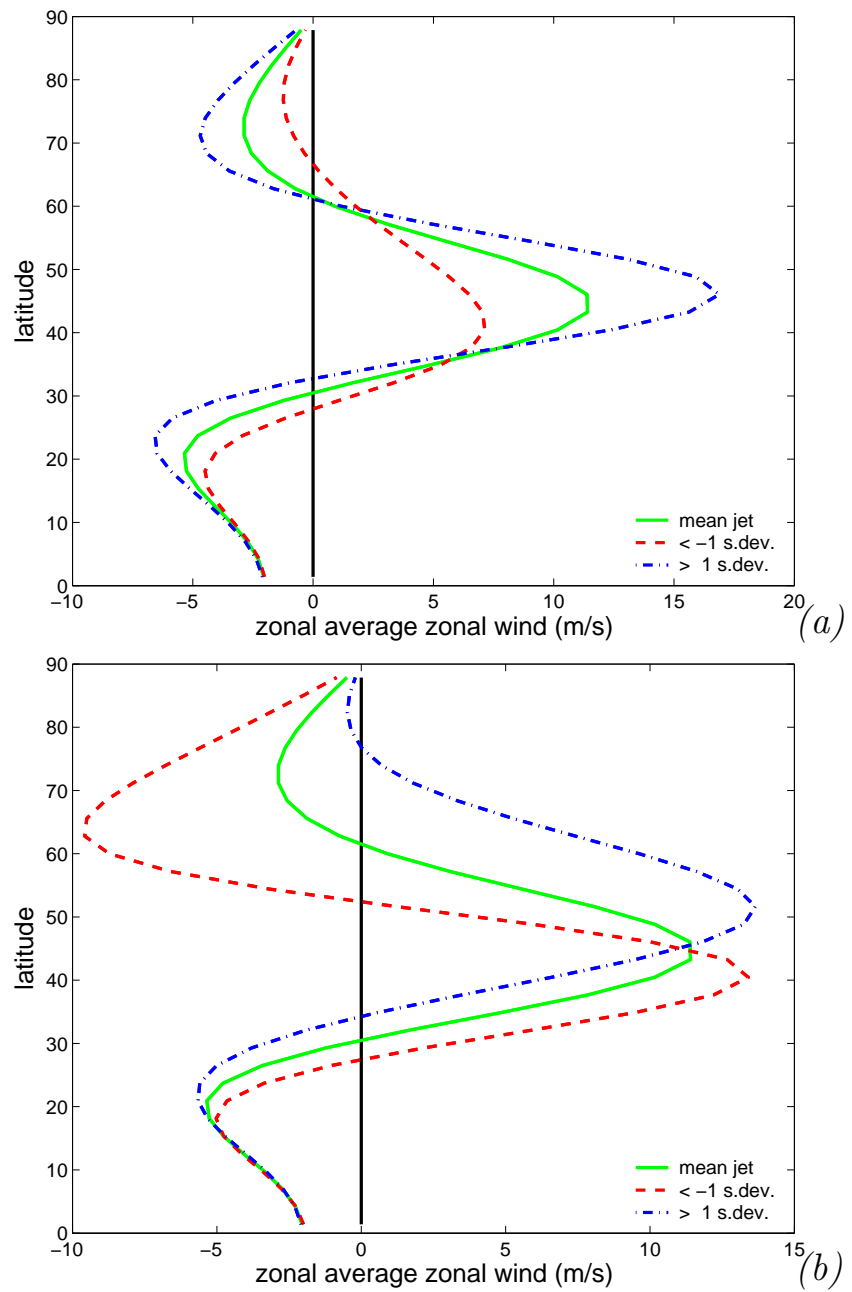


Figure 2.11: (a) Composites of the zonally averaged zonal wind, averaged over periods when it is particularly strong or particularly weak, for experiment Z1. The mean jet is solid, the other lines corresponding to averages over periods when its peak value deviates by more than a standard deviation from the mean, as indicated in the legend. (b) Composite of the zonally averaged zonal wind, as in (a), except now the composites are averaged over periods when its first principal component exceeds or is less than a standard deviations from its mean.

#### 2.4.4 Low and high index states

As noted, the mean position of the jet is slightly poleward of the center of the stirring. The stronger the jet the more poleward the mean jet position, as indicated in Figure 2.11, although the effect is rather weak and the displacement of the jet is no more than  $5^\circ$ . However, a stronger jet is also noticeably narrower than a weak one, and the easterlies on its equatorial flank are noticeably stronger and extend further poleward. In a model with a baroclinic subtropical jet, or the real atmosphere, the effect of this would be to enhance the separation between the eddy driven jet and the subtropical jet, and to make the midlatitude surface westerlies both stronger and slightly more poleward. Both of these effects are seen in the observations during high index states (Ambaum et al. 2001).

### 2.5 Results from Zonally Asymmetric Model

Suppose we now enhance the stirring in a longitudinal region in order to roughly mimic the effects of a storm track. However, we keep the simple meridional structure used in the zonally symmetric case, and the stirring maximum is at the same latitude for all longitudes. Specifically, the longitudinal structure of the amplitude of the stirring is

$$|F_\zeta| = A \left( 1 + B \exp(-(x - x_0)^2 / 2\sigma_x^2) \right) \quad (2.5.1)$$

where  $A$  and  $B$  are constants.  $A$  determines the strength of the uniform background stirring and  $B$  that of the zonal inhomogeneity, centered around longitude  $x_0$ . We have conducted experiments with  $B$  ranging from 0 to about 10, with a value of order unity best representing the enhanced stirring of the storm track regions over the Atlantic and Pacific. The parameter  $\sigma_x$  determines the zonal width of the enhanced stirring region.

Figure 2.12 shows the fields of eddy kinetic energy and the first EOF in an asym-

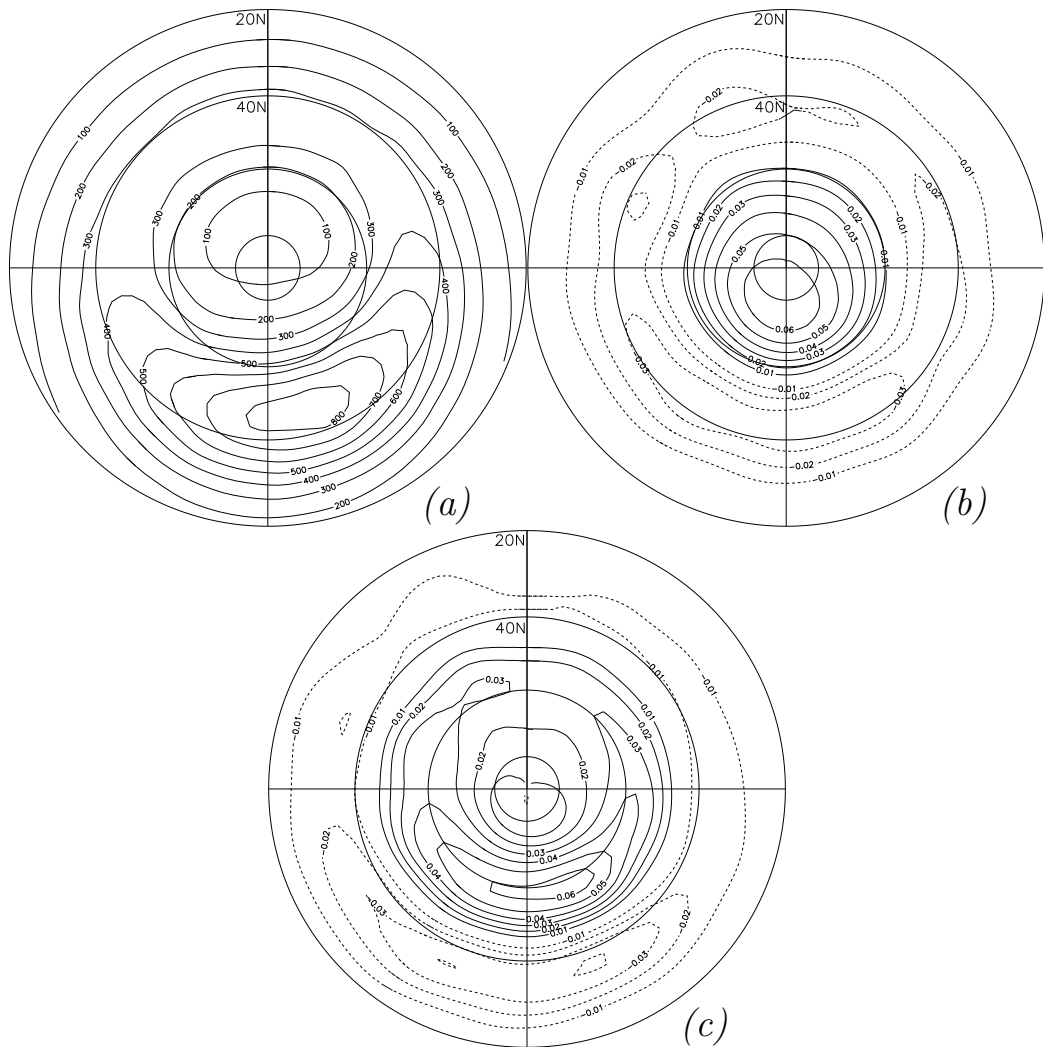


Figure 2.12: (a) Eddy kinetic energy when the model is forced in a zonally asymmetric configuration with a single enhanced region of forcing (A1). (b) The leading EOF of the streamfunction (18% variance accounted for; 6% variance in the second EOF). (c) The leading EOF of the zonal wind (12% variance; 6% variance in the second EOF). The zero contours are omitted.

metric integration (A1) with  $B = 1$  and  $\sigma_x = 45^\circ$ , producing an eddy rich region roughly comparable to the major ocean storm tracks. The meridional half-width of the forcing is  $12^\circ$ . The eddy kinetic energy is a direct reflection of the enhanced stirring and, clearly, the EOF is centered around the enhanced stirring and reflects the more vigorous activity in that region. The localized dipole structure of the streamfunction is similar to that appearing in zonally asymmetric GCMs (e.g., Cash et al. 2005) and in the observations (e.g., Ambaum et al. 2001). This structure is fairly robust to variations in parameters — for example, Figure 2.13 shows the EOF is a similar zonally asymmetric configuration but when the forcing region has only a  $6^\circ$  half-width, and a qualitatively similar structure is seen.

The one point correlation function (Figure 2.14), with a base point at the longitude where the EOF is a maximum, picks up the meridional dipole structure of the EOF, just as in the zonally symmetric case. In the zonal direction, the correlation function is somewhat more localized than the EOF and is not, in fact, very dissimilar from that in the zonally symmetric case (Figure 2.9). The day-to-day synoptic activity in the two cases is rather similar, but in the zonally asymmetric case there is a slight preference for dipole structures to form in the region of enhanced stirring, and this is detected by the EOF analysis. In the zonally symmetric case, similar two-dimensional structures form locally, but with no longitudinal preference and as a consequence the first EOF is almost zonally uniform.

To assess the zonal coherence of the flow, we calculated the EOFs based solely on the fields in the region of the enhanced stirring, as well as the EOFs in the opposite quadrant. The EOFs in the enhanced stirring region show a similar dipole structure

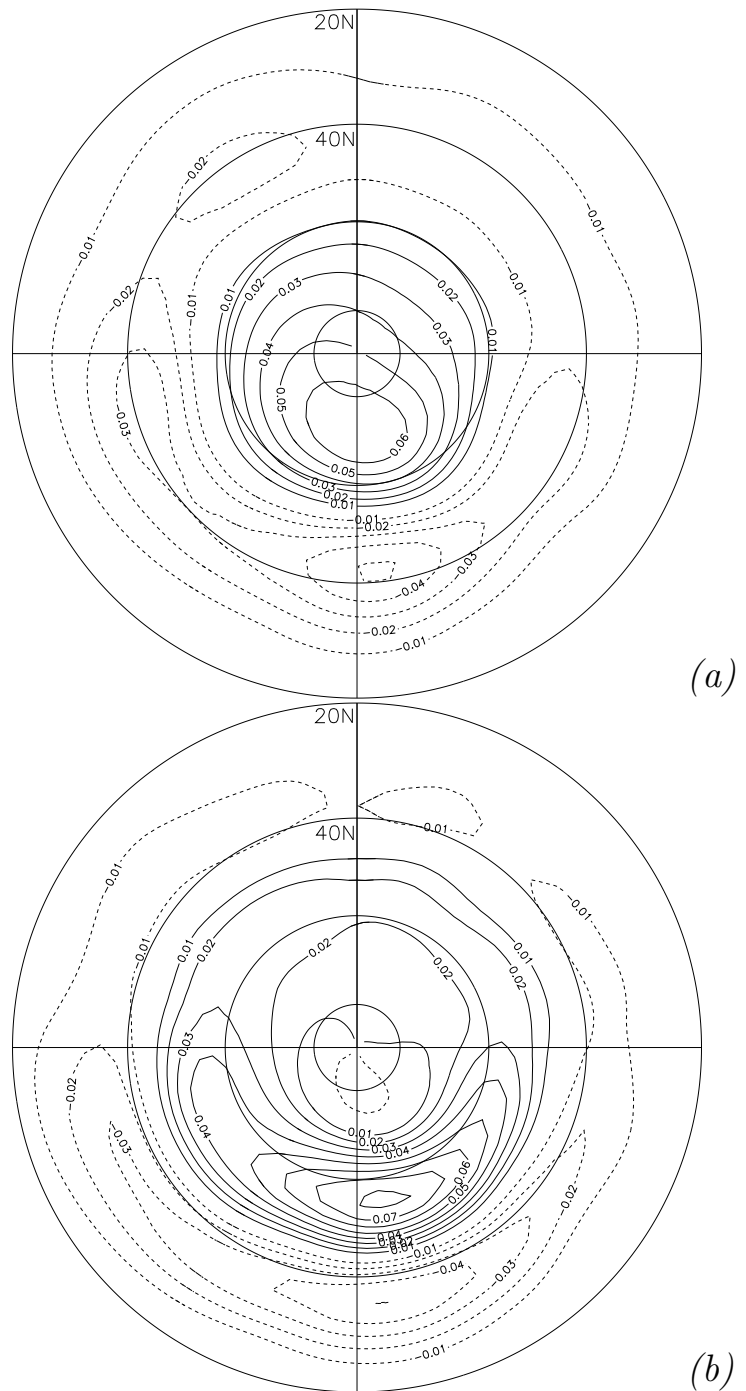


Figure 2.13: (a) The leading EOF of the streamfunction (15% variance accounted for, 7% variance in the second EOF). (b) The leading EOF of the zonal wind (11% variance, 5% variance in the second EOF). These differ from the results in Figure 2.12 only in that the forcing half-width is  $6^\circ$ .

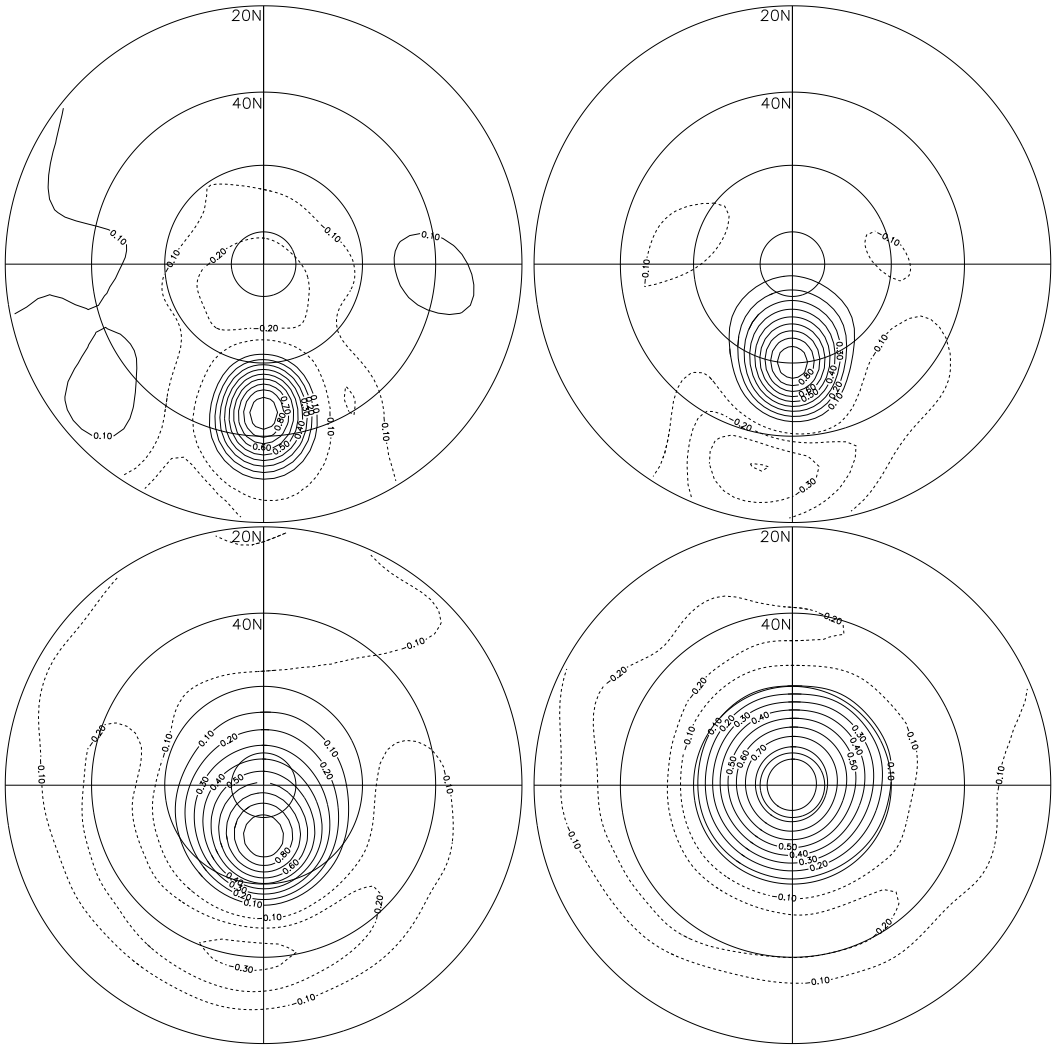


Figure 2.14: The one-point correlation of the streamfunction, for the same zonally asymmetric integration as Figure 2.12. The longitude of the base points is chosen to be along that of the strongest stirring, which is close to the longitude where the EOF has its maximum value. The zero contours are omitted.

to those of Figure 2.12 and, in an analogous fashion to (2.4.1), we calculate

$$C(Z, Q1) = 0.57 \quad (2.5.2a)$$

$$C(Z, Q2) = 0.72 \quad (2.5.2b)$$

$$C(Q1, Q2) = 0.11 \quad (2.5.2c)$$

where  $Q2$  denotes the region of enhanced stirring,  $Q1$  the opposite quadrant, and  $C(Z, Q1)$  and  $C(Z, Q2)$  are the correlations between the principal components of the zonal EOF and the regional EOFs, and  $C(Q1, Q2)$  is the correlation between time series of the two regional EOFs. Thus, the principal component of EOF constructed from the hemispheric flow has correlates well with the principal component of the EOF constructed in the region of enhanced stirring.

The structural similarity between the EOF and the teleconnection, and the similarity between the barotropic model, the GCM results of Cash et al. (2002), and the observations, are all suggestive of the robustness of the mechanism identified. We make two additional points. First, this is a *nonlinear* effect. If localized stirring is added to the linear barotropic vorticity equation, then the response is a superposition of beta plumes that trail westward from the source but which produce no vorticity flux, an effect familiar to most physical oceanographers. (Of course, one might construct a linear model to mimic the nonlinear effects, but one would have to specify the structure of the vorticity fluxes.) Second, the dipole structure that is evocative of the NAO arises robustly when the stirring is somewhat stronger than the zonal mean stirring (i.e., when  $B$  in (2.5.1) is of order one). However, if the localized stirring is extremely intense (e.g.,  $B = 10$ ) then more exotic patterns (not shown) occur. Now the theory of Section 2.2.1 becomes invalid because of the extreme zonal inhomogeneity.

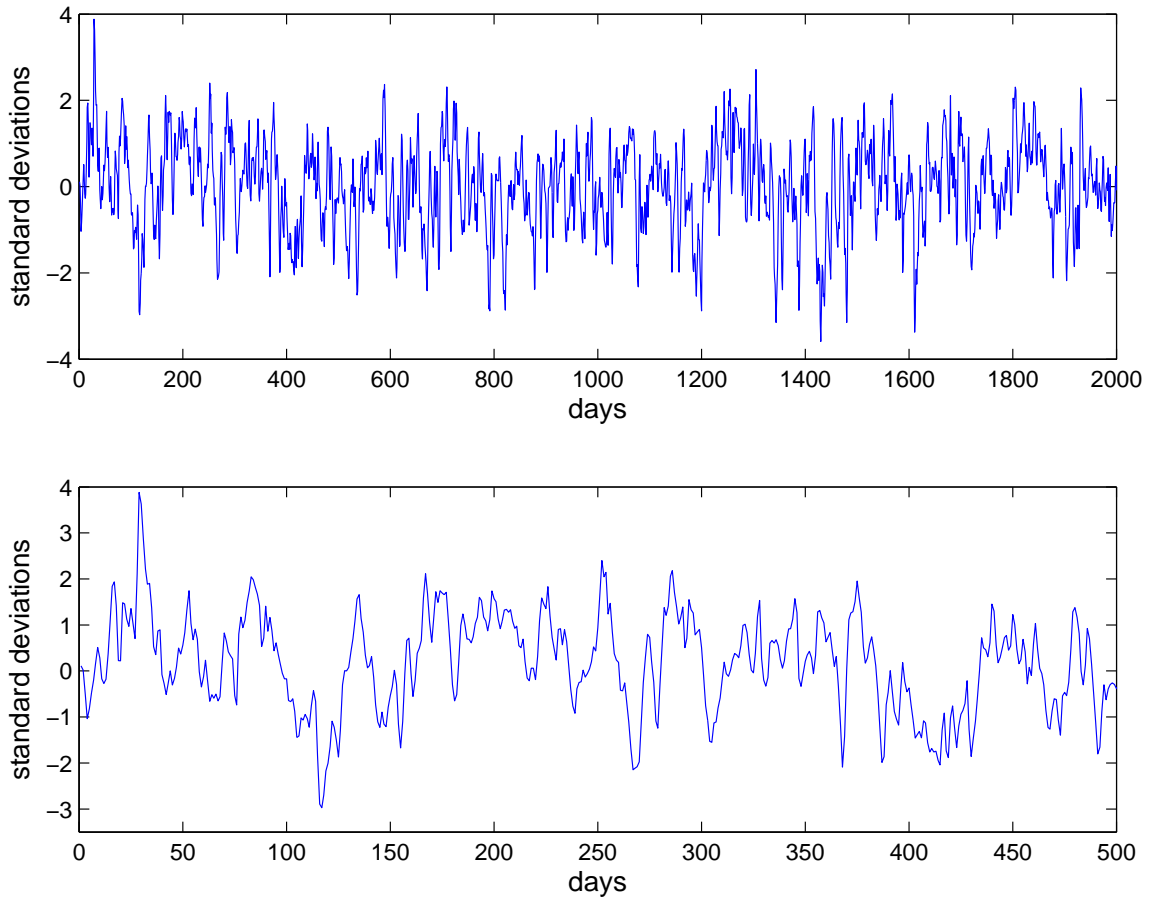


Figure 2.15: Sample time series of the principal component of the leading EOF of zonal wind in the zonally symmetric integration, Z1. The lower panel is a blow up of the first 500 days of the upper panel.

## 2.6 Temporal Structure

Apart from the signals due to El Niño and the seasonal cycle, the large-scale patterns of extratropical variability in the atmosphere appear to have a fairly red spectrum, with no really significant peaks (Feldstein 2000b). However, it is unclear whether the power in these patterns continues to increase for timescales longer than the interannual — that is, whether the spectrum continues to redden for increasingly long timescales or whether it flattens out and whitens (see Stephenson et al. 2000). Notwithstanding that uncertainty, the decorrelation timescale associated with the NAO and similar patterns is of order 10 days. Now, in our numerical model the

various possible timescales are the timescale of the forcing, a frictional timescale determined by the value of  $r$  in (2.3.1), a nonlinear eddy turnover time for some scale  $L$  given by  $L/|U_L|$  where  $U_L$  is the velocity magnitude at the scale  $L$ , and a timescale associated with Rossby wave propagation  $\sim 1/(L\beta)$ . The external parameters are those associated with the forcing and friction — the eddy turnover time is ultimately given by the magnitude of the forcing and how effective it is in generating flow. If we choose our forcing decorrelation time to be of order a few days to represent baroclinic activity, then we must tune its magnitude to give flow velocities with a magnitude similar to those observed, and in that case the only remaining external free parameters are  $r$  and  $\beta$ .

Friction is one important element in determining the spectral response to the forcing, as we see from the linear version of (2.3.1). The equation is

$$\frac{\partial \zeta}{\partial t} + \beta \frac{\partial \psi}{\partial x} = S - r\zeta \quad (2.6.1)$$

and this can be solved analytically if the power spectrum of  $S$  is known. Assuming a solution of the form

$$\psi = \text{Re}\Psi e^{i(\mathbf{k}\cdot\mathbf{x}-\omega t)}. \quad (2.6.2)$$

where  $\text{Re}$  indicates the real part should be taken, and substituting into (2.6.1) gives

$$|\Psi|^2 = \frac{S_\omega^2}{[(k^2\omega + \beta k_x)^2 + r^2 k^4]} \quad (2.6.3)$$

and so the solution has a redder spectrum than the forcing. The solution is completed by the addition of the homogeneous problem, a decaying Rossby wave.

Numerical solutions of the nonlinear problem show that this effect contributes, but is not the whole story. In Figure 2.15 we see a representative time series of the first EOF in a zonally symmetric forced simulation. [The EOF itself is first obtained using

temporally low-passed (10 day running mean) data, but the figure shows the daily, unfiltered, values of the corresponding principal component.] Figure 2.16 show the corresponding power spectra, which are characteristically red. The auto-correlation of the first two EOFs is shown in Figure 2.17, and these are of order 5–10 days. The wobbling mode typically has a longer decorrelation than the pulse. For shorter frictional timescales the decorrelation timescale (the e-folding timescale) is similar to the frictional timescale, as expected in an Ornstein-Uhlenbeck type process. However, inspection of Figure 2.16a and Figure 2.17b indicates that the correlation timescale does not increase as quickly as the frictional timescale increases; for frictional timescales of 6 days, 12 days and 23 days we find e-folding decorrelation timescales of 3.8 days, 4.4 days and 7 days respectively. Evidently, the chaotic dynamics of the large-scale fields are limiting the temporal correlations.

The auto-correlation of the simulation with the higher damping (12 days) has virtually as much power at very long times as the simulation with a 23-day damping timescale, another indication that frictional effects are not the sole determinant of the power at low-frequencies. Note that it is also apparent from the time series that quite long excursions from the mean are possible. For example, there are frequent excursions of order 100 days. [Long term variability was also found by James and James (1992) in a simplified general circulation model, although the variability they found involved the subtropical jet, which is absent in this model.]

## 2.7 Summary and Conclusions

We have presented a simple dynamical model of the North Atlantic Oscillation and the related annular modes. We have shown that spatial structures qualitatively similar to those associated with the North Atlantic Oscillation and annular modes can be robustly and easily reproduced with a stochastically forced, but nonlinear, nondi-

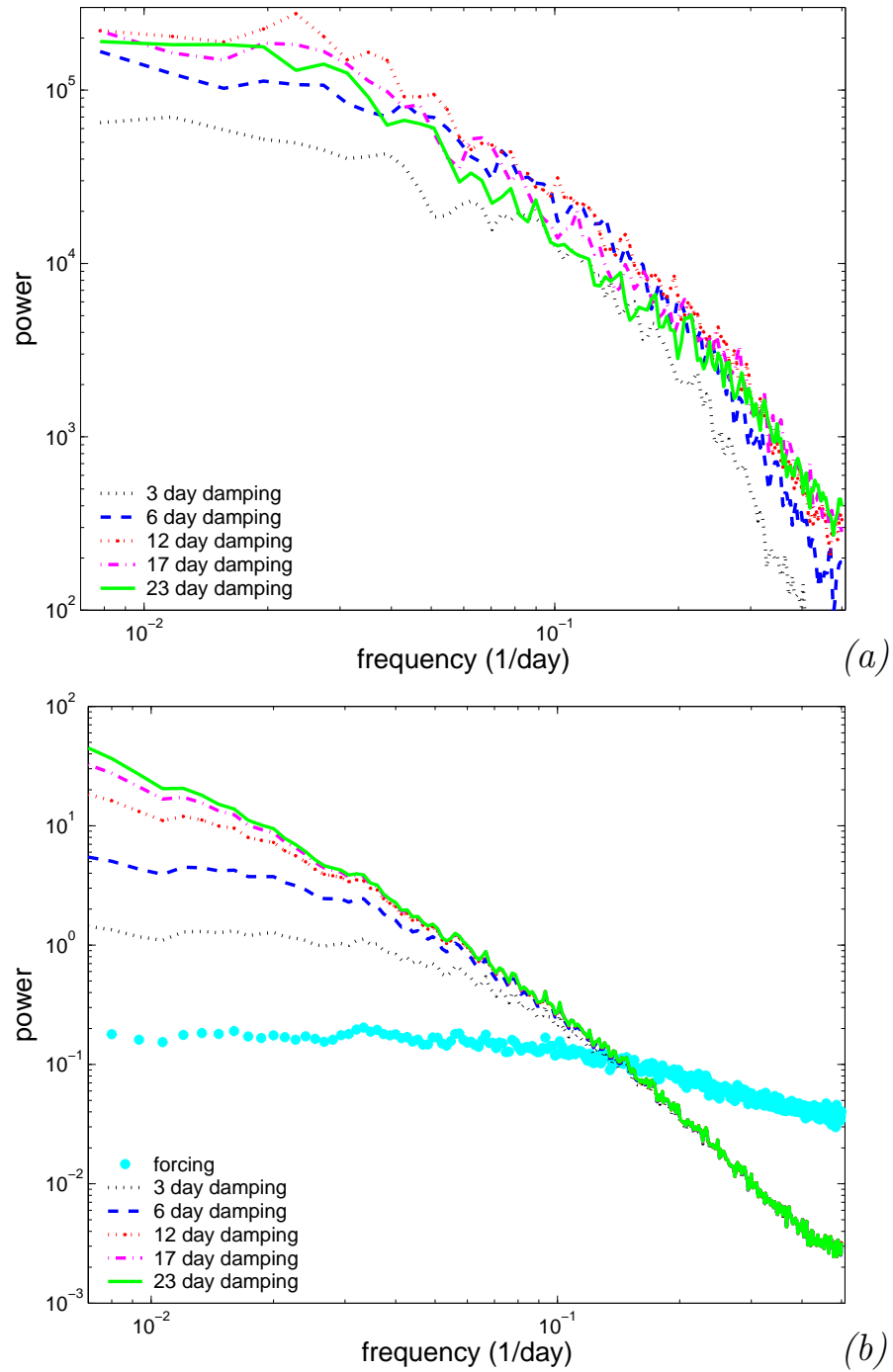


Figure 2.16: (a) Power spectra of the principal components of the leading EOFs of the zonal wind in zonally symmetric integrations with varying values of the frictional parameter  $r$ , corresponding to frictional timescales of approximately 3, 6, 12, 18 and 23 days. (b) Power spectra of the stochastic process,  $dz/dt = S - rz$ , for the same values of  $r$  used in (a), and  $S$ , the stochastic forcing, also having the same power spectra as used to force the model.

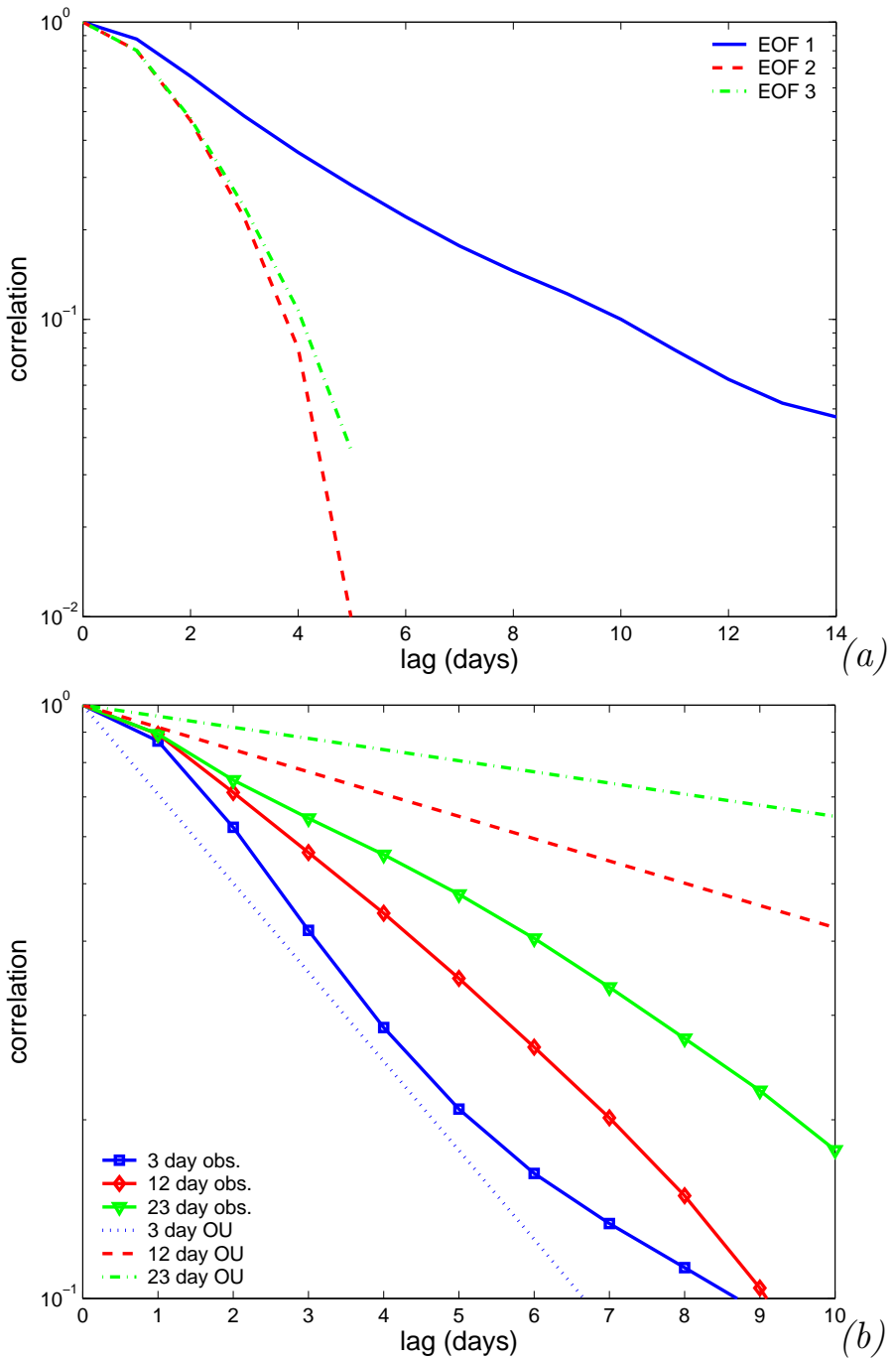


Figure 2.17: (a) Autocorrelation of the principal components (PCs) of the first two EOFs of the zonal wind for zonally symmetric integration (Z1), with a frictional timescale of 6 days. (b) Autocorrelations of the PCs of the first EOFs of three model integrations, each with a different value of the damping timescale (denoted ‘obs’), and the autocorrelations for three Ornstein-Uhlenbeck processes with the same damping timescales (denoted OU). The model decorrelates faster than the corresponding OU process, especially when friction is weak.

vergent barotropic model. The stochastic forcing has a very simple spatial structure and need not be extensively tuned for the patterns to appear.

The model suggests that the NAO and annular modes are, essentially, two sides of the same coin. The (single) phenomenon is associated with variations in the mid-latitude circulation caused by fluctuating stirring from baroclinic eddies. The fluctuating stirring produces both a variation in the intensity and position of the zonal jet, and a dipolar circulation anomaly. This in turn leads to a dipolar structure in the streamfunction (i.e. the pressure field) variability, and so a dipolar EOF, much as is observed.

If the eddy statistics are zonally uniform, then the leading EOF of the zonal velocity and the streamfunction are also approximately zonally uniform. Wave-mean flow interaction has produced variability in the zonally averaged flow, and this may be interpreted or defined as an annular mode. However, the variability of an annular mode is (in this interpretation) not the hemispheric-wide synchronous variability or heaving of a polar vortex. Rather, it is associated with the projection onto the zonally averaged flow of eddy dynamics.

The North Atlantic Oscillation is to be differentiated from the annular mode primarily by its scale, not its mechanism. As will be further established in Chapter 4, the presence of an Atlantic storm track provides stronger stirring, and if the longitudinal extent of the storm track is greater than that of a single eddy, the same dynamics that produce variations of the zonally averaged flow will still act, just more intensely, over that region. Thus, the jet variations will be stronger here than elsewhere, and any measure of that variability, such as the first EOF of pressure or streamfunction, will show a dipole centered near the eddy activity. Now, when the stirring is stronger — i.e., when the storm track is stronger — the barotropic jet is strengthened and tightened, whereas any subtropical jet would be little altered. Thus, during periods of high eddy activity the eastward advection will be strongest at latitudes poleward of

its mean position. Conversely, quiescent periods will have a weaker barotropic jet and the eastward advection will be somewhat equatorward of its mean position. Thus, at one extreme we can expect eddy-rich activity with a strong eastward jet somewhat poleward of its mean position; at the other extreme we expect weaker eddy activity with a weaker, slightly more equatorward jet. This is, of course, a characteristic of the NAO.

Another way of expressing this is to say that it is the organization of the baroclinic activity into spatially coherent large scale patterns (i.e., storm tracks) that gives rise to coherent large scale vorticity stirring, and this in turn produces patterns like the NAO. Because the mean amplitude of the vorticity-stirring varies zonally, the eddy forcing has a stationary component (i.e., there is a zonal asymmetry in the time mean eddy fluxes) and it is this stationary component that produces the NAO. Momentum fluxes from stationary waves are really the same as the spatially nonuniform eddy fluxes we have parameterized, and that such forcing is responsible for the zonally asymmetric patterns of variability seems consistent with the observational analyses of Limpasuvan and Hartmann (2000).

If this mechanism holds in the real world, then there should be a corresponding phenomena in the Pacific as well as the Atlantic corresponding to the Pacific storm track. Such a ‘North Pacific Oscillation’ (NPO) may well exist [indeed Walker and Bliss (1932) commented on it] although it may not be as noticeable as the NAO because there are many other phenomena occurring in the Pacific, such as ENSO and the Pacific North American pattern (to which the NPO may be related). There may well be additional, more subtle differences in the storm tracks between these regions and we recognize that the differences between the NAO and NPO are unlikely to be fully explained by our proposed mechanism.

The decorrelation timescale of the NAO and annular modes are observed to be about 10 days, and this is well reproduced by the model, albeit it is partly dependent

on the frictional timescale chosen. The eddy forcing itself, even the stationary-eddy forcing, has a much shorter decorrelation timescale (a day or two). The jet integrates this forcing, to produce a redder spectrum, with both the nonlinear dynamics and damping processes providing a limit to the reddening process. The barotropic model does produce variability on long timescales, evidently up to 200 days, although the presence of a seasonal cycle would affect this. Determining whether this long-term variability corresponds to that seen in the observations will require a more detailed study of both model and observations, since the nature of such long-term variability is currently unclear in both. [Feldstein (2000b) concludes that the NAO is a Markov process with an e-folding timescale of about 10 days, whereas Stephenson et al. (2000) note the presence of ‘long-range dependencies’ (a red spectrum) on inter-annual timescales. These may not be contradictory, if the tails in the autocorrelations are nonzero but small.]

It has, of course, been known for some time that rather simple dynamical models and idealized GCMs can reproduce realistic patterns of intra-seasonal variability, including annular modes and patterns like the NAO, and that these are associated with variability in the momentum flux. It is also generally accepted that neither a stratosphere nor sea surface temperature anomalies are necessary ingredients for these phenomena. Here we have sought to present perhaps the simplest possible model of this as a way of elucidating the dynamics and clarifying the relationship between the NAO and annular modes. In particular, baroclinic effects are modeled by a simple wave maker that is not related to the strength of the barotropic jet. This suggests that a state dependence of the stirring (that is to say, a feedback from the mean flow to the stirring) is not a crucial ingredient in producing an annular mode or NAO-like structure.

However, we do not claim that we have definitively established that such a feedback is not important, and more careful studies with a simple GCM in Chapter 5 suggest

that such a feedback can be important in lengthening the timescales of the variability. But before we increase the complexity of our model, we take a step in the opposite direction, simplifying the dynamics – almost removing them entirely – as to better understand the nature of our analysis techniques.

# Chapter 3

## The Stochastic Model: Constraints on the Circulation

### 3.1 Introduction

Many analyses of the spatial structure of extratropical variability result in meridional dipole patterns – they appear in Empirical Orthogonal Function (EOF) analysis and single point correlation maps of observations of both the geopotential height and zonal wind (e.g., Wallace and Gutzler 1981; Barnston and Livezey 1987) and in models (e.g., Limpasuvan and Hartmann 2000; Cash et al. 2002). The zonal structure of the EOFs is generally more uniform, especially in the Southern Hemisphere, while the correlation patterns are more local. Interpreting such patterns has been problematic, for they do not clearly differentiate between a hemispheric scale dynamical mode of oscillation (Thompson and Wallace 2000) and dynamics that are more regional in nature (Ambaum et al. 2001).

The meridional dipole pattern was a robust feature in the barotropic model discussed in the previous chapter. The model also reproduced the more problematic features of the zonal structure. The zonal scale of the variability, as characterized by

EOF analysis, could be shaped by the structure of the baroclinic stirring. Single point correlation maps of the zonally symmetric and asymmetric simulations, however, did not show as appreciable a change in the local correlation structure. Furthermore, the annular mode of the model did not necessarily indicate the presence of a zonally uniform dynamical mode, but rather appeared to reflect the fact that the same “meridional dipole forming mechanism” was acting at all longitudes.

That such a simple model of the atmospheric circulation could so well capture these features suggests that they are a very basic element of the extratropical circulation. In this chapter, we develop a purely stochastic model for understanding the spatial structure of the single point correlation maps and EOFs characterizing the NAO and AO, using only the bare essential dynamics. In particular, we seek to explain the ubiquitous nature of the meridional dipole - which appears so robustly in many analysis techniques of variability - and the more sensitive nature of the zonal structure. We find that, to a large extent, these sensitivities are in part due to the nature of the analysis techniques.

EOF analysis allows one to represent a variable of interest in the most efficient set of orthogonal modes, using only the variable’s covariance function as input. It further quantifies the variance represented by the modes, reflecting the importance of each in describing the covariance structure.<sup>1</sup> Stochastic models, that is, models of “random motions,” have long been used to better understand EOF and correlation patterns. An understanding of the space of all potential motions can provide insight into the space of observed motions. Batchelor (1953) notes in Section 2.5 that the statistical stationarity of homogeneous turbulence necessitates the choice the trigonometric functions when seeking an orthogonal basis. North and Cahalan (1981) report

---

<sup>1</sup>For data on a finite grid, EOFs are the eigenvectors of the covariance matrix, whose  $ij^{\text{th}}$  entry is the covariance between points  $i$  and  $j$ . The corresponding eigenvalues quantify the variance represented by each eigenvector. The generalization of EOF analysis to continuous functions is also known as a Karhunen-Loéve decomposition. See von Storch and Zwiers (1999), Chapter 13, for a complete discussion.

a theorem by Obukhov (1947) that the EOFs of a statistically uniform random field on the sphere are the spherical harmonics. In both cases, the variance represented by each EOF is dependent on the decorrelation spectrum. If the field is “white” in space, the spectrum is flat; all modes are degenerate, explaining the same fraction of variance. When the field is “reddened,” so that spatial correlations decay over a finite distance, the modes separate. If this reddening is simple, so that covariance between two points decorrelates monotonically as the distance between them increases, e.g., exponential decay, the largest mode allowed by the geometry of the system will be the top EOF, and the variance represented by each mode decreases with increasing wavenumber.

With idealized three-dimensional turbulence in a box with periodic boundaries and random motion on the sphere, symmetries in the system lead to the selection of the EOF basis. The extratropical atmosphere is more constrained than homogeneous turbulence, and we may wonder what the symmetries and constraints of the circulation imply for the selection of an EOF basis. In Section 3.2 we present a one-dimensional model of the barotropic zonally averaged zonal wind which suggests that the oft observed meridional dipole pattern is a natural consequence of angular momentum conservation on a sphere, or zonal momentum conservation in a channel. We extend the model to two dimensions in Section 3.3 to illustrate the potential for annular modes in a system with no zonally coherent motions. In Section 3.4, we find that the addition of a relatively small degree of zonal inhomogeneity, i.e., a storm track, localizes an annular mode-like pattern to a NAO-like pattern. We then discuss the relation between EOFs of zonal wind and of pressure in Section 3.5. Differences are illustrated by two one-dimensional models of the zonally averaged surface pressure, where we find that the conservation of mass plays a similar role as the conservation of momentum in establishing the dipole pattern. From the outset, we seek to explain the observations from the barotropic model in Chapter 2, but believe the results have

relevance to the AO and NAO of the atmosphere. As noted earlier, the contents of this chapter appeared previously in Gerber and Vallis (2005).

## 3.2 A One-Dimensional Model

### 3.2.1 Theory

We begin our discussion with the barotropic zonally averaged zonal wind. Our model is a stochastic process  $M(\omega, y)$  designed to catalog all possible anomalies of the barotropic jet. The variable  $y \in [0, 1]$  is our meridional coordinate, 0 being the equator and 1 the pole.  $\omega$  marks the process in probability space: for each particular  $\omega^*$ ,  $M(\omega^*, y)$  represents one realization of an anomalous zonally averaged barotropic wind profile. Sampling  $M$  is analogous to sampling the wind profile from a dynamically evolving model over time increments sufficiently long enough for the zonal anomalies to be independent of one another, say 10 days to a month.

We keep  $M$  as general as possible, but each realization should be in keeping with the basic physical properties of the atmospheric jet.

1. The jet varies little in the tropics.
2. The jet must vanish at the pole.
3. The fluid motions that generate the jet conserve zonal momentum.

Constraint (1) is motivated by the barotropic model, which suggests that NAO/AO variability arises from the eddy driven component of the midlatitude jet, with little variation at low latitudes. At the pole, geometry fixes the zonal wind at zero. Constraint (3) accounts for the fact that fluid motions, midlatitude eddies in particular, conserve momentum, and so can only reorganize momentum within the atmosphere; anomalous momentum convergence at one latitude must then be at the expense of

momentum lost at another. We enforce this constraint by requiring that realizations of  $M$  have zero mean. We thus ignore variations of the density with latitude and approximate the hemisphere as a channel, but this does not qualitatively affect our conclusions. Likewise, one could view  $M$  as a model of the angular momentum, where the application to spherical geometry is more straightforward. The complete mathematical translation of the three constraints is then that  $M$  must satisfy

$$M(\omega, 0) = 0 \quad (3.2.1a)$$

$$M(\omega, 1) = 0 \quad (3.2.1b)$$

$$\int_0^1 M(\omega, y) dy = 0 \quad (3.2.1c)$$

for all  $\omega$ .

Momentum conservation is ultimately regulated by dissipation at the surface, where on average there can be no net transfer of momentum. Assuming an effective drag coefficient,  $c_d$ , independent of latitude, we have

$$\int_0^{\pi/2} c_d \langle \bar{u}_s \rangle d\theta = 0 \quad (3.2.2)$$

where  $\theta$  is the latitude and  $\langle \bar{u}_s \rangle$  the time and zonally averaged surface wind. In constraint (3.2.1c), we further assume that there is no significant exchange of net momentum between atmosphere and surface at any time, so that  $\langle \bar{u}_s \rangle$  can be replaced by the zonally averaged wind,  $\bar{u}_s$ .

Lastly, we must specify a probability space to govern the randomness of  $M$ . For simplicity, let us begin with a discrete random walk formulation. Consider a random walk of  $N$  steps from  $y = 0$  to 1. At each step, the path moves forward  $1/N$  units in  $y$ , and to the left or right  $d$  units with equal probability. As we begin at the origin, all  $2^N$  possible paths satisfy (3.2.1a). Only a fraction of them, however, will be bridge-like, in that they both begin and end at the same point. To satisfy (3.2.1b), the path

N	Satisfying (3.2.1a)	Satisfying (3.2.1a),(3.2.1b)	Satisfying (3.2.1a)-(3.2.1c)
4	16	6	2
8	256	70	8
12	4096	924	58
16	65536	12870	526

Table 3.1: Number of Possible Random Walks of length  $N$ . Note that all walks begin at the origin, and so trivially satisfy (3.2.1a).

must take an equal number of steps to the left as to the right. Hence  $N$  must be even, and, from combinatorics, we deduce that only  $N!/[(N/2)!]^2$  are possible. The final condition, (3.2.1c), further limits the number of paths. We find that  $N$  must be a multiple of 4 for any such mean zero, bridge-like paths to exist. While we do not present a formula for determining the number of them, it is easily computed by exhaustion for small  $N$ , and values are listed in Table 3.1. This subset of paths is a discrete implementation of the process  $M$ ; each path is a possible jet anomaly profile. By construction, each potential anomaly pattern is equally likely to occur, providing a well defined probability measure on the subset.

Formally, one could obtain Brownian motions from these random walks by allowing  $N$  to go to infinity and setting the right and left step size  $d = \sqrt{1/N}$ . By the central limit theorem, the distribution of the position of the path at any  $y$  between 0 and 1 will be Gaussian, and this choice of  $d$  sets the mean and variance of the distribution to 0 and  $y$ , respectively. This particular limit of the random walk is the Wiener process,  $W(\omega, y)$ , the canonical Brownian motion. The fraction of paths satisfying the first two conditions becomes smaller as  $N$  increases, even though the number of such paths is growing. In the limit  $N \rightarrow \infty$ , there will be an infinite number of bridge-like paths, but they will occupy a set of measure zero inside the set of all possible Wiener paths. The same holds for paths satisfying all three conditions. There are an infinite number of mean zero, bridge-like paths, that is, realizations of  $M$ , but they occupy a set of measure zero within the set of paths satisfying the first two conditions. Noting

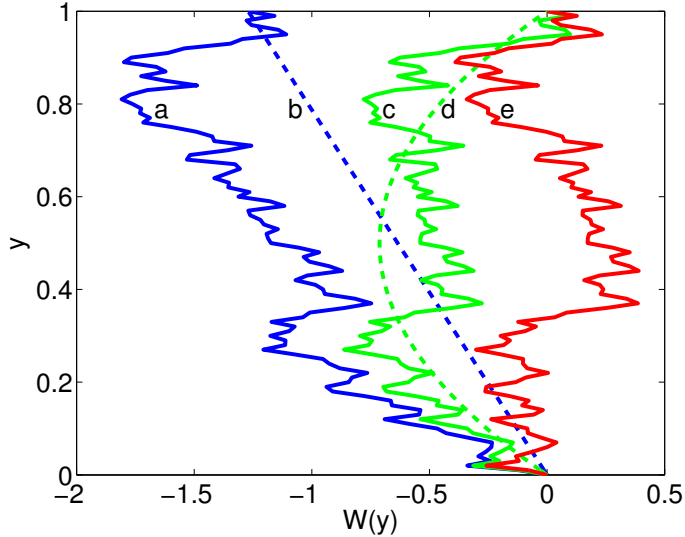


Figure 3.1: A sketch of the procedure of transforming a Wiener path to a path of  $M$ . (a) is one realization,  $W(\omega^*, y)$ , of the Wiener Process. Line (b) is the expected, or average, path taken by all Wiener paths that end at  $W(\omega^*, 1)$ . (c) is the Brownian Bridge  $B(\omega^*, y)$ , formed by taking the difference (a)-(b). Curve (d) is the expected path taken by all Brownian Bridges that have the same integral in  $y$  as  $B(\omega^*, y)$ . (e) is the Mean Zero Brownian Bridge  $M(\omega^*, y)$ , formed by subtracting (d) from (c).

these points, we use the Wiener process, which is well developed in the literature, to construct the probability space of  $M$ .

We first sketch the procedure by which a realization of  $M$  is obtained from a realization of  $W$ , as illustrated in Figure 3.1. We begin with a Wiener path  $W$  (curve a) which trivially satisfies (3.2.1a). We then detrend  $W$  to satisfy the second endpoint constraint, (3.2.1b). The resulting path,  $B$  (curve c) is a realization of a process known in stochastic calculus literature as a “Brownian Bridge,” as it arches from  $(0, 0)$  to  $(1, 0)$ . Lastly, we eliminate the mean in  $y$  from  $B$  to satisfy (3.2.1c), thus attaining a realization of  $M$  (curve e).

To establish notation, given a function  $f(\omega, y)$ , we define its expectation,

$$E[f(\omega, y)] = \int_{\Omega} f(\omega, y) P_W(\omega) d\omega, \quad (3.2.3)$$

where  $\Omega$  is the space of all  $\omega$  and  $P_W(\omega)$  is the Wiener probability density function. The  $E[f(\omega, y)]$  is the expected, or average, value of  $f$  at  $y$ . The conditional expectation of  $f$ , given  $Z = z$ ,  $E[f(\omega, y)|Z = z]$ , is the expected value of  $f$  computed over the subset of  $\Omega$  where the event  $Z = z$  is true.

A construction of  $B$  from  $W$  is well known in the literature (e.g., Karatzas and Shreve 1991, pp 358-360). We begin with a realization of the Wiener process,  $W(\omega^*, y)$  on the interval 0 to 1.  $\omega^*$  is marked with \* to stress that this is a single path, and so fixed when an expectation with respect to  $\omega$  is computed.  $B(\omega^*, y)$  is constructed by detrending  $W(\omega^*, y)$  with the *average* path taken by all Wiener paths  $W(\omega, y)$  that terminate at  $W(\omega^*, 1)$ , that is,

$$B(\omega^*, y) \equiv W(\omega^*, y) - E[W(\omega, y)|W(\omega, 1) = W(\omega^*, 1)] \quad (3.2.4)$$

$$= W(\omega^*, y) - y W(\omega^*, 1). \quad (3.2.5)$$

It can be shown that (3.2.5) yields the most general space of Wiener paths, or Brownian motions, that satisfy the fixed end point constraint,  $B(0) = B(1) = 0$ .

$B$  can be generated equivalently from a sinusoidal basis (Knight 1981, pp 12-14),

$$B(\omega, y) = \frac{\sqrt{2}}{\pi} \sum_{n=1}^{\infty} \frac{\zeta_n}{n} \sin(\pi n y), \quad (3.2.6)$$

where the  $\zeta_n$  are identically and independently distributed Gaussian variables with zero mean and unit variance. With this formulation, we may more intuitively define the space of  $\omega$ : an infinite dimensional vector space of independent Gaussian random variables.

$$\omega = (\zeta_1, \zeta_2, \dots) \quad (3.2.7)$$

We will see shortly that it is really only the first few degrees of freedom, which govern the small wavenumbers, that matter for our question.

We construct  $M$  from  $B$  by employing a similar procedure as was used to construct  $B$  from  $W$ . That is, we subtract from a realization of  $B$  the expected path taken by all Brownian Bridges that have the same integral. Given a specific Brownian Bridge,  $B(\omega*, y)$ , let  $\mu(\omega*)$  be its mean,

$$\mu(\omega*) = \int_0^1 B(\omega*, y) dy. \quad (3.2.8)$$

We then obtain a Mean Zero Brownian Bridge,  $M(\omega*, y)$ , using

$$M(\omega*, y) \equiv B(\omega*, y) - E\left[B(\omega, y) \middle| \int_0^1 B(\omega, y) dy = \mu(\omega*)\right] \quad (3.2.9)$$

$$= B(\omega*, y) - 6\mu(\omega*) y(1 - y) \quad (3.2.10)$$

To get from (3.2.9) to (3.2.10), we must compute the expected, or average, path taken by all Brownian Bridges with mean  $\mu$ . For simplicity, we define this average path by the function  $F(y, \mu)$ ,

$$F(y, \mu) \equiv E\left[B(y, \omega) \middle| \int_0^1 B(y, \omega) dy = \mu\right]. \quad (3.2.11)$$

Using the sinusoidal decomposition of  $B$ , equation (3.2.6), we have that

$$\int_0^1 B(y, \omega) dy = \frac{2\sqrt{2}}{\pi^2} \sum_{n=1,3,\dots}^{\infty} \frac{1}{n^2} \zeta_n. \quad (3.2.12)$$

(3.2.11) can then be written in terms of the  $\zeta_n$ ,

$$\begin{aligned} F(y, \mu) &= E\left[\frac{\sqrt{2}}{\pi} \sum_{n=1}^{\infty} \frac{\zeta_n}{n} \sin(\pi n y) \middle| \frac{2\sqrt{2}}{\pi^2} \sum_{n=1,3,\dots}^{\infty} \frac{1}{n^2} \zeta_n = \mu\right] \\ &= \frac{\sqrt{2}}{\pi} \sum_{n=1}^{\infty} \frac{E[\zeta_n | \mu]}{n} \sin(\pi n y), \end{aligned} \quad (3.2.13)$$

where  $E[\zeta_n|\mu]$  is given by

$$E[\zeta_n|\mu] = E\left[\zeta_n \middle| \frac{2\sqrt{2}}{\pi^2} \sum_{n=1,3,\dots}^{\infty} \frac{1}{n^2} \zeta_n = \mu\right]. \quad (3.2.14)$$

In the second step of 3.2.13 we have used the fact that, for random variables  $X$  and  $Y$  and scalars  $a$  and  $b$ ,  $E[aX + bY] = aE[X] + bE[Y]$ , extended to the infinite sum.

We note that the condition on the mean of  $B$  only involves the odd  $\zeta_n$ . As the  $\zeta_n$  are independently distributed, knowledge about the values of the odd random variables provides no information about the even variables. Hence,

$$E[\zeta_n|\mu] = E[\zeta_n], \quad n = 2, 4, \dots \quad (3.2.15)$$

and  $E[\zeta_n] = 0$ , by construction.

For the odd terms, the problem is now to compute the expected value of each Gaussian variable, given the sum of them all. We use a result from probability theory: for independent, standard Gaussian variables  $X$  and  $Y$  and scalars  $a$  and  $b$  and  $z$ ,

$$E[X|aX + bY = z] = \frac{a}{a^2 + b^2} z. \quad (3.2.16)$$

(3.2.16) can also be written,

$$\begin{aligned} E[aX|aX + bY = z] &= \frac{a^2}{a^2 + b^2} z \\ &= \frac{\text{var}(aX)}{\text{var}(aX + bY)} z \end{aligned} \quad (3.2.17)$$

so that the expected contribution of each variable to the sum is proportional to its variance. The result generalizes to an infinite sum of Gaussian variables, so that for

$n$  odd,

$$\begin{aligned} E[\zeta_n | \mu] &= \frac{n^{-2}}{\sum_{m=1,3,\dots}^{\infty} m^{-4}} \frac{\pi^2 \mu}{2\sqrt{2}} \\ &= \frac{24\sqrt{2}}{\pi^2} \frac{\mu}{n^2} \end{aligned} \quad (3.2.18)$$

where we use the sum

$$\sum_{m=1,3,\dots}^{\infty} m^{-4} = \frac{\pi^4}{96} \quad (3.2.19)$$

Inserting this result into (3.2.13) we conclude that,

$$F(y, \mu) = \frac{48\mu}{\pi^3} \sum_{n=1,3,\dots}^{\infty} \frac{1}{n^3} \sin(n\pi y) \quad (3.2.20)$$

$$= 6\mu \sum_{n=1,3,\dots}^{\infty} \frac{8}{n^3 \pi^3} \sin(n\pi y) \quad (3.2.21)$$

$$= 6\mu y(1-y) \quad (3.2.22)$$

where in the last step, we make use of the fact that on the interval  $[0, 1]$ ,

$$y(1-y) = \sum_{n=1,3,\dots}^{\infty} \frac{8}{n^3 \pi^3} \sin(n\pi y). \quad (3.2.23)$$

In passing, we note that  $y(1-y)$  is the variance of  $B$ , so that its expected path, given the mean, is simply the variance function, suitably normalized. As observed when constructing the Brownian Bridge, the expected path of a Wiener process, given its endpoint  $W(1)$  is  $W(1)y$ . The variance of  $W(\omega, y)$  is also just  $y$ , so that here, too, the expected path is given by the variance.

The Fourier decomposition of  $M$  is

$$\begin{aligned} M(y) &= \frac{\sqrt{2}}{\pi} \sum_{n=1,3,\dots}^{\infty} \left( \left( \frac{1}{n} - \frac{96}{n^5 \pi^4} \right) \zeta_n - \frac{96}{n^3 \pi^4} \sum_{m=1,3,\dots, m \neq n}^{\infty} \frac{\zeta_m}{m^2} \right) \sin(n\pi y) \\ &\quad + \frac{\sqrt{2}}{\pi} \sum_{n=2,4,\dots}^{\infty} \frac{\zeta_n}{n} \sin(n\pi y) \end{aligned} \quad (3.2.24)$$

It is interesting to observe that all the even Fourier modes are unaffected by the transform, as they are naturally mean zero.

$M$  is fundamentally different from  $W$  and  $B$  in that it is not Markovian. That is to say,  $W$  and  $B$  can be formulated as diffusion processes in which the evolution of the system in space depends only on the current state of the system, but evolution of paths of  $M$  depend on the entire history of the process. In generating  $M$  from  $B$ , we have assured that  $M$  satisfies (3.2.1), but we have not proven that  $M$  is the most general Brownian motion satisfying them. Numeric results, in which we sample large numbers of Brownian Bridges, accepting only those with absolute mean smaller than a threshold  $\epsilon$ , suggest that this is in fact the most general formulation.

### 3.2.2 Results

In Figure 3.2 we show realizations of each process. Both  $M$  and  $B$  are anomaly patterns, that is,

$$E[B(\omega, y)] = E[M(\omega, y)] = 0 \quad (3.2.25)$$

for all  $y$ , so that on average, paths of both integrate to zero in  $y$ . Paths of  $M$ , however, integrate to zero in  $y$  for every  $\omega$ , (3.2.1c). The effect of this strict conservation of momentum is clear in their covariance functions, shown in Figure 3.3. As  $M$  and  $B$  are mean zero in  $\omega$ , the covariance function (of  $M$ , for example) is the expectation

$$\text{cov}(x, y) = E[M(\omega, x) M(\omega, y)]. \quad (3.2.26)$$

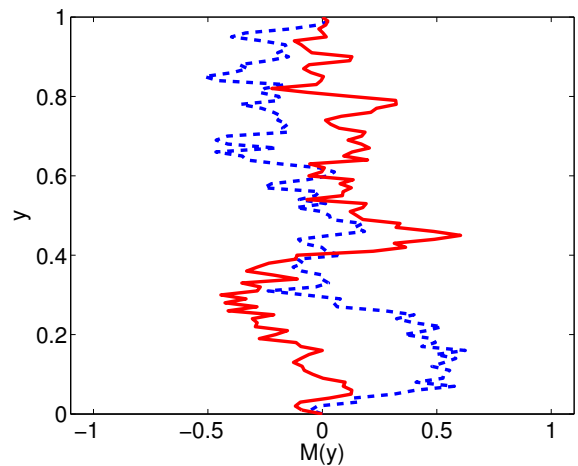
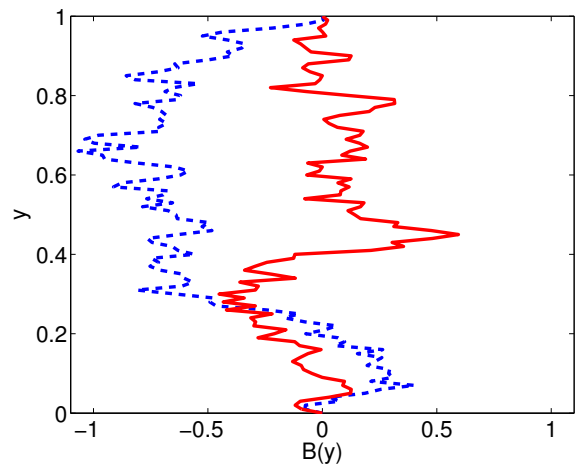


Figure 3.2: Two sample paths of  $B(\omega, y)$  (top), and the corresponding paths of  $M(\omega, y)$  (bottom) constructed as detailed in the text.

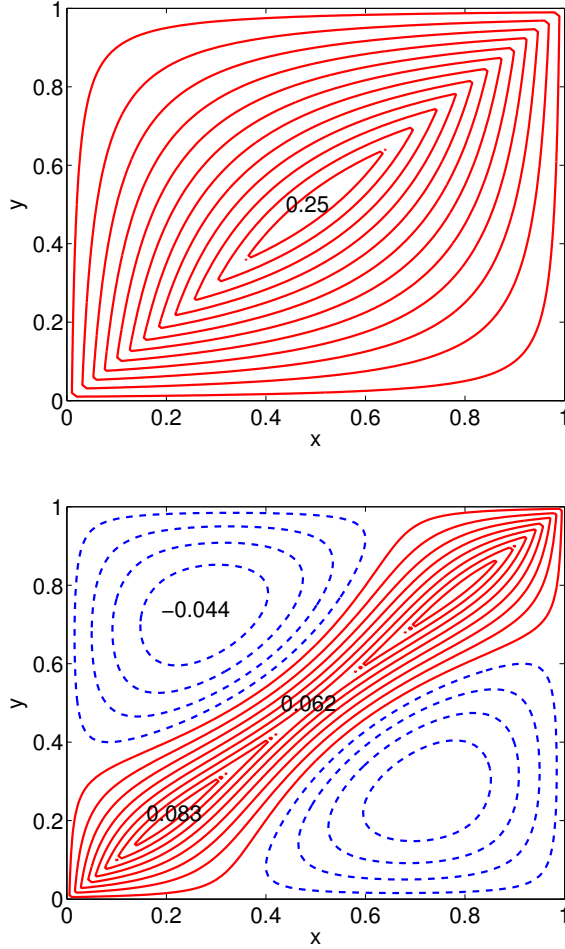


Figure 3.3: Covariance function of  $B$  (top) and  $M$  (bottom). Positive contours are solid and negative dashed. The contour interval is 0.02 for  $B$ , with contours  $(..., -0.01, .01, .03, ...)$  and 0.1 for  $M$ , contours  $(..., -0.005, .005, .015, ...)$ .

The diagonal  $y = x$  of the covariance function shows the variance of the process as a function of  $y$ . For the Brownian Bridge, the variance is largest at the midpoint, where  $B$  is the least constrained. For  $M$ , however, variance is slightly suppressed at the midpoint, peaking at  $y = 0.25$  and  $0.75$ . Vertical (or horizontal) lines in the covariance function are single point covariance maps. For example, the line  $x = 0.5$  shows the covariance of all points with respect to the process at 0.5. For the Brownian Bridge, the covariance function is strictly positive. The only drift of  $B$ , on average, is toward 0 at the endpoints; if it is known to be positive (negative) at any point,

it is expected to be positive (negative) over the whole domain. For  $M$ , however, the covariance function is not always positive. When two points are close, a positive correlation is observed, reflecting the continuity of  $M$  in  $y$ . As the distance between the points increases, however, the covariance becomes negative. This is a reflection of the fact that, for a profile to be mean zero, when it is positive in one region, it must be negative elsewhere, i.e. a westerly anomaly in one region must be balanced by easterly anomaly elsewhere. The single point covariance maps of points near 0.25 and 0.75 indicate a dipole pattern, whereas points in the middle exhibit tripole.

These differences in the covariance functions manifest themselves in the corresponding EOFs, as demonstrated by Figure 3.4. As the Fourier coefficients of  $B$  are independent, as shown in (3.2.6), the sine modes are the natural way to decompose the motion of the Brownian Bridge. For  $M$ , however, only the even modes are perfect sinusoidal functions. The mean zero constraint mixes the odd Fourier modes together, and they are recombined to be orthogonal in both  $y$  and  $\omega$  space. Most importantly, the first sine mode, which is inherently not mean zero, has been lost; the integral constraint has removed a degree of freedom from the system, eliminating this mode. The remaining odd modes are reorganized so that each is mean zero. The dipole pattern is now the gravest mode allowed by the system, and takes position as the foremost EOF.

As a measure of the robustness of these results, we return to the discrete random walk. For the case  $N = 12$ , there are 924 possible bridge-like paths and 58 mean zero, bridge-like paths. The top EOFs describing the space of these walks are shown in Figure 3.5. Even at such coarse resolution the dipole pattern is clearly the dominant mode of variability in the fully constrained case.

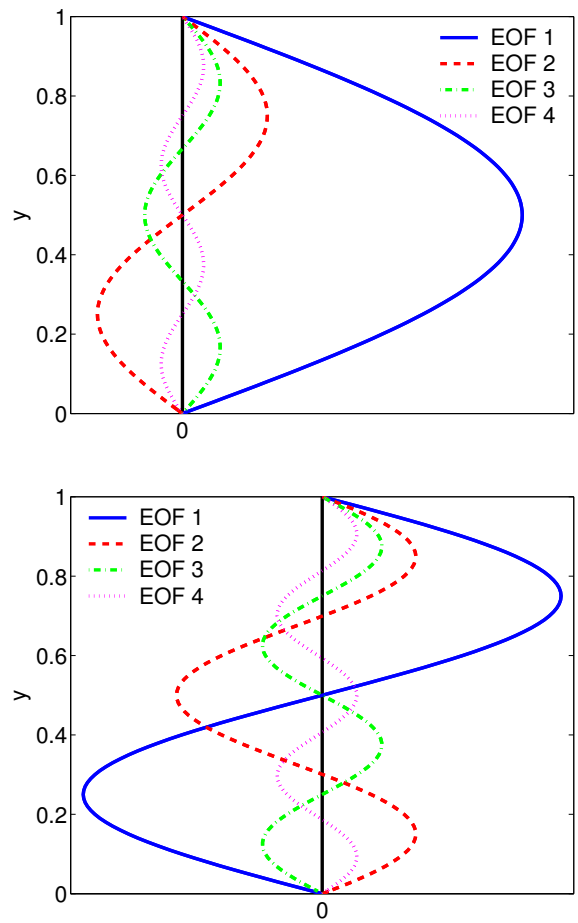


Figure 3.4: First four EOFs of  $B(\omega, y)$  (top) and  $M(\omega, y)$  (bottom). The EOFs (and EOFs in all subsequent Figures) are normalized by the variance accounted for by each mode.

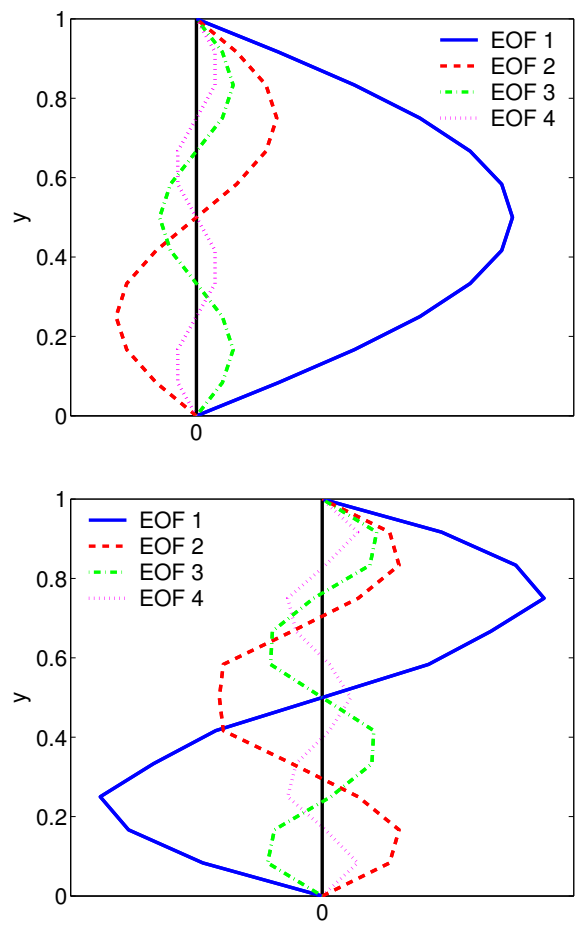


Figure 3.5: First four EOFs of a 12 step random walk constrained by 3.2.1a and 3.2.1b (top) and 3.2.1a-3.2.1c (bottom).

### 3.2.3 Comparison with Observations

NCEP/NCAR reanalysis zonal winds were obtained from the NOAA-CIRES Climate Diagnostics Center, Boulder, Colorado, USA, from their Web site at <http://www.cdc.noaa.gov/>. The reanalysis procedure is described by Kalnay et al. (1996). We used the 0.995  $\sigma$ -level zonal winds sampled every 6 hours from 1958 to 1997 on a 2.5 x 2.5 latitude-longitude grid. After the zonal average was taken at each time step, the annual average was computed and smoothed by a 30 day running mean. EOFs were then calculated from the residual winds left after the removal of the smoothed annual cycle. The covariance matrix was weighted appropriately to account for the decrease in area with latitude (North et al. 1982).

Surface winds were chosen for comparison as they provide the best indication of the barotropic circulation driven by midlatitude eddies. The top EOFs of the Southern Hemisphere are shown in the upper half of Figure 3.6. They are quite consistent with those describing  $M$ ; EOF analysis has performed a Fourier-like decomposition of the winds, and the first mode is the dipole pattern.

In the lower panel of Figure 3.6 we show the top EOFs of the angular momentum of the Southern Hemisphere barotropic flow,

$$\Phi(\theta) = r_0 \bar{u}_s(\theta) \cos^2 \theta \quad (3.2.27)$$

where  $\theta$  is latitude,  $r_0$  is the radius of the earth, and  $\bar{u}_s$  is the zonally averaged surface wind. One would expect the angular momentum to provide the best comparison with model predictions. With the exception of the second EOF, this is largely the case. The  $\cos^2 \theta$  factor focuses the activity in lower latitudes, where the subtropical jet may play a larger role. This may explain in part the skewness of the second EOF, where the equator-most lobe of the tripole is disproportionately large.

The observational results are extremely robust. For both the zonal winds and

implied angular momentum, the results remain largely the same when (1) analysis is restricted to half of the time record, (2) linear trends are removed, (3) the degree of smoothing of the seasonal cycle is increased or decreased, and (4) the data set is restricted to a particular season, i.e., winters only. Similar results are also obtained from analysis of the Northern Hemisphere surface winds and the zonally and vertically averaged zonal winds of both hemispheres. With the vertically integrated winds there appears to be a greater degree of mixing between the dipole and tripole EOFs, so that in a few cases the top two EOFs are both skewed tripole patterns. The dipole structure of the first EOF is further corroborated by other authors in more extensive studies of the observed winds, Lorenz and Hartmann (2001) and Feldstein and Lee (1998).

The fractions of the total variance represented by the top EOFs of the various models and reanalysis data are shown in the Table 3.2. With  $B$  and  $M$ , the variance represented by EOFs of wavenumber  $n$  decay as  $n^{-2}$ , as can be seen from equations (3.2.6) and (3.2.24). The variance accounted for by the top EOFs is relatively independent of resolution, but the total variance, and hence the relative variance described by each mode, is altered when small scales are truncated. Hence the top EOFs of the constrained 12 step random walks explain a larger fraction of the variance. The variance represented by EOFs of the barotropic model and the reanalysis data appear to decay exponentially with wavenumber  $n$ , suggesting that the dynamics are producing a smooth profile, in which both the function and its derivatives are continuous.

As a consequence of choosing Brownian motion to model the anomalous zonal wind, we have assumed that the underlying vorticity anomalies are “white” in space. The zonally averaged vorticity anomalies implied by  $M$  show no preference for any scale. Formally, this can be seen from (3.2.24), where every Fourier mode of  $-dM/dy$  (with the exception of the first) will have nearly equal weighting. Given that we also neglect spherical effects, the match between  $M$  and the reanalysis winds in the

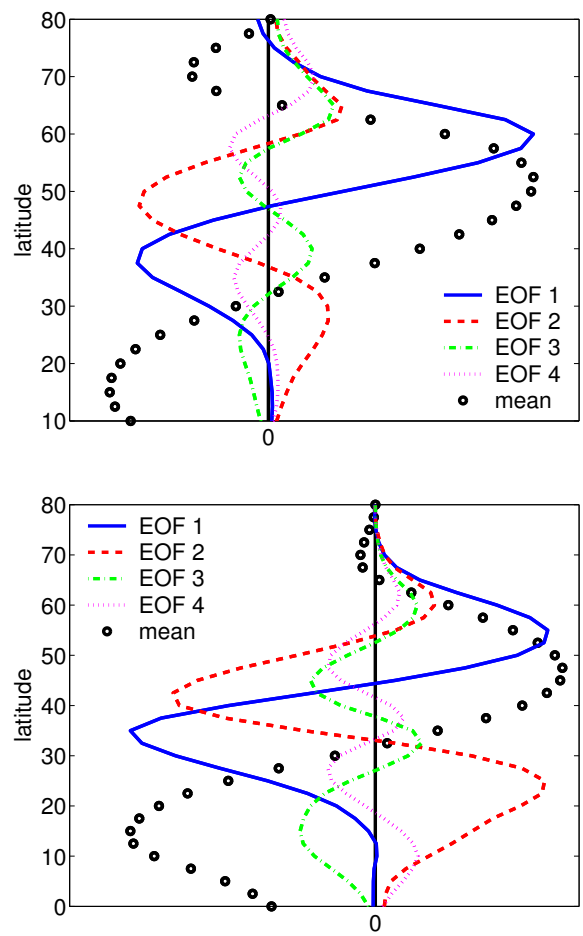


Figure 3.6: First four EOFs of the NCEP-NCAR reanalysis surface winds (top) and angular momentum (bottom). The “mean” curves refer to the climatological surface winds and angular momentum, respectively, scaled for ease of comparison with the EOFs.

nodes	$B(\omega, y)$	$M(\omega, y)$	BRW	MRW	BT	SH $u_s$	SH $\Phi$	NH $u_s$	NH $\Phi$
0	60.7	-	61.6	-	-	-	-	-	-
1	15.2	38.0	15.6	42.2	51.1	37.0	31.1	32.0	43.4
2	6.8	18.6	7.2	18.7	26.6	21.3	27.6	21.7	23.3
3	3.8	9.5	4.2	11.5	10.9	9.8	11.3	12.2	7.9

Table 3.2: Percent variance represented by the top EOFs. BRW refers to the 12 step random walk constrained to be bridge-like and MRW the same walk further constrained to be mean zero. BT refers to the EOFs of the zonally averaged zonal wind of the barotropic model with zonally symmetric stirring from Chapter 2. The Southern Hemisphere values for the EOFs of  $u_s$  and  $\Phi$  are based on the full data set. In the calculations of the Northern Hemisphere winds, only data from the winter months (DJF) were used.

Southern Hemisphere is perhaps a bit fortuitous. One might expect the EOFs of the angular momentum to better compare with the predictions of the model, as it is the conserved quantity. Here the second EOF appears to be stronger at the expense of the first. While EOFs of the Northern Hemisphere winter winds have the same structure as those in the Southern Hemisphere, the relative importance of the modes differs. For the zonal wind, there are more energy in higher EOFs, while the EOFs of angular momentum more closely match the values predicted by  $M$ .

### 3.3 A Two-Dimensional Model

#### 3.3.1 Theory

We now turn to the zonal structure of EOFs and correlation functions by constructing a simple two-dimensional model using the process  $M$  as a source of variability. In particular, we seek to understand the robust appearance of apparent annular modes in EOF analyses, despite the general absence of annular patterns in single point correlation maps and other measures of zonal correlation.

In Chapter 2, it was shown that anomalous stirring of the vorticity (i.e. anomalous baroclinic eddies in the atmosphere) leads to anomalous convergence of momentum,

and hence a dipole anomaly in the stream function. While this theory only applies strictly to the zonally averaged flow, as long as the zonal averaging is sufficient to cover a few eddies, the result approximately holds. Thus enhanced stirring in one region, e.g. a storm track, leads to enhanced variability in that region and an NAO-like pattern. We approximate this process by directly simulating the local zonal flow (by which we mean flow in the neighborhood of one longitude) with the process  $M$ . We then specify the correlation of the field in the zonal direction, seeking to replicate the local structure observed in the single point correlation maps of models and observations.

While  $M$  was constructed to simulate anomalies of the zonally averaged barotropic wind, we can also use the process to simulate the local reorganization of zonal momentum by eddies. Any longitudinal zonal wind profile in a two-dimensional, incompressible random flow field applicable to the extratropical atmosphere should obey constraints (3.2.1). The end point constraints still apply if we continue with the assumption that the variation of the flow in the tropics is weak. Assuming there is no flow across the equator, continuity implies that the latitude integrated flow is independent of longitude, establishing (3.2.1c).

### 3.3.2 The Model

We begin with a simple discrete example, and then generalize to a larger class of momentum conserving flows. For simplicity we simulate the flow in a channel with zonally periodic boundaries. Suppose there are  $n_f$  degrees of freedom in the channel, that is, given a channel of length  $L$  and length scale of eddy anomalies  $L_e$ ,  $n_f$  is of order  $L/L_e$ . To generate one realization of the flow field,  $n_f$  independent realizations of  $M$ , denoted  $m_j$ ,  $j = 1, 2, \dots, n_f$ , are sampled. The flow at  $n_f$  representative longitudes,  $\hat{m}_j$ ,  $j = 1, 2, \dots, n_f$ , are then constructed from the  $m_j$ . We build in a simple zonal

correlation structure, where

$$\begin{aligned}\hat{m}_j &= (1/\sqrt{2})(m_j + m_{j+1}) \quad j \neq n_f \\ \hat{m}_{n_f} &= (1/\sqrt{2})(m_{n_f} + m_1).\end{aligned}\tag{3.3.1}$$

This structure specifies that the flow at any given longitude is 0.5 correlated with the flow at neighboring longitudes and uncorrelated with all others. For comparison we also construct a null case in which the flow at each of the  $n_f$  representative longitudes is uncorrelated with the others:  $\hat{m}_j = m_j$ .

We first compute numeric solutions.  $n_f$  is varied from 2 (where the structure is just that of our one-dimensional process) to 13. In Figure 3.7 we compare two snapshots of random fields with  $n_f = 8$ , one the null case with no zonal correlation, the other described by (3.3.1). The zonal correlation of the latter is much easier to detect in single point correlation maps, Figure 3.8. By construction, zonal correlation stretches out one step in either direction from the base point, but no further. Similar to the single point correlation maps of streamfunction observed with the barotropic model, Figures 2.9 and 2.14, a dipole pattern appears when the base point is chosen poleward or equatorward of the jet center, but when points are chosen near the center of the jet, a meridional tripole pattern is observed.

Figure 3.9 illustrates the percent variance represented by the top 20 EOFs for the null case and the correlated case with  $n_f = 8$ . With the uncorrelated run, we have tiers of 8 degenerate EOFs, corresponding to 8 independent meridional dipole patterns, tripole patterns, and so forth (none shown). Differences in the variance accounted for by each EOF within the tier reflect the finite length of the simulation, and provide a measure of the convergence. The addition of zonal correlation in the second simulation separates one EOF above the rest: an annular mode-like structure shown in Figure 3.10. Deviation from perfect zonal uniformity is a product of the

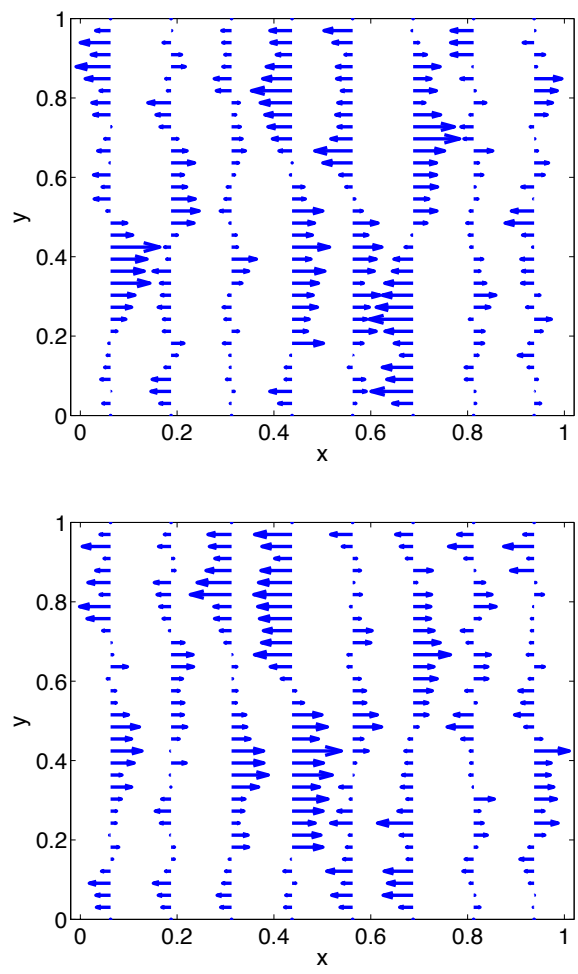


Figure 3.7: Realizations of the two-dimensional random flow fields with  $n_f = 8$ . On the top is the null case, with no zonal correlations. On the bottom, the flow has the simple correlation described in (3.3.1). EOFs are computed at discrete grid points indicated by the position of the arrows.

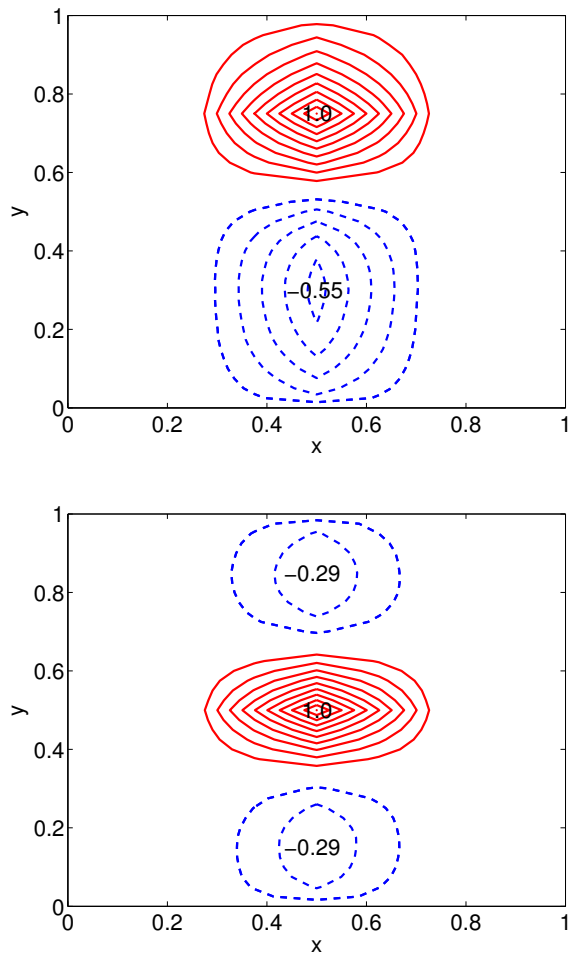


Figure 3.8: Single point correlation maps from the random field with zonal correlation given by (3.3.1) with  $n_f = 8$ . The base points are those with correlation 1. Contour interval is 0.1, and the zero contour has been omitted. A dipole or tripole pattern is found by varying the position of the base point, as observed with the barotropic model, Figures 2.9 and 2.14.

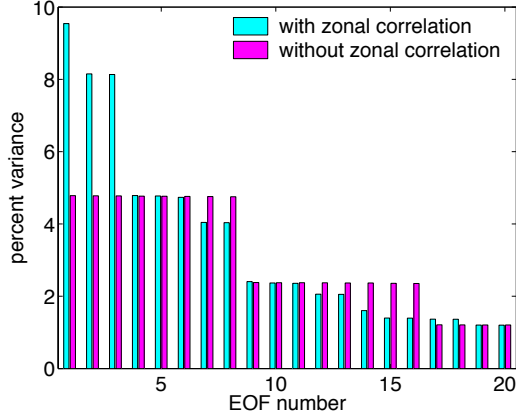


Figure 3.9: Percent variance accounted for by top EOFs,  $n_f = 8$ . Values for the uncorrelated and correlated simulations are shown for comparison. The annular mode-like EOF shown in Figure 3.10 is top EOF of the correlated simulation.

finite sampling. The next two EOFs (not shown) are also meridional dipole patterns, but with zonal wavenumber 1. The two are degenerate and in quadrature with each other; their phase is arbitrary, given the lack of any zonal asymmetry in the model.

The value of  $n_f$  does not govern the existence of the annular mode-like EOF in this model, but rather its separation from other modes. The annular mode-like pattern is always the first EOF, but its separation from higher wavenumber patterns is a function of  $n_f$ , as indicated in Figure 3.11. Beyond  $n_f = 13$ , the wavenumber 0 and 1 patterns are poorly separated and begin to mix in simulations. This could be remedied of course by still larger sampling, but from a practical point of view, such small separation is meaningless. Note that as  $n_f$  increases, the physical system described by (3.3.1) changes, in that the zonal scale of the correlation decreases if one assumes that the zonal scale of the channel is fixed. If one were to appropriately increase the correlation between modes (for example,  $\hat{m}_j = f(m_{j-1}, m_j, m_{j+1})$ ) so that the zonal scale of the correlation remained constant relative to the length of the channel, then the first EOF would be expected to remain annular and distinct.

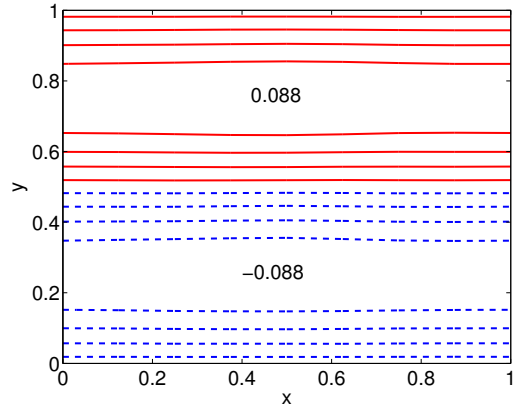


Figure 3.10: First EOF of the model with zonal correlation (3.3.1) and  $n_f = 8$ , an “Annular Mode.” Contour interval is 0.02, contours ( $\dots, -0.01, .01, .03, \dots$ ). As will be shown in analytic computations in Section 3.3.3, with infinite sampling the EOF is perfectly uniform in  $x$  and sinusoidal in  $y$ .

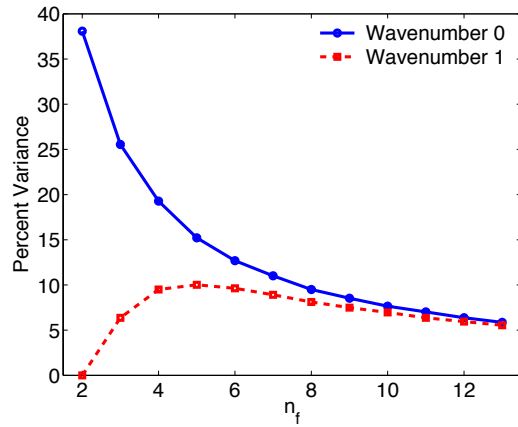


Figure 3.11: Percent variance represented by the first (wavenumber 0, solid line) and second (wavenumber 1, dashed line) EOFs as a function of  $n_f$  for the model with zonal correlation (3.3.1).

### 3.3.3 Analytic Solutions

As the zonal correlation is independent of latitude, the zonal structure of an EOF is independent of the meridional structure. Hence, a two-dimensional EOF can be separated into meridional and zonal components, that is,

$$\mathbf{E}_{k,l} = V_l U_k \quad (3.3.2)$$

where matrix  $\mathbf{E}_{k,l}$  is the two-dimensional EOF, meridional EOF  $V_l$  is a column vector, and zonal EOF  $U_k$  is a row vector. The subscript  $k$  refers to the  $k^{\text{th}}$  zonal eigenvector, and  $l$  for the  $l^{\text{th}}$  meridional eigenvector. The two-dimensional eigenvalues,  $\lambda_{k,l}$ , are the product of the meridional and zonal eigenvalues,  $\lambda_{k,l} = \lambda_k \lambda_l$ . Hence, the fraction of the total variance accounted for by a two-dimensional EOF is given by the product of the fractional variances represented by the zonal and meridional EOFs.

The meridional EOF structure, that of  $M$ , was diagnosed in Section 3.2 . The zonal EOF structure is determined from the zonal covariance matrix  $\mathbf{C}$ , where the  $ij^{\text{th}}$  entry is defined by

$$(c_{i,j}) = \text{cov}(\hat{m}_i, \hat{m}_j). \quad (3.3.3)$$

The zonal correlation matrix  $\mathbf{C}$  for the uncorrelated null case is simply the identity matrix. All eigenvalues are degenerate and equal to 1. The sum of all eigenvalues, the trace of the matrix, is  $n_f$ , so that each EOF explain  $1/n_f$  of the variance. The two-dimensional EOFs then clump in groups of  $n_f$ : the first  $n_f$  each represent  $0.38 \cdot 1/n_f$  of the total variance, the second set  $0.19 \cdot 1/n_f$ , and so forth. For  $n_f = 8$  the corresponding values are 0.048 and 0.023, as observed in the numeric simulation.

For the correlated cases the covariance matrix has three non-zero diagonals (plus

nonzero corners, a result of the periodic boundaries),

$$c_{i,j} = \begin{cases} 1 & \text{if } i = j \\ 1/2 & \text{if } i = j \pm 1 \text{ or } (i, j) = (1, n_f), (n_f, 1) \\ 0 & \text{otherwise} \end{cases} \quad (3.3.4)$$

As the sum of each row of  $\mathbf{C}$  is 2, a vector of all ones is an eigenvector with eigenvalue of 2. All other eigenvalues are less than 2, so this mode is nondegenerate and the foremost EOF: the annular mode. It explains  $2/n_f$  of the zonal variance, so that the full two-dimensional annular mode EOF explains  $0.38 \cdot 2/n_f$  of the variance. The  $n_f^{-1}$  power law observed in Figure 3.11 is thus an expression of the fact that each “annular mode” in this model represents the same amount of variance, but the total variance in the system increases linearly with  $n_f$ . The remaining eigenvalues are distributed between 0 and 2, and the wavenumber of the associated eigenvector increases for the smaller values. For  $n_f = 8$ , the first three eigenvalues are 2, 1.7, and 1.7. The annular mode then accounts for  $0.38 \cdot 2/8 = 0.095$  of the variance, and the degenerate second and third EOFs, with wavenumber 1, account for  $0.38 \cdot 1.7/8 = 0.081$  of the variance, each.

We can easily compute the EOFs of more general patterns as long as we keep the zonal correlation independent of latitude, so that the meridional and zonal structure of the EOFs remain independent. Rather than mechanically construct the correlations,  $\hat{m}_j = f(m_1, \dots, m_{n_f})$ , as in the model above, one may specify the covariance matrix  $\mathbf{C}$  directly, or, in the continuous limit, specify the covariance function. EOF analysis is possible provided  $\mathbf{C}$  is symmetric and positive semi-definite, and the EOFs themselves (or any rotation thereof) can be used to construct a flow with this zonal structure from the  $m_j$ . One can then construct a model with an arbitrarily large number of zonal degrees of freedom,  $n_f$ , while maintaining reasonable zonal correlations by filling out the diagonals of  $\mathbf{C}$ . In the continuous limit, the system can be viewed as a stochastic

process on a circle. As discussed by North et al. (1982), rotational invariance then leads EOF analysis to the trigonometric functions. The ranking of modes follows the same principal as expressed before. A simple red spectrum favors the gravest mode with zero wavenumber: the annular mode.

It is zonal symmetry of the covariance statistics, not necessarily of the motions themselves, that is required to produce an annular pattern. Zonal symmetry of the statistics implies that each row in the matrix is a translation of the others. Any such matrix will exhibit a zonally uniform EOF. A sufficient condition for this to be the dominant EOF is that the covariance decay monotonically over some finite length as the distance between points increases. As illustrated by our discrete model, local correlation — only three nonzero diagonals in the covariance matrix — is sufficient to produce such a pattern. Zonal symmetry of the motions, that is, long distance correlation in the zonal direction, would be manifested by nonzero values filling out the diagonals of the covariance matrix. This too would lead to zonally uniform EOFs, but is not a necessary condition.

### 3.4 An NAO-like Pattern

With the barotropic model, it was observed that enhanced stirring of the vorticity in a particular region led to enhanced local zonal wind anomalies and consequently an NAO-like pattern. We may use our stochastic process to model this, that is, use  $M$  to directly simulate the response of the zonal flow to inhomogeneous eddy forcing. For a simple illustration we employ the same  $\hat{m}_j = f(m_j)$  structure as in (3.3.1), but the strength of the random fluctuations of the zonal flow in one region (one  $m_j$ ) is

increased. For  $n_f = 8$ , we make the following changes,

$$\begin{aligned}\hat{m}_4 &= \sqrt{1/2} m_3 + \sqrt{a - 1/2} m_4 \\ \hat{m}_5 &= \sqrt{a - 1/2} m_4 + \sqrt{1/2} m_5.\end{aligned}\quad (3.4.1)$$

for  $a > 1/2$ . The corresponding zonal covariance matrix is

$$\mathbf{C} = \begin{pmatrix} 1 & 0.5 & 0 & 0 & 0 & 0 & 0 & 0.5 \\ 0.5 & 1 & 0.5 & 0 & 0 & 0 & 0 & 0 \\ 0 & 0.5 & 1 & 0.5 & 0 & 0 & 0 & 0 \\ 0 & 0 & 0.5 & a & a - 0.5 & 0 & 0 & 0 \\ 0 & 0 & 0 & a - 0.5 & a & 0.5 & 0 & 0 \\ 0 & 0 & 0 & 0 & 0.5 & 1 & 0.5 & 0 \\ 0 & 0 & 0 & 0 & 0 & 0.5 & 1 & 0.5 \\ 0.5 & 0 & 0 & 0 & 0 & 0 & 0.5 & 1 \end{pmatrix} \quad (3.4.2)$$

so that  $a$  sets the variance of the “storm track” region. If we take  $a$  to be 2, thus doubling the variability in the storm track, the first three eigenvalues are 3.6, 1.9, and 1.7. The trace of  $\mathbf{C}$  is 10, so that the top EOF represents  $0.38 \cdot 3.6/10 = 0.14$  of the total variance. Combining this with the first meridional EOF, we obtain the NAO-like mode shown in Figure 3.12. It is well separated from the next EOF, which explains only  $0.38 \cdot 1.9/10 = 0.072$  of the total variance.

Zonal inhomogeneity shifts EOF analysis from an annular pattern to a more localized NAO-like pattern. Figure 3.13 illustrates the degree to which the EOF has localized as a function of  $a$ . As a measure of the asymmetry of the first EOF, we plot the ratio  $m/M$ , where  $m$  is the minimum of the zonal EOF and  $M$  the maximum. For example, in the case when  $a = 2$  above,  $m/M = 0.0067/0.69 = 0.0096$ . For  $a = 1$  the variance is equal at all longitudes, and so is the first EOF. When  $a$  is 1.25, the

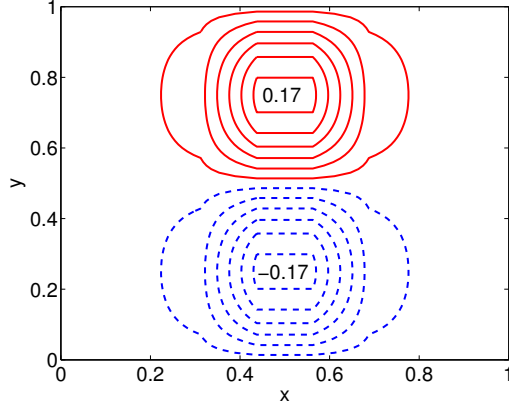


Figure 3.12: The first EOF from a simulation with enhanced variability in one region, described by (3.4.1). Contour interval is 0.03, with contours (...,-.015,.015,.045,...). It is NAO-like in being a zonally localized dipole pattern.

variance of the flow is only 25% stronger in one region, but the first EOF weights this region roughly five times as much as on the opposite side of the channel.

In general, the first EOF computed by numerical simulation of the two-dimensional model with zonally uniform zonal correlations ( $a = 1$ ) was slow to converge to the analytic solution. The analytic first EOF is zonally uniform, projecting only on to zonal wavenumber 0. The first EOF based on simulation was always dominated by zonal wavenumber 0, but mixed with small wavenumber 1 or higher anomalies. Only with a long simulation did these higher wavenumber patterns disappear. Such slow convergence to a perfect zonal wavenumber 0 pattern was also observed when the barotropic model was forced with statistically zonally uniform forcing.

The steep slope of the ratio  $m/M$  near  $a = 1$  in Figure 3.13 suggests an explanation for the slow convergence. Zonal EOF patterns are quite sensitive to small inhomogeneities in the covariance matrix. For example, when  $a$  is 1.01, so that the variance in one region is just 1% greater than the rest of the domain, the ratio of  $m/M$  is 0.94, indicating a 6% zonal inhomogeneity in the top EOF. Coupled with the slow convergence of the experimentally determined covariance matrix,<sup>2</sup> this sensitiv-

---

<sup>2</sup>The magnitude of the absolute error between the estimated covariance matrix (that is, the

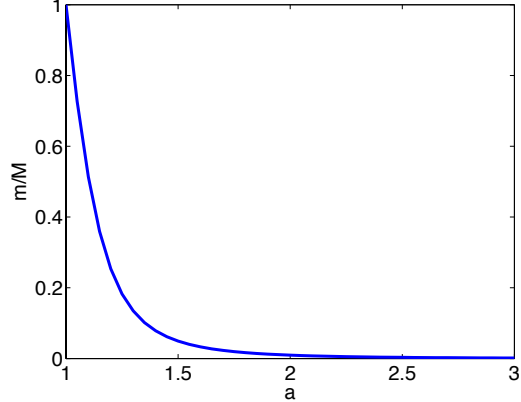


Figure 3.13: EOF localization as a function of  $a$ .  $m/M$  is the ratio of the minimum value of the first zonal EOF to its maximum value, and hence a rough measure of the asymmetry of the mode.

ity necessitates long simulations to achieve the pure analytical zonal wavenumber 0 structure.

## 3.5 Pressure Models

How does our decision to model the zonal winds, as opposed to another variable, affect our conclusions? To answer this question, we formulate two simple models of the zonally averaged surface pressure to compare with our model  $M$  of the zonally averaged zonal winds. By hydrostatic balance, surface pressure provides a measure of the vertically integrated mass of the atmosphere. Conservation of mass then establishes a constraint on the zonally averaged surface pressure. What does this constraint imply in the selection of an EOF basis?

### 3.5.1 Model $P_1$

Using the same notation as for  $M(\omega, y)$  in Section 3.2.1, we construct the stochastic process  $P_1(\omega, y)$  to model the space of zonally averaged surface pressure anomalies.

---

covariance matrix computed from a finite simulation with  $n$  independent observations) and the true covariance matrix decays with the square root of the number of independent observations,  $n^{-1/2}$ .

To enforce the conservation of mass, we require that all anomalies have zero mean, so constructing a model of the zonally averaged pressure in a homogeneous channel. We further assume there is no surface pressure anomaly at the equator (the lower boundary of the channel), in keeping with our thinking that the NAO and annular modes are primarily midlatitude phenomena. The process is then very similar to  $M$ , but for the omission of constraint (3.2.1b), which pins the zonal winds to zero at the pole. Paths are constructed from the Wiener process by the same procedure used to obtain  $M$  from  $B$ ,

$$P_1(\omega^*, y) = W(\omega^*, y) - E\left[W(\omega, y) \middle| \int_0^1 W(\omega, y) dy = \int_0^1 W(\omega^*, y) dy\right] \quad (3.5.1)$$

$$= W(\omega^*, y) - \left[ \int_0^1 W(\omega^*, y) dy \right] \frac{3y}{2}(2-y) \quad (3.5.2)$$

The expected path taken by a Wiener Process, given its mean,

$$E\left[W(\omega, y) \middle| \int_0^1 W(\omega, y) dy = \mu\right] = \frac{3y}{2}(2-y)\mu. \quad (3.5.3)$$

is computed by the same procedure used to compute the expected path of the Brownian Bridge, given its mean, in (3.2.11) to (3.2.23). The Fourier decomposition of the Wiener Process,

$$W(y) = \frac{\sqrt{2}}{\pi} \sum_{n=1}^{\infty} \frac{\zeta_n}{n} \sin[(n-1/2)\pi y] \quad (3.5.4)$$

is used in place of the decomposition of the Brownian Bridge, (3.2.6), and we make use of the result

$$\frac{3y}{2}(2-y) = \sum_{n=1}^{\infty} \frac{6}{n^3 \pi^3} \sin[(n-1/2)\pi y] \quad (3.5.5)$$

on  $[0, 1]$ . There is no decoupling between odd and even modes, as all basis functions have non-zero mean.

The Fourier decomposition of  $P_1$  is

$$P_1(y) = \frac{\sqrt{2}}{\pi} \sum_{n=1}^{\infty} \left( \frac{\zeta_n}{n - 1/2} - \frac{6}{\pi^4(n - 1/2)^3} \sum_{m=1}^{\infty} \frac{\zeta_m}{(m - 1/2)^2} \right) \sin[(n - 1/2)\pi y]. \quad (3.5.6)$$

Realizations of  $P_1$ , which are just Brownian motions constrained to have zero mean, are shown in Figure 3.14.

Also shown in Figure 3.14 are the top EOFs of model  $P_1$ . The first EOF is a dipole of pressure: an annular mode. We again have a Fourier-like decomposition of the field, but now EOFs take the form of  $\sin[\pi(n + 1/2)]$ , modified so that each has zero mean. Individual paths of  $P_1$  are not differentiable, so one cannot speak of the geostrophic wind implied by individual realizations. The EOFs are differentiable; the geostrophic winds implied by the first indicate a dipole in the wind, the second a tripole, and so forth. The implied winds, however, neither conserve momentum nor decay to zero at equator and pole.

The use of Brownian motion as our starting point makes it problematic to improve this model to account for the constraints on the zonal wind. We cannot enforce the conservation of momentum without the existence of geostrophic winds on a path by path basis, and it is the coupling of momentum conservation with continuity that allows us to extend our model of  $M$  to two dimensions in Section 3.3. There are of course a number of differentiable stochastic processes which would enable us to overcome this limitation. To avoid the introduction of new mathematics, however, we explore one option based on our previous work with  $M$ .

### 3.5.2 Model $P_2$

Realizations of our second model of the zonally averaged surface pressure,  $P_2(\omega, y)$ , are obtained from paths of  $M$  by integration, so inheriting geostrophic winds satisfying

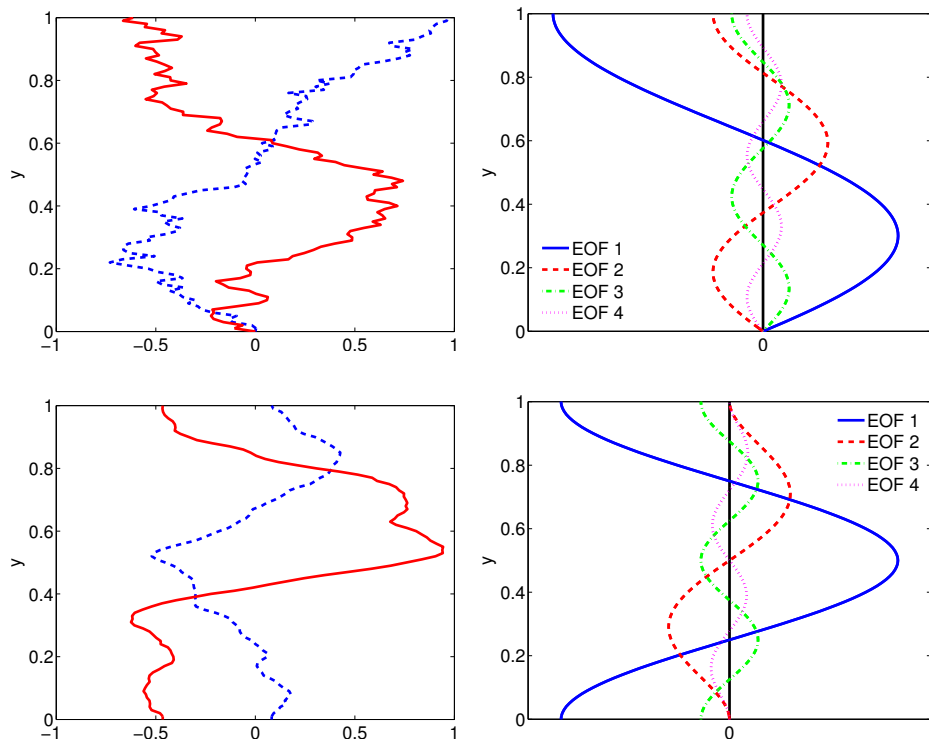


Figure 3.14: On the left, sample paths from models  $P_1$  (top) and  $P_2$  (bottom). On the right, the first four EOFs of two respective models.

constraints 3.2.1,

$$P_2(\omega*, y) = c(\omega*) + \int_0^y f_0 M(\omega*, x) dx. \quad (3.5.7)$$

$f_0$  is the Coriolis parameter (assumed to be constant) and  $c(\omega)$  is an integration constant determined on a path by path basis to ensure that each realization has zero mean. While  $c(\omega)$  enforces the conservation of mass, it also eliminates our control of the pressure at the equator; pressure profiles are now free at both ends. The loosening of boundary conditions can be seen in the sample paths of  $P_2$  and the corresponding EOFs shown in the lower half of Figure 3.14.

Model  $P_2$  is obtained from  $M$  by integration of (3.2.24). The Fourier decomposition is

$$\begin{aligned} P_2(y) &= \frac{f_0\sqrt{2}}{\pi^2} \sum_{n=1,3,\dots}^{\infty} \left( \frac{\zeta_n}{n^2} - \frac{96}{n^4\pi^4} \sum_{m=1}^{\infty} \frac{\zeta_m}{m^2} \right) \cos(n\pi y) \\ &\quad + \frac{f_0\sqrt{2}}{\pi^2} \sum_{n=2,4,\dots}^{\infty} \frac{\zeta_n}{n^2} \cos(n\pi y). \end{aligned} \quad (3.5.8)$$

Given the one-to-one relationship between paths of  $P_2$  and  $M$ , it is not a surprise that there is a one-to-one correspondence between their EOFs. The EOFs of  $M$  are exactly the geostrophic winds implied by the EOFs of  $P_2$ . What is perhaps of interest are the variances represented by each EOF, shown in Table 3.3. EOF 1 corresponds to the same motion in  $P_2$  and  $M$ , but the first EOF of pressure explains a much larger fraction of the variance, 65% as compared to 38%.

Pressure, as the *integral* of the zonal winds, contains more energy in larger scales. In these idealized models, this can be seen in the decay rates. While the variance of EOFs of  $M$  decay with wavenumber as  $n^{-2}$ , they decay as  $n^{-4}$  for  $P_2$ . The increased dominance of the first EOF of model  $P_1$  relative to  $M$ , however, does not follow from the same reasoning; both are Brownian motions with  $n^{-2}$  decay. Rather, it is a function of the wavenumbers allowed by the systems. Motions with wavenumbers

$1, 3/2, 2, \dots$  are allowed in  $M$ , while  $P_2$  is characterized by  $3/4, 5/4, 7/4, \dots$ . Albeit the  $n^{-2}$  decay is strictly true only in the limit as  $n \rightarrow \infty$ , it applies roughly to the small wavenumbers. Hence the ratio of the variances of the first two EOFs can be estimated by  $(5/3)^2 \approx 2.8$  for  $P_1$  as compared to  $(3/2)^2 = 2.25$  for  $M$ .

### 3.5.3 Comparison with observations

NCEP/NCAR reanalysis sea level pressure data were obtained in the same form as the surface zonal winds and EOFs computed with the same procedure. In Figure 3.15 we show the EOFs of sea level pressure in the Southern Hemisphere. Data over Antarctica (poleward of  $80^0$  S) were omitted in these calculations, but repeat computations with the full hemispheric pressure field produced nearly identical results. As shown by Thompson and Wallace (2000), the pressure EOF patterns are very robust. The same EOFs are observed in computations based on subsets of the time record, and in similar analysis of the Northern Hemisphere. The percent variance represented by the top EOFs are listed in Table 3.3. The first EOF in the Northern Hemisphere winter is less dominant than its southern counterpart. This difference appears to be relatively independent of the data used to compute the EOF; similar results are found when observations are limited to a season in the Southern Hemisphere or extended to the whole year in the North.

Model  $P_1$  performs much better in capturing the basic structure of the observed EOFs. EOF analysis is quite sensitive to boundary conditions; the modes describing  $P_2$  must satisfy constraints on their derivatives, and the cosine-like modes capture the end point constraints on the geostrophic winds. This is not to say that conservation of momentum and mass are competing effects. Rather, both constraints aid in the selection of the dipole EOF. A more complex model could integrate both constraints, as done naturally by atmospheric motions.

As seen in Table 3.3, the relative importance of the top EOFs in the atmosphere

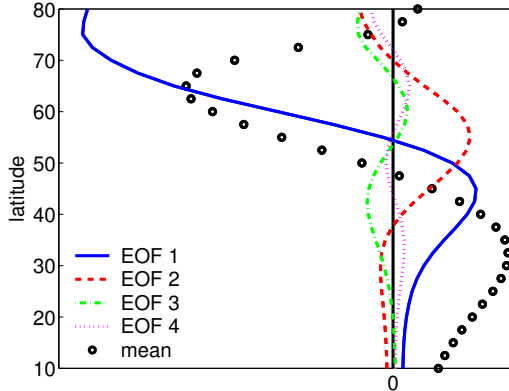


Figure 3.15: Top EOFs of sea level pressure in the Southern Hemisphere. Data poleward of  $80^{\circ}$  S were omitted from the calculation. The mean sea level pressure is shown as the anomaly from the hemispheric mean and scaled for comparison with the EOFs.

fall between models  $P_1$  and  $P_2$ . It is somewhat problematic that both models  $M$  and  $P_1$  so closely match the variance structure of atmospheric EOFs. Given geostrophic balance, it is not possible for both the winds and pressure to be described by Brownian motion. Spherical geometry is more important for the surface pressure than zonal winds (North et al. 1982), so that comparison of models  $P_1$  and  $P_2$  to the atmosphere is more tenuous; the result may be the product of canceling errors. Also, the reanalysis winds and pressure EOFs appear to decay exponentially with wavenumber. The differences in the relative importance of EOFs between model  $M$  and  $P_2$  is a result of low order algebraic decay. With exponential decay, the top EOFs of both pressure and winds can explain the same fraction of the variance. The atmosphere is likely somewhere in between these extremes.

What do these pressure models say about our initial question concerning the impact of variable choice on EOF analysis? Perhaps the most important point is seen in Tables 3.2 and 3.3, where we find the top EOFs of pressure, the “annular modes,” to be more dominant than the top EOFs of zonal wind. In the atmosphere fields are noisier and the decorrelation spectrum is not monotonic. The robustness of EOFs hinges on their separation. The larger separation between the top pressure EOFs

EOF	$P_1(\omega, y)$	$P_2(\omega, y)$	SH slp	NH slp
1	50.2	64.7	60.9	51.3
2	17.0	26.5	19.0	25.2
3	8.5	4.0	8.3	11.5

Table 3.3: Percent of the variance represented by the top pressure EOFs. EOFs of the Southern Hemisphere are computed from reanalysis sea level pressure observations between 0 and  $80^0$  S. EOFs of the Northern Hemisphere are based on wintertime (DJF) observations from 0 to  $90^0$  N.

makes it more probable for the zonally averaged signal to remain distinct in a noisy two-dimensional field. There is less separation between scales in the zonal winds, and consequently the annular signal is more likely to be overwhelmed.

## 3.6 Summary and Conclusions

We have constructed a series of stochastic models to determine the implications of the symmetries of the eddy driven, barotropic circulation in the selection of an EOF basis. Previous studies by Obukhov (1947), Batchelor (1953), and North and Cahalan (1981) have illustrated the effects of topological symmetries and decorrelation structure on an EOF basis constructed to describe random motions. We have added information about the fluid dynamics — in particular that mass and momentum be conserved — to models of random motions. We show that in various cases the resulting EOFs and correlation structures resemble those of the atmosphere. Meridional dipole structures robustly arise in both EOF and correlation analysis, and, depending on the zonal correlation structure of the stochastic model, either zonally elongated or zonally localized EOFs resembling annular modes and the North Atlantic Oscillation, respectively, are found. Zonally uniform EOFs arise when the zonal correlation is independent of longitude and decays monotonically with zonal distance, but do not require hemispheric scale correlations for their existence.

In our simplest model,  $M$ , we explored the space of zonally averaged barotropic

wind anomalies by constructing Brownian motions that are consistent with observed anomalies in a channel, specifically the conservation of zonal momentum. This constraint proved pivotal in the determination of the EOF basis. The result is a dominant meridional dipole pattern similar to that observed in the NAO and AO. The dipolar sinusoidal pattern is the gravest mode that satisfies the integral constraint required by the conservation of momentum. With this stochastic process, the dipole pattern is not indicative of a dynamical oscillation. Rather, it is part of a Fourier-like decomposition, the most efficient statistical expression of the variability. The EOF patterns predicted by the model are similar to those observed, as shown in Section 3.2.3.

The two-dimensional model illustrates a second important point. While zonally symmetric motions are sufficient to produce annular patterns of variability, they are not necessary. The necessary condition for zonally uniform EOFs is zonal symmetry of the covariance statistics. Our model makes explicit a case where the motions are not symmetric, as seen in the finite zonal correlation patterns, Figure 3.8, but zonal symmetry of the statistics produces the annular mode, Figure 3.10. Ambaum et al. (2001) make a similar point with a low order model of the Arctic Oscillation.

We also found that the EOF structure of the two-dimensional model was quite sensitive to small asymmetries in the covariance statistics. In particular, if we increase the variance in the stochastic model in a zonally localized region, the annular EOFs are replaced by EOFs that resemble those of the NAO, as shown in Figure 3.12.

Lastly, we compared models of surface pressure to models of the zonal wind. Our first model,  $P_1$ , is similar in spirit to  $M$ , consisting of Brownian motions constrained to behave as anomalies of the zonally averaged surface pressure. In particular, anomalies must conserve mass. EOF analysis again produces Fourier-like modes consistent with the essential constraints and boundary conditions; the first and gravest mode is a dipole in pressure, or mass, between the pole and lower latitudes. Both the EOF patterns and the variance represented by each mode compare well with reanalysis

observations.

Our second pressure model,  $P_2$ , was based directly on  $M$  in an effort to account for constraints on both the zonal winds and pressure. While the model does not predict the observed EOF structure as well as  $P_1$ , it illustrates an important point concerning EOF analysis and the choice of variable. In choosing Brownian motion to model the zonal wind, we assumed a white vorticity field, constrained only to conserve angular momentum and satisfy the boundary conditions of the zonal wind. In EOF analysis of this vorticity field (not shown), all modes are almost degenerate, explaining nearly the same fraction of the variance. Integration to compute the zonal wind anomalies,  $M$ , separates modes with a  $n^{-2}$  spectrum, and the annular mode of the zonally averaged winds appears. A second integration to obtain the pressure,  $P_2$ , produces EOFs that decay as  $n^{-4}$ , further emphasizing the separation of scales.

While the atmospheric spectrum is not so extreme, there is a greater separation of scales with pressure (or geopotential height) than zonal winds. That the first EOF of pressure then explains a larger fraction of the variance is significant. Modes found in our simple models are more likely to be observed in the atmosphere if they are well separated, and thus more robust to rearrangement when the covariance structure is perturbed.

Why do these EOF patterns arise? Both the meridional dipole and annular zonal patterns are grave modes. In a field with a red spectrum, neighboring points are positively correlated. Hence, they will likely appear as the same sign in an EOF that will, by design, maximize the variance it can represent. Given this connection, EOF analysis simply links point to point seeking to capture the entire domain in the first EOF. In the zonal direction this favors annular patterns. In the meridional, conservation of mass and zonal momentum provide an additional constraint; there must be at least one node, and clearly, less pairwise variance is sacrificed with a single node than with two.

Zonal wavenumber zero modes are expressions of rotational symmetry and meridional wavenumber one modes are expressions of mass and momentum conservation. It is therefore natural that such patterns are observed in simple dynamical models, full Global Climate Models, and observations alike. This does not, of course, preclude the possibility that these patterns may be real dynamical modes. However, these are simply the patterns that one would expect to observe if the atmospheric velocity field were characterized by a random walk, subject to the constraints specified in (3.2.1). Thus, they provide a starting point for searching out the dynamically interesting side of extratropical low frequency variability. Deviations from these patterns, for example, may suggest that other dynamics is occurring.

# Chapter 4

## The Dry Dynamical Core I: The NAO and Annular Modes

### 4.1 Introduction

In light of stochastic models presented in the previous chapter, particularly the two dimensional models in Section 3.3 and Section 3.4, the results of Chapter 2 seem less surprising. The conclusions from the barotropic study, however, that movement of the jet characterized by the NAO and annular modes are driven by eddy momentum flux convergence, provides a physical mechanism for the phenomena, even if such motions are fairly random.

It is perhaps to be expected that the variability in the barotropic model be close to the random limit investigated in the stochastic model. The interactions were only in one direction; we prescribed the eddy stirring, and witnessed how it controlled the patterns of intraseasonal variability. To more fully understand the dynamics of the intraseasonal variability, we need a model where the large scale patterns can in turn influence the eddies that generate them. Also of interest are the features of the mean state that give rise to zonal localization of the eddy stirring: topography and

zonal asymmetries in temperature created by land sea contrast. In the barotropic model we in essence took the storm tracks for granted, prescribing a localization of the synoptic stirring. To investigate the two-way interactions of the eddies and low frequency variability and understand the processes that produce the storm tracks, we turn to our third model, a dry, primitive equation model on the sphere.

Moving to a model with vertical structure also addresses a significant limitation of the one layer model. With a barotropic atmosphere there is ambiguity as to which part of the atmosphere the circulation represents. It is most readily interpreted as a model of the surface winds, which characterize the barotropic circulation generated by the eddies. But this is problematic, as the eddy interactions generating this circulation occur in the upper atmosphere. To see this, we return to the equations modeling the maintenance of the surface westerlies in Section 2.2.1. Implicit in the transfer of momentum by eddies described by (2.2.9) is the meridional propagation of Rossby waves. This meridional propagation is responsible for expanding the “damping,”  $\overline{\zeta' D'_\zeta}$  so that it is wider than the “stirring,”  $\overline{\zeta' F'_\zeta}$ , giving rise to the upgradient movement of momentum observed in Figure 2.3. While the stirring and damping processes are nonlinear, the meridional propagation depends on the wave-like properties of the upper atmosphere, where stronger westerlies allow for linear dynamics.

Linear theory shows that the particle displacement,  $\eta$ , varies inversely to the separation between the speed of the zonal mean flow and the phase speed of the wave,

$$\eta \sim \frac{\psi}{\bar{u} - c}, \quad (4.1.1)$$

where  $\psi$  is the streamfunction perturbation and  $c$  the phase speed of the wave. This follows from the fact that the period of the oscillations  $\omega^{-1} \sim 1/k(U - c)$  and the perturbation meridional velocity  $v = \psi_x \sim k\psi$ . Thus, even for infinitesimally small perturbations, the particular displacements become large near the critical line where  $\bar{u} - c = 0$ , and nonlinearity will become important. In the atmosphere, Randel and

Held (1991) found that waves tend to break 10-20° before they reach their critical lines. As the zonal winds in the barotropic model were relatively weak – of the magnitude of surface winds, not upper level winds – linear interactions were limited. This limitation was reflected in the fact that the RMS eddy speed was nearly double the time average zonal wind speed; the model had to be over zealously forced to produce a reasonable circulation. In the atmosphere, eddy wind speeds are comparable to the jet speed.

In working with a simplified GCM, we begin to tread closer to existing scholarship. Many studies have been completed with simplified GCMs, (e.g Limpasuvan and Hartmann 2000; Cash et al. 2002, 2005), and two-layer primitive equation models (e.g. Feldstein and Lee 1996; Robinson 1996). Our model fits in between these studies, lacking the complexity of convection and boundary layer parameterizations of the idealized GCMs, but representing the three dimensional dynamics more accurately than simpler two layer models. But more importantly, we differentiate our work in our focus. Here, we investigate the impact of zonally asymmetric forcing on the variability, and the criterion for establishing a realistic storm track. Next, in Chapter 5, we turn our attention to the temporal scales, determining how they are affected by changes in model parameters and zonally asymmetric forcing.

The focus of this chapter – zonal asymmetries – is most similar to the Cash et al. (2005) study of an aquaplanet GCM. There, the lower boundary conditions, specifically topography and land-sea surface, were modified to create a local maximum in the baroclinicity. This created a zonally localized storm track – a region of enhanced “stirring” – and the pattern of low frequency variability localized as in Chapter 2, becoming more NAO-like in character. The authors found that the localization of the low frequency patterns was roughly linear with the localization of the storm track. Here we complete series of intermediate experiments to fill in the gap between Cash et al. (2005) and the barotropic model in Chapter 2.

We establish the model and our analysis techniques in Section 4.2. Then, in

Section 4.3, we explore the effect of simple topographic and large scale thermal forcing on the baroclinicity and synoptic variability. What are the basic ingredients for building a storm track in a primitive equation model, and how does the storm track affect the intraseasonal variability? We find that a localized NAO-like pattern replaces the more annular patterns of variability only with the correct alignment of large scale topographic and thermal forcing. Particular attention is focused on the role of eddy heat and momentum fluxes, establishing a connection between the eddy life cycle and the NAO. In Section 4.4, we characterize the patterns of low frequency variability, and we investigate the differences between local and global patterns of variability in Section 4.5. In Section 4.6, we present an alternative strategy for characterizing changes in the extratropical jet, which ultimately provides similar information about the jet than EOF analysis. This classification suggest a physical interpretation of the NAO as the interaction of two like signed vortices (two jets), whose merger and separation, is in essence, the NAO. Lastly, we summarize our results and conclusions in Section 4.7.

## 4.2 Experimental Setup

We use the GFDL dry dynamical core, a primitive equation spectral model of the atmosphere. “Dry” refers to the fact that water and water vapor are not in the model; the equations describe the motions of an ideal, non-precipitating gas. While moist convection plays a critical role in the atmosphere, a simplification of the temperature equation approximates its effect to leading order. The term “dynamical core,” refers to the fact that the model was developed to implement the dynamics of a full GCM. A realistic GCM can be constructed by coupling the dynamics of the “core” to realistic radiative transfer, convection, surface flux schemes, etc.. In our case we use a simplified forcing as described in Held and Suarez (1994), hereafter denoted

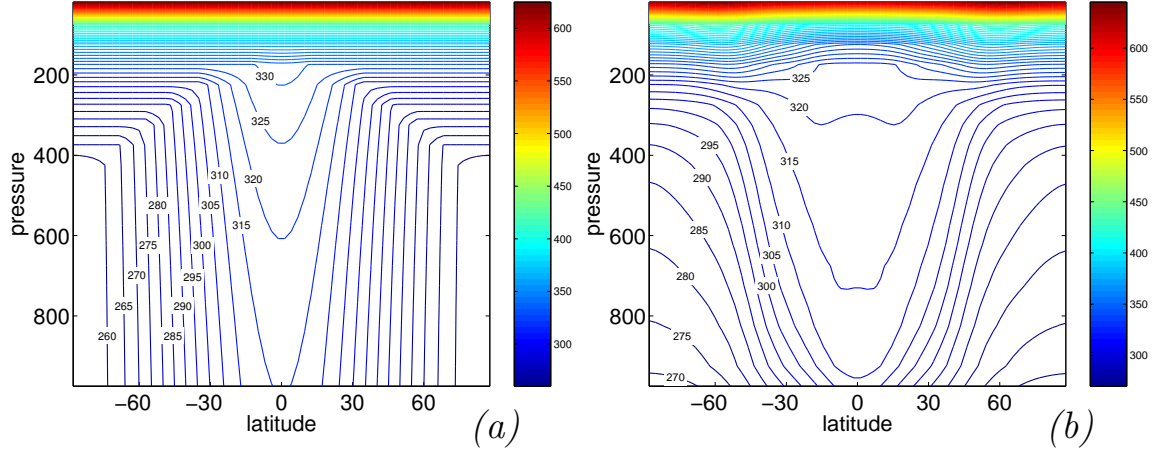


Figure 4.1: The (a) equilibrium and (b) time and zonal average temperature profiles of the model. The units are in potential temperature to illustrate the stability of the equilibrium state. The model output is from a control simulation with zonally symmetric forcing, run at T42 resolution with 20 evenly spaced  $\sigma$ -levels.

by HS. The chief simplification is in the temperature equation; in lieu of radiation and convection schemes, a simple Newtonian relaxation to a prescribed temperature profile  $T_{eq}$  is applied:

$$\frac{DT}{Dt} = -k_a(T - T_{eq}). \quad (4.2.1)$$

In the standard HS configuration,  $T_{eq}$  and  $k_a$  are zonally uniform. The damping,  $k_a$ , is almost everywhere set to  $40^{-1}$  day $^{-1}$ , the exception being in the low level tropics, where it is increased to  $4^{-1}$  day $^{-1}$  at the surface to give the model a more realistic Hadley Circulation.

The equilibrium temperature profile and the time average profile from the model output are shown in Figure 4.1. In the vertical, the potential temperature in the equilibrium profile is almost constant in the troposphere, implying near zero-stability. It thus forces the atmosphere towards a state of radiative-convective equilibrium. As can be inferred from the differences between the equilibrium and time average profile, the circulation acts to increase the stability in the vertical, settling cold air down and raising warmer air upward, and to reduce the equator-to-pole temperature gradient.

The equator-to-pole temperature gradient of the equilibrium profile is controlled by the parameter  $\Delta T_{eq}$ . It is kept at the standard HS value of 60 K for this study. We present results from simulations when  $\Delta T_{eq}$  is varied in Chapter 5, as it influences the timescales of the variability. These changes, however, do not affect the conclusions of this chapter.

In lieu of a boundary layer scheme, the HS forcing makes use of a Rayleigh drag near the surface,  $DU/Dt = \dots - f(U, \sigma)$ , where

$$f(u, \sigma) = \begin{cases} \frac{\sigma - \sigma_0}{1 - \sigma_0} k_f U, & \sigma \geq \sigma_0 \\ 0, & \text{otherwise} \end{cases} \quad (4.2.2)$$

The drag at the surface is set by  $k_f = 1 \text{ day}^{-1}$ , and decreases linearly to the  $\sigma_0 = 0.7$  surface, where it vanishes. A  $\nabla^8$  damping is included to remove enstrophy at small scales. The damping time on the smallest resolved scale is 1/10 of a day.

### 4.2.1 Zonally Asymmetric Forcing

The zonal symmetry of the HS forcing is broken by the addition of Gaussian topography and perturbations to equilibrium temperature profile. Our goal is to create a zonally localized region of increased synoptic variability, or storm track. In our study, we define storm tracks with Eulerian statistics, such as the average kinetic energy as a function of space, but the term makes more sense in its historical context. Such regions were originally identified by meteorologists following the paths of individual weather systems. They found preferred tracks taken by midlatitude storms along the East Coasts of the continents. As illustrated by Hoskins and Hodges (2002), this Lagrangian view of storm activity offers a slightly different view of synoptic variability than the Eulerian view we have adopted.

Routines have been written to add Gaussian mountains in latitude-longitude space to the dynamical core. We have experimented with mountains of varying shape

and height, and found the results to be relatively robust provided the topography is positioned as to block the extratropical jet. In the simulations described below, we have added a 2000 m high ridge, comparable in vertical and horizontal scale to the Rocky Mountains, or Andes in the Southern Hemisphere. The ridge is  $40^{\circ}$  long in latitude and centered about  $40^{\circ}$  N. It tapers off with a half width of  $12.5^{\circ}$  at either end, so that it does not extend into the Southern Hemisphere. The half-width of the ridge in longitude is  $12.5$  degrees.

The basic effect of topography can be illustrated with a simple one-layer quasi-geostrophic model (e.g. Vallis 2005). In computing the linear response of the flow to orography, one finds a resonant wave. The scale of the wave depends on the particulars of the topography, but there is always a resonant wavelength. To address the singularity, one must add damping. With a simple Rayleigh drag, all free waves are damped away, and the resonant wave stabilizes with bounded amplitude  $1/4$  wavelength out of phase with the topography, much as observed in the primitive equation model in Figure 4.5a. The standing wave tightens the lines of constant temperature, producing a local increase in the baroclinicity of the flow just downstream of the orography, followed by a local minimum, and so forth until the standing wave damps away.

Hoskins and Valdes (1990) illustrate the importance of diabatic heating in the maintenance of the storm tracks. Diabatic effects include the release of latent heat associated with convection in midlatitude storms, and the changes in surface fluxes between land and sea. Both help maintain the sharp temperature gradients that provide the source of energy for baroclinic storms; otherwise, the eddy activity destroys the baroclinicity in the jet, choking off the storm track. We approximate these effects by adding a high latitude region of cooling (i.e. a continent) and warming (i.e. an ocean) with a sharp change between them, as is seen on the Eastern coasts of Asia and North America. The cooling at high latitudes increases the temperature gradient

to south, creating a strong baroclinic zone, while the high latitude heating reduces the overall gradient, producing a weak baroclinic zone.

We experimented with several variations, settling with a simple perturbation  $\delta T_{eq}$  to the zonally uniform profile that produced the desired zonal asymmetry in the synoptic variability,

$$\delta T_{eq}(\lambda, \theta, \sigma) = k f_\lambda(\lambda) f_\theta(\theta) f_\sigma(\sigma). \quad (4.2.3)$$

where  $\lambda$ ,  $\theta$ , and  $\sigma = p/p_s$  are the longitudinal, latitudinal, and vertical coordinates, respectively. The horizontal profile was constructed from sine functions,

$$f_\lambda(\lambda) = \begin{cases} 0 & \lambda < \pi/2 \\ \sin(2\sigma) & \pi/2 \leq \lambda < 3\pi/2 \\ 0 & \sigma \geq 3\pi/2 \end{cases} \quad (4.2.4)$$

$$f_\theta(\theta) = \begin{cases} 0 & \theta < 0 \\ \sin(\theta) - \sin(3\theta)/3 & \theta \geq 0 \end{cases} \quad (4.2.5)$$

In the vertical, the profile is maximum at the surfaces, and decays by a cosine function in  $\sigma$  to zero near the tropopause,

$$f_\sigma(\sigma) = \begin{cases} \cos(\pi \frac{1-\sigma}{1.6}) & \sigma \geq 0.2 \\ 0 & \sigma < 0.2 \end{cases} \quad (4.2.6)$$

Note that in the implementation of the HS forcing,  $T_{eq}$  is not allowed to drop below 200 K, the temperature of the model's stratosphere. We have kept this constraint when applying the perturbation  $\delta T_{eq}$ , thereby truncating the cooling anomaly in upper levels at high latitudes where the temperature would otherwise drop below 200 K.

The decision to keep the profiles simple was deliberate; a more optimized profile could surely be found through trial and error or an iterative method, but here the intent was to keep the forcing basic, so that conclusions are not dependent on par-

simulation	topography	thermal forcing
LSC	none	yes
RM	90 E	no
LSC+RM1	90 E	yes
LSC+RM2	120 E	yes

Table 4.1: Specifications of the zonally asymmetric simulations. The longitude of the ridge (if applicable) is listed in the column marked topography. For reference, the boundary between the cold and warm anomalies is located at 180° E, and in Figures, the “prime meridian” is always positioned at noon.

ticulars of the model forcing. The amplitude of the pattern was set to produce a heating/cooling rate of approximately 4 K per day, large, but of the same order as that observed in Hoskins and Valdes (1990).

### 4.2.2 Simulation Specifications

The model is run at  $T42$  resolution with 20 evenly spaced levels  $\sigma$ -levels in the vertical. Unfortunately the temporal variability of the model is known to be sensitive to resolution, as will be discussed Section 5.4. The behavior at this resolution appears to be robust, as confirmed by simulations at higher resolution. Data is sampled daily for 9000 days (approximately 25 years) after a spin up period of 250 days.

We focus on four simulations, LSC (land-sea contrast), RM (Rocky mountains), LSC+RM1 and LSC+RM2. In the latter two simulations, topography and heating anomalies were combined to optimize the zonal localization of the storm track and intraseasonal variability. They differ in the location of the topography relative to the heating anomaly. The best alignment was found in simulations LSC+RM1, when the topography was located at the western boundary of the cooling anomaly. In LSC+RM2, the topography was shifted 30° east of its position in LSC+RM1. For reference, a list of the experiments to be discussed are found in Table 4.1.

Model output was sampled daily. Computations were completed on the native  $\sigma$ -coordinates and the results interpolated to pressure surfaces where appropriate. High-

pass statistics were computed with a Lanczos filter with cutoff frequency  $f_c = 10^{-1}$ , thereby capturing frequencies between roughly  $2^{-1}$  and  $10^{-1}$  days. A digital window of  $2n + 1 = 41$  provided sufficient breadth for a clean frequency cutoff (Duchon 1979). Low-pass statistics with  $f_c = 30$  day cutoff were computed with a larger  $2n + 1 = 201$  window. The bias due the decrease in separation of grid points at high latitudes in Empirical Orthogonal Function (EOF) computations was corrected by weighting fields with a factor of  $\cos^{1/2} \theta$  as instructed by North et al. (1982).

The reanalysis eddy kinetic energy was computed from NCEP-NCAR reanalysis data, obtained from the NOAA-CIRES Climate Diagnostics Center, Boulder, Colorado, USA, via their Web site at <http://www.cdc.noaa.gov/>. The reanalysis procedure is described by Kalnay et al. (1996). We used the meridional and zonal winds sampled daily from 1958 to 1997 on a  $2.5 \times 2.5$  latitude-longitude grid. Eddies were defined as deviations from the annual average smoothed by a 30 day running mean.

## 4.3 Simulation Results

### 4.3.1 The Baroclinic Storm Track: Simulation LSC

We first consider simulation LSC, where a storm track is generated with thermal forcing alone. Here the relationship between the large scale forcing and the variability is most transparent. In Figure 4.2 we characterize important features of the mean state. The heating and cooling regions are marked by magenta contours. The maximum tropospheric average cooling (heating) rate over the “continent” (“ocean”) are  $-/+ 4$  K/day, an input of approximately  $400 \text{ Wm}^{-2}$  to the column. While these values are high, they are not unreasonable for an earth-like climate system.

To anticipate the effect of the zonal asymmetries of the mean climate on the variability, we are most interested in baroclinicity of the flow. Following Hoskins and Valdes (1990) and Chang and Orlanski (1993), the baroclinicity is quantified by the

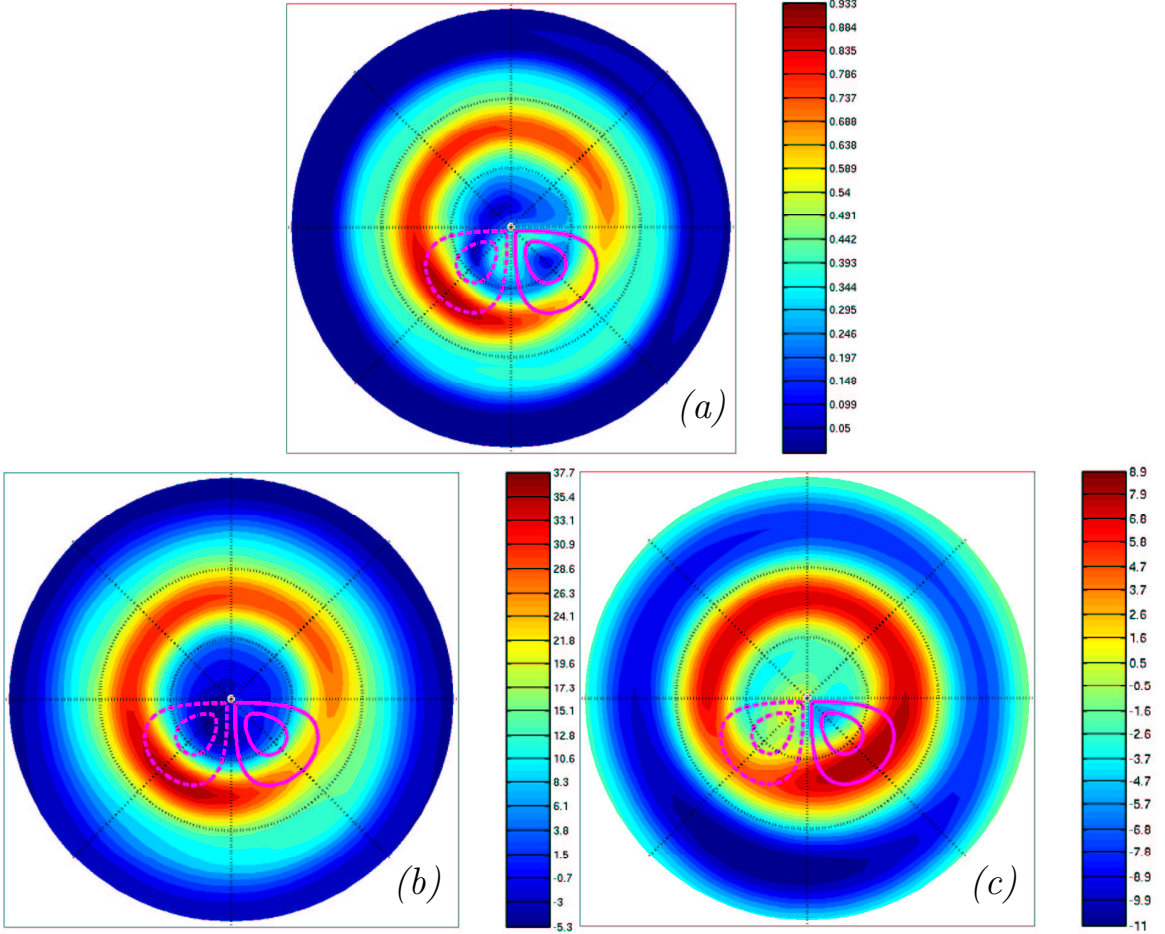


Figure 4.2: Mean properties of simulation LSC. (a) the Eady growth rate parameter,  $\sigma_{BI}$  (day $^{-1}$ ), (b) the time average zonal winds at 250 hPa (ms $^{-1}$ ) and (c), the time average winds on the 0.975  $\sigma$ -surface (ms $^{-1}$ ). The magenta contours denote the heating and cooling regions. Contours roughly delineate regions where the heating anomaly is -3, -1, 1, and 3 K/day, with negative contours dashed.

maximum Eady growth rate parameter,  $\sigma_{BI}$ ,

$$\sigma_{BI} = 0.31f \left| \frac{\partial \mathbf{V}}{\partial z} \right| N^{-1}. \quad (4.3.1)$$

$N$  is the Brunt-Väisälä frequency,

$$N^2 = \frac{g}{\theta} \frac{\partial \theta_E}{\partial z}, \quad (4.3.2)$$

where  $\theta_E$  is the environmental profile of potential temperature. The growth rate ap-

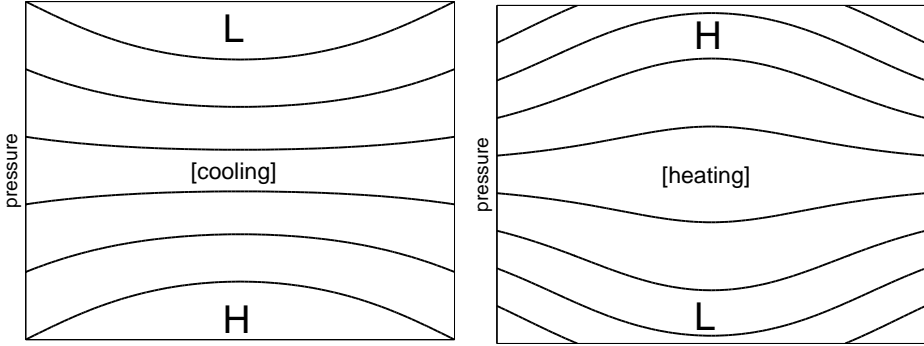


Figure 4.3: Cartoons illustrating the influence of the large scale diabatic anomalies on the circulation. Contours reflect the deviations of isentropic surfaces.

plies strictly only in the simplified Eady context, but it combines two quantities of interest, the variation of the vertical shear and the static stability. Baroclinic instability is favored by strong vertical shear, which indicates strong horizontal temperature gradients by thermal wind balance and hence a source of potential energy, and weak stratification (small  $N$ ).

The value of  $\sigma_{BI}$  computed from the mean flow is shown in Figure 4.2a. We show the growth rate at 500 hPa, but have found features of the growth rate are robust through the lower and mid-troposphere. Comparison of  $\sigma_{BI}$  to the upper level and surface winds illustrated in Figure 4.2b and c reveals that the growth rate is determined primarily by the vertical shear. As sketched in Figure 4.3, the cooling and warming anomalies establish a baroclinic circulation superimposed on the midlatitude circulation. The cooling produces a surface high, and the associated anticyclone reduces the westerlies near the surface. At height, we find lower than average pressure, and a cyclone that increases the westerlies at height, thereby increasing the baroclinicity of the jet. The converse occurs over the warming ocean, leading to sharp drop of the baroclinicity and the Eady growth rate.

Having perturbed the baroclinicity of the flow as a function of longitude, we ask how the variability of the flow has changed. It has been demonstrated by several

authors that a localization of the baroclinicity is not sufficient to create a localized storm track. Pierrehumbert (1984) studied the problem from a linear perspective, differentiating absolute, or “local” instability, from convective, or “global” instability. In the former case, the local flow is sufficiently unstable to support an exponentially growing mode at a fixed point in space, despite advection by a mean flow. In the latter, the tendency to advect the instability away from the local region is too great, and the instability can only grow over time by continually recirculating over the baroclinic region. This implies that in a case with a westerly jet, one would expect to see a localized region of eddy energy only when the flow is absolutely unstable - not just baroclinically unstable.

The analysis of Pierrehumbert (1984) is limited to the linearized system. As non-linearities would first truncate the growth of the most unstable modes, one would expect a fully nonlinear system to be less localized than the linear case. Chang and Orlanski (1993) consider the nonlinear evolution of eddies in a channel with zonally varying baroclinicity. They found that ageostrophic geopotential fluxes propagated eddy energy downstream, and can sustain eddy energy through regions of lower baroclinicity. Thus, despite a substantial drop in the baroclinicity in the channel, the eddy kinetic energy was approximately constant throughout the domain.

Figure 4.4a illustrates the transient eddy kinetic energy (EKE) of the flow at 250 hPa. Clearly we have established sufficient asymmetry in the baroclinicity to localize the EKE. The energy varies by a factor of two around the latitude circle, reaching a maximum value of approximately  $430 \text{ m}^2\text{s}^{-2}$ , comparable in magnitude to the EKE of the atmosphere, shown in Figure 4.9b. The black contours sketch the position of the Eady growth rate parameter at 500 hPa, indicating that the EKE maximum is approximately  $60^\circ$  downstream of the peak baroclinicity. This is consistent with the fact that the mean flow advects growing eddies downstream, so that they reach maturity downstream of the region with maximal growth rates. Inspection of the

eddy heat and momentum fluxes, shown in Figure 4.4b and c, further clarifies the relationship between the eddy life cycle and the storm track.

A high pass filter isolates the heat fluxes associated with baroclinic eddies. The eddy heat fluxes are strongest in the lower troposphere, though they also reach a secondary maximum in the model's stratosphere. Simmons and Hoskins (1978) found a similar vertical structure in computations of initial perturbations of wavenumber 6 and 9. The heat fluxes in the model nearly coincide with the regions of large  $\sigma_{BI}$ , suggesting that the Eady growth rate parameter well captures the baroclinicity of the mean flow. As the shape of  $\sigma_{BI}$  is determined primarily by the vertical shear, we can interpret the baroclinicity parameter as a map of the temperature gradient by applying thermal wind balance. This suggests that the eddy fluxes could be well approximated by an eddy diffusivity, fluxing heat down the temperature gradient. By reducing the temperature gradient, particularly at low levels, the eddies reduce the vertical shear and make the flow more barotropic.

Upper level eddy momentum fluxes, on the other hand, are associated with eddy decay and the transfer of eddy energy to the mean flow. These fluxes are largest at the end of the storm track, where eddy decay dominates. Clearly the momentum fluxes cannot be approximated by an eddy diffusion; momentum converges upgradient, as illustrated in the barotropic model, (2.2.10). While the overall effect of the eddy forcing makes mean flow more barotropic, the eddy momentum fluxes by themselves modify the baroclinicity of the flow. They are much larger in the upper levels than in the lower levels, as the strong westerlies at height increase the linearity of the flow, permitting Rossby wave propagation. Thus, they tend to increase the baroclinicity in the jet core and decrease it on the flanks. As suggested in Chapter 5, this may play a role in enhancing the persistence of intraseasonal variability. The EKE maximum is found in between the eddy growth region marked by strong eddy momentum fluxes and the decay region marked by eddy momentum fluxes.

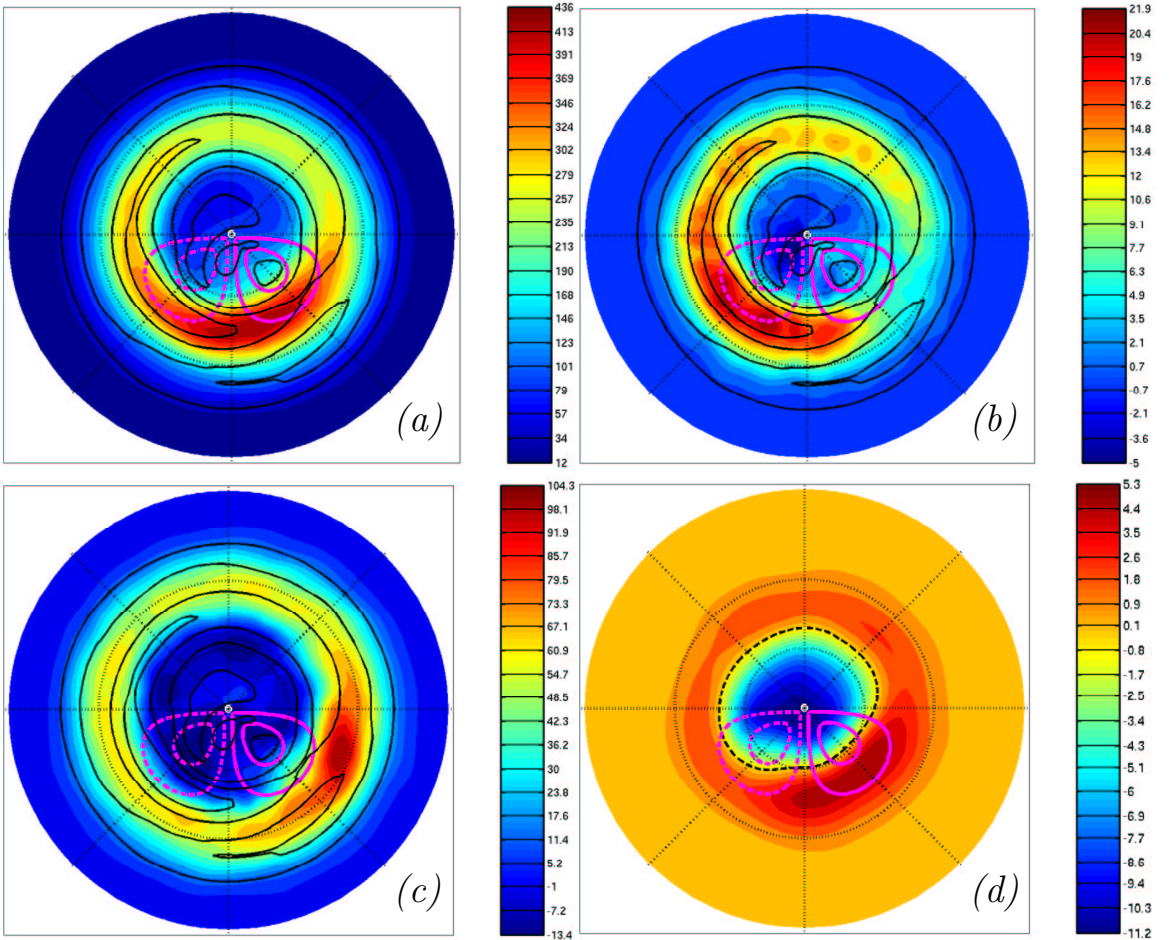


Figure 4.4: The variability of simulation LSC. (a) The time average transient eddy kinetic energy at 250 hPa ( $\text{m}^2\text{s}^{-2}$ ), (b) the high pass (frequencies from  $10^{-1}$  to  $2^{-1}$  day $^{-1}$ ) eddy heat fluxes at 750 hPa ( $\text{mKs}^{-1}$ ), (c) the eddy momentum fluxes at 250 hPa ( $\text{m}^2\text{s}^{-2}$ ), and (d), the first EOF of the 10 day averaged sea level pressure (hPa). The pattern has been given units by regressing the first principal component time series on the surface pressure, and corresponds to anomaly of +1 standard deviation. Black contours mark levels of  $\sigma_{BI}$ .

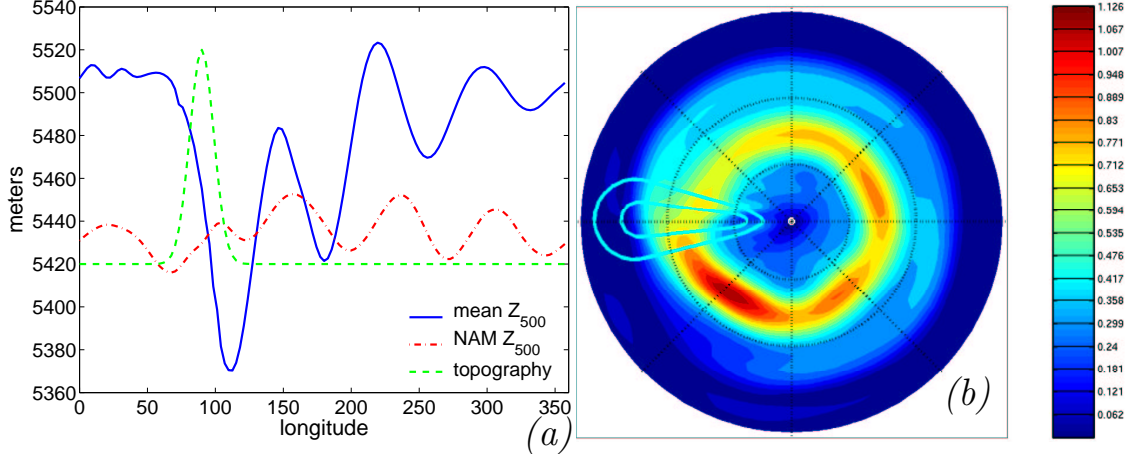


Figure 4.5: Mean properties of simulation RM. (a) The time average 500 hPa height field at 40° N and the profile of the model’s NAM at the same latitude. The NAM profile was normalized for ease of comparison next to the 500 hPa height field. (b) The Eady growth rate parameter,  $\sigma_{BI}$  ( $\text{day}^{-1}$ ).

Figure 4.4d provides a first measure of the intraseasonal variability in simulation LSC; the first EOF of surface pressure is an annular meridional dipole pattern with pronounced focus in storm track region. The peak variability is slightly downstream of the EKE maximum, closer to the region of maximum eddy momentum fluxes in the exit region of the jet than to the eddy heat fluxes in the entrance region. From comparison with Figure 4.2, we see that maximum variability occurs in the region where the baroclinicity is weakest. But before further probing the lower frequency variability of the model, we consider the effect of topography.

### 4.3.2 Topography Alone: Simulation RM

The addition of topography sets up a standing wave pattern similar to that predicted by the simple one layer QG model, as seen in Figure 4.5a. The wavetrain is a mix of wavenumbers 5 and 6, but mostly wavenumber 5. Simulations with varied mountain size and heights (such as a mountain characteristic in scale to the Tibetan plateau) exhibited similar wavetrains. As suggested by linear theory, all mountains will excite

the resonant mode of the model, which is largely a function of the jet speed and stratification, and not so dependent on the specifics of the topography. The slow decay of the wave in longitude is a cause for concern in the model. The dynamical core appears to lack an effective mechanism to damp the standing wave pattern generated by the topography. Changes to the surface friction and the thermal damping timescales have profound effects on the rest of the circulation, as discussed in Section 5.5, and do not provide a convenient way to tune away this problem.

There is localization of the baroclinicity despite the persistence of the wavetrain, as illustrated in Figure 4.5b. The standing wave generates several maxima in the baroclinicity, but the first is the most prominent. Note that the color scale is not the same as in Figure 4.2b. The baroclinicity is in general larger in this simulation than in LSC.

Figure 4.6a reveals that simulation RM does not exhibit a well defined storm track. The EKE is reduced in the neighborhood of the ridge, but is relatively constant over other longitudes, despite a variation of the baroclinicity by roughly a factor of 1/3. The high pass EKE, shown in the second panel, shows somewhat enhanced localization, indicative of the fact that baroclinic growth is strongest downstream of the ridge, but advection and downstream development extend the EKE all the way around the globe. Given the lack of localization of the synoptic variability, it is little surprise that the variability at lower frequencies is not very localized. The first EOF of the 10 day averaged sea level pressure picks up a low frequency wavetrain circling the globe. The wavenumber of the variability is a mix of wavenumbers 5 and 6, as was the stationary wavetrain shown in Figure 4.5a.

In simulation LSC, the high pass EKE (not shown) was less localized than the full EKE, taking the shape of the high pass eddy heat fluxes shown in Figure 4.4b. The regions of baroclinic growth are equally localized in both simulations, but the overall EKE is quite different. The difference in the overall shape of the baroclinicity, as

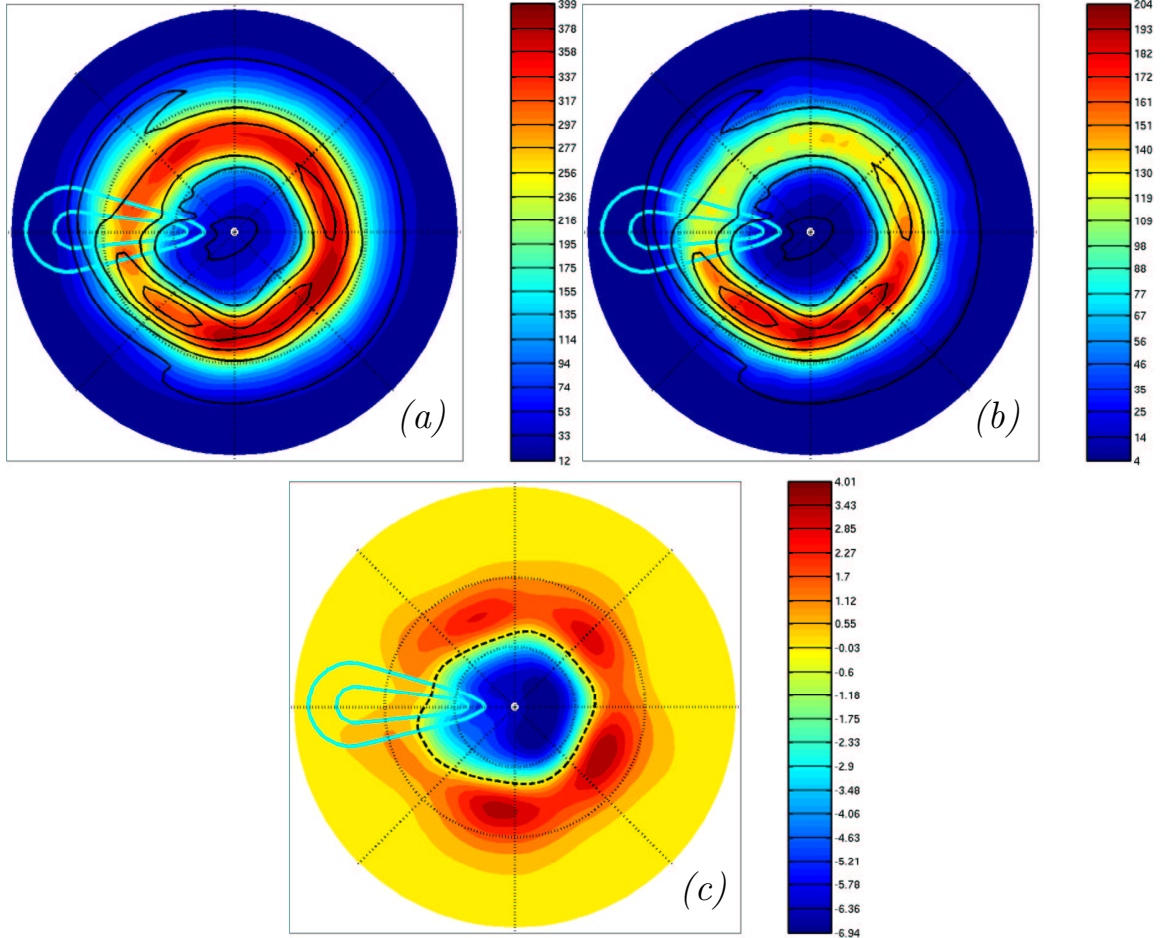


Figure 4.6: The variability of simulation RM. (a) The time average transient eddy kinetic energy at 250 hPa ( $\text{m}^2\text{s}^{-2}$ ), (b) the high pass eddy kinetic energy, also at 250 hPa ( $\text{m}^2\text{s}^{-2}$ ), and (c), the first EOF of the 10 day averaged sea level pressure, given units of hPa as in Figure 4.4d. Black contours mark levels of  $\sigma_{BI}$ .

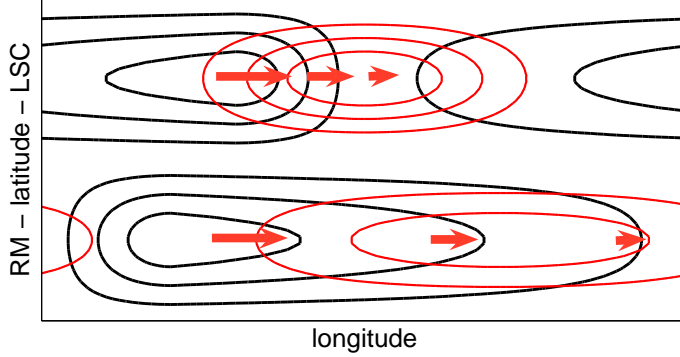


Figure 4.7: A cartoon illustrating the key differences in the structure of the baroclinicity and storm tracks of simulations LSC (upper half) and RM (lower half). Thick black contours denote the baroclinicity, thinner red contours the EKE, and thick red arrows the EKE fluxes, which are dominated by advection and downstream ageostrophic geopotential height fluxes. The EKE becomes localized when the convergence of eddy kinetic energy fluxes dominates the local tendency for eddies to grow baroclinically. In LSC, this occurs in the weak baroclinic region immediately downstream of the baroclinicity maximum. In RM, downstream EKE fluxes compensate for the changes in baroclinic growth, and the EKE is not well localized.

illustrated in the cartoon shown in Figure 4.7, highlights a key difference between the simulations. In RM, the baroclinicity is maximum just downstream of the mountain chain, and then slowly decays around the globe to a minimum value just upstream of the ridge. In LSC, the baroclinicity is minimum in the warming region, and then slowly builds to a peak in the cooling region. The minimum in baroclinicity in LSC is strong enough to prevent the downward extension of storm track, and the downstream ageostrophic eddy energy fluxes act to further enhance the localization of EKE, piling it up at the storm track. This “pile up” may explain why the EKE maximum is greater in LSC, despite the fact that baroclinicity is weaker overall. In RM, the downstream eddy energy fluxes make up for the slow decrease in the growth rates, and the EKE is not localized.

### 4.3.3 Confluence of Topographic and Thermal Forcing: the NAO

While topography alone fails to generate a storm track in this particular model, simulations LSC+RM1 and LSC+RM2 demonstrate that it plays an important role in shaping the intraseasonal variability. Figure 4.8a and b show the baroclinicity and EKE of simulation LSC+RM1. The baroclinicity maximum is as strong as in RM, but sharp and followed by a minimum as in LSC. This produces a well defined storm track, and, as seen in Figure 4.8c, a well localized first EOF of surface pressure.

The first EOF of LSC+RM1 bears a remarkable similarity to the NAO. The equatorial lobe of the mode is quite localized, much more so than in first EOF of LSC in Figure 4.4d. In addition, the polar lobe of the EOF has been displaced off the pole, forming a local dipole over the “ocean” sector of the model that is, the region of warming. This differentiates the pattern from the more annular patterns, where the poleward low is positioned over the pole. The wavetrain created by the ridge appears to be instrumental in displacing the poleward lobe off the pole.

The first EOF of sea level pressure of simulation LSC+RM2, shown in Figure 4.8d, highlights the importance of the phase relationship between the topography and the diabatic forcing. The only difference in this simulation is a 30° eastward shift of the topography, but the EOF pattern is substantially more global in scale, reflecting the wavenumber 5 pattern seen in the first EOF of simulation RM. Here the response of the variability to the two zonal perturbations is linearly additive, and can largely be decomposed into the individual responses to land-sea contrast and topography shown Figures 4.4d and 4.6c.

The same does not hold for LSC+RM1, where the response of the variability pattern is more nonlinear. Elements of the EOF patterns produced by the diabatic anomalies and topography still exist, but the variability is significantly more zonally localized than one would expect from the overlap of the individual patterns. This

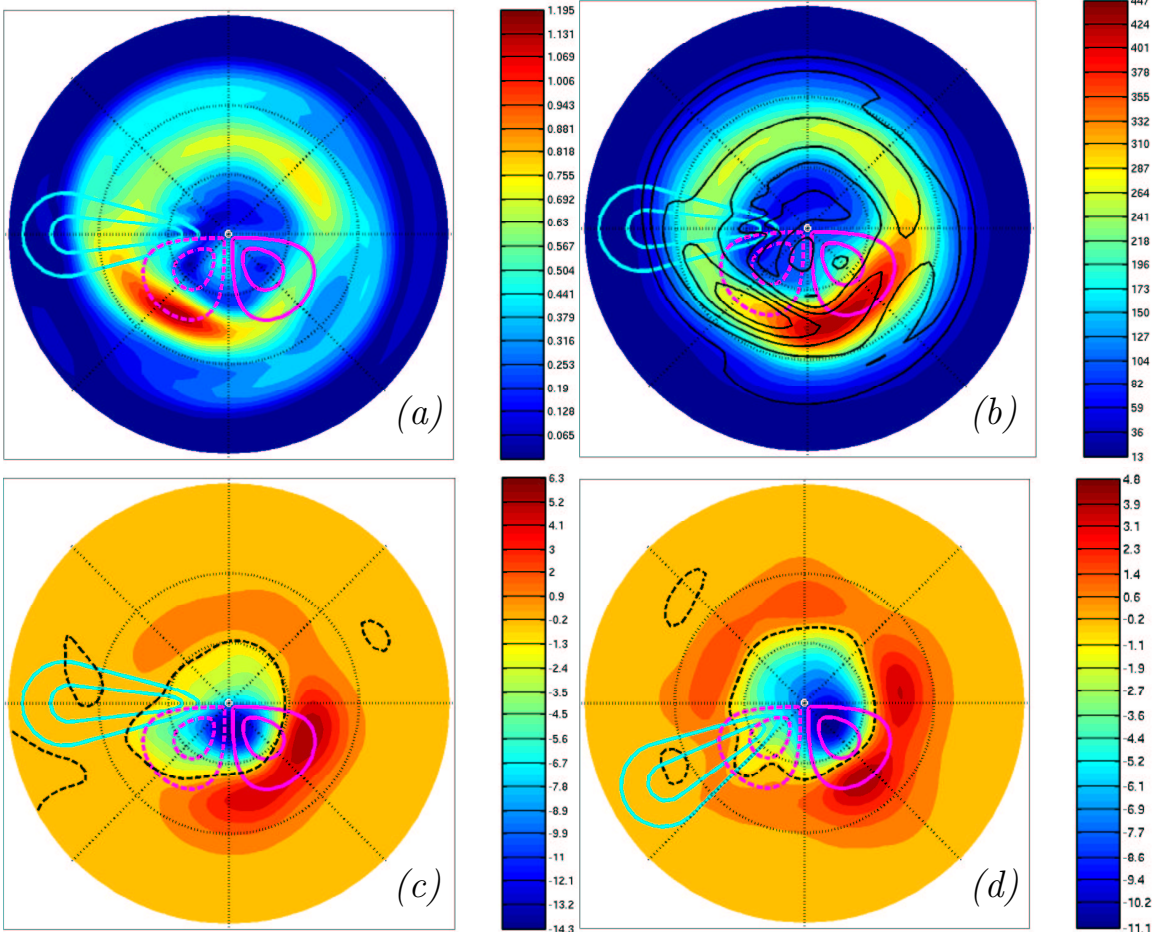


Figure 4.8: Topography and land-sea contrast. (a) the Eady growth rate parameter,  $\sigma_{BI}$  ( $\text{day}^{-1}$ ) for simulation LSC+RM1, (b) the time average eddy kinetic energy at 250 hPa ( $\text{m}^2\text{s}^{-2}$ ) for simulation LSC+RM, (c), the first EOF of the 10 day averaged sea level pressure for simulation LSC+RM1, and (d) the same EOF for simulation LSC+RM2. Both EOFs are given units of hPa as in Figure 4.4d. Black contours mark levels of  $\sigma_{BI}$  in (b).

suggests that a fortuitous overlap of orographic and diabatic forcing is important in producing localized modes of variability.

#### 4.3.4 A Comparison with Observations

For comparison, we show  $\sigma_{BI}$  computed for the Northern Hemisphere wintertime atmosphere by Hoskins and Valdes (1990) in Figure 4.9a. (While it is slightly lower in the atmosphere, 780 hPa, than the 500 hPa level shown in our Figures, we have found the baroclinicity in the dynamical core to be relatively independent of altitude through the lower and mid-troposphere.) The zonal asymmetry is more pronounced in observations. The growth rates fall by over two thirds between maxima and minimum in the midlatitude baroclinic region. In LSC and RM, the baroclinicity decreases by only about one third, while in LSC+RM1 it decreases by approximately one half.

Figure 4.9b and c show the observed eddy kinetic energy. The model does not reproduce the abrupt drop in both the baroclinicity parameter and eddy kinetic energy observed at the end of the North Atlantic storm track. The eddy kinetic energy in the jet core varies by a factor two in the model simulations. Given the simplicity of the dynamical core, there are likely several factors that lead to this disconnect with observations. Chang and Orlanski (1993), demonstrate that an increase of surface friction over land relative to ocean can play a large role in localizing the storm track. Also, the latent heat release associated with moist convection may play a role in localizing storm activity that cannot be captured with the simple diabatic anomalies in our model.

In the 250 hPa EKE fields illustrated in Figure 4.9, the North Atlantic and Pacific storm tracks appear merged as one. They appear more separated if one considers different measures, such as the vertically integrated EKE or the meridional heat fluxes.

A perhaps more substantial difference between the atmospheric circulation and

the model circulation is the course of the midlatitude jet. Due to the configuration of land mass and orography, the observed midlatitude westerlies spiral inward, beginning furthest southward over the Mediterranean, and slowly shifting poleward until the jet ends over the North Atlantic. Only in simulations LSC+RM1 and 2 do the winds break down reasonably abruptly, as they do over the North Atlantic. The spiraling nature of the midlatitude westerlies creates a well defined end to both the jet and storm track over Northern Europe. As demonstrated by the differences between simulations LSC and RM, a region of weak baroclinicity to stop eddy growth is an essential element in localizing the storm track, perhaps more important than a peak in the baroclinicity that initiates it. The pile up of eddy kinetic energy over the North Atlantic likely plays a role in the dominance of the NAO over a similar oscillation in the Pacific. But as suggested by LSC+RM1 and 2, the fortuitous overlap of the Rocky Mountains and the strong temperature gradients on the East Coast of North America is also important.

## 4.4 Intraseasonal Variability

In the previous section we have identified patterns of intraseasonal variability with the first EOF of sea level pressure. As observed in the atmosphere, the patterns of variability in the model are equivalent barotropic. Thus patterns identified at the surface are consistent with patterns higher in the troposphere, such as the first EOF of the 500 hPa height surface. By “consistent” we mean that the principal components time series associated with both fields highly correlated. Another way to say this is that spatial field obtained by regressing the principal component time series of the sea level pressure EOF on the 500 hPa surface is roughly the same as the spatial pattern of the first EOF of the 500 hPa surface; only one index in time is needed to characterize the variability of both fields.

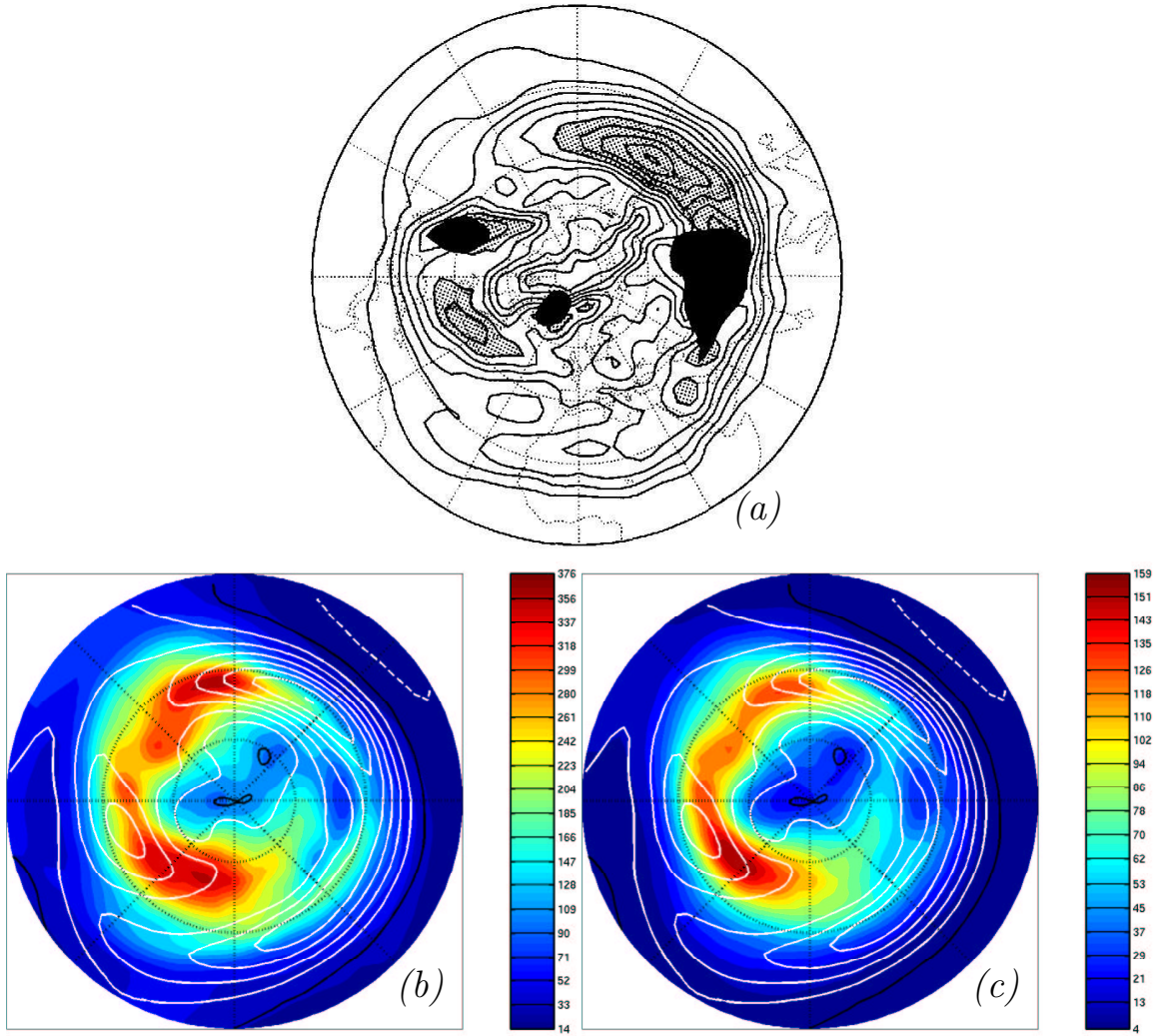


Figure 4.9: (a) The baroclinicity parameter  $\sigma_{BI}$  at about 780 hPa for the Northern Hemisphere winter mean, from (Hoskins and Valdes 1990). The contour interval is 0.1 day $^{-1}$ , with zero at the equator and values below 0.1 day $^{-1}$  at the pole. Regions where  $\sigma_{BI}$  exceeds 0.6 day $^{-1}$  are stippled, and regions within 1 km of the surface are blacked out, as they are likely in the boundary layer. (b) The DJF average eddy kinetic energy at 250 hPa computed from NCEP-NCAR reanalysis data ( $m^2/s^2$ ). The white contours denote the 250 hPa zonal winds, spaced at an interval of 5 m/s. The black contour is the zero wind line. (c) The same as in b, but the high pass energy, with frequencies of roughly  $10^{-1}$  to  $2^{-1}$ . The prime meridian is located at 6 o'clock in all panels.

	SLP	$Z_{500}$	$u_{surf}$	$\bar{u}$
SLP	1	0.91	0.92	0.72
$Z_{500}$	-	1	0.90	0.80
$u_{surf}$	-	-	1	0.81
$\bar{u}$	-	-	-	1

Table 4.2: Correlation of the principal component time series of EOFs computed from various fields in simulation LSC+RM1. The surface winds,  $u_{surf}$ , are the zonal winds on the .975  $\sigma$ -surface.

Furthermore, we have found a dynamic consistency between EOFs of zonal wind and pressure. For example, the first EOF of the surface zonal wind is the same as the pattern of zonal winds implied by geostrophy in the surface pressure EOF. Thus the time series associated with patterns identified from different variables are also highly correlated. Table 4.2 verifies these claims for simulation LSC+RM1. The correlations between the various principal component time series are higher in simulations with less zonal asymmetry. Given the consistency in the dynamical core, we focus our attention on understanding the sea level pressure field without any loss of generality. Ambaum et al. (2001) note that such dynamical consistency is found in regional EOFs characterizing the NAO, but not for the hemispheric EOFs that characterize the Northern Annular Mode.

#### 4.4.1 Spatial Structure

##### EOF Analysis - the Annular Modes

Empirical Orthogonal Function analysis identifies the single pattern that expresses the most variance in the system, and produces a set of modes orthogonal in time and space. As illustrated with the stochastic model in Chapter 3, the EOFs do not necessarily produce modes associated with underlying dynamics, and it can be problematic if one interprets them in the same respect as a teleconnection pattern. We have shown the first EOF associated with the 10 day averaged SLP in the three

	Northern Hemisphere			Southern Hemisphere		
	LSC	RM	LSC+RM	LSC	RM	LSC+RM
EOF 1	29	23	20	35	33	31
EOF 2	11	7.9	13	5.1	5.4	5.6
EOF 3	8.3	6.2	10	4.7	5.0	5.2
EOF 4	5.7	5.1	6.8	4.6	4.6	4.9
EOF 5	4.6	4.9	5.5	4.4	4.4	4.7

Table 4.3: The fraction of the variance of the 10 day averaged sea level pressure field represented by the top 5 EOFs.

simulations in Figures 4.4d, 4.6c, and 4.8c. We will refer to these patterns as the Northern Annular Modes (NAM) of the model. Similar, but zonally uniform modes were found in analysis of the southern hemisphere, the model’s SAM.

The variance expressed by the top five EOFs in both hemispheres is listed in Table 4.3. These EOFs are statistically robust according the “rule of thumb” proposed by North et al. (1982). They determined that the spatial (and temporal) structure of an EOF pattern is stable to sampling error when the separation between its eigenvalue and the nearest eigenvalue associated with neighboring EOFs,  $\Delta\lambda$ , is greater than the sampling error of the eigenvalue,

$$\delta\lambda \approx \lambda(2/N)^{-1/2}. \quad (4.4.1)$$

Given 9000 days of simulation times,  $\Delta\lambda$  is approximately  $0.05\lambda$ . In the NH, the top 4 or 5 EOFs are robust. In the SH there is less separation in higher EOFs. As illustrated in Chapter 3, symmetries can lead to degeneracy, and pairs or groups of EOFs that represent the same fraction of the variance. As will be shown below, the persistence of EOFs in the Southern Hemisphere is much greater. The enhanced persistence accounts for the fact that the SAM in each model represents a larger fraction of the variance than the NAM. In general, the fraction of the variance represented by an EOF is greater when the EOF is larger in scale and more persistent in time.

We have also considered in the effect of averaging the SLP in time on the EOF

patterns. As observed by Thompson and Wallace (2000), averaging does not affect the spatial structure of the annular mode. When the averaging is increased, the top EOF explains a larger fraction of the remaining variance. The top EOFs have more power at lower frequencies relative to higher order modes, and so become more pronounced as one focuses on lower frequencies. While the EOFs are computed from a 10-day averaged field, we calculate daily time series by projecting the EOF pattern on the daily output.

### **Teleconnection Analysis - the “NAO”**

We also characterize the variability with teleconnection pattern analysis, as described by Wallace and Gutzler (1981). Application of teleconnection analysis is more subjective than EOF analysis, but the patterns have the advantage of being more intuitive; points that appear in the same phase are correlated, and points of opposite phase are anticorrelated. Such is not necessarily the case for EOFs. Given the lack of a zonally localized storm track in simulation RM, we focus only on LSC and LSC+RM1.

We begin by computing the correlation of the sea level pressure at each point in our domain (here restricted to the Northern Hemisphere alone) with the sea level pressure at every other point. In Figure 4.10, we plot the most negative correlation associated with each point. That is, for each point we have computed a single point correlation plot, and identified the strongest negative correlation in the map. The difference between the two columns is in the pressure signal used for the computations; on the left the daily SLP was used, while on the right, the SLP was first smoothed with a 30 day low pass filter. The basic pattern is the same in both columns, but the degree of anticorrelation is stronger when higher frequencies are filtered out.

The patterns associated with LSC are easier to interpret. There are two bands of strong anticorrelation, centered at approximately 40 and 70 degrees latitude. Analysis below shows that points in the lower band are linked with points in the upper band; a

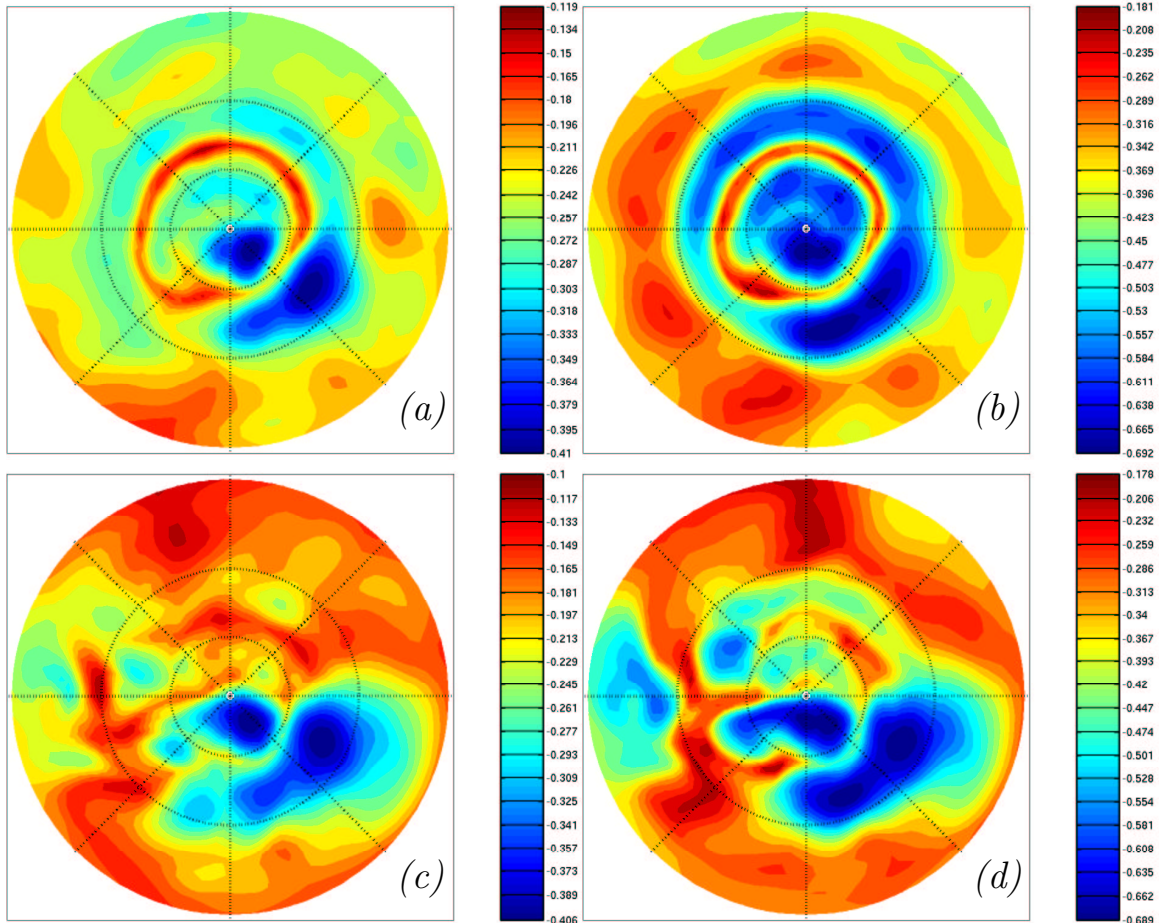


Figure 4.10: The minimum correlation associated with each point in the Northern Hemisphere. (a) and (c) are based on the daily SLP in simulations LSC and LSC+RM1, respectively. (b) and (d) are based on the 30 day low pass filtered SLP of the two respective simulations.

series of local dipole patterns. The amplitude of anticorrelation is approximately 20-30 percent stronger in the exit region of the storm track. The plots are more complicated when topography is added. There are still two bands of points anticorrelated with each other, but they are mixed with wavenumber 5 and 6 signals. The wave pattern is similar to that observed in the first EOF of simulation RM Figure 4.6c, and seen in the minimum correlation pattern for simulation RM (not shown). Around the topography there are more complex structures associated with zonal wavetrains; here one cannot easily line up points in the lower latitudes with points in the higher latitudes.

The NAO of Wallace and Gutzler (1981) was found by combining information from two “centers of action,” two points in the domain associated with the strongest anticorrelation. In Figure 4.11, we show the single point correlation maps associated with the two chief centers of action in simulation LSC+RM1, found near 40°N, 250°W and 75°N, 225°W, for both the daily and 30 day low pass filtered analysis. The patterns associated with the low pass filtered sea level pressure are in general more zonally elongated.

We determine the teleconnection pattern from the two centers of action as follows. The time series of the two point teleconnection pattern,  $T1_{2pt}(t)$  is determined from the time series of the sea level pressure at the two centers of action,  $(\lambda_1, \theta_1)$  and  $(\lambda_2, \theta_2)$ .

$$T1_{2pt}(t) = k \left( \frac{p_{sl}^*(\lambda_1, \theta_1, t)}{\text{std}[p_{sl}(\lambda_1, \theta_1, t)]} - \frac{p_{sl}^*(\lambda_2, \theta_2, t)}{\text{std}[p_{sl}(\lambda_2, \theta_2, t)]} \right), \quad (4.4.2)$$

where  $p_{sl}$  is the sea-level pressure,  $*$  denotes deviations from the time mean, ‘std’ refers the standard deviation, and  $k = 1/(2 - 2\text{cor}[p_{sl}(\lambda_1, \theta_1, t), p_{sl}(\lambda_2, \theta_2, t)])$  is a normalization constant to give the time series unit variance. We have normalized the time series of the centers of action by their standard deviation to keep the teleconnection pattern equally weighted. (This varies slightly from Wallace and Gutzler (1981), who did not balance the weights of the two time series.) The teleconnection pattern,  $P1_{2pt}(\lambda, \theta)$  is then determined by regressing  $T1_{2pt}(t)$  on the full sea level pressure

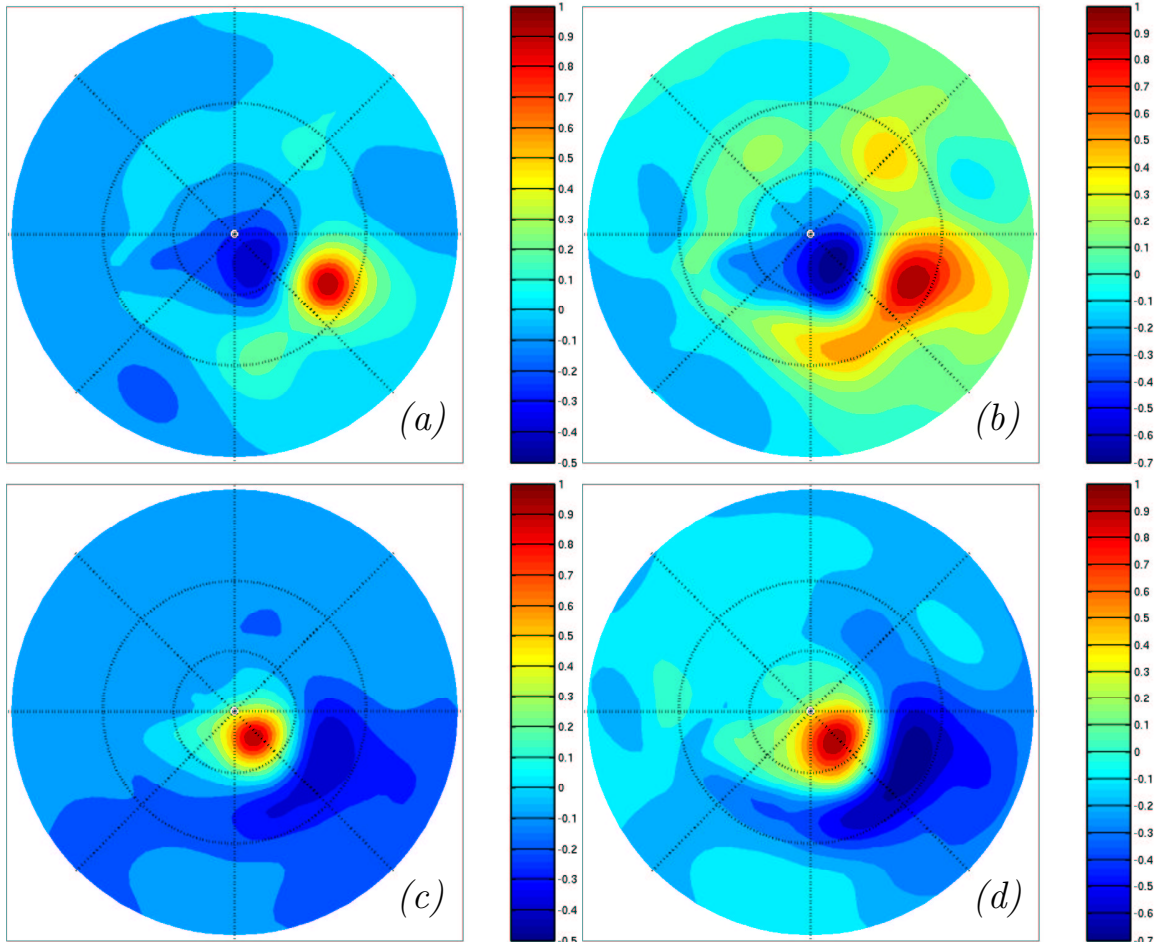


Figure 4.11: Single point correlation maps from simulation LSC+RM1. (a) and (b) are associated with the low latitude center of action, and (c) and (d) with the high latitude center of action. In the left column, daily data was used, in the right column, the 30 day low pass filtered pressure.

field,

$$P1_{2pt}(\lambda, \theta) = \frac{1}{n} \sum_{t=0}^{t=n} p_{sl}^*(\lambda, \theta, t) T1_{2pt}(t). \quad (4.4.3)$$

The patterns associated with the strongest anticorrelation in the daily data are shown in the left column of Figure 4.12. The patterns  $P30_{2pt}$  associated with the 30 day low pass filtered teleconnection pattern time series  $T30_{2pt}$  are shown on the right.

Despite the numerous normalizing coefficients in (4.4.2) and (4.4.3) to give the patterns meaningful units, teleconnection patterns are easy to interpret. The spatial pattern is exactly what one would obtain by differencing the single point correlation maps of the two centers of action. [This gives you an “average” single point correlation map, as the pattern from the first center of action is reverse that of the second.] Thus the pattern in Figure 4.12c is simply the difference of the single point correlation maps shown in Figure 4.11a and c.

With EOF analysis, there is a “reversible” relationship between the spatial pattern and its associated principal component time series. The EOF pattern is the regression of the generating data set on the principal component time series, and likewise, the principal component time series is the projection of the EOF pattern onto the generating data set as a function of time (modulo appropriate normalization constants). As our data is discrete, we express this mathematically by

$$\text{PC}(t) = k_1 p_{sl}^*(\lambda, \theta, t) \cdot \text{EOF}(\lambda, \theta) \quad (4.4.4)$$

$$\text{EOF}(\lambda, \theta) = \frac{k_2}{n} \sum_{t=0}^{t=n} p_{sl}^*(\lambda, \theta, t) \text{PC}(t) \quad (4.4.5)$$

where  $k_1$  and  $k_2$  are normalization constants. This property follows from the fact that EOFs are orthogonal in time and space.

The same property does not extend to teleconnection patterns, or other sets of patterns that are not constructed to be orthogonal both in time and space, such as Rotated EOFs. The time series associated with the two centers of action used to

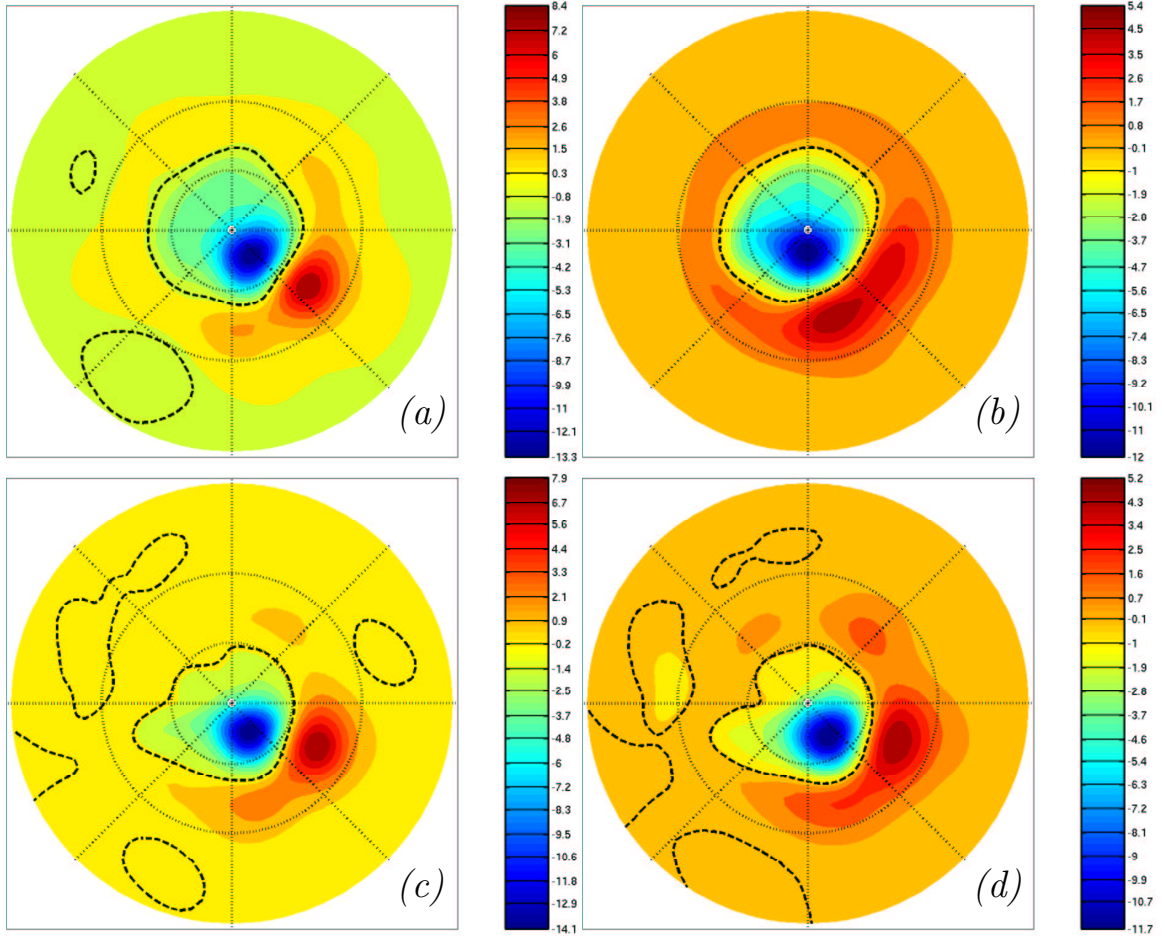


Figure 4.12: The “NAO” of the dynamical core. On the left, (a) and (c), the two point teleconnection pattern,  $P1_{2pt}(\lambda, \theta)$  of simulations LSC and LSC+RM1, respectively. On the right, (b) and (d), the same patterns based on the 30 day low pass filtered SLP,  $P30_{2pt}(\lambda, \theta)$ .

create the two point teleconnection pattern ( $T1_{2pt}(t)$ ) is not the same as the time series found by projecting the two point teleconnection pattern on the SLP. To differentiate the two point time series used to generate the teleconnection pattern from the time series found by projecting the pattern onto the SLP field, we call this new time series  $T1_{ld}(t)$ , “ld” for “local dipole,” as the teleconnection pattern looks similar to the SLP EOFs, but is more zonally localized.

$$T1_{ld}(t) = p_{sl}^*(\lambda, \theta, t) \cdot P1_{2pt}(\lambda, \theta). \quad (4.4.6)$$

The new time series  $T1_{ld}(t)$  is very similar to the time series  $T30_{2pt}(t)$ , the one used to generate the teleconnection patterns from the 30 day low pass filtered surface pressure. In projecting the pattern back on the data, we are effectively applying a spatial filter, which is equivalent to filtering in time as in both cases we remove the synoptic variability and focus on the larger scale circulation. For simulation LSC, the square of the correlation coefficient between the two time series is 0.70, and in LSC+RM1, 0.66.

The iterative process started above can be continued; a new spatial pattern can be found by regressing the new time series on the SLP, and then a new time series by projecting this pattern back on the SLP, etc.. In each step, weight is added to points correlated with the pattern of variability, extending the amount of variance it represents; iterations will converge when the pattern has maximized the fraction of variance that can be captured: the first EOF! This iterative approach to maximizing the variance is the procedure Walker and Bliss (1932) used to first identify the North Atlantic Oscillation with their hand calculations. As suggested by Wallace (2000), had they had a more complete data set, they would likely have found the annular mode.

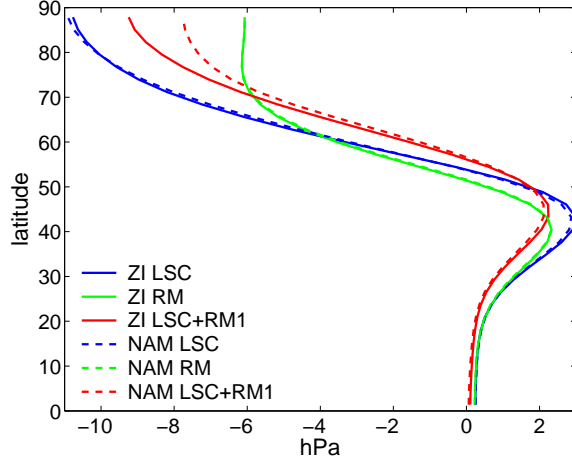


Figure 4.13: The first EOF of the zonally averaged sea level pressure (denoted by ZI, for the zonal index), compared to the zonal average of the first EOF of the full two-dimensional surface pressure (NAM), for simulations LSC, RM, and LSC+RM1.

### The Zonal Index

Lastly, we consider the most historic measure of low frequency variability, the zonal index (ZI), which tracks the variation of the zonally averaged flow. Here we define the ZI as the principal component associated with the first EOF of the zonally averaged sea level pressure, which are shown in Figure 4.13. The proper cosine of latitude weighting is particularly important for zonally averaged EOFs of the surface pressure. The patterns are remarkably similar to those predicted from the conservation of mass in Section 3.5 in the stochastic model.

#### 4.4.2 Temporal Structure

How unique are the different measures of low frequency variability? We compute the correlation between the time series associated with the different modes of variability. In the Southern Hemisphere, the principal component of the SAM and zonal index are almost identical, with the square of correlation coefficient,  $R^2$ , always greater than 0.999. This implies that one gains no additional information by computing the

	LSC				LSC+RM1			
	ZI	NAMI	$T1_{ld}(t)$	$T1_{2pt}(t)$	ZI	NAMI	$T1_{ld}(t)$	$T1_{2pt}(t)$
ZI	1	0.97	0.91	0.44	1	0.81	0.76	0.43
NAMI	-	1	0.87	0.40	-	1	0.86	0.53
$T1_{ld}(t)$	-	-	1	0.66	-	-	1	0.77
$T1_{2pt}(t)$	-	-	-	1	-	-	-	1

Table 4.4: The square of correlation coefficient,  $R^2$ , between the time series associated with the various patterns of low frequency variability.

first EOF of surface pressure from the full two dimensional field. However, we find that the zonal index and annular mode in the Northern Hemisphere also are highly correlated - despite the significant zonal asymmetries in the flow.

The correlation  $R^2$  between the time series associated with the zonal index, NAM, and measures of the local variability,  $T_{2pt}$  and  $T_{ld}$  are shown in Table 4.4. The high correlation between ZI and the NAM index (NAMI), should not be surprising, despite the fact that the variability is quite zonally localized. The zonal average signal is determined primarily by variability in the storm track region where the NAM is focused. Hence, there is not a loss of information when the sea level pressure is zonally averaged. The pattern obtained by regressing the ZI on the two dimensional pressure field is nearly identical to the NAM in all simulations. The correlations are notably weaker with the two point “NAO” time series,  $T_{ld}$ . This two point index contains both the signal of the large scale intraseasonal variability and the signal of synoptic variability in the storm track region, that is, the projection of individual eddies crossing over the two points.

## Persistence

The autocorrelation function of the first principal component time series measures the persistence of the models “annular mode.” In Figure 4.14, we show the autocorrelation functions of the model’s NAM and SAM. We find a significant drop in the persistence of the pattern in the hemispheres with zonally asymmetric forcing. While

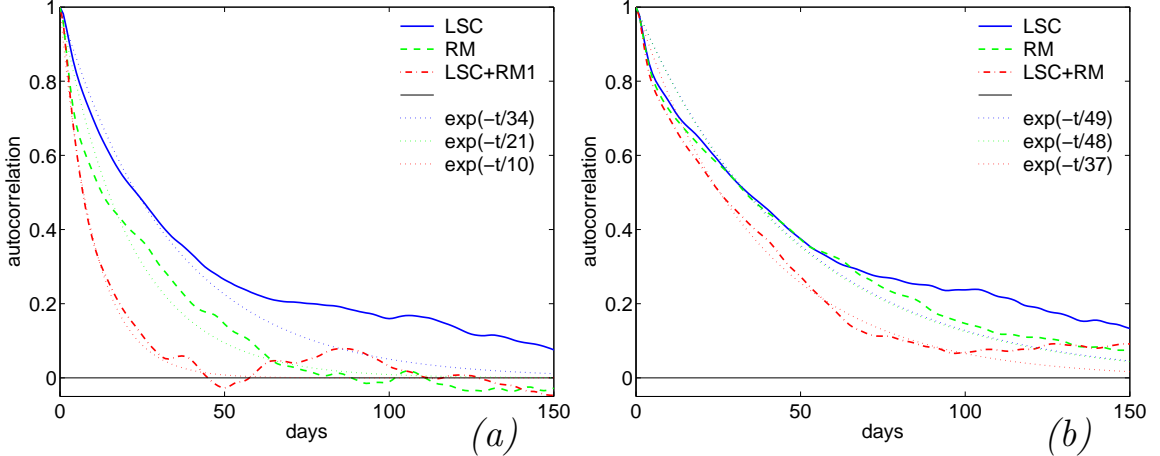


Figure 4.14: Autocorrelation functions of the principal component time series associated with the first EOF, for the (a) Northern and (b) Southern Hemispheres.

the Southern Annular Mode appears to be equally persistent in all simulations, the annular mode in the Northern Hemisphere grows and decays on a timescale roughly 2/3 as short in LSC, 1/2 as short in RM, and only 1/4 the time in LSC+RM.

The dotted lines show the best fit exponential curves to the autocorrelation function. (We fit only until the autocorrelation drops below 0.3, as the pattern becomes less exponential with time.) The decay pattern is not perfectly fit by an exponential curve, with faster decay at initial times and slower decay at longer lags, thus exhibiting a “broad shoulder.” But as the decay appears to be self similar, the best fit e-folding timescale provides a reasonable relative measure of the persistence. In Table 4.5 we list the e-folding growth/decay times of the annular modes, zonal indices, and teleconnection time series of the Northern Hemisphere.

In general, the autocorrelation function exhibits the non-exponential decay features noted in Figure 4.14: faster growth/decay at early times (relative to the best fit exponential) with slower growth/decay at long lags. It is particularly the case for  $T1_{2pt}$  (not shown). Here the autocorrelation drops off quickly at first, but then hits a very broad shoulder. As suggested above, the two-point time series is determined

	Northern Hemisphere			Southern Hemisphere		
	LSC	RM	LSC+RM1	LSC	RM	LSC+RM1
ZI	33	20	9.4	49	48	37
AM	34	21	10.3	49	48	37
$T1_{ld}(t)$	31	-	9.8	-	-	-
$T1_{2pt}(t)$	8.7	-	6.0	-	-	-

Table 4.5: The e-folding time scale  $\tau$  determined from a best fit of the autocorrelation function to an exponential  $e^{-t/\tau}$ . ZI refers to the zonal index, AM to the annular mode,  $T1_{ld}$  to the time series found by projecting the two-point teleconnection pattern on the pressure field, and  $T1_{2pt}$ , the two-point teleconnection pattern time series.

by synoptic eddies on shorter timescales, and the large scale variability on longer timescales, which produces the long shoulder. I suspect that the non-exponential decay in all the autocorrelation functions is due in part to the mixture of the signals of synoptic variability and of the large scale movement of the jet. In Section 5.9 we show that the annular mode is made up of a slowly evolving, zonally uniform signal and short lived projections of individual eddies onto the dipole pattern.

Given the high correlation between the zonal index, NAM index, and the time series derived from the “local dipole” pattern,  $T1_{ld}$ , it is not surprising that their persistence is about the same. That all techniques measures indicate the dramatic drop in persistence with increasing zonal asymmetry suggests that this feature is robust, and not an artifact of any analysis technique. In general, extended persistence is a problem with models with a Held and Suarez (1994) forcing. With the addition of both topography and a zonally asymmetric diabatic forcing, the persistence becomes more consistent with observations. Feldstein (2000b) found the NAO to decay with a 9.5 day e-folding time scale.

That the two-point teleconnection pattern time series  $T1_{2pt}$  decays on a faster time scale than the other measures should not come as a surprise. There is no spatial or temporal filtering to remove the synoptic variability from this index. The fact that the persistence of  $T2pt$  does not vary as significantly between the different simulations as the persistence of the low frequency variability suggest that the difference between

the models is not as much in the synoptic variability, but in the interaction between higher frequency variability and the low frequencies.

We explore the timescale of variability in the dynamical core in the next chapter. The dramatic changes in the variability with the addition of zonal asymmetries are investigated in Section 5.6.

## 4.5 Local and Global Patterns of Variability: NAO or Annular mode?

The teleconnection patterns  $P1_{2pt}$  are NAO-like patterns of variability, zonally localized meridional dipoles of pressure found in the exit region of the storm track. A comparison of their dynamics with the dynamics of the model’s annular mode may shed light on the relationship between global and local patterns of variability in the atmosphere. Comparison is in part problematic due to lack of consistency between the time series used to generate the teleconnection pattern,  $T1_{2pt}$ , and the time series one obtains by projecting the pattern on the sea level pressure data,  $T1_{ld}$ . As seen in Table 4.4, the latter series is extremely well correlated with the model’s NAM index.

With the barotropic and stochastic models we have argued that the annular mode is the aggregation of “local” meridional dipoles. Fluctuations of the jet are driven by eddy momentum fluxes in the upper troposphere, and as the momentum fluxes only redistribute momentum in the atmosphere, they conserve momentum. The dipole pattern is the gravest mode that satisfies this constraint. Thus, the null explanation for the “NAO” is simply that the momentum fluxes are largest in the exit region of the storm tracks, as seen in Figure 4.4c, and hence one would expect the meridional dipole to be the strongest there. Is there anything else that makes the variability in this region dynamically different from others?

To address this question, we analyze the variability of local teleconnections as a

function of longitude. As the latitude circle is quite small relative to the correlation scale of the surface pressure at the high latitudes, we focus on the lower center of action for our survey. We select 32 evenly spaced longitudes,  $\lambda_{i,1}$ ,  $i = 1, 2, \dots, 32$ , around the globe, beginning at the longitude of the strongest teleconnection pattern,  $T1_{2pt}$ . At each longitude we identify a low latitude center of action,  $(\lambda_{i,1}, \theta_{i,1})$ , choosing the point that exhibits the strongest anticorrelation with some other point in the domain. The point that shares this strongest anticorrelation,  $(\lambda_{i,2}, \theta_{i,2})$ , becomes the second center of action. Note that we do not constrain the second center of action to be fixed at longitude  $\lambda_{i,1}$ , as the strongest anticorrelation is often not found along a single line of longitude. Given the two centers of action, we define the two-point teleconnection time series  $T1_{i,2pt}(t)$  as in (4.4.2), the pattern  $P1_{i,2pt}(\lambda, \theta)$  as in (4.4.3), and the “local dipole” time series associated with the projection of this pattern,  $T1_{i,ld}(t)$ , as in (4.4.6). Our intent is to analyze the local variability at all longitudes, but to leave the procedure as unconstrained as possible otherwise.

In Figure 4.15 we show the 32 centers of action found in the simulations, connecting the linked centers with line segments. There is a slight spiraling of patterns, visible in simulation LSC in particular, with a break in the entrance region to the storm track. For simulation LSC+RM1, the teleconnections are grouped into clusters associated with the wave train generated by the topography.

Outside of the storm track region, the dominant teleconnection pattern at each longitude is a meridional dipole pattern like the NAO. Three of the teleconnection patterns from simulation LSC and LSC+RM1 are shown in Figure 4.16. The patterns shown in the first two columns are  $120\text{-}180^\circ$  apart, but have nearly identical structure. The scale over which points tend to become decorrelated in the model, roughly 1500 km, does not vary significantly over longitude, and sets the zonal extent of the teleconnection patterns. This scale is likely set by the length scale of baroclinic eddies.

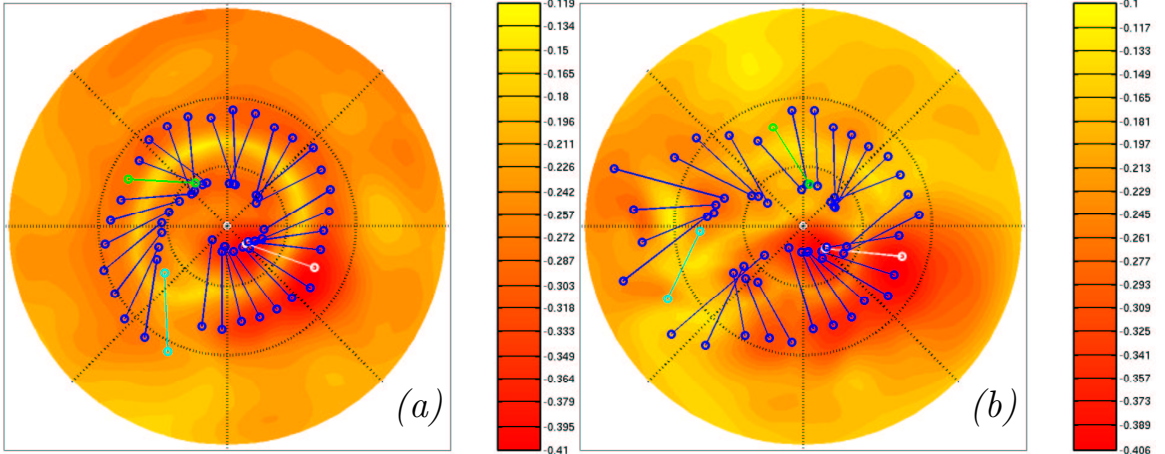


Figure 4.15: The centers of action of the 32 teleconnection patterns connected by line segments, overlying the minimum correlation maps. (The minimum correlation maps are also shown in Figure 4.10a and c.) (a) simulation LSC and (b) simulation LSC+RM1. The strongest teleconnection pattern, the models “NAO” is shown in white. The green and cyan line segments denote the other teleconnection patterns shown in Figure 4.16

It is only in the storm track, near the topography or the strong baroclinic region created by the cooling anomaly, that meridional dipole patterns cease to dominate. Stronger negative correlation is found in zonal wavetrains oriented with the jet. Meridional dipole patters are still found, as shown in Figure 4.16c and f, but they are shifted equatorward and slanted.

In Figure 4.17 we compare the significance of teleconnection patterns as a function of longitude. On the right we plot a measure of the strength of the two point teleconnection pattern: the magnitude of the covariance between the two centers of action,

$$-\text{cov}[p_{sl}(\lambda_{i,1}, \theta_{i,1}, t), p_{sl}(\lambda_{i,2}, \theta_{i,2}, t)]. \quad (4.5.1)$$

We choose this as opposed to the variance of the two points to focus on the correlation between the two points in addition to their individual variability. On the left, we plot the relative variance of the time series  $T_{1,ld}$ . Both plots tell the same story; the local

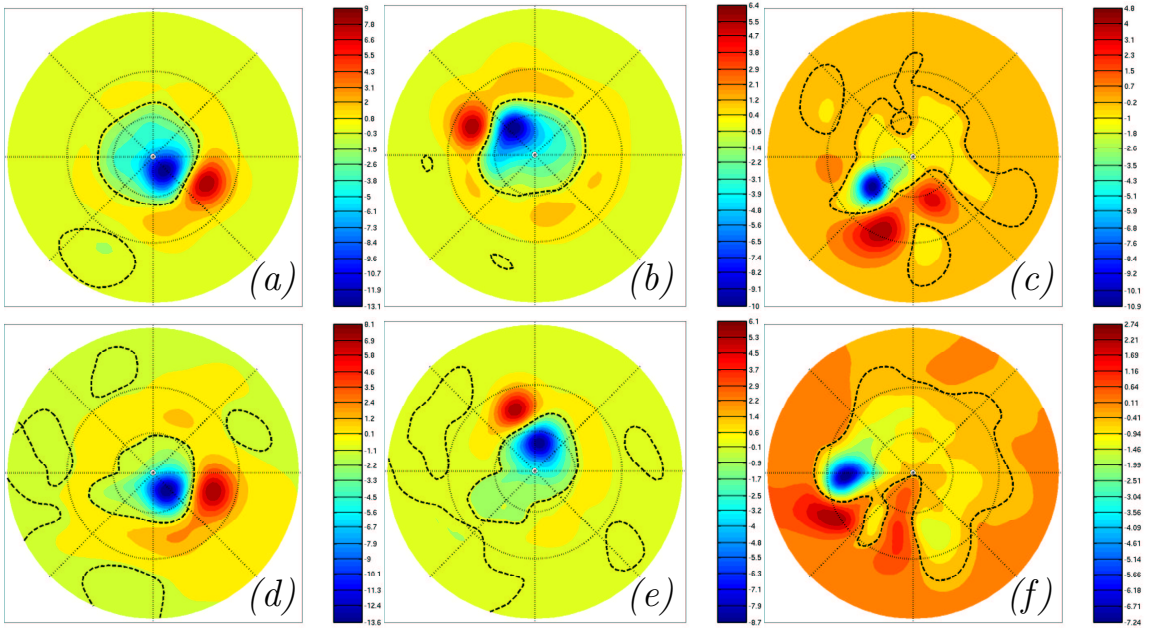


Figure 4.16: Sample teleconnection patterns at different longitudes. In the left column, (a) and (d): the primary teleconnection patterns  $P_{1,2pt}$  of simulations LSC and LSC+RM1. (These are the same patterns shown in the left column of Figure 4.12, and have the strongest anticorrelation.) In the center column, (b) and (e), we show patterns where the lower center of action is rotated 120-180° from the center of action in the left column, again for simulations LSC and LSC+RM1. Lastly, in the right column, (c) and (f), we show examples of the weaker teleconnections pattern found in the entrance to the storm track.

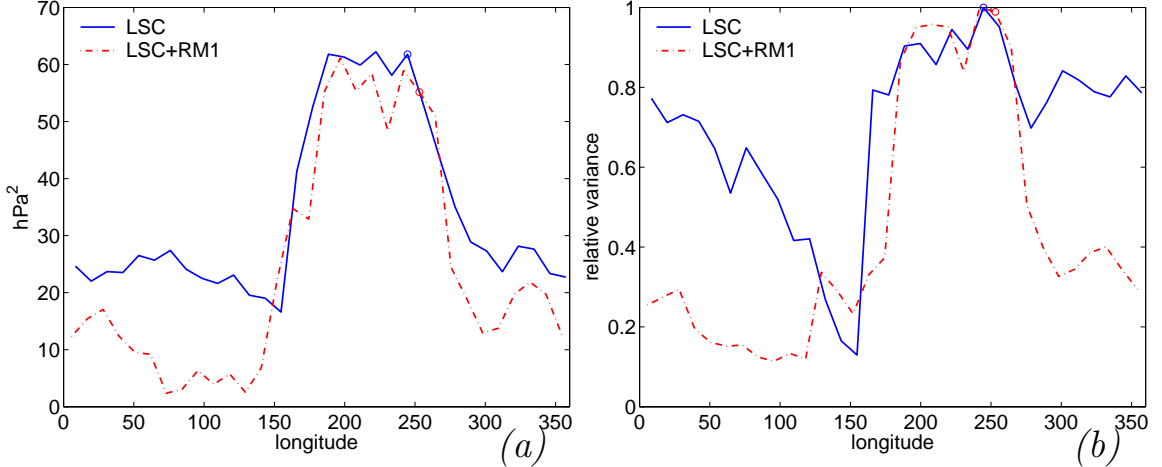


Figure 4.17: The strength of the local teleconnection patterns,  $T1_{i,2pt}$  in (a), and  $T1_{i,ld}$  in (b) as a function of longitude (that is, for all  $i$ ). The circles marks the position of the strongest teleconnection pattern analyzed in Section 4.4.1. In (a) we show the covariance between the two centers of action. In (b), we compare the relative variance of the projection of the two point patterns onto the full SLP field.

dipole patterns are strong in the exit region of the storm track, and relatively weak at most other longitudes, reaching minimum values at the entrance to the storm track, where the flow is most baroclinic.

In the upper panels of Figure 4.18 we plot the persistence of the dipole teleconnection as a function of longitude. The patterns derived by projecting the full two point dipole pattern on to the sea level pressure signal (on the left) are more persistent, as we observed earlier, but overall both pictures show the same trend. The persistence is weak in the baroclinic storm track region, where the teleconnection patterns become more zonal, but otherwise, it is about the same at all longitudes. *The meridional dipole pattern appears to be roughly equally persistent at all longitudes, independent of the variance of the pattern.*

We do not mean to gloss over the huge difference in the timescales of the local dipole projection time series seen in panel (b). The large scale flow is much more persistent in LSC than in LSC+RM1. This topic will be addressed further in Chapter

5. For now we note that the persistence of the 2 point time series does not vary nearly as much as for the local dipole projection, suggesting that the change is the large scale circulation, not in the synoptic variability.

In the lower panel of Figure 4.18, we show the correlation of the localized teleconnection patterns with the annular mode. In general, the persistence of the pattern is directly related with the correlation to the NAM; the stronger the persistence, the higher the degree of correlation. In LSC+RM1, the NAM is substantially more focused in the exit region of the storm track. As the NAM time series is well correlated with the zonal index, we conclude that hemispheric correlation appears is weaker in the model.

Based on these results, we make the following observations

- The local correlation structure is relatively similar at all longitudes outside the baroclinic entrance to the storm track. The persistence of the local variability appears to be independent of the intensity. This suggest that the dynamics giving rise to the NAO – the strong momentum fluxes in the exit region of the storm track – do not impart additional variability at low frequencies to the flow here than at other longitudes. Rather the variability is just larger here at all frequencies. *The same dynamics occur at all longitudes.*
- The disconnect between the scale of the variability suggested by teleconnection analysis and EOF analysis is probably best explained by the results in Chapter 3. There is a global signal, found when we filter out high frequencies in space, or small scales in time, but the significance of this is overestimated by EOF analysis and the zonal index, which also reflect the uniformity of the statistics of the flow.

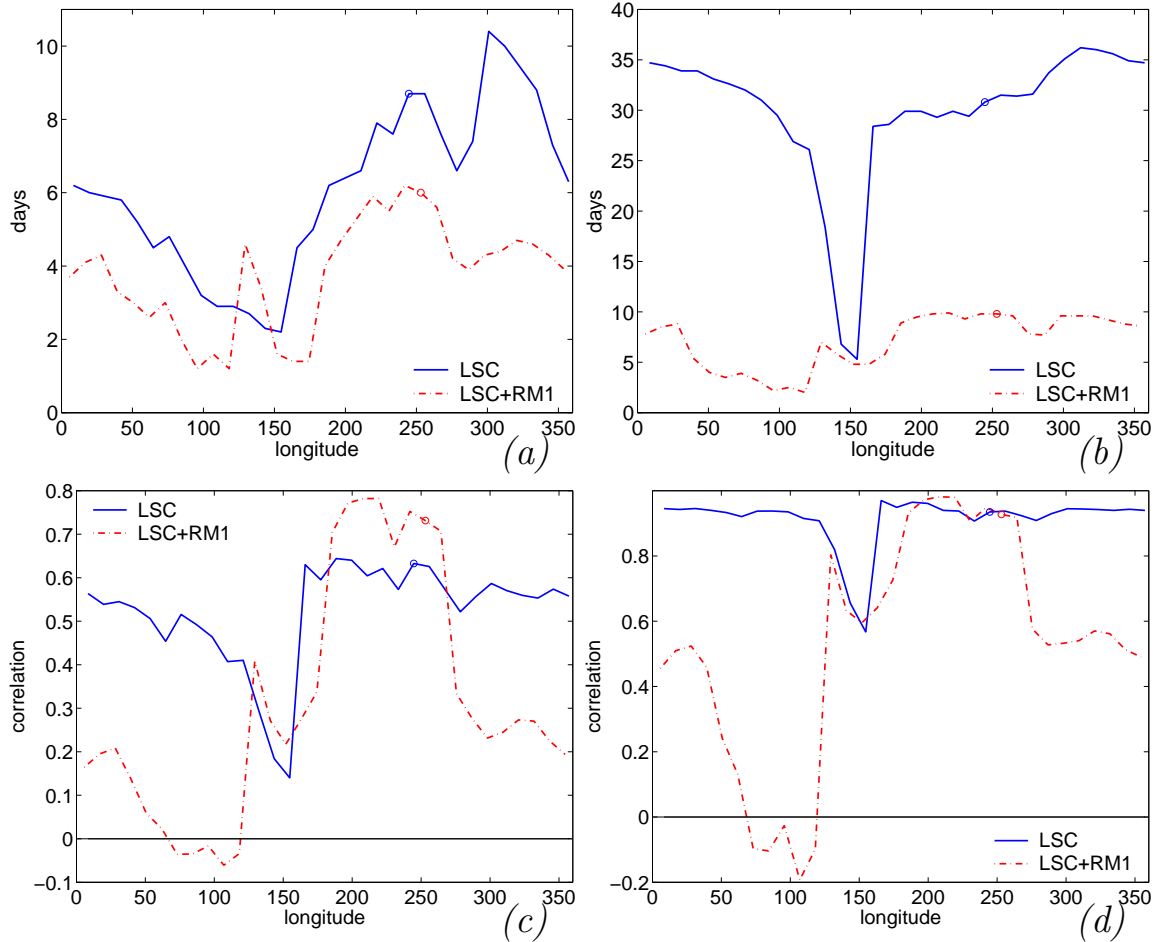


Figure 4.18: Properties of the teleconnection patterns as a function of longitude. On top, the persistence of the pattern: the best fit e-folding time scale of the autocorrelation functions of (a)  $T_{1,2pt}$  and (b)  $T_{1,ld}$ . On the bottom, the correlation of the two respective time series with the NAM. As in Figure 4.17, the circles marks the position of the strongest teleconnection patterns analyzed in the previous selection.

## 4.6 A More Physical Interpretation

Ambaum et al. (2001) note that the physical interpretation of the positive and negative annular mode is quite different in the Pacific and Atlantic regions. In the Pacific region, the jet stream cannot be easily differentiated into a extratropical (i.e. eddy driven) jet and a subtropical, thermally maintained jet. A positive (negative) phase of the annular mode corresponds to a weakening (strengthening) of the one jet. In the Atlantic, the system can more readily be viewed as the interaction of two jets, one subtropical and one extratropical. When the NAM is positive, there are two jets, while in the negative phase, there is only one.

This suggest that in the Atlantic, then, the NAM/NAO can be interpreted as transition between one and two jet states. With this in mind, we consider a new diagnostic of the zonal flow in simulation LSC+RM1, which has the most NAO-like mode of variability. We consider the zonal flow averaged over separate quadrants of the hemisphere,

$$\bar{u}_i(t, p, \theta) = \frac{2}{\pi} \int_{(i-1)\pi/2}^{i\pi/2} u d\lambda \quad (4.6.1)$$

for  $i$  from 1 to 4. The partition is centered so that the peak baroclinic region is fully captured by the second quadrant,  $\bar{u}_2$ , and the NAM projects most heavily onto the third quadrant,  $\bar{u}_3$ . We filter the  $\bar{u}_i$  with a digital filter with a 10 day low pass cutoff, to smooth the signal.

At each time step, we then classify the number of maxima in  $\bar{u}_i(\theta)$  between 10 and  $60^\circ$  along the .225  $\sigma$ -surface. The  $60^\circ$  upper bound was determined empirically. We found that there are occasionally maxima in the winds poleward of this latitude, but these maxima were always small, and not well associated with the subtropical or extratropical jets. (It is likely that many were associated with individual eddies, as the quadrant average becomes very short at high latitudes.) The number of instances that the zonal winds were best classified by  $n$  jets, are shown in Figure 4.19a. At first

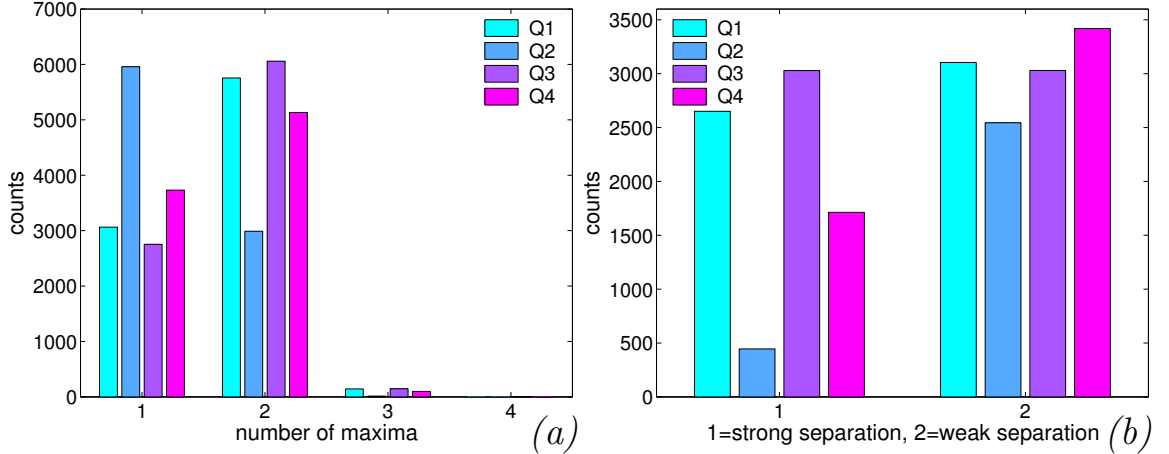


Figure 4.19: (a) The quadrant average zonal winds,  $\bar{u}_i$ , grouped by the number of distinct maxima between  $10^\circ$  and  $60^\circ$  on the  $0.225\sigma$ -surface, from simulation LSC+RM1. After filtering, there were 8962 time steps available for classification. In the second quadrant, Q2, where the flow is most baroclinic, it is twice as likely to find one distinct jet than two separate maxima. In the other quadrants, we find the reverse; it is almost twice as likely to find two jets than one. (b) Instances when the zonal winds have two distinct maxima, divided into cases where the two maxima are well separated and weakly separated, as discussed in the text.

glance, the second quadrant appears distinct from the others. Here, in the baroclinic region, it is much more likely to find one distinct jet maximum than to find multiple maxima. The likelihood of finding two jets is greatest in the third quadrant, where the NAM projects heavily, but it does not appear to be demonstratively different from the fourth and first quadrants following it.

If we raise the criterion for two “distinct” jets, we find the third quadrant to be more unique. We say that the two jets are well separated if there exist a minimum between them that falls more than  $m = 5.15$  below both either of the maxima. (For example, if the jet maxima and minimum were 20, 12, 32, we would say the two jets are well separated, but if the maxima and minima were 20, 18, 32, we would define them to be more weakly separated, as the first maximum is more of a shoulder.) We determined  $m = 5.15$  empirically to evenly divide the cases for the third quadrant. Figure 4.19b shows the separation for all instances of two jets in the four quadrants.

The jet is more likely to be well separated in the third quadrant than the first or fourth, albeit the statistics for the first quadrant are not so different.

We have now classified (almost all) instances of the jet in the third quadrant into one of three bins: one jet, two weakly separated jets, or two well separated jets, with each bin holding approximately one third of the cases. (1.6% of the time the jet has three maxima, but this occurs sufficiently rarely to be excluded from the present analysis.) We now form averages of the jet from these three bins, comparing them to averages of the jet based on the annular mode index. In forming composites from the annular mode index, we divide the 8962 events into three groups, negative states, where the index is below  $-c$ , neutral states, when it is between  $-c$  and  $c$ , and positive states, when it is above  $c$ . The value of the cutoff,  $c = 0.427$  was chosen as to evenly partition the time series. We note that the annular mode index is skewed negative, so that there are slight fewer events in the positive bin.

As illustrated in Figure 4.20, the partition based on the state of the jet (one jet vs, a split jet), provides largely the same picture as the partition based on the annular mode index. This suggest a more physical characterization of the NAM in simulation LSC+RM1. In a high index state, the eddy driven jet is well separated from the subtropical jet, generating two well defined peaks in the relative vorticity. In the low index state, the two jets have merged, leaving only one maximum in the vorticity. This allows one to view transition from a negative to positive NAO as an interaction between two vortices. Their separation and merger is, in essence, the NAO.

Similar interactions occur in the first quadrant, and to a lesser extent, the fourth quadrant. (I suspect that lingering elements of the wavetrain induced by the topography limit separation in the fourth quadrant.) In the second quadrant, however, the subtropical jet is considerably stronger, and there is generally only one jet in this region. A figure similar to Figure 4.20 cannot be constructed for the other quadrants largely because the NAM index only applies to the exit region of the storm track,

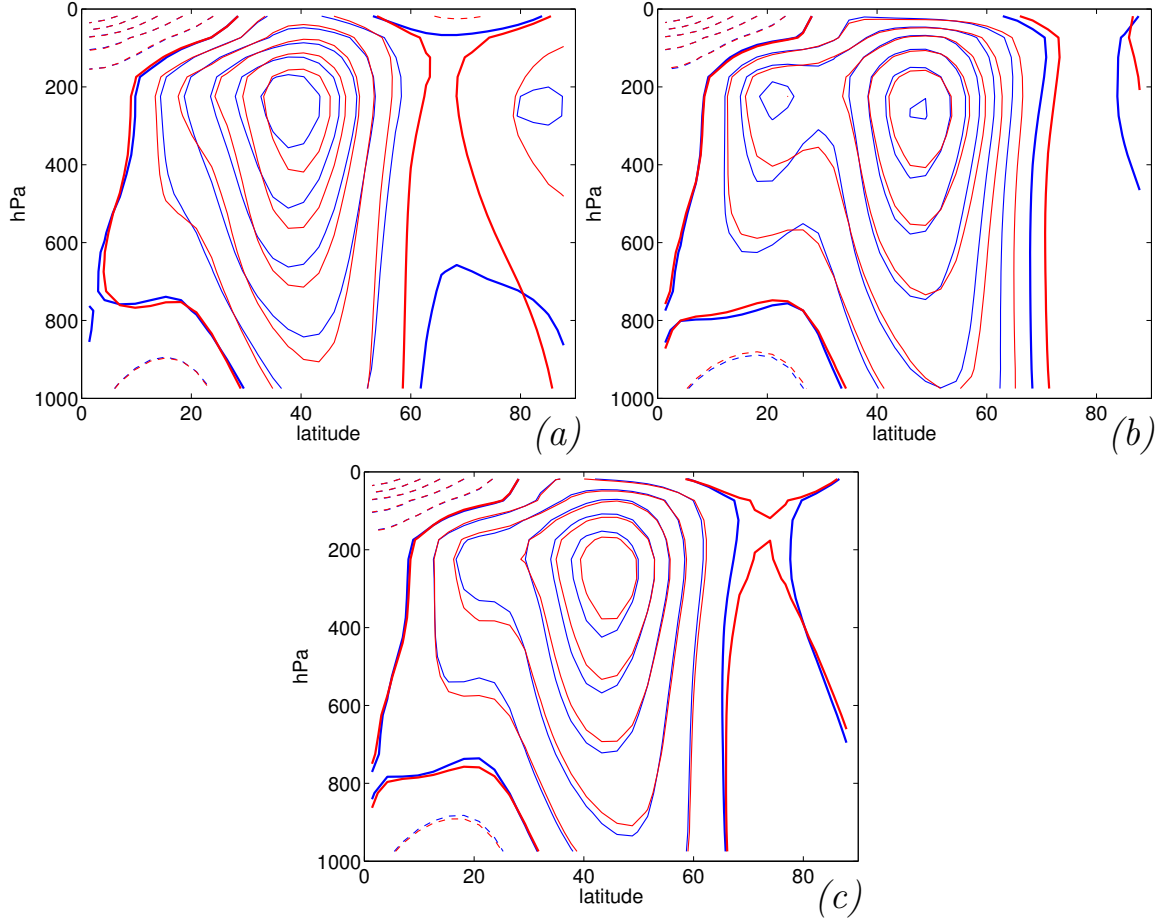


Figure 4.20: Third quadrant average zonal winds based on state of the jet (blue contours) and the annular mode index (red contours), from simulation LSC+RM1. (a) Average over times when there is one jet, and when the annular mode index is below -0.427. (b) Average over times with two well separated jets and when the annular mode index is greater than 0.427. (c) Average over times when there are two jets, but weak separation between them, and when the annular mode index is between -0.427 and 0.427. The contour interval is 5 m/s, negative contours are dashed, and the zero contour is bold. The criterion “0.427” was chosen to divide the annular mode index states into three bins of near equal size.

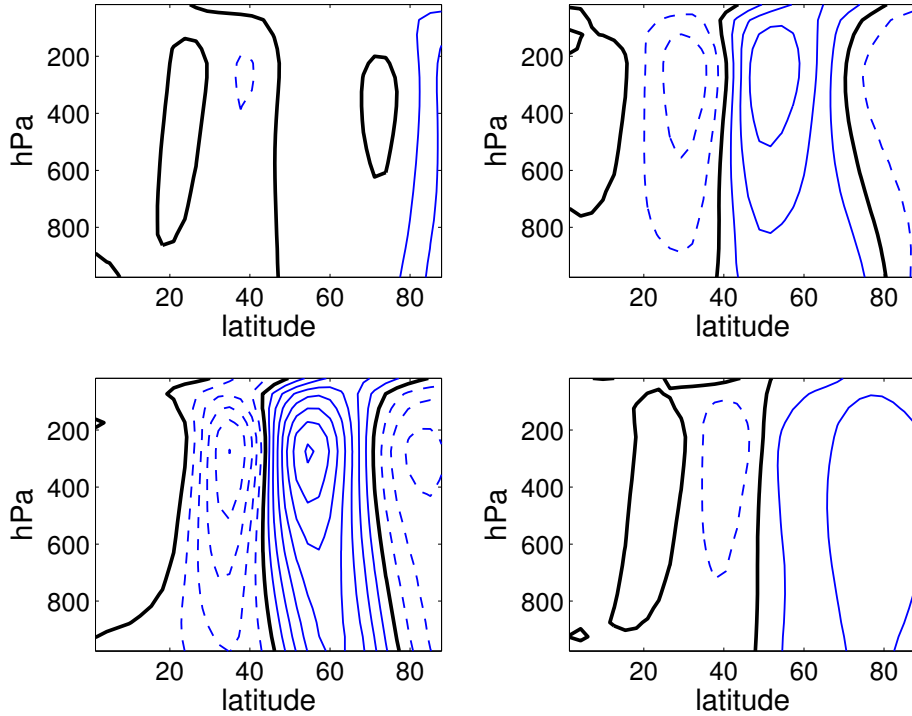


Figure 4.21: Regression of the annular mode index on the quadrant averaged flows  $\bar{u}_i$  for the (top) first and second quadrants and (bottom) third and fourth quadrants. A positive one standard deviation event is shown, with contour interval 1 m/s, negative contours dashed, and the zero contour is black.

as seen by regressions of the index on the four individual quadrants shows in Figure 4.21. As stressed in the previous section, it is the intensity of the circulation in the exit region of the storm track that differentiates it from the flow in other regions. The region highlighted by the NAO-like pattern in this model is not so unique in its dynamics, but in the intensity of the flow here.

## 4.7 Summary and Conclusions

We have investigated the effect of simple topographic and large scale thermal forcing on the patterns of intraseasonal variability in a dry primitive equation model. As argued in Chapter 2 and Cash et al. (2005), the zonal structure of the low frequency variability is controlled by the zonal structure of baroclinic instability, the “high

frequency stirring.” A Gaussian ridge similar in scale to the Rocky Mountains and heating anomalies approximating the effect of a cold continent and warm ocean were used to create asymmetry in the baroclinicity of the flow and produce zonally localized storm tracks. Once the synoptic variability was localized, the variability at lower frequencies, as characterized by EOF and teleconnection analysis, became amplified in the exit region of the storm tracks where eddy momentum fluxes are largest. Patterns of variability resembling the atmospheric Northern Annular Mode and the NAO were generated with the confluence of the topographic and baroclinic forcing.

Particular care was taken to create a realistic storm track in such an idealized, dry model. Pierrehumbert (1984) and Chang and Orlanski (1993) show that a localization of the baroclinicity is not sufficient to localize the synoptic variability. Advection by the mean flow competes with the local growth tendency, limiting the influence of a local maximum in the baroclinicity, and downstream energy fluxes by the fully nonlinear eddies both act to smear out the influence of a local maximum in the baroclinicity. These effects are well illustrated in simulation RM, where topography generated a relatively sharp maximum in the baroclinicity (and baroclinic eddy growth, as evidenced by the localization of high pass eddy heat fluxes), but little localization of the eddy kinetic energy.

Hoskins and Valdes (1990) demonstrate the importance of diabatic effects in maintaining the localization of the storm track. As the eddies act to break down the temperature gradients that provide energy to the eddies, a strong restoring force is required to maintain the baroclinicity. In simulation LSC, a large cooling and warming anomaly were added to the model in the high latitudes to approximate cooling influence of a large continent and the warming by an ocean, as is observed in the atmosphere during the winter. Here the baroclinicity was not much more localized than in the simulation with just topography, but the synoptic variability was substantially more localized. The difference appears to be in the shape of the baroclinicity.

Given the tendency of eddies to propagate energy downstream, a “dead” zone of reduced baroclinicity is required to prevent the downstream extension of the storm track. When eddy growth was sufficiently reduced, eddy energy piles up and the eddy momentum fluxes grow large, suggesting the eddy decay dominates eddy growth.

While the increase in baroclinicity created by topography appears to have a limited effect on the localization of the synoptic variability in the model, topography is still important in shaping the intraseasonal variability. Significant localization of the poleward lobe of the models NAM is dependent on the low frequency wavetrain associated with the topography. Only in simulations LSC+RM1 and LSC+RM2 is the poleward lobe displaced off the pole, giving the first EOF a structure more characteristic of the NAO than of the annular mode. The variation in structure seen between these two simulations indicates the sensitivity of the variability patterns to the overlap of topographic and thermal effects. In LSC+RM1 the interaction between them lead to nonlinear change in the intraseasonal variability, that is, more localization than would be expected by simply adding the individual response of topography and land-sea contrast together. This suggest that the precise relationship between the Rocky Mountains and North Atlantic storm track might be important in localizing variability in the NAO, and that the interaction between the Tibetan Plateau and the North Pacific storm track might not be as advantageous for localized variability over the Pacific.

The addition of zonal asymmetries to the model forcing also had a dramatic effect on the persistence of low frequency variability. While the model’s Southern annular modes grew and decayed on a time scale of 45-50 days, the time scale of the Northern annular modes varied between 10 and 33 days, becoming less persistent as the degree of asymmetry was increased. Primitive equation models with Held and Suarez (1994) forcing are known to be overly persistent (Walter Robinson, personal communication). Zonally asymmetric forcing, particularly topography, make the model’s variability

more consistent with the NAO and NAM of the atmosphere, which decay on a time scale of approximately 10 days Feldstein (2000b). Zonal asymmetries, topography in particular, also made the persistence of the model's annular mode less sensitive changes in the models equator-to-pole temperature gradient. These effects are studied in greater detail in Chapter 5.

Given a model with a reasonable synoptic storm track and localized low frequency variability - simulation LSC+RM in particular - we explored the null hypothesis that the localization of the variability is due to increased intensity of the eddy momentum forcing - that is, more stirring - and not “unique dynamics” specific to the region of variability. To this end, we applied teleconnection analysis to the flow around the latitude circle to compare the local variability in the storm track region to the unperturbed flow outside it. As seen in Figure 4.16, away from topography and the region of highest baroclinicity, the local teleconnections have the same spatial structure, meridional dipoles in pressure of perhaps 60 degrees in zonal extent, reflecting no change in the length scales. More importantly, the persistence of these patterns is roughly equivalent. The only significant difference between them was in their variance. Given the underlying zonal asymmetry of the synoptic variability, then, the structure of the annular modes and correlation maps could well be described by simpler models in Chapters 2 and 3.

The link between eddy heat and momentum fluxes and the NAO-like modes in the model suggest an important relationship between intraseasonal variability and the baroclinic life cycle, as sketched in Figure 4.22. In the eddy life cycle, eddy growth is characterized by strong low level heat fluxes and eddy decay by momentum fluxes and transfer of energy to the mean flow (Simmons and Hoskins 1978). Both eddy growth and decay occur simultaneously at all longitudes, but zonal asymmetries in the baroclinicity tend to segregate these processes. Eddy growth – strong heat fluxes – dominates in the baroclinic region in the entrance to the storm track, where the jet

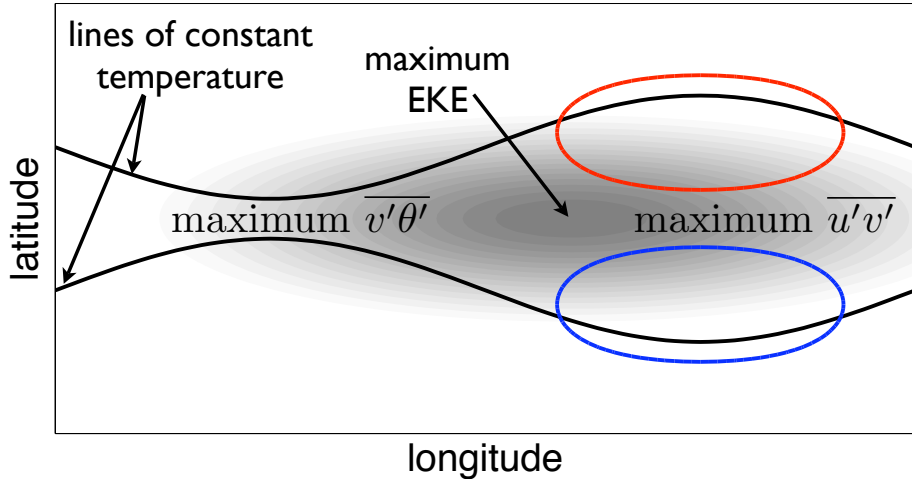


Figure 4.22: A cartoon illustrating the relationship between intraseasonal variability (the dipole pattern shown with red and blue contours), the baroclinicity of the flow, as inferred from the black contours of temperature, and the eddy statistics. Intraseasonal variability is greatest just downstream of the EKE maximum, where eddy decay processes generate strong momentum fluxes.

and temperature gradients are greatest. Here variability and persistence of the zonal flow is minimal, limited to a large extent by the chaotic nature of baroclinic instability, and by the fact that eddy momentum fluxes are weak. Eddy decay dominates in exit region of the storm track, where the baroclinicity is minimal and eddy momentum fluxes are greatest. It is here where we find the greatest variability of the jet at low frequencies, where there can be positive reinforcement of the jet by eddy momentum fluxes.

The physical interpretation of the NAO offered in Section 4.6 is consistent with this thinking. In the exit region of the storm track the subtropical jet is weakening and bent by the standing wave generated by the topography. The strong eddy momentum fluxes here (see Figure 4.2) can separate the eddy driven jet from the subtropical jet. The two jets, two local maxima of relative vorticity, then interact as two vortices. Generally, two like signed vortices will tend to merge. It is only when the eddy forcing is strong enough that eddies can completely separate the eddy driven jet from the subtropical jet.

Based on this we may speculate why the North Atlantic Oscillation is a much more dominant pattern of variability than the “North Pacific Oscillation,” a similar pattern in the Pacific identified by Walker and Bliss (1932) in one of the original papers on large scale teleconnection patterns. The jet in the North Hemisphere (see Figure 4.9) can be thought of a spiral, to some extent, beginning over the Mediterranean Sea and slowly edging poleward until it ends over the North Atlantic. The “end of the jet” over the North Atlantic is a region of extremely weak baroclinicity, and so weak eddy growth, where the momentum fluxes of decaying eddies are free to interact with the weakening flow. The storm track over the Pacific, on the other hand, does not exhibit such a definite region where decay overwhelms growth. In fact, by some measures, the Pacific and Atlantic storm tracks appear merged (see Hoskins and Hodges (2002) or Figure 4.9). We acknowledge that other processes in the Pacific, including the dominance of other teleconnection patterns, notably ENSO and PNA, and mid-winter suppression of baroclinic activity, may be responsible for the lack of an “NPO.” None the less, the understanding provided by simple models such as the one in this study may aid in understanding and interpreting the behavior of both more sophisticated models and the atmosphere itself.

# Chapter 5

## The Dry Dynamical Core II: Timescales of Variability

### 5.1 Introduction

We wish to understand the processes that set the intraseasonal timescale of the annular modes and NAO. By intraseasonal, we mean timescales of 10-100 days, longer than the timescale of baroclinic instability, but not so long as to permit significant changes in the boundary conditions, such as sea surface temperature. At these shorter timescales, we must look to internal processes in the atmosphere that extend the persistence of low frequency patterns beyond synoptic timescales. As suggested by the studies of Feldstein discussed in Section 1.1, the variability in this range may account for a large fraction of the variability of the NAO and annular modes on interannual timescales.

Given our focus, a dry primitive equation model of the atmosphere provides an ideal context for addressing the problem. The model resolves the full three dimensional dynamics, but its climate is defined by a small set of well defined parameters, allowing us to explore the variability over a wide range of mean states. Further, the

computational simplicity of the model permits us to run simulations for sufficiently long periods to fully characterize the variability.

The barotropic model in Chapter 2 provides a first order explanation for the enhanced persistence of anomalies of the zonal wind. As the integral of eddy vorticity fluxes, the spectrum of zonal flow anomalies are redder than the eddies that force them. The barotropic model, however, did not allow for feedback between the eddy stirring and the lower frequency anomalies. As the dynamical core permits these interactions, should we expect more enhanced variability? Also, there was not a substantial change in the timescales of variability with the addition of zonal asymmetry to the barotropic model. As seen in Section 4.4.2, however, there are significant changes with the dynamical core. This is a first indication that this more realistic system exhibits new dynamics.

In Section 5.2 we review previous work on the timescales of intraseasonal variability, and for evidence of a feedback between high frequency stirring and the large scale meanders of the jet. In Section 5.3 we discuss our model setup and our analysis procedures. We then discuss a troubling relationship between the timescales of variability and the resolution of the model in Section 5.4. Once we establish the regimes where the model simulations appear robust, we survey the model over parameter space in Section 5.5. We find that the model responds similarly to changes in three critical parameters, the equilibrium equator-to-pole temperature gradient, and the temperature and momentum damping coefficients. The timescales of the intraseasonal variability are quite sensitive, varying by over an order of magnitude. We then use the temperature gradient to probe the variability of the model as a function of the zonal asymmetry of the forcing in Section 5.6. We find that the sensitivity of the timescales is dramatically reduced in the presence of zonally asymmetric forcing.

The meat of our analysis is found in the next sections. In 5.7 we present evidence that the eddy momentum fluxes are being organized at low frequencies - on timescales

substantially longer than those of individual eddies. We do so by testing the null hypothesis proposed by Lorenz and Hartmann (2001), that the eddy forcing should be independent of the state of the jet. Then in Section 5.8 we sketch out a potential mechanism by which the barotropic circulation generated by eddies can enhance the persistence of the jet. The mechanism, however, is not sufficiently well defined to explain why the feedback appears to be strong in certain parameter regimes and weak in others. In an effort to address this problem, we seek to better understand the nature of the annular mode in Section 5.9. As discussed in Chapter 3, the zonal symmetry of the annular mode does not necessarily imply symmetric dynamics, and this has ramifications on the mechanism proposed in Section 5.8. We then present a simple model of the feedback which captures the importance of the zonal structure of the dynamics in Section 5.10. While this helps explain the reduction in sensitivity to parameters in the presence of zonal asymmetry, we have not been able to address all the features observed in the model. In Section 5.11, we discuss the state of our understanding and directions we hope to pursue in the future. We conclude this portion of the thesis in Section 5.12.

## 5.2 Background

In Section 5.8 we present a mechanism for extending the persistence of the annular mode. This mechanism has been discussed previously in various forms by many authors, (e.g. Branstator 1992, 1995; Robinson 1994, 1996, 2000; Lorenz and Hartmann 2001, 2003). It is well documented that the annular modes and NAO are forced by eddy heat and momentum fluxes. Harder to pin down, however, has been the potential for low frequency variability to influence eddies, thereby completing a feedback loop. One must explain how the intraseasonal variability shapes the eddy stirring in such a way as to sustain the anomaly. As our work is heavily influenced by these

earlier studies, we find it important to review a few of them here.

Branstator (1992) and (1995) provide evidence for the extended maintenance of low frequency anomalies. In the first study, he demonstrates the role of high frequency eddies in maintaining low frequency anomalies in a idealized primitive equation model, establishing the first leg of the feedback. In the second he completes the feedback, demonstrating the organization of high frequency variability by the low frequency patterns. His strategy is to predict the high frequency variability associated with a positive or negative phase low frequency variability anomaly with a linearized version his model. Changes in the linear growth rates of baroclinic instability lead to a shift of the storm tracks, and the nonlinear momentum fluxes that would be associated with this shift would tend to reinforce the low frequency anomaly. Whitaker and Sardeshmukh (1998) employed a similar technique to predict the mean storm tracks from a linearized model based on the mean flow. Their study supports the argument that instability predicted from a linear model can predict the synoptic variability of the nonlinear system. This suggest that although the low frequency anomalies are largely equivalent barotropic, they can shape the baroclinicity of the flow.

Robinson (1994) finds a eddy feedback in a dry primitive equation model with 2 levels and R15 resolution. He argues that eddy activity (or eddy enstrophy) is greatest in the jet core. The stronger winds have a greater carrying capacity, in that eddies of more phase velocities will behave linearly. When the jet is displaced, this region of peak eddy activity is also displaced. This implies a divergence of eddy activity at former location and a convergence at the new location. This in turn implies momentum convergence at the former position of the jet and momentum divergence from the new position; a negative feedback on the displacement. He fleshes out the feedback by prescribing a periodic forcing of the jet, and observing the phase of the eddy forcing.

Robinson (1996) proposes another mechanism that enhances the persistence of jet anomalies. Surface friction acts to increase the baroclinicity of the flow at the jet core by increasing the shear. He conducts experiments with the same two-layer model, finding that the persistence of the annular mode increases as the surface friction increases (a rather counterintuitive result) in certain ranges. He fleshes out the feedback by fixing the barotropic component of the jet, thus disabling the feedback, and noting that the persistence of the zonal index decreases.

These ideas are further refined in an analytic model in Robinson (2000). There he discussed the importance of the effect of both the eddy heat fluxes and the momentum fluxes. The transient response to eddy heat fluxes produces a negative feedback, as eddies reduce the baroclinicity at the jet location. The response at lower frequencies, however, involves the meridional transport of momentum aloft, and can produce a positive feedback. As he points out, at zero frequency (the steady state), momentum fluxes help maintain the jet by transferring momentum up gradient – a clear positive reinforcement. Thus, the positive feedback at low frequencies can be understood in part by the eddy response at zero frequency.

Lorenz and Hartmann (2001), hereafter denoted LH, find a feedback between high frequency eddies and the zonal average flow to explain enhanced persistence of the zonal index in the Southern Hemisphere on intraseasonal timescales. Their analysis contrasts the behavior of the first EOF of the zonal and vertical average flow (the zonal index), a dipole corresponding to a North-South wobble of the jet, with that of the second EOF, a tripole corresponding to a strengthening/weakening, or pulsing of the jet. They observe that first EOF is more persistent than the second. With the aid of a simple model, they explain this enhanced persistence of the first EOF as a feedback with the eddy forcing that does not occur with the second EOF. They argue that shifts in the latitude of the jet lead to changes in the refractive index that shape the divergence of wave activity. This leads to eddy momentum flux divergence

that strengthens anomalies of the zonal average zonal winds. As the second EOF characterizes a change in the intensity of the jet, the refractive index is not shifted, and there is no positive reinforcement.

Their analysis provided a clear definition of “enhanced persistence,” by contrasting observations against the null hypothesis that the eddies forcing is *independent* of zonal average state. They base their model on the assumption that one may analyze the relationship between the zonal wind and eddy forcing in EOF space, one mode at a time, so that nonlinear interactions between different modes of variability are not important at first order. The model consist of a simple relationship between the state of the zonal flow and the eddy momentum fluxes.

$$\frac{dz}{dt} = m - \frac{z}{\tau} \quad (5.2.1)$$

$z$  is the amplitude of the first (second) EOF of the vertical and zonal mean flow,  $m$  is the projection of the eddy momentum forcing,  $-\partial \bar{u}'v'/\partial y$ , on to the first (second) EOF, and  $\tau$  is a simple linear damping zonal index, meant to account for all the decay process acting on the zonal flow.

They suppose that  $m$  can be broken down into a component dependent on the state of the zonal index - a feedback - and an independent component, a random forcing generated by the chaotic nature of the eddies that is not affected by the state of  $z$ ,

$$m = bz + \tilde{m}. \quad (5.2.2)$$

Here  $b$  measures the strength of the feedback and  $\tilde{m}$  is the component of the forcing that is independent of  $z$ . By “independent” they mean uncorrelated at large positive lags, for the linear relationship between  $z$  and  $m$  of course implies a relationship between the eddies and zonal flow. They explore the importance of the feedback by contrasting the nature of the observed zonal index  $z$  with the zonal index  $\tilde{z}$  which

would occur in the absence of any feedback:

$$\frac{d\tilde{z}}{dt} = \tilde{m} - \frac{z}{\tau} \quad (5.2.3)$$

The key to the analysis is the estimation of the Raleigh damping  $\tau$ , which is computed from cross-spectrum analysis of  $m$  and  $z$ . The assumption that the eddy forcing be independent of the mean flow is equivalent to the assertion that the eddies have no energy at frequencies lower than that set by the friction. (Otherwise, there would be an in-phase relationship between  $m$  and  $z$ .) Combining (5.2.1) and (5.2.2), the zonal index with the feedback,  $z$ , is given by

$$\frac{dz}{dt} = \tilde{m} + bz - \frac{z}{\tau} \quad (5.2.4)$$

$$= \tilde{m} - \frac{z}{\tau_2} \quad (5.2.5)$$

where  $\tau_2 = (\tau^{-1} - b)^{-1}$ . If we assume that the eddy forcing  $\tilde{m}$  has a relatively white spectrum, at least at low frequencies, (5.2.3) and (5.2.5) imply that  $\tilde{z}$  and  $z$  are stochastically forced oscillators with damping timescales  $\tau$  and  $\tau_2$ . The strength of the feedback,  $b$ , is determined by the degree that the observed annular mode  $z$  persists longer than the natural damping scale of the model,  $\tau$ .

While the first EOF is observed to be more persistent than the second EOF, they find that the natural damping timescale  $\tau$  in both cases is the same. The enhanced persistence of first EOF can thus be explained by a feedback not present in the second. This supports their argument that a change in the index of refraction is essential for a coupling between the eddies and mean flow. As shown by Feldstein (1998), eddy interactions with the zonal flow can lead to poleward propagation of zonal wind anomalies. Spherical geometry tends to refract the wave activity associated with an anomaly of the jet more towards the equator. The resulting equatorward eddy momentum fluxes shift zonal wind anomalies poleward. LH found evidence of

poleward propagation in a phase relationship between the first two EOFs.

Our strategy is shaped by Robinson's two layer model studies. We vary model parameters to control the timescales of variability, allowing us to narrow in on the processes which influence the variability. In diagnosing the presence of a feedback in our model, we apply the strategy established by LH, which provides a means of simplifying the dynamics. The dynamical core provides a testing ground at intermediate complexity, enabling us to connect conclusions found in two-layer models to observations from the atmosphere.

### 5.3 Experimental Setup

We use the GFDL dry dynamical core, a dry primitive equation model with a steady Held and Suarez (1994) (hereafter denoted HS) forcing, as described in Section 4.2. It is a spectral model with triangular truncation and  $\sigma = p/p_s$  vertical coordinates. Our study with the model can be divided into three experiments to determine the sensitivity of the intraseasonal variability to (1) resolution, (2) parameters, and (3) zonal asymmetries in the forcing.

#### Experiment I: Sensitivity to Resolution

Table 5.1, lists simulations performed to assess the dependence of the intraseasonal variability on the resolution. In each simulation, the model was allowed 200-300 days to spin up before data was collected; the times in Table 5.1 denote length of the simulation after the initial spin up period. The standard HS forcing was applied in all simulations, with parameters  $\Delta T_{eq} = 60$  K,  $k_a = 40^{-1}$  day $^{-1}$ , and  $k_f = 1$  day $^{-1}$ . The forcing is the same in both hemispheres, allowing us to sample from both and double the effective simulation time. The annular modes in the hemispheres act independently of one another.

simulation	horizontal resolution	vertical resolution	strat.	
		sponge	length	
T42L20e	T42	20 even	-	6000
T42L40e	T42	40 even	-	2500
T42L25u	T42	25 uneven	-	9500
T42L20st	T42	20 strat+	-	3000
T42L20su	T42	20 surf+	-	3000
T42L20e-S	T42	20 even	yes	3000
T63L20e	T63	20 even	-	3700
T63L25u	T63	25 uneven	-	2300
T63L50u	T63	50 uneven	-	1800
T63L20e-S	T63	20 even	yes	1800
T85L20e	T85	20 even	-	1800

Table 5.1: Simulations I: Resolution Tests. These simulations were completed to characterize sensitivities of the model to resolution and processes in the under-resolved stratosphere.

In simulations marked with “even” vertical resolution,  $\sigma$ -levels are spaced equally in pressure, thus equally resolving the atmosphere in terms of mass. In simulations with “strat+” vertical resolution, the  $\sigma$ -levels are spaced evenly in  $\sigma$  in the lower atmosphere, and transition to exponential spacing in  $\sigma$  at the upper boundary of the model. This provides even spacing in  $z$  in the upper atmosphere. The spacing for “surf+” is the opposite, even in  $\sigma$  in the upper and middle atmosphere, but better resolved near the surface, and “uneven” provides enhanced resolution at the top and the bottom. Simulations were completed with “uneven” spacing to make the output more easy to compare with more sophisticated models that required better surface resolution for boundary layer schemes. The four vertical spacing schemes are illustrated in Figure 5.1.

The unevenly spaced profiles are controlled by three parameters,  $\alpha$ ,  $\beta$ , and  $\gamma$ . The position of the  $k^{\text{th}}$  vertical grid point in  $\sigma$ -coordinates is given by

$$\sigma_k = \exp(-\gamma[\beta z + (1 - \beta)z^\alpha]) \quad (5.3.1)$$

where  $z = 1 - (k - 1)/N$ ,  $N$  is the number of vertical grid points, and  $k = 1, 2, \dots, N$ .

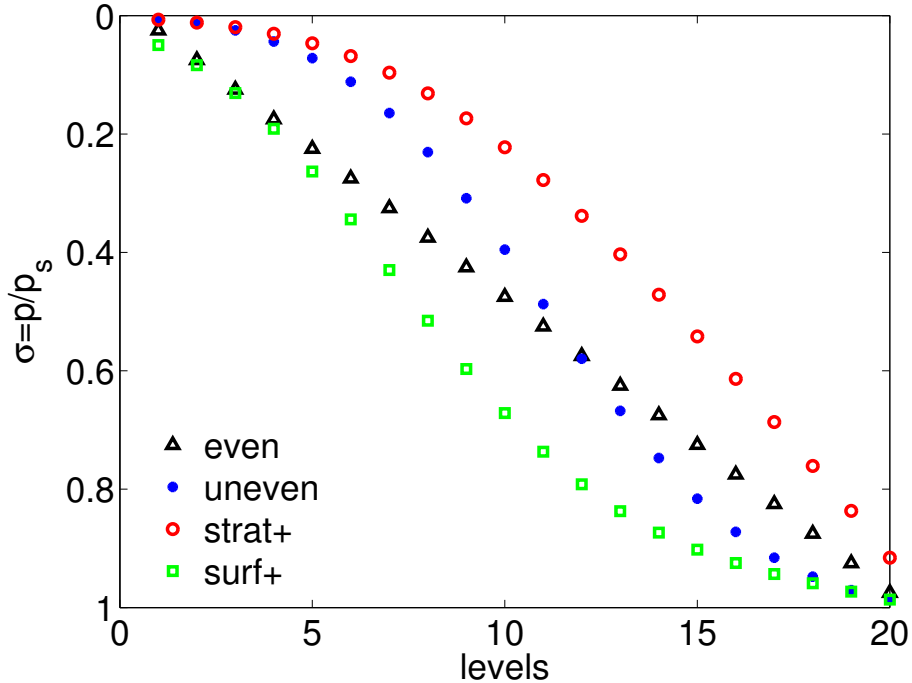


Figure 5.1: Spacing of  $\sigma$ -levels, for  $L=20$ , in the four configurations used in this study. Increasing the number of levels increases the density of points along the curve, but does not change the shape of the profile.

Parameter  $\beta$  provides control over the resolution near the surface, while  $\alpha$  and  $\gamma$  provide control over resolution at height. Simulations with “uneven” spacing used parameters  $(\alpha, \beta, \gamma) = (3, 0.05, 5)$ . Simulations with “strat+” and “surf+” resolution used parameters  $(3, 0.35, 5)$  and  $(4, 0.09, 3)$ , respectively.

In certain simulations a stratospheric sponge was implemented with the intent of damping wave activity in the upper atmosphere, where resolution is insufficient to simulate the physical processes of wave breaking. The sponge is a function of the wind and  $\sigma$ ,  $DU/Dt = \dots - s(\mathbf{U}, \sigma)$  where

$$s(\mathbf{U}, \sigma) = \begin{cases} \frac{(\sigma_b - \sigma)^2}{\sigma_b^2} \frac{\mathbf{U} - \overline{\mathbf{U}}}{\tau_s} & \sigma \leq \sigma_b \\ 0 & \text{otherwise} \end{cases} \quad (5.3.2)$$

Here (and below) we use an overbar to denote the zonal average of a quantity, and

$\langle \rangle$  to denote the time average. The sponge  $s(U, \sigma)$  acts only on deviations from the zonal mean flow acting on levels above  $\sigma_b = 0.1$ . Shepherd and Shaw (2004) stress the importance of damping only anomalies from the zonal mean; otherwise spurious circulations reaching the surface can develop. The damping is maximum at the upper boundary of the atmosphere, where it reaches  $\tau_s$ . We found that damping did not appreciably affect the results unless it was turned up quite high, to 1/10 day. As will be discussed in the text, there is a danger of reflection and other non-physical effects when the drag is applied too rapidly in height.

## Experiment II: Parameter Sweeps

Once the robustness of the model to resolution was established, we explored the influence of three parameters in the HS scheme on the intraseasonal variability.

- $\Delta T_{eq}$ : the magnitude of the equator-to-pole gradient of the equilibrium forcing.  
In the control simulation, this is 60 K. (In HS, this parameter is just  $\Delta T$  - we add the subscript to stress that this controls the gradient of the equilibrium profile, not necessarily the mean profile of the model.)
- $k_a$ : the thermal damping. In the control simulation it is set to  $40^{-1}$  day $^{-1}$  outside the low-level tropics.
- $k_f$ : the momentum damping at the surface. The default value is 1 day $^{-1}$ .

The role of each of these parameters was briefly reviewed in Section 4.2.

Table 5.2 lists the experiments conducted in the parameter study. All were completed with 20 evenly spaced  $\sigma$ -levels in the vertical. Simulations with T42 resolution were run for 6000 days after a spin up period of 250 days. Data from both hemispheres were collected as independent realizations of one generic hemisphere, providing 33 years of simulation time. Simulations at T63 resolution were run for 3700 days after a 300 day spin up period, providing over 20 years of simulation time.

simulation	horizontal resolution	vertical resolution	$\Delta T_{eq}$ (K)	$k_a$ (day $^{-1}$ )	$k_f$ (day $^{-1}$ )
Z30	T42	20 even	30	$40^{-1}$	1
Z40	T42	20 even	40	$40^{-1}$	1
Z50	T42	20 even	50	$40^{-1}$	1
Z60*	T42	20 even	60	$40^{-1}$	1
Z70	T42	20 even	70	$40^{-1}$	1
Z80	T42	20 even	80	$40^{-1}$	1
Z90	T42	20 even	90	$40^{-1}$	1
Z40-T63	T63	20 even	40	$40^{-1}$	1
Z60-T63*	T63	20 even	60	$40^{-1}$	1
Z80-T63	T63	20 even	80	$40^{-1}$	1
ka=30	T42	20 even	60	$30^{-1}$	1
kaz=30 <sup>†</sup>	T42	20 even	60	$30^{-1}$	1
ka=60	T42	20 even	60	$60^{-1}$	1
kf=.75	T42	20 even	60	$40^{-1}$	$0.75^{-1}$
kf=1.5	T42	20 even	60	$40^{-1}$	$1.5^{-1}$

Table 5.2: Simulations II: Parameter Tests. All simulations listed here were run with forcing independent of longitude. “Z” refers to zonal symmetry of the temperature gradient simulations, as they will be compared with zonally asymmetric simulations in the next experiment. \*Simulation Z60 and Z60-T63 are the control simulations. In Experiment I they were listed as simulations T42L20e and T63L20e, respectively. <sup>†</sup>In simulation kaz=30, the damping on the zonal mean flow is separated from the damping on eddies, as described in the text. Note that we refer to the damping timescales (as opposed to the coefficients) in simulations with ka and kf.

As part of the HS forcing scheme, the thermal damping is increased to  $4^{-1}$  day $^{-1}$  below  $\sigma = 0.7$  in the low latitudes to promote a more realistic Hadley Circulation. In simulations where  $k_a$  was varied, we leave the low level tropical heating intact, as to cause minimal change to the tropical circulation. In simulation kaz=30, the thermal damping of the zonal average flow was split from the thermal damping of eddies,

$$\frac{DT}{Dt} = -k_{az}(\bar{T} - T_{eq}) - k_{ae}(T - \bar{T}) \quad (5.3.3)$$

Parameter  $k_{az}$  was set to  $30^{-1}$  day $^{-1}$ , while the thermal damping on the eddies remained the default value,  $k_{ae} = 40^{-1}$ .

### Experiment III: Zonal Asymmetries

As seen in Section 4.4.2, zonal asymmetries in the forcing make a dramatic difference in the variability. Table 5.3 lists simulations completed with zonally asymmetric forcing. These simulations were run for 9000 days (approximately 22 years) after an initial 250 day spin up period. All were completed with T42 resolution and 20 evenly spaced  $\sigma$ -levels, and the momentum damping  $k_f$  and thermal damping  $k_a$  were fixed at the control values, 1 and  $40^{-2}$  day $^{-1}$ , respectively. As there is some influence of zonal asymmetries on the variability in the opposite hemisphere, anomalies were positioned only in the models Northern Hemisphere.

The construction of the zonal anomalies was discussed in Section 4.2.1. Briefly, “LSC” refers to a cooling and heating anomaly established to approximate the effect of cold continent and warm ocean, and hence land-sea contrast. “RM” refers to a ridge similar in scale to the Rocky Mountains.

simulation	topography	thermal forcing	$\Delta T_{eq}$
LSC40	-	yes	40
LSC60	-	yes	60
LSC80	-	yes	80
RM40	2000	no	40
RM60	2000	no	60
RM80	2000	no	80
rm40	1000	no	40
rm60	1000	no	60
rm80	1000	no	80
LSC+RM1-40	2000	yes	40
LSC+RM1-60	2000	yes	60
LSC+RM1-80	2000	yes	80
LSC+RM2-60	2000	yes	80

Table 5.3: Simulations III: Zonal Asymmetries. The values under topography refer to the height of the ridge in meters. With the exception of LSC+RM2-60 (where the ridge is located at 60° W) the topography is located at 90° W. The thermal forcing is position so that the prime meridian marks the boundary between the cooling and warming anomalies. Values for  $\Delta T_{eq}$  are given in K.

### Analysis Techniques

Filtered statistics were computed using a digital Lanczos filter, as described in Section 4.2.2. All computations were done in the native  $\sigma$ -coordinates and then interpolated to pressure surfaces as appropriate.

The annular mode is defined as the first EOF of sea level pressure, which was found by linear extrapolation in simulations with topography. The EOFs were computed as in Section 4.4. The zonal index is defined as the first EOF of the zonally averaged zonal winds. As seen in the previous chapter, both measures provide equivalent information of the variability.

## 5.4 Sensitivities of the Model to Resolution

The mean climate and variability of the primitive equation model are sensitive to model resolution, particularly in the vertical. While computational resource limita-

tions prevented full sampling of the two dimensional resolution landscape, we have documented robust changes in the mean state with shifts in resolution. We have also found trends in the model’s intraseasonal variability, but changes in lower frequencies were harder to verify, as higher resolution simulations were not run long enough for sufficient sampling.

When the vertical resolution is fixed with 20 evenly spaced  $\sigma$ -levels, the climate is relatively stable when the horizontal resolution is increased from T42 to T63 to T85. As seen in Figure 5.2a, there is a slight equatorward shift of the extratropical jet ( $\sim 2^\circ$ ) and a more subtle poleward extension of the subtropical jet with increased resolution. Most of the change occurs between T42 and T63 resolution, suggesting that the climate has converged at T63. The shift in the jet (and hence the temperature gradients) is associated with an equivalent shift in eddy activity. The total eddy kinetic energy increases with resolution, as to be expected given the inclusion of more scales. The timescales of intraseasonal variability (quantified by the e-folding timescale of the annular mode shown in Table 5.4) are relative unchanged between T42 and T63, but appears to drop at T85. We note, however, that the T85 simulation was not run sufficiently long to resolved the large scale variability.

The model is more sensitive to changes in the vertical resolution. Trends in vertical resolution, however, are sensitive to the horizontal resolution, and so cannot be discussed independently of it. The mean climate of all the simulations tends to fall into one of two classifications, or regimes. The two states, as characterized by the zonal average winds, are illustrated by representative members in Figure 5.2b. All simulations with finer resolution near the top of the model’s atmosphere<sup>1</sup> are similar to T42L20st, denoted by the magenta contours. Simulations where resolution in the upper atmosphere is not as fine are similar to T42L20e, marked with the blue contours. As the Hadley cell stays the same in all the simulations, the  $5^\circ$  equatorward

---

<sup>1</sup>With  $\sigma$ -coordinates the upper boundary of the model increases in simulations with higher resolution. It is possible that this plays a role in the change.

simulation	jet location (° latitude)	average EKE ( $m^2 s^{-2}$ )	AM persistence (days)	circulation “regime”
T42L20e	46	112	36	LR-SJ
T42L40e	41	117	65	HR-MJ
T42L25u	41	116	66	HR-MJ
T42L20st	41	117	57	HR-MJ
T42L20su	46	113	27	LR-SJ
T42L20e-S	40	112	99	HR-MJ
T63L20e	44	137	40	LR-SJ
T63L25u	42	136	29	HR-MJ
T63L50u	42	136	40	HR-MJ
T63L20e-S	42	131	19	HR-MJ
T85L20e	44	146	22	LR-SJ

Table 5.4: Properties of the mean state and variability as function of resolution. The jet location marks the latitude of upper level zonal wind maximum, but the peak surface winds are found at the same latitudes. The EKE is averaged over the jet core. The persistence of the annular mode is quantified by the best fit e-folding timescales. Note that the decorrelation patterns are not perfectly exponential, as seen in Figure 5.3. These values are less robust for higher resolution simulations, which were run for shorter periods. LR-SJ and HR-MJ refer to a categorization of the circulation discussed in the text, and stand for “low resolution-split jet” and “high resolution-merged jet”.

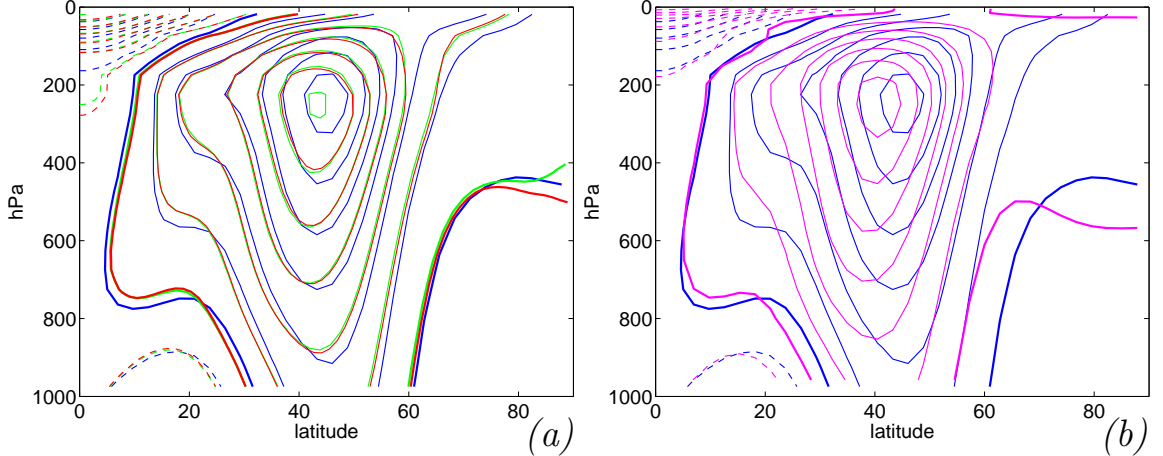


Figure 5.2: The zonal average zonal winds. Contour interval is 5 m/s, negative contours are dashed, and the zero contour is bold. In (a) the horizontal resolution is varied: simulations T42L20e (blue), T63L20e (green) and T85L20e (red). In (b) the vertical resolution is varied: simulations T42L20e (blue) and T42L2st (magenta). These two simulations characterize the two regimes, LR-SJ and HR-MJ, respectively.

shift of the midlatitude winds with finer resolution leads to more pronounced merger of the subtropical and extratropical jets. We have categorized the simulations in Table 5.4 into the regimes HR-MJ and LR-SJ, denoting “higher resolution-merged jet” and “lower resolution-split jet” respectively. We stress that the only difference between the simulations in Figure 5.2b is in the vertical resolution near the top of the model. Simulations with enhanced resolution in the lower atmosphere, such as T42L20su, are similar to T42l20e. The shift of the jets is associated with an equivalent shift of the eddy activity. The total energy does not change substantially, but at T42 resolution, there is a marked increase in the timescales of low frequency variability in the HR-MJ regime. For example, the e-folding timescale of the annular mode of T42L20e is 37 days, while in T42L20st, it is 57 days.

This enhanced persistence has been noted as a troublesome problem with the model by other authors (Walter Robinson; Paul Kushner, personal communication). The standard configuration the model (T42L20e) is substantially more persistent than the atmosphere as is (where the annular mode decays on a timescale of 10

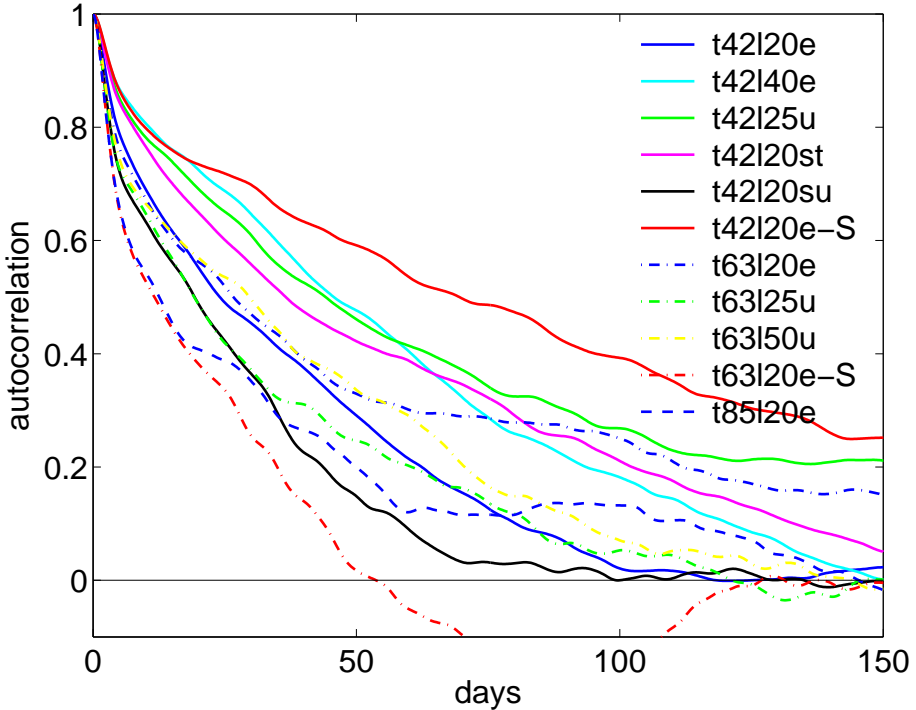


Figure 5.3: The autocorrelation function of the annular mode index.

days), but with higher resolution near the top of the model, the persistence balloons to values exceeding 100 days. Speculating that the problem may involve reflection of waves off the upper boundary, we implemented the stratospheric wave drag (5.3.2) in the model with low upper atmosphere resolution: simulation T42L20e-S. The lower boundary of the sponge,  $\sigma_b$ , was set to 100 hPa to prevent the drag from interfering with tropospheric processes. We observed little effect until the amplitude of the drag was increased to  $\tau_S = 0.1$ . At this strength, the jet shifted equatorward, as in T42L20st, and the annular mode became extremely persistent, decaying with an e-folding timescale of 99 days.

The response of the model to changes in the vertical resolution when the horizontal resolution is fixed at T63, however, suggests that the dramatic change in the persistence of the annular mode observed at T42 is an artifact. There is not a robust increase in the e-folding timescale of the intraseasonal variability associated with in-

creased vertical resolution at T63. With respect to the mean climate, however, we do observed the same regime split, an equatorward shift of the extratropical jet (leading to its merger with the subtropical jet) when the vertical resolution is increased, albeit the response is muted: a  $2^\circ$  shift instead of a  $5^\circ$  shift. Application of the strong stratospheric wave drag at T63L20 resolution led to a shift in the mean state equivalent to an increase in the vertical resolution, but no increase in the persistence of the annular mode.

It is troubling that the model is so sensitive to resolution. The consistency of the equatorward shift associated with enhanced resolution, and the fact that the behavior was replicated by a stiff stratospheric sponge, suggests that it is not an artifact like the changes in persistence. It is not necessarily true, however, that the model is becoming more realistic. The stratosphere of the HS model was designed to be relatively quiet, and it is possible that increased resolution exposes the weaknesses of the forcing there. It is also possible that the sponge came on to abruptly in height, inducing artificial reflection instead of preventing it. With 20 evenly spaced layers, the drag acts on only two.

Effort was made to understand what triggered the changes in the intraseasonal variability at T42 resolution, but no clear evidence was found in any of our analyses. In simulations where zonal asymmetries were introduced into one hemisphere, we also observed large increases in the persistence of the annular mode in the *unperturbed* hemisphere, suggesting that many processes may be able to cause the artificial persistence. It is likely that it is due to changes in the stratosphere, and as this study is primarily concerned with tropospheric processes, we did not pursue this topic thoroughly.

As the simulation with T42 horizontal resolution and 20 evenly spaced  $\sigma$ -levels appears to capture the intraseasonal variability of the model seen at higher resolutions, we have elected to take this resolution as our standard configuration. We are not so

much interested in the numeric value of the timescales exhibited by the model, but rather in the processes that control these timescales, and how these processes respond to changes in the model forcing. Mindful of the model’s tendency to exhibit artificial persistence, we have verified trends observed at T42 resolution in simulations at T63.

## 5.5 Parameter Sensitivities

Having addressed the issue of resolution, we return to our goal of understanding the processes that set the timescale of the intraseasonal variability. We survey the model in parameter space to identify parameters that influences the timescales, which we can use as knobs to tune the variability. We consider three parameters in the HS forcing:  $\Delta T_{eq}$ ,  $k_a$ , and  $k_f$ .

### 5.5.1 A Remarkable Consistency in the Response

By several measures, the response of the mean state and the variability is extremely similar to equivalent changes in each parameter. Figure 5.4 highlights the similarities in the jet structure. If all other parameters are held fixed, reducing the equilibrium temperature gradient by 1/3, reducing the thermal damping by 1/3, or increasing the momentum damping by 1/3, causes the jet to shift equatorward by 5-8°. The reverse, an increase of the temperature gradient or the damping thermal, or reduction of the surface damping, leads to a poleward shift of the jet 1-3°. The difference between the simulations bears a striking similarity to the difference between the HR-MJ and LR-MJ regimes in Section 5.4.

Perhaps more striking is the fact that the three parameters have the similar effect on the intraseasonal variability, as illustrated in Figure 5.5. In the three simulations where the jet was shifted poleward (strong temperature gradient, strong thermal damping, weak momentum damping), the e-folding timescale of the annular mode

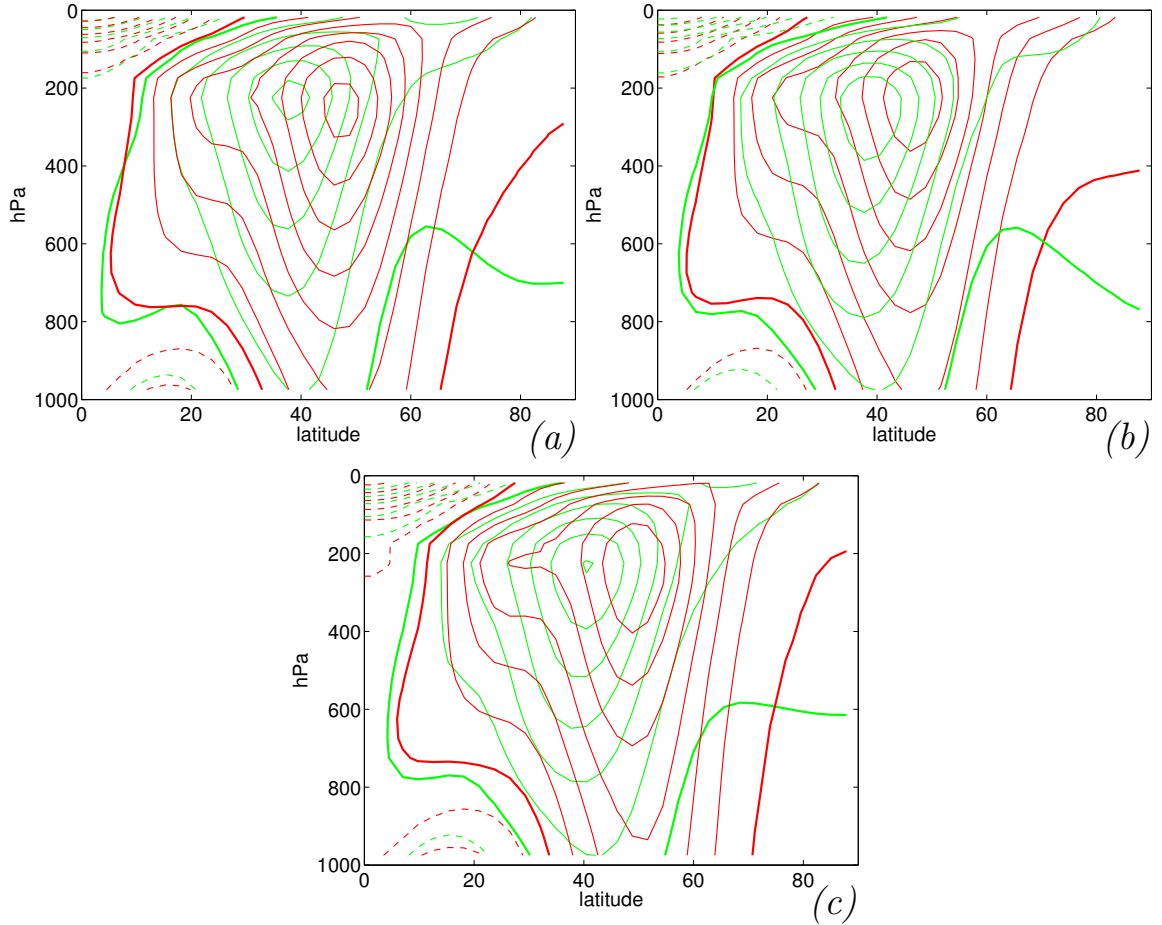


Figure 5.4: The zonal average zonal winds. Contour interval is 5 m/s, negative contours are dashed, and the zero contour is bold. In (a) the temperature gradient is varied: simulations Z40 (green) and Z80 (red). In (b) the thermal damping is varied: simulations  $ka=30$  (green) and  $ka=60$  (red). In (b) the momentum damping is varied: simulations  $kf=.75$  (green) and  $kf=1.5$  (red). Not only is the response of the model in each case nearly the same, but the two cases look very much like the HR-MJ and LR-SJ regimes, respectively.

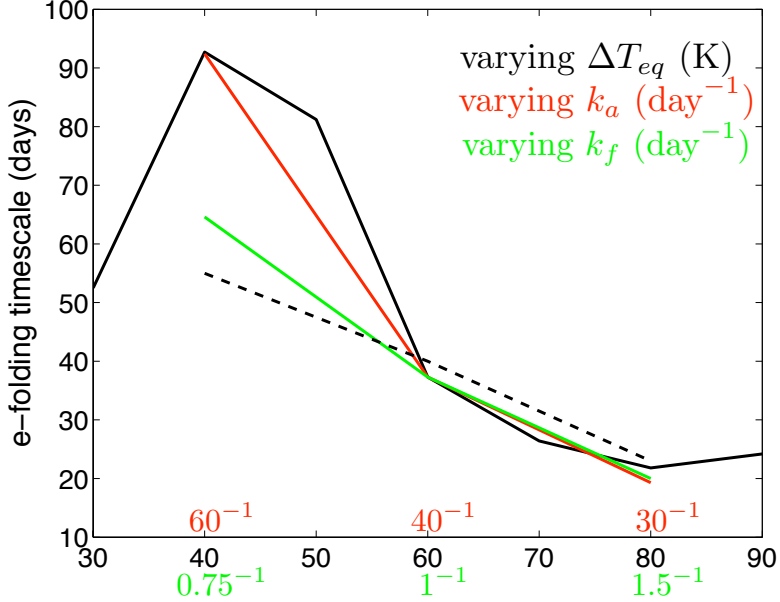


Figure 5.5: The e-folding timescale of the annular mode as function of the (black) equilibrium temperature gradient, (red) thermal damping, and (green) momentum damping. The solid lines are based on simulations at T42 resolution, and the dashed line on T63 resolution. In each case, only one parameter was varied and the others held at their default values,  $\Delta T_{eq} = 40$  K,  $k_a = 40$  day $^{-1}$  and  $k_f = 1$  day $^{-1}$ . See Table 5.5 for further comparison of the simulations.

drops from 37 days to 21, 19, and 20 days, respectively. The converse, weak gradient, weak thermal damping, or strong momentum damping, leads to increases in the persistence, to 93, 92, and 65 days, respectively. While it makes intuitive sense that decreasing the thermal damping or weakening the baroclinicity of the atmosphere by decreasing the equator-to-pole temperature might make the annular mode more persistent, it is less clear why an *increase* in the momentum damping would *increase* the persistence of the annular mode. This counterintuitive result was discovered by Robinson (1996) in a simpler GCM. He argued that the key lay in the fact that the increased drag created a stronger feedback between the eddies and mean flow by increasing the baroclinicity of the flow.

The fact that an artificial increase in the persistence was observed with the resolution regime change is of concern. Simulations at T63 horizontal resolution confirm

the trend with respect to the equilibrium temperature gradient. Here the decrease in persistence associated with stronger temperature gradients is the same, albeit the increase in persistence with the weaker temperature gradient is smaller. Given the sensitivity of the results to resolution, we focus on the trends and not the specific numbers.

The intraseasonal variability of the model is reasonably characterized by a red spectrum in time in all simulations. This is to say, there is no single timescale that dominates the spectrum, so that at low frequencies the spectrum is white, with approximately equal energy at all frequencies. In Chapter 2, we showed how such red spectra can be approximated by a stochastically forced, linearly damped oscillator, or Ornstein-Uhlenbeck process (see Figure 2.16, and the surrounding discussion). This allows us to quantify the temporal structure by a single number, the e-folding timescale. This timescale can be thought of as the damping time of the simple stochastic oscillator fit to approximate the data. A longer damping timescale implies greater power lower frequencies.

The similarity in the sensitivity of the model to changes of  $\Delta T_{eq}$  and  $\tau_T$  is perhaps more easy to understand, as both play a role in setting the zonal average heating,  $k_a(\bar{T} - T_{eq})$ . Increasing  $\Delta T_{eq}$  or  $k_a$  will act to increase the temperature gradients. Baroclinic instability will then increase, acting to mute the increase in the actual temperature gradient. In the theory of baroclinic adjustment (Stone 1978), it is taken that the eddies are perfect in their ability to maintain the flow at the cusp of instability. If we assume that the stability does not change significantly, then the temperature gradients will not change drastically despite the changes to the equilibrium profile. As illustrated in the cartoon in Figure 5.6, if the actual zonal average temperature profile  $\bar{T}$  changes little, then an increase in the equilibrium gradient (from  $\Delta T_{eq1}$  to  $\Delta T_{eq2}$ ) will have the same effect on the atmosphere as increasing  $k_a$ ; in both cases there is more heating in the tropics and cooling in the high latitudes.

simulation	jet latitude	$\bar{u}$ (ms $^{-1}$ )		EKE (m $^2$ s $^{-2}$ )		AM persistence (days)
		jet core	surface	full	high pass	
Z30	34	25	3.8	52	16	53
Z40	38	27	5.1	76	27	93
Z50	43	29	7.2	98	36	81
Z60	46	32	8.9	112	48	37
Z70	46	35	10.0	129	59	26
Z80	47	37	10.8	140	69	21
Z90	48	38	11.4	152	75	24
Z40-T63	38	26	5.4	92	31	55
Z60-T63	44	30	8.1	137	60	40
Z80-T63	46	35	10.1	170	86	23
ka=30	46	34	10.7	126	59	19
ka=60	38	29	5.0	99	36	92
kf=.75	41	30	5.0	112	46	65
kf=1.5	49	34	14.3	108	52	20

Table 5.5: Properties of the climate and variability. The jet latitude marks the latitude of the maximum upper level winds, which are found between 225 and 275 hPa. The maximum surface ( $\sigma = 0.975$ ) winds are found at approximately the same latitude. The eddy kinetic energy is averaged over longitude, pressure, and  $\pm 18$  degrees from the jet core in latitude. The high pass EKE is computed from eddies of frequencies higher than  $10^{-1}$  day $^{-1}$ . The persistence of the annular mode is the best fit e-folding timescale.

This heating must then be balanced by changes in the mean and eddy heat transport. In a sense, the atmosphere does not know the timescale of  $k_a$ , or the strength of the equilibrium temperature gradient, only the heating rate which is proportional to their product,

$$\frac{DT}{Dt} = k_a(\bar{T} - T_{eq}) \propto k_a \Delta T_{eq}. \quad (5.5.1)$$

While perfect baroclinic adjustment is not found in practice, it holds approximately, Figure 5.8a shows the baroclinicity as defined by the Eady growth rate; it increases modestly despite a doubling of the temperature gradient or the thermal restoring force. However, as shown in Figure 5.8b, the stability does change, particularly over the high latitudes. There are thus more substantial changes to the heating than implied by Figure 5.6, and a more subtle explanation is needed to explain the similar response of the model to changes in  $k_a$  and  $\Delta T_{eq}$ .

That the decay of the annular mode is proportional to the product  $k_a \Delta T_{eq}$  suggests that it is largely a coincidence that decay timescale of the annular mode, 37 days at T42 and 40 days at T63, is nearly equal to the thermal damping timescale of 40 days in the standard configuration. Based on these empirical observations, one would expect the model to have same 40 day timescale of intraseasonal variability with  $k_a = 30^{-1}$  days $^{-1}$  and  $\Delta T_{eq} = 80$  K, or  $k_a = 60^{-1}$  days $^{-1}$  and  $\Delta T_{eq} = 40$  K.

The argument in (5.5.1) only calls upon the effect of  $k_a$  on the zonal mean flow. Problems could arise if the damping of zonal anomalies is important. We separated the damping in  $k_a=30z$ , damping only the mean flow with a timescale of 30 days and the eddies with the default timescale, 40 days. The two simulations were almost indistinguishable, implying that the effect of the thermal damping on the eddies is minimal. One would only expect it to play a role if the damping timescale was increased to the point where it was comparable to the eddy timescales of 2-10 days.

It is less clear why changes in  $k_f$  cause such a similar shift in both the mean state and the intraseasonal variability. Before addressing this question further, we highlight

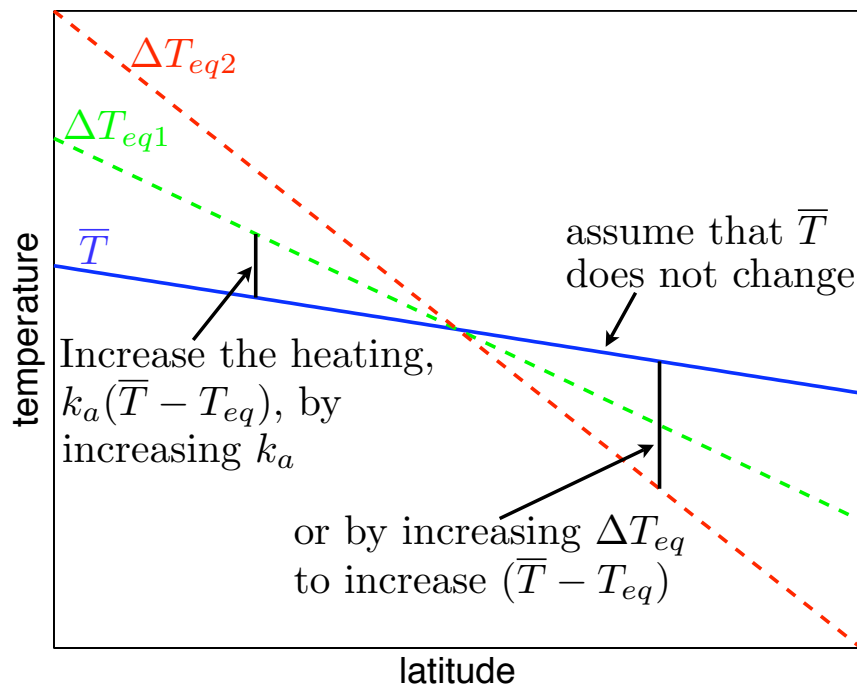


Figure 5.6: A sketch for an argument that the atmosphere is controlled by the product of  $k_a \Delta T_{eq}$ . If the overall zonal average temperature profile (the blue line) remains the same, increasing the equilibrium temperature gradient from the green curve to the red curve will cause the same net heating change as keeping the temperature gradient fixed and increasing the thermal damping,  $k_a$ .

some key differences between the simulations.

### 5.5.2 Important Differences in the Response

As shown from the transient eddy kinetic energy (EKE) statistics in Table 5.5, the eddies do not respond as consistently to changes in the parameters as the mean state or the intraseasonal variability. With respect to  $\Delta T_{eq}$  and  $k_a$ , simulations with an equatorward shifted jet and enhanced persistence are associated with weaker eddies. But the eddies are much more sensitive to the temperature gradient. For example, while simulations Z40 and ka=60 have a similar mean state and persistence, the EKE is substantially larger in Z40. As will be shown shortly, the mean state is not kept constant as would be suggested by baroclinic adjustment. There is little change in the eddy kinetic energy associated with changes in  $k_f$ . The total EKE is greater in the simulation with stronger surface friction, but at synoptic frequencies, there is larger energy when  $k_f$  is smaller.

The trends in the eddy heat fluxes, shown in Figure 5.7a, are similar to the trends in EKE. The high pass heat fluxes are given by  $\langle \overline{v^h \theta^h} \rangle$ , where the subscript ‘h’ denotes a high pass filtered statistic, where frequencies lower than  $10^{-1}$  day $^{-1}$  have been removed. The heat fluxes increase sharply with increasing equilibrium temperature gradient, and more subtly with increasing thermal damping. It seems to weaken in both simulations where  $k_f$  was varied, but it drops more in the simulation with stronger drag.

The baroclinicity of the flow, as characterized by the Eady growth rate parameter (defined in Section 4.3) is shown in Figure 5.8a. The peak baroclinicity varies slightly with equilibrium temperature gradient, but not as much as one would expect based on changes in the temperature gradient alone. Rather, increases in the model average temperature gradient are offset by increases in the stability, as shown in Figure 5.8b. There is a significant change in the shape of the baroclinicity associated to shifts in the

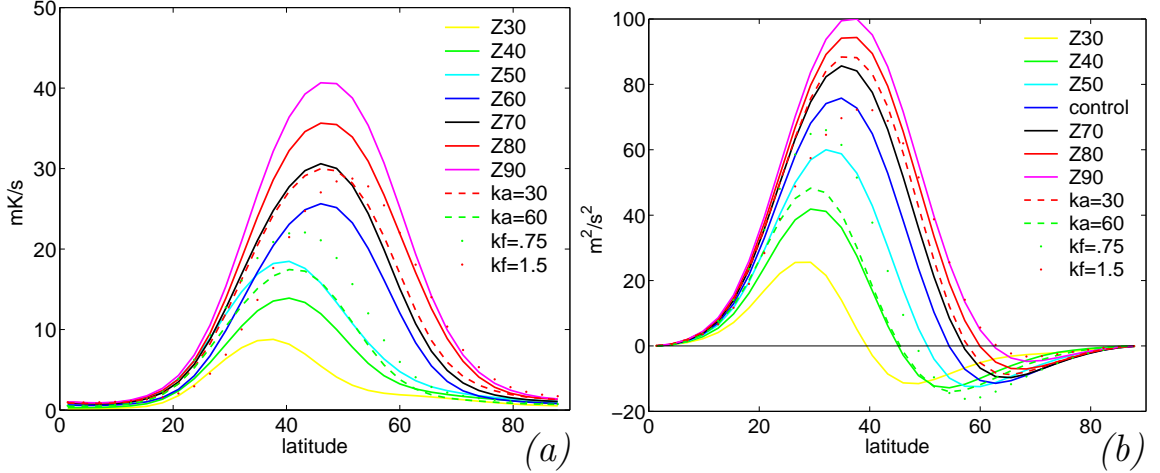


Figure 5.7: (a) The high pass meridional eddy heat fluxes on the  $0.775\sigma$ -surface, and (b) the meridional momentum fluxes at the height of the jet core ( $\sigma = 0.225$ ).

climatological jet. When the peak winds are further poleward, there are two distinct maxima, corresponding to the subtropical and extratropical jets. When the peak winds are shifted further equatorward, there is only one maximum in the baroclinicity.

The fact that the peak baroclinicity remains about the same supports the argument made in Figure 5.6 to justify the fact that variability depends on the product  $k_a \Delta T_{eq}$ , rather than either term independently. Figure 5.8b shows that the situation is a bit more complicated.  $k_a$  leads to large changes in the stability of the atmosphere in the tropics, while  $\Delta T_{eq}$  leads to variation in the stability in the midlatitudes.

There is more consistency between simulations with like intraseasonal variability in the meridional eddy momentum fluxes,  $\langle \bar{u}^* v^* \rangle$  (where an asterisk denotes deviations from the time mean flow), shown in Figure 5.7b. Simulations Z40 and ka=60 are more alike in the momentum fluxes than in the heat fluxes, or total EKE. Given the similarities in the winds, particularly the at the surface, this should not come as a surprise. It does suggest that process that determine the eddy momentum fluxes, which are more associated with eddy decay and wave breaking, are not tied directly to eddy production.

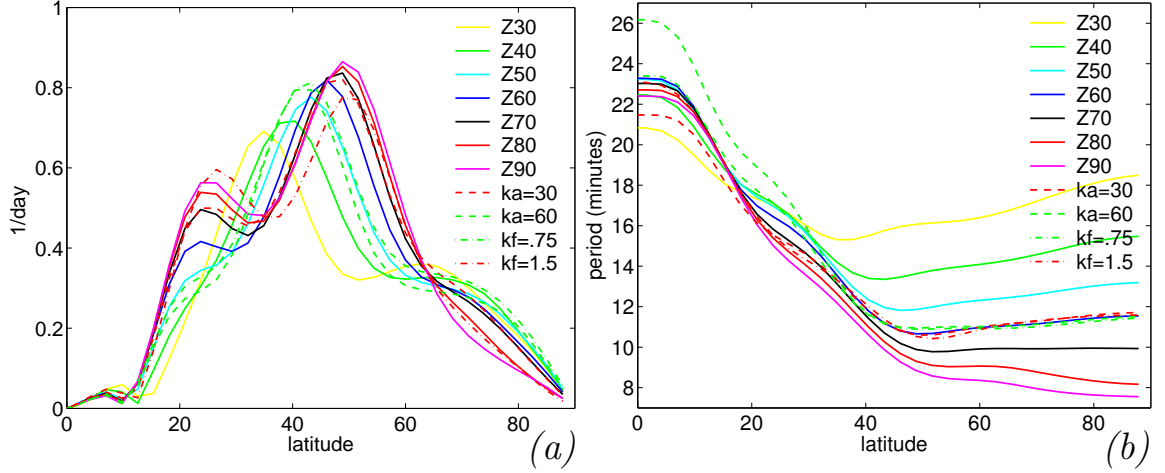


Figure 5.8: (a) The Eady growth rate parameter,  $0.31f |\frac{\partial \mathbf{V}}{\partial z}| N^{-1}$  at 525 hPa, which reflects the baroclinicity of the atmosphere. In both cases, the 525 hPa surface provides a fair measure of the difference between the simulations. (b) The period of the buoyancy oscillation,  $2\pi/N$ , where  $N$  is the Brunt-Väisälä frequency, at 525 hPa. This provides a measure of the stability of the atmosphere.

We probed the relationship between  $\Delta T_{eq}$  and the variability over a wide range. At either end of the spectrum, the trend of decreasing persistence with increasing gradient appears to saturate or break down. When the gradient becomes sufficiently weak, 30K, there does not appear to be sufficient instability to maintain eddy stirring necessary for the annular mode. At the other end, the persistence appears to saturate around 20 days.

In exploring the response of the variability to zonally asymmetric forcing, we have used  $\Delta T_{eq}$ , as it is perhaps the most physical parameter, and can be related to a change in the climate (e.g. a reduction of the ice-albedo effect due to a global warming might reduce temperature gradients). We are fairly confident of the consistency between changes in  $\Delta T_{eq}$  and  $k_a$ . It is possible that different processes are responsible for the response of the variability to changes in  $k_f$ , but the striking similarities between the mean states of the simulations suggest that all parameters might be related.

## 5.6 Zonal Asymmetries and Timescales of Variability

As noted in Section 4.4.2, the addition of zonal asymmetries in the model forcing dramatically reduces the persistence of the annular mode. We also find a marked decrease in the sensitivity of the variability to changes in the equilibrium temperature gradient. Figure 5.9 illustrates the e-folding timescale of the annular mode in response to zonal asymmetries as a function of the equilibrium temperature gradient. Zonally symmetric simulations Z40, Z60, and Z80 are included to show the contrast in both the timescales and the trends. To highlight the differences, we note that when the equilibrium temperature gradient is varied from 40 to 80 K in the zonally symmetric model, the e-folding timescale of the annular mode decreases over four fold, from 93 to 21 days. When the gradient is varied to the same extent in simulation LSC+RM1 (where we have introduced both topography and a diabatic heating anomaly to model land-sea contrast), the e-folding timescales are substantially shorter and nearly independent of the equilibrium temperature gradient, varying from 10-13 days.

We showed in Table 4.4 that the annular mode captures the same variability as found in the zonal index and other measures of the low frequency variability. Hence the timescales of the variability shown here are a fair indication of the overall low frequency variability of the model, and not sensitive to this particular analysis technique.

As the introduction of zonal asymmetries modifies the baroclinicity of the flow, the changes in the persistence could be explained by the same processes that controls the persistence in the zonally uniform forcing case. It is possible, for example, that the maximum baroclinicity is most important for setting the timescale of variability, so that zonal asymmetries. [Pierrehumbert (1984) noted that the linear characteristics of

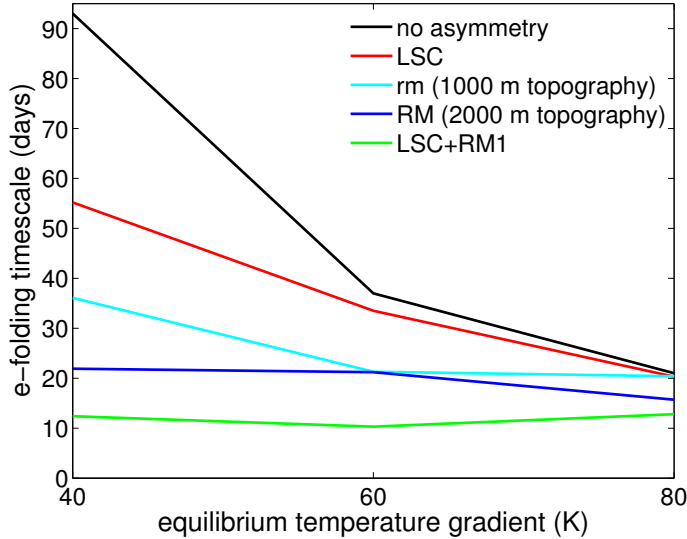


Figure 5.9: Influence of zonally asymmetric forcing and the equilibrium temperature gradient on the e-folding timescale of the annular mode. The e-folding timescale of the annular mode in simulation LSC+RM2-60 (which is not shown in the figure) is 13 days, comparable to the timescales in the LSC+RM1 simulations.

baroclinic instability depended on the local properties of the flow.] This explanation, however, is only really plausible for the changes observed in the simulations with diabatic heating anomalies alone. In simulations with topography – even relatively small topography, just a 1000 m high ridge – the relationship between the thermal forcing of the flow and the persistence of the annular mode is all but destroyed. Further, we found that the timescale of the annular mode saturated at approximately 20 days when the equilibrium temperature gradient was varied, rendering it difficult to explain timescales of approximately 10 days.

Feldstein (2000a) and (2000b) determined the timescales of the zonal index, NAM, and NAO of the atmosphere to be 18, 10.6, and 9.5 days, respectively. Insofar as our model captures reality, these results suggest that topography plays a critical role in setting these timescales.

In seeking a robust characterization of the model response to low frequency variability, we have produced a rather long list of features that seem to influence the

timescale of intraseasonal variability. For convenience, we summarize the most important here.

- Changes in parameters that tend to shift the climatological jet equatorward appear to increase its persistence. Absent zonal asymmetries, the timescales can become markedly longer than any natural timescale in the model, suggesting the presence of a dynamic feedback.
- Modulation of different parameters suggest that the timescales of interannual variability are not so sensitive to the total eddy kinetic energy or heat fluxes associated with increased eddy growth.
- The timescales do appear to be more sensitive to changes in eddy momentum fluxes, and so the processes regulating eddy decay and wave breaking.
- Zonal asymmetries in the flow, topography in particular, appear to dramatically limit the timescales of variability, and its sensitivity to other parameters.

Given these constraints, we now turn our attention to understanding the processes that control the variability.

## 5.7 Enhanced Persistence: Potential for Interaction Between the Large-scale Flow and Eddies

The timescale of the annular mode in the barotropic model in Chapter 2 was found to be in between those set by the eddy stirring (2 days) and damping ( $r^{-1} = 6$  to 23 days). As the eddy forcing is white at timescales longer than 2 days by construction, the frictional timescale provided an upper bound on the persistence. This is to say, if the timescales of the eddy vorticity flux in (2.2.5) were white like eddy forcing, one would expect the persistence of the zonal flow to be set by the damping  $r^{-1}$ .

The timescale was less than this in practice, largely due to the fact that system is nonlinear. Transfer of energy from one EOF to another (which can be viewed as simply as the advection of an eddy that initially projects on one EOF to another EOF, and so forth) occurs on timescales set by the eddies. It may be a difficult question to determine the timescale of the annular mode in this model analytically – as it is determined by the balance between the chaotic nature of the eddy forcing and the organization of the eddy momentum fluxes by linear wave propagation – but one does not need to call upon additional dynamics to understand the system.

With the dynamical core, a similar analysis is complicated by the fact that there is not such a clear damping timescale. We have shown that the persistence of the annular mode is not easily attributed to the prescribed timescales of the dynamical core,  $k_a^{-1}$  and  $k_f^{-1}$ . For  $k_f$ , the trend is in the opposite direction as one might expect: increasing the damping increases the persistence. With respect to  $k_a$ , we have found that the timescale is better determined by the product  $k_a \Delta T_{eq}$ , so that an increase/decrease of  $k_a$  can be balanced by an appropriate change to the equilibrium temperature gradient and have no effect on the intraseasonal variability.

In Figure 5.10, we show that the timescales of intraseasonal variability are not easily related to the internal eddy turnover timescale as well. The eddy turnover timescale,  $L = K^{1/2}/L$  depends on the kinetic energy  $K$  and the eddy length scale  $L$ . There is little change in the eddy length scale in all simulations, so variation of the eddy timescale is determined primarily by  $K$ . In simulations with varied equilibrium temperature gradient, we found  $K$  to be linearly related to gradient,  $K \propto \Delta T_{eq}$ , so that the eddy turnover scale varies as the square root of the gradient. As the timescale of the interannual variability is far more sensitive, we suspect that there must be a more fundamental change in the dynamics. Furthermore, there was not a substantial change in the kinetic energy in the simulations in which  $k_a$  and  $k_f$  were varied.

Hence timescale of the annular mode appears to be largely independent of the

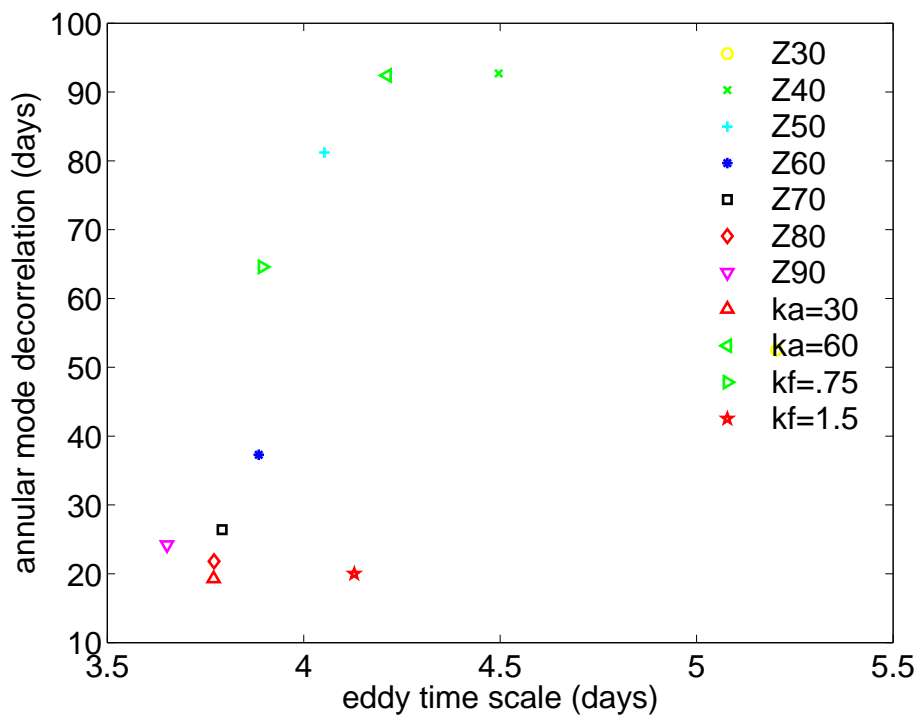


Figure 5.10: Here we plot the decorrelation time scale of the annular mode index with the eddy time scale,  $L/U$ .

natural timescales of the model, suggesting that there may be a need for additional dynamics to account for the persistence of the annular mode, particularly in simulations where it persists longer than any of the damping timescales. The barotropic model lacked a mechanism for coupling the stirring of the flow (that is, the generation of baroclinic instability) to the state of the flow. Does such coupling occur in the dynamical core, particularly in simulations where the annular mode becomes very persistent?

To address this question, we turn to analysis of the Eliassen-Palm (E-P) fluxes to interpret the interaction between the eddies and the zonally averaged flow. Briefly, the E-P flux vector  $\mathbf{F}$ , is given by

$$\begin{aligned}\mathbf{F} &= \{F_{(y)}, F_{(p)}\} \\ &= \{-\overline{u'v'}, \frac{f}{\partial\bar{\theta}/\partial p}\overline{v'\theta'}\}\end{aligned}\quad (5.7.1)$$

where a prime denotes an anomaly from the zonal mean. As shown by Edmon et al. (1980), the E-P vectors point in the direction of the group velocity of wave propagating in the latitude-height plane, so characterizing the propagation of wave activity. Furthermore, their divergence captures the total impact of the eddy forcing on the mean flow.

$$\frac{\partial\bar{u}}{\partial t} - f\bar{v}^* - \bar{\mathcal{F}} = \nabla \cdot \mathbf{F} \quad (5.7.2)$$

where  $\mathcal{F}$  is the Eulerian mean friction and the “residual mean meridional velocity” is

$$[v^*] = \bar{v} - \frac{\partial}{\partial p} \left( \frac{\overline{v'\theta'}}{\partial\bar{\theta}/\partial p} \right) \quad (5.7.3)$$

As seen in (5.7.1), the first component captures the effect of meridional eddy momentum flux on the flow. The second captures the effect of meridional heat fluxes on the momentum budget, as eddy induced changes to temperature structure impact

the flow via thermal wind balance. We will refer to them as the momentum and heat components of the E-P fluxes, respectively.

As noted above, the annular mode is essentially capturing the variability of the zonal mean flow, even in simulations with a well defined storm track and localized EOF patterns. In these cases, the variability of the zonal mean flow is dominated by variability in the storm track, so that E-P flux analysis is naturally focused on these important regions. As the time series of the models zonal index (first EOF of the zonally average flow) is the same as the time series of the annular mode (the first EOF of the horizontal flow), we use the two interchangeably for the remainder of the section.

The use of a Rayleigh drag in the model to remove momentum from the flow near the surface, as opposed to a more complicated boundary layer scheme, allows for a simplified interpretation of the E-P fluxes. Momentum damping in the model extends to the  $0.7\sigma$ -surface. Below this level, the E-P flux divergence is dominated by the thermal component. Eddy heat fluxes are strongest in these lower layers. They contribute to the momentum budget by reducing the vertical shear, extracting momentum from the flow at height to balance the frictional torque. Momentum fluxes, associated with meridional propagation of Rossby wave activity, are minimal here, given the slow speeds of the flow. Above the  $0.7\sigma$ -level the vertical divergence of the E-P heat flux component is generally negative, implying the loss of momentum. The large zonal flow in the free troposphere, particularly in the jet core, permit significant meridional propagation of Rossby waves, and momentum fluxes become non-zero.

We simplify our analysis by splitting the flow into two regions at  $\sigma = 0.7$ , averaging each slice in the vertical. This allows one to analyze the dynamical core as if it were a two layer model. Both the baroclinic and barotropic effects of the eddy heat and momentum fluxes on the mean flow are captured, but the vertical dimension is reduced

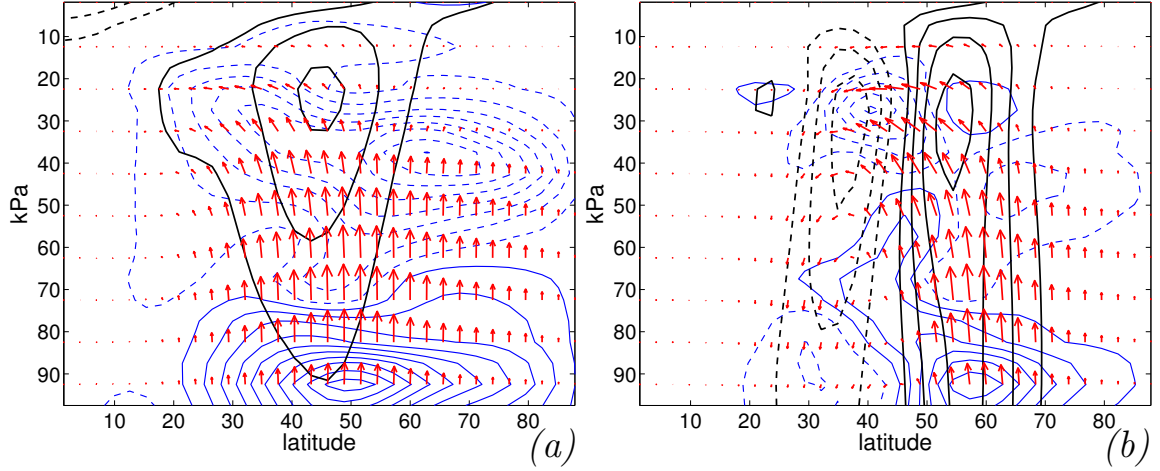


Figure 5.11: E-P flux vectors (arrows) and divergence (blue contours) in simulation Z60, the control. In (a) the time average is depicted and (b) the fluxes are regressed against the annular mode time series, offset so that the fluxes lead the annular mode by 4 days. The divergence contour interval is  $2 \text{ ms}^{-1}\text{day}^{-1}$  (-1,1,2) in (a) and  $0.5 \text{ ms}^{-1}\text{day}^{-1}$  (-0.25,0.25,0.75) in (b). The units of the fluxes correspond to an acceleration of the zonal winds at that particular latitude. (The E-P flux divergence in Edmon et al. (1980) was shown in units of net forcing of the latitude-pressure tube around the latitude circle.) The black contours illustrate the zonal average zonal wind. In (a), they show the time mean jet with a contour interval of  $10 \text{ ms}^{-1}$ , and in (b), they show the anomaly associated with the annular mode at zero lag. In both cases, the zero contour is omitted.

to make lag-latitude covariance analysis tractable.

The time average E-P fluxes and divergence, and the fluxes and divergence associated with the build up of the annular mode, are shown in Figure 5.11. The two layer decomposition is quite natural for the average state. There is some vertical structure not captured by this simple two layer reduction in the case of the annular mode. The overlap of the E-P forcing with the pattern of the mode does confirm that the intraseasonal variability is driven by eddy fluxes.

We focus on simulations Z40 and Z80 in particular because they characterize two extremes of intraseasonal variability; the annular mode of Z40 is over four times more persistent than that in Z80. Figure 5.12 illustrates the forcing of the upper level flow by the momentum and heat fluxes for simulation Z40, a case of extended persistence.

The source of the wave energy, baroclinic stirring, is revealed by the divergence of the E-P heat flux component in the lower levels shown in panel (a). The positive anomaly at higher latitudes (peaking at  $50^\circ$  N) implies the divergence of wave activity produced by anomalous baroclinic instability. The flux divergence of the heat component is opposite in the upper layers by construction; the heat fluxes extract momentum at height and bring it to the surface. The negative anomaly in the heat flux divergence centered at  $30^\circ$  implies a weakening of the baroclinic stirring here, and hence a weakening of the eddy's action to reduce the shear. The pattern of the zonal index is shown on the right side of the panel for reference. The heat fluxes act to balance the frictional dissipation of the zonal index at the surface, thus sustaining the anomaly. In reducing the shear, however, heat fluxes oppose the anomaly at height.

The momentum flux divergence in upper levels acts to balance the negative feedback of the thermal forcing. Meridional propagation of wave activity towards the equator converges momentum at  $50^\circ$ , to balance the downward transport of momentum by the thermal eddy fluxes, extracting it from low latitudes. By themselves, the momentum fluxes reorganize momentum in the upper levels only, since the flux divergence in lower layers is almost negligible. Only when the thermal and momentum forcing of the eddies are taken together does one see the barotropic impact of the eddy forcing.

If we lump the forcing of the flow by the TEM meridional circulation in with other forms of dissipation, and approximate them, to first order, as a linear drag, (5.7.2) becomes

$$\frac{\partial \bar{u}}{\partial t} = \nabla \cdot \mathbf{F} - \frac{\bar{u}}{\tau} \quad (5.7.4)$$

For timescales shorter than  $\tau$ , the dominant balance in the equation is between the first two terms – an inertial balance – and we expect an out of phase relationship between the zonal wind anomaly  $\bar{u}^*$  and anomalies of  $\nabla \mathbf{F}$ . For timescales longer than  $\tau$ , the dominant balance is between the latter two terms – a frictional balance

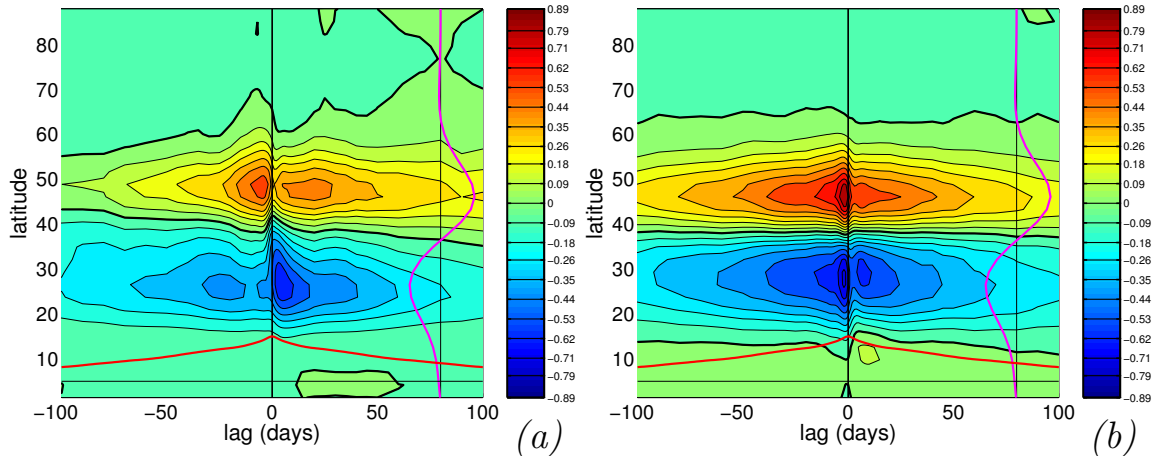


Figure 5.12: The lag covariance between the annular mode and the E-P fluxes. Mean (a) lower level ( $0.7 < \sigma < 1$ ) thermal forcing:  $\partial_p(f\bar{v}'\theta')/\bar{\theta}_p$  and (b) upper level ( $0 < \sigma < 0.7$ ) momentum forcing:  $\partial_y(-\bar{u}'v')$ . The E-P fluxes lead the annular mode index on the left and follow it on the right. The units are in  $\text{ms}^{-1}\text{day}^{-1}$ , but the fluxes have been multiplied by  $\cos^2(\theta)$  so they reflect a torque on the flow around the latitude circle. The values are normalized to reflect the average acceleration of the upper level flow at  $45^\circ$  N. The magenta line at the right shows the spatial pattern of the NAM as regressed on the zonal average zonal winds. The red curve at the bottom shows the autocorrelation function of the annular mode time series.

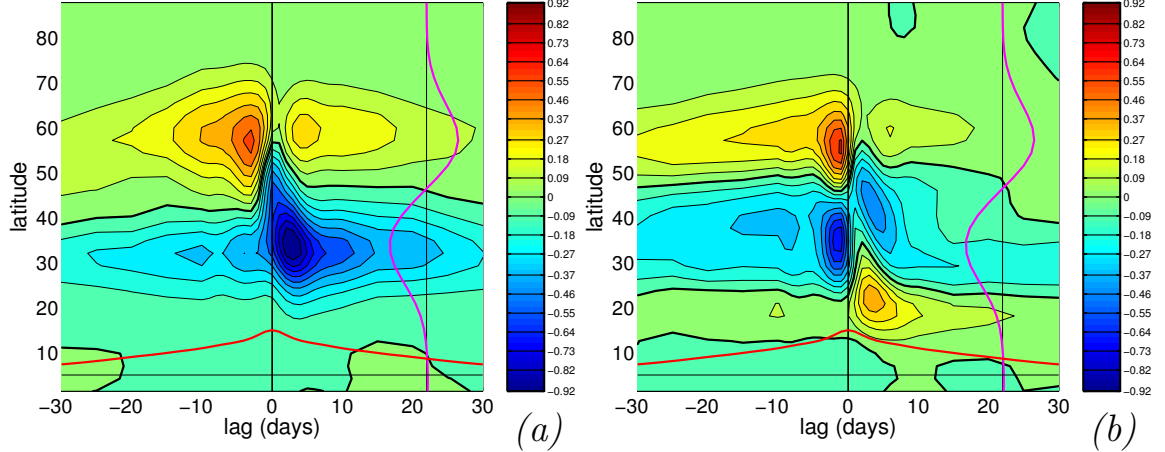


Figure 5.13: The same as Figure 5.12, but for simulation Z80.

– and we expect an in-phase relationship between the wind anomaly  $\bar{u}^*$  and the anomalous eddy forcing.

At short lags, say, within 5-10 days, we observe an out of phase relationship between the eddy forcing and the NAM, whose autocorrelation function is shown by the red curve along the bottom of the figure. There is an increase in heat flux divergence at high latitudes preceding the NAM, suggesting a burst of baroclinic stirring, that is associated with the meridional propagation of eddy energy at upper levels, transporting momentum poleward. Here the E-P fluxes are driving a shift in the pattern.

However, at longer lags, the E-P forcing is practically in phase with the zonal wind anomaly. Clearly the persistence of the annular mode in this simulation cannot be explained by abnormally weak damping (small  $\tau$ ). Rather, something is giving the eddies enhanced power at lower frequencies.

We contrast the eddy forcing associated with the annular mode in Z40 with the eddy forcing in Z80 and LSC+RM1-60, shown in Figures 5.13 and 5.14. First note the change in the time axis, which stretches from lead -30 to lag 30, instead of -100 to 100. The entire picture has also been translated poleward, consistent with the poleward

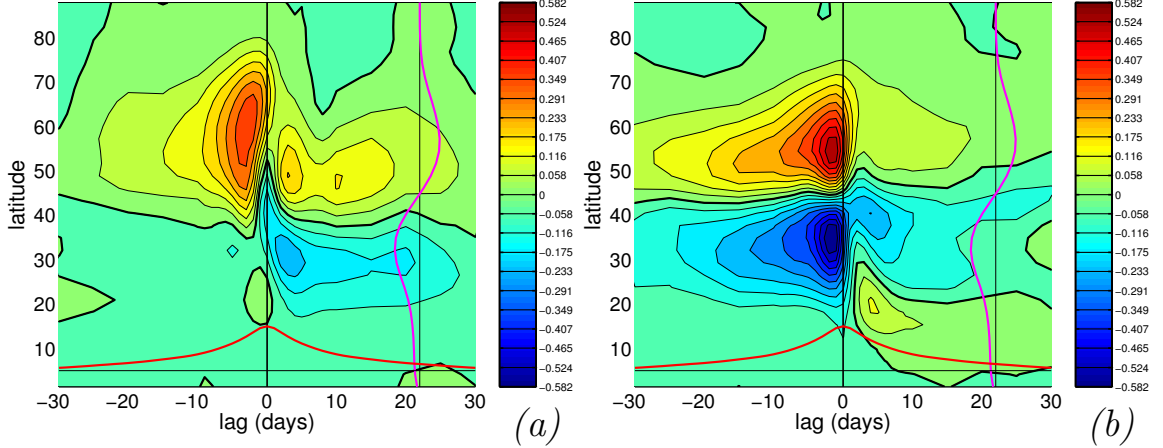


Figure 5.14: The same as Figure 5.12, but for simulation LSC+RM1-60.

shift of the mean jet relative to the jet in Z40. There is still the weak suggestion of an in-phase component of the E-P fluxes for simulation Z80, but in LSC+RM1-60, the E-P forcing almost exclusively precedes the annular mode. The key difference between these simulations and Z40 is not a dramatic drop in the frictional timescale (which would be reflected in a change in the out-of-phase component of the E-P fluxes), but a drop in the energy of the annular mode and E-P flux divergence at lower frequencies.

As explained in Section 5.2, LH used cross spectrum analysis to estimate  $\tau$ , the timescale of the damping associated with the zonal flow. Their model follows from (5.7.4) with the additional assumption that the damping timescale in physical space is the same as the damping scale in EOF space. (As suggested by the barotropic model, in a nonlinear system this may not be the case.) Figure 5.15 is the similar to Figure 5 of their study, but for simulations Z40, Z80, and LSC-RM1-60. The black curve shows the cross correlation between the zonal index time series,  $z(t)$ , with the time series  $m(t)$  obtained by projecting the time and zonal average divergence of the E-P fluxes onto the time and zonal average zonal wind anomaly associated with the zonal index. [We also show the cross-correlation with the time series  $m^f(t)$ , which we define

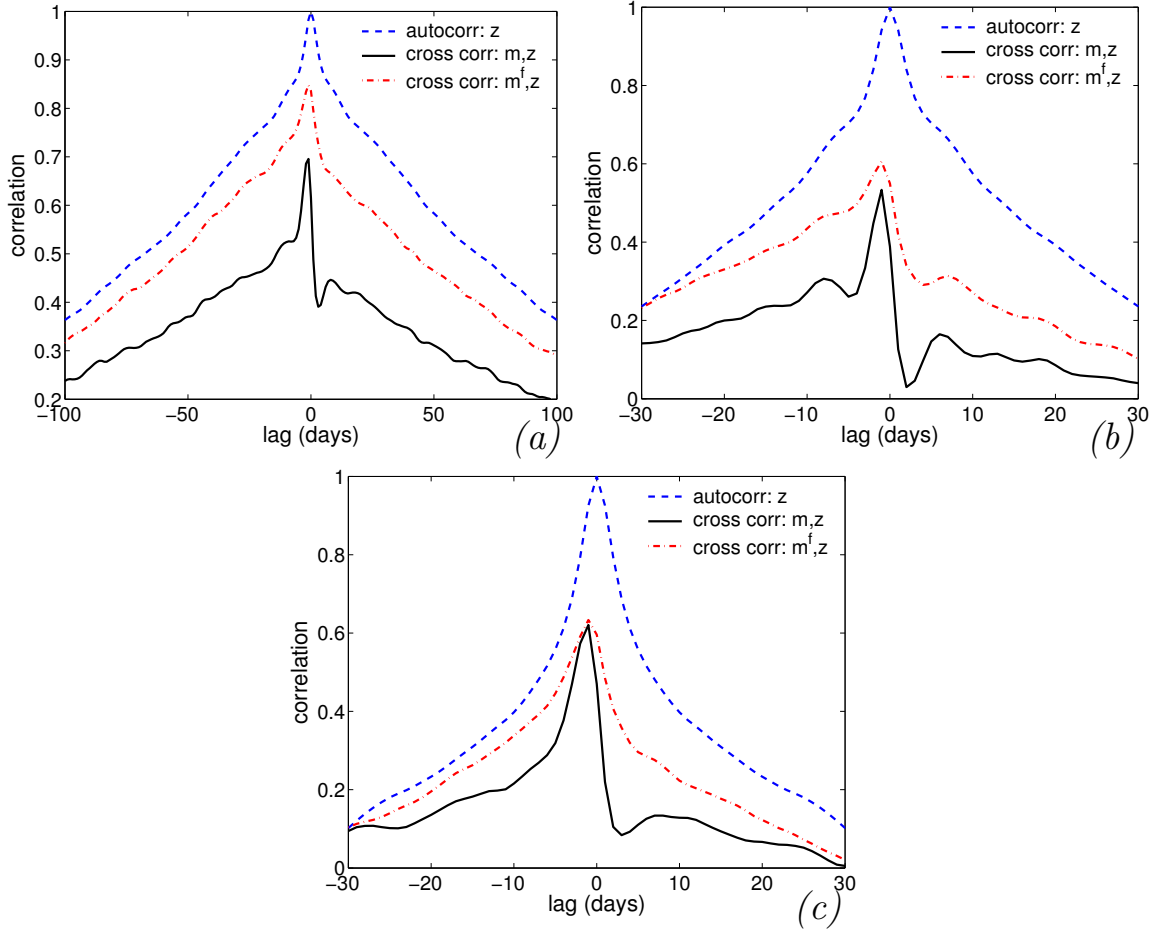


Figure 5.15: Comparison of the cross-correlation of  $m$  and  $m_f$ , with the zonal index,  $z$ , and the autocorrelation of the zonal index. (Similar to LH, Figure 5.) (a) is for simulation Z40, (b) for Z80, and (c) for LSC+RM1-60.

identically to  $m$ , but use only the 10 day hi-pass filtered E-P fluxes. This provides a measure of the correlation between the synoptic forcing and the annular mode.] For reference, we have included the autocorrelation function of the zonal index,  $z(t)$ , which provides an envelope for the eddy correlations. In all cases we observe positive eddy forcing at large positive lags, where the eddy forcing lags the annular mode. This confirms that the eddy forcing cannot be white over all low frequencies. No matter how weak the damping  $\tau$ , we would not find positive eddy forcing at positive lags unless the eddies were organized on timescales longer than  $\tau$ .

LH and Lorenz and Hartmann (2003) found the damping timescale of the zonal

index to be 8.9 and 7.2 days in the Southern and Northern Hemispheres, respectively. The estimated damping times for the dynamical core are pretty consistent with these timescales. For the zonally symmetric simulations discussed in Section 5.5, the timescale varied from 5.2 to 9.1 days. The timescale is quite insensitive to changes in the temperature gradient, varying between 7.4 and 8.8, with no discernible trend. There appeared to be more variation when the damping timescales were altered. When the timescale of the thermal forcing,  $k_a^{-1}$  was doubled from 30 to 60 days, the damping time scale of the zonal index increased from 7.3 to 9.1. As this change is not much larger than changes seen between the different temperature gradient simulations, we cannot be very certain that it is significant. With the surface friction, there appeared to be a bigger shift; when the damping time  $k_f^{-1}$  was doubled from 2/3 days to 4/3 days, the damping timescale of the annular mode increased from 5.2 to 8.9 days. For  $k_a$ , the increase in  $\tau$  with increased thermal damping is consistent with the trend in the annular mode persistence, but for  $k_f$  the trend is the opposite direction. With greater surface friction, the zonal index (annular mode) is damped more strenuously, but persists longer!

The timescale of the zonal index damping estimated from the zonally asymmetric simulations in Section 5.6 do not vary considerably, either. Excepting the simulations with both land sea contrast and topography, the estimated damping timescale varies between 6.6 and 8.6 days, with no trends associated with changes in the equilibrium temperature gradient. The simulations with topographic and thermal forcing appeared to be damped more heavily, with timescales between 5.8 and 6.5 days. Cross-spectrum analysis of these simulations, however, suggested a breakdown in the simple model, perhaps due to nonlinear interactions between the first EOF with higher order EOFs.

If the eddy forcing were random, i.e. white in time on timescales greater than those of baroclinic instability, the zonal index would decorrelate on the timescale computed

from the cross-spectrum analysis. As the damping timescale on the zonal flow does not vary outside of 5-10 days, while the timescale of the intraseasonal variability varies from 10-100 days, we must conclude that something is organizing the eddies.

## 5.8 A Mechanism for Enhanced Persistence

LH concluded that the additional power of the eddy forcing of the zonal index came from a positive feedback between the dipolar zonal flow anomaly and the eddy forcing based on changes to the index of refraction. We present a different view of their feedback argument (one that has also been discussed in various forms by other authors as well, as discussed in Section 5.2). We begin with a heuristic explanation, and then attempt to show how the mechanism relates to what is observed in the model.

As we assumed with the barotropic model, we assert that movements of the mean jet (for example, a transition from a negative zonal index state to a positive zonal index state) are driven by stochastic variations of the eddy momentum and heat fluxes. This follows from the fact that the baroclinic zone is wider than the jet, and the chaotic nature of synoptic variability. We argue, however, that interactions between the eddies and the mean flow tend to retard the movement of the jet. In other words, there is a negative feedback between the eddies and mean flow that makes the jet “sticky,” tending not to move as freely as it might in the absence of the influence of the jet on the eddies.

Our mechanism is similar to the positive feedback articulated by Robinson (2000), as a positive reinforcement of the current position of the jet has the same effect on the persistence of the zonal index as a negative feedback on the movement of the jet. Coupling the argument in terms of a negative feedback, however, allows us to avoid an argument that the eddy driven circulation increases the baroclinicity of the flow. The eddies are always acting to break down the vertical shear; the key is that they

are more effective in reducing the shear on the flanks of the jet than in the jet core.

We illustrate our understanding of the interaction between the mean flow and the eddies in Figure 5.16. We suppose the eddy growth is determined primarily by the lower level baroclinicity. In the absences of a strong barotropic shear (and a barotropic governor influence), growth is likely to occur in a neighborhood about the peak baroclinicity. We contrast two events, one where an eddy forms in the jet core, and a second where an eddy forms on one of the flanks. For now we ignore geometric effects and assume symmetry about the jet core.

First focus on the upper panels, (a) through (c), where we illustrate the influence on the mean flow by an eddy generated in the jet core. Panel (a) shows the effect of the eddy heat fluxes associated with a growing eddy on the mean flow. Down gradient meridional heat fluxes are associated with the vertical propagation of wave activity (the green lines), which act to reduce the shear by drawing momentum from the upper level flow to the lower level flow. Before the wave activity is damped in the upper layers, however, meridional propagation is possible, as shown in panel (b). Linear theory suggest that irreversible mixing (the damping of wave activity) in upper levels occurs at critical layers where the phase speed of the waves  $c$  equals that of the mean flow  $\bar{u}$ . Particle displacements,  $\eta$ , scale as  $\psi/(\bar{u} - c)$  (where  $\psi$  is the streamfunction perturbation), so that displacements will grow unbounded even for infinitesimal perturbations, leading to nonlinearity. Randel and Held (1991) show that nonlinear effects become relevant before waves reach critical layers, so that most of the dissipation is associated with the wave breaking 10-20 degrees before waves reach the critical layer.

The zonal average flow  $\bar{u}$  is augmented in the jet core by eddy induced barotropic circulation, allowing Rossby waves to propagate away from the latitude they were generated and damp on the flanks of the jet, where  $\bar{u}$  is weaker. This produces divergence of wave activity in the jet core and convergence on the flanks, leading to

the upgradient transfer of momentum into the jet core at upper levels. As shown in (c), the net effect of the eddy is still a weakening of the upper flow above the eddy, but the weakening has been spread out to the flanks. As the lower level momentum fluxes are balanced by friction, preventing the surface winds from becoming too large, the change in the baroclinicity is determined primarily by the changes in the upper level flow, not at the surface. Thus while the eddy reduces the shear at the jet core, it also reduces it on the flanks, and there is not a pronounced tendency for the next eddy to occur outside of the jet core as opposed to in it.

Now contrast this picture with what happens when an eddy grows on either flank of the jet, as illustrated in Figure 5.16d. The first step is the same; eddy heat fluxes are associated with vertical E-P fluxes. But the weaker zonal velocity  $\bar{u}$  at upper levels limits meridional propagation. Thus, the tendency of the heat fluxes to reduce the shear is not balanced by a convergence of momentum. There is then a substantial change in the shear (i.e. the baroclinicity) in the location of the eddy, making it less favorable for a second eddy to form at this latitude. Such a negative feedback then limits the ability of the jet to move, in effect reinforcing current position of the jet.

The key is that the barotropic circulation induced by the eddies tends to stick where it is. Meridional momentum fluxes at upper levels are made possible by the large zonal winds, and mollify the tendency of the heat fluxes to break down the gradient at the jet core. The mechanism suggests that the persistence of purely barotropic anomalies can be enhanced, even though they do not shape the baroclinicity at all in themselves. The eddy mean flow interaction rests on the fact that the barotropic circulation spreads out the tendency of the eddies in the jet core to reduce the shear. Hence the barotropic anomaly increases the baroclinicity of the flow *relative* to the flow on its flanks.

In this sense that the mechanism enables the barotropic circulation to organize the stirring. It is not because the eddy driven circulation increases the baroclinicity.

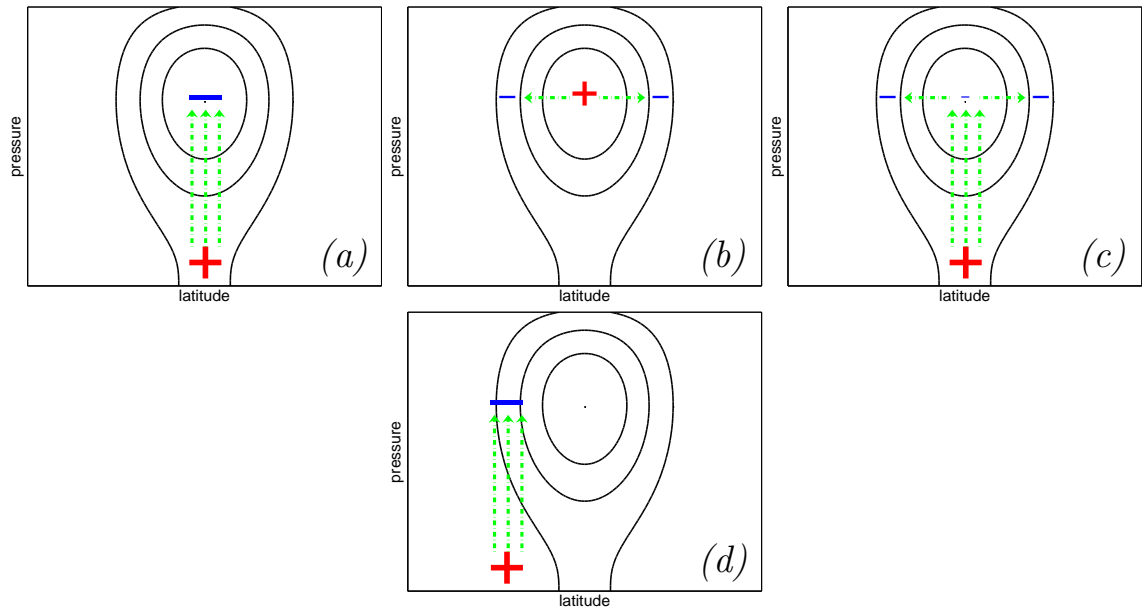


Figure 5.16: A cartoon illustration of the eddy mean flow feedback that extends the persistence of the zonal index and annular mode. Black contours mark the position of the zonal mean winds. Dashed green arrows denote the propagation of wave activity, or, equivalently, the direction of E-P fluxes. Plus and minus signs indicate divergence and convergence of the E-P fluxes, and so a torque on the mean flow.

Rather, the barotropic circulation prevents the eddy fluxes from efficiently breaking down the existing baroclinicity of the flow in the jet core, thus sustaining temperature gradients for future eddies. As the eddies can more effectively break down the shear on the flanks of the jet, which is not so shielded, baroclinic instability will be less likely to occur at the flanks on average.

Although we have expressed the mechanism as a negative feedback, this does not mean it is necessarily weak. It becomes more powerful as the eddy momentum fluxes aloft become more efficient. In the limit that all of the eddy activity generated at the surface propagates away at upper levels, eddy activity ceases to reduce the shear in the jet core, and the jet can become very stable away from its mean location. The mean thermal forcing tends to increase the baroclinicity everywhere in the midlatitudes, so some reduction of the shear by the eddies is required to maintain constant baroclinicity of the flow.

### Evidence for the Mechanism

To show evidence of a feedback loop, we need to demonstrate the interaction between the eddies and large-scale flow in both directions. Thus we must show (1) that eddies drive shifts in the barotropic circulation, and (2) that the barotropic circulation in turn shapes the production of eddies.

The first point is well established, both in the literature discussed in Section 5.2 and from our experiments. It is most readily seen in the barotropic model in Chapter 2, where stochastically driven eddy momentum fluxes create the surface westerlies in the midlatitudes, and variation of the eddy fluxes lead to variations of the jet. It is also evident that eddy momentum fluxes generate the anomalies of the zonal wind in the dynamical core, as seen from the favorable E-P divergence preceding the zonal index in Figures 5.12-5.14.

The second point, that the barotropic circulation influences the baroclinicity of

the flow, which in turn shapes the eddy stirring, is more problematic. It is difficult to establish causality. The jet is itself created by the eddy momentum fluxes; thus changes in the jet will always be associated with shifts in the eddy forcing, both in systems where the jet is shaping the stirring, and in systems without any dynamical feedback. The only evidence is found in the persistence of the eddy forcing. Absent organization of the eddies by the mean flow, one would expect eddy anomalies to damp on the timescale suggested by the LH cross-spectrum analysis, generally about 6-8 days for the dynamical core.

The linear theory suggesting that the spread of wave activity in upper levels is shaped by the zonal velocity of the flow is well established in the theory and models Held and Phillips (e.g. 1987) and observations, Randel and Held (e.g. 1991). The relationship between the baroclinicity and eddy generation is less transparent. As seen in the simulations of in Section 4.3, increases of the baroclinicity in zonally localized regions did not always lead to increases in the local eddy activity. A more careful analysis on the sensitivity eddy fluxes to changes in the baroclinicity is needed to establish this part of the feedback. For now, we turn our attention to better understanding the influence of topography and model parameters on this potential feedback.

## 5.9 On the Structure of the Annular Mode

We demonstrated in Section 3.3 that it is possible to have an annular mode in a system without zonally coherent motions – that is, a system where the correlation between the flow at two points vanishes as the distance between them in longitude increases. In such a system the annular mode is best thought of as a statistical feature, an indication that the statistics of the flow are zonally symmetric, and not as an indication of a mode with zonally uniform dynamics. In analysis of the flow

of the barotropic model in Section 2.4.3 we found the annular mode was more of the statistical nature. While EOFs reveal a uniform oscillation of the jet, comparison of the winds averaged over separate quadrants suggested that the zonal flow was not well correlated around the latitude circle. The mechanism for coupling the eddy forcing to the large scale anomalies associated with the zonal wind in the previous section, however, draw upon wave processes which are fundamentally non-local. Does this require a more physical annular mode, that is to say, how effective could such a mechanism be if the annular mode is more statistical in nature, and there is no coherent movement of the jet.

To address this question, we present a new diagnostic of the annular mode as a function of both *time* and *longitude*. We begin by computing the first EOF of the zonally averaged surface ( $\sigma = .975$ ) winds,  $u_s$ . This EOF can be interpreted as the spatial structure of the zonal index. These patterns, shown in Figure 5.17, exhibit the characteristic dipole. The shift of the pattern in latitude in the various simulations is consistent with the shift of the mean jet; the dipole is always out of phase with the mean flow, as to characterize a “wobble” of the jet.

We then project this dipole pattern onto the flow at all times and longitudes to generate a local dipole index,

$$DI(t, \lambda) = \alpha \int_0^{\pi/2} Z(\theta) u_s^*(t, \theta, \lambda) \cos(\theta) d\theta \quad (5.9.1)$$

where  $Z(\theta)$  is the first EOF of  $\bar{u}_s$ , the cosine term is added to account for the diminishing radius of the sphere with latitude, and the normalization constant  $\alpha$  is chosen so that the zonal average of the dipole index has unit variance. Thus, when the local index is of unit amplitude, the wind anomaly at that longitude is of amplitude comparable to one standard deviation shift of the zonally averaged flow. As seen in Section 4.4, the variability captured by EOFs of the surface winds is comparable

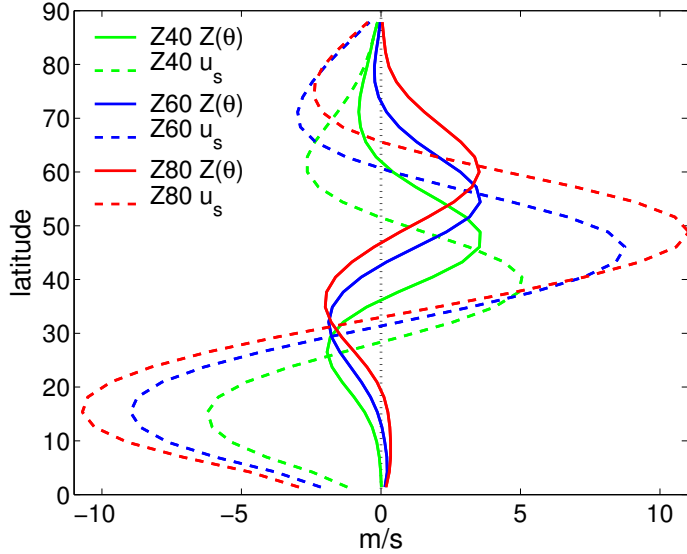


Figure 5.17: The time and zonal average surface winds,  $\langle \bar{u}_s \rangle$ , and the zonal index,  $Z(\theta)$  (the first EOF  $\bar{u}_s$ ), for simulations Z40, Z60, and Z80. The zonal index does not appear to be sensitive to zonally asymmetric forcing, e.g. the zonal index computed for simulation LSC+RM1-60 is quite similar to that of Z60.

to the variability capture by other physical variables (such as the surface pressure or geopotential height at higher levels in the troposphere). Hence this dipole index fairly characterizes the contribution of the local flow to the hemispheric variability as function of time.

Figure 5.18 illustrates the evolution of the local dipole index for simulations Z40 and Z80. Both diagrams are dominated by short lived, eastward propagating features of limited zonal scale, perhaps  $50\text{-}60^\circ$ . Even in this short time slice we observe a pronounced increase in the persistence of the zonally averaged signal in Z40. However, this slowly evolving signal is clearly built of, or perhaps masked by, these short events. Kushner and Lee (2006) found similar eastward propagating features in a related study of the local structure of the annular mode in the atmosphere, suggesting that they are not an artifact of the dynamical core.

We compute the lag-longitude correlation map of the dipole index,  $\rho_{DI,\tilde{\lambda}}(\lambda, t)$ , to better characterize the average variability. The  $\tilde{\lambda}$  denotes the reference longitude of

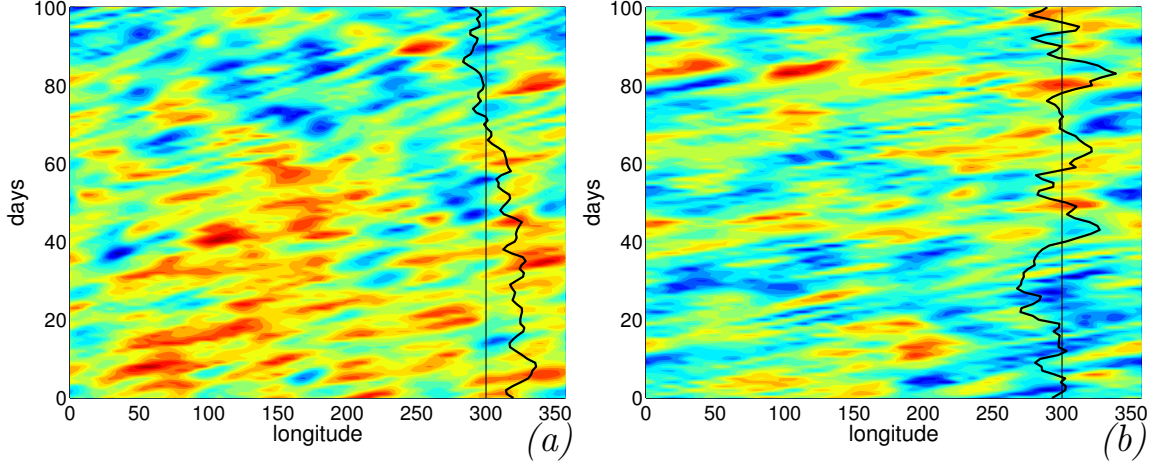


Figure 5.18: Hövmöller diagrams of the dipole index  $DI(t, \lambda)$  for simulations Z40 and Z80. The black line at  $300^\circ$  shows the behavior of the zonal average index as a function of time. This 100 day slice in time was randomly selected from the 9000 day record.

the correlation map. Given the zonal symmetry of these simulations, the lag-longitude correlation can be averaged over all longitudes to improve the statistics, producing one overall correlation map,  $\rho_{DI}(t, \lambda)$ . The maps in Figures 5.20 - 5.22 are based from a reference longitude at  $180^\circ$ , but characterize the flow at all longitudes. In Figure 5.20 we focus on the dominant feature of the lag-longitude correlation map, which captures the scale and slow eastward propagation of the local structures dominating Figure 5.18. The features extend over a range of  $50\text{--}60^\circ$  and persist for 2–4 days in both simulations. They slowly propagate eastward at approximately  $7^\circ$  a day ( $8 \text{ ms}^{-1}$  at the latitude of the jet maximum) in Z40 and  $16^\circ$  a day ( $14 \text{ ms}^{-1}$ ) in Z80.

Such spatial and temporal scales suggest that these features are the projection of a single eddy onto the meridional structure of the dipole index, as depicted in the cartoon in Figure 5.19. Indeed, composites of such features in (Kushner and Lee 2006) had a baroclinic structure in the vertical – suggesting a composite of baroclinic eddies that have projected onto the dipole index. The spatial and temporal scales of these features are consistent with the unfiltered single point correlation maps shown

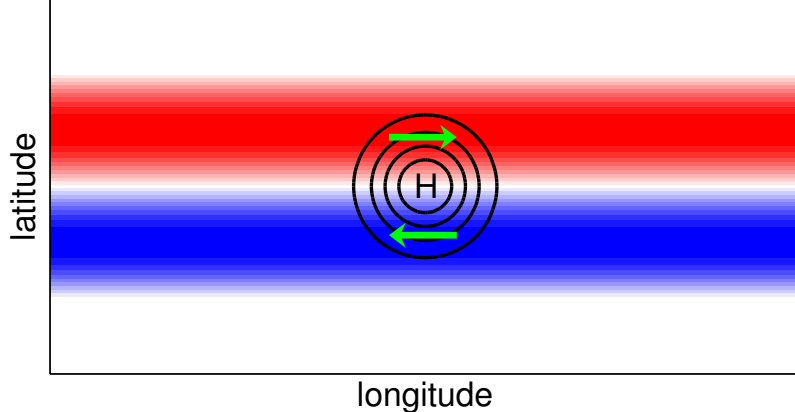


Figure 5.19: A cartoon illustrating the potential for a single eddy to project strongly on the annular mode (or zonal index). The annular mode of the surface zonal wind is illustrated with the red (positive) and blue (negative) bands, and the eddy marked by black contours of pressure. If the annular mode index is dominated by such local projections, the zonal symmetry of the mode is best appreciated a statistical feature, as opposed to a dynamic one.

in barotropic model in Figure 2.9 and the dynamical core in Figure 4.11.

We broaden our view of the lag-lead correlation map in Figure 5.21, but stay focused on synoptic timescales. The correlation color scale has been saturated at 0.4 to reveal a wavetrain structure about the local feature shown in Figure 5.20. The wavetrain further suggests that we are seeing the projection of synoptic eddies onto the zonal index (or annular mode) pattern. The wave packet in Z40 is characterized by wavenumber 6 and propagates at  $23^\circ$  a day. In Z80, the packet is of wavenumber 5, and propagates at  $38^\circ$  a day. (We note that the jet is located further poleward in Z80, so that although the wavenumber of the wave train has decreased, the length scale has not increased significantly.) If we again convert these to velocities, based on the latitude of the jet maximum, the respective group velocities are  $24$  and  $33 \text{ ms}^{-1}$ , respectively, consistent with the jet speeds in the two simulations,  $27$  and  $37 \text{ ms}^{-1}$ .

Thus far we have focused on synoptic features projecting onto the zonal index, which are generally the same in both simulations. It is quite apparent in Figure 5.21, however, that the wavetrain in Z40 is superimposed on a background correlation

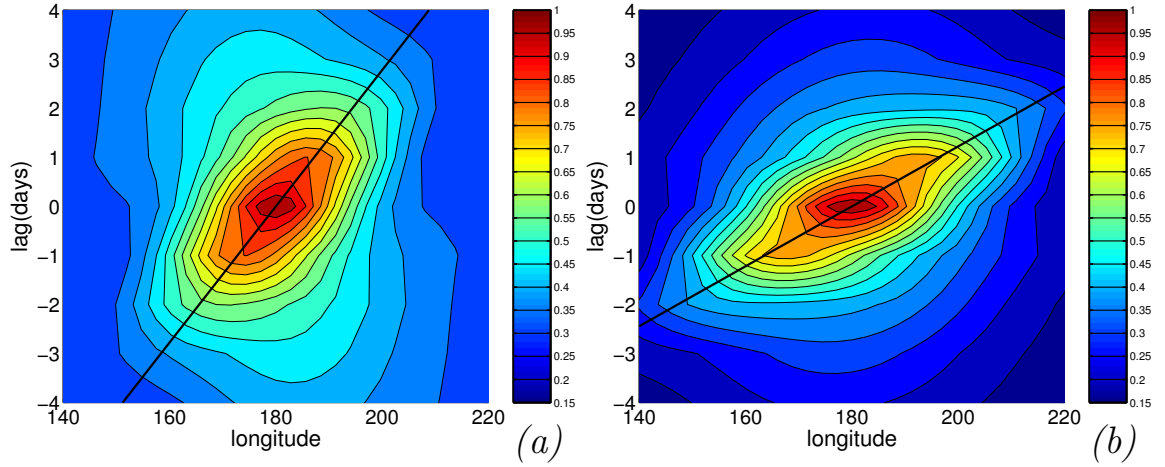


Figure 5.20: The lag-longitude correlation of the dipole index  $DI(t, \lambda)$  of (a) Z40 and (b) Z80. As noted in the text, the figures are represented from a base point at  $180^\circ$ , but have been averaged over all longitudes for improved statistics. The black lines mark an estimate of the local phase velocity,  $7^\circ/\text{day}$  for Z40 and  $16^\circ/\text{day}$  for Z80.

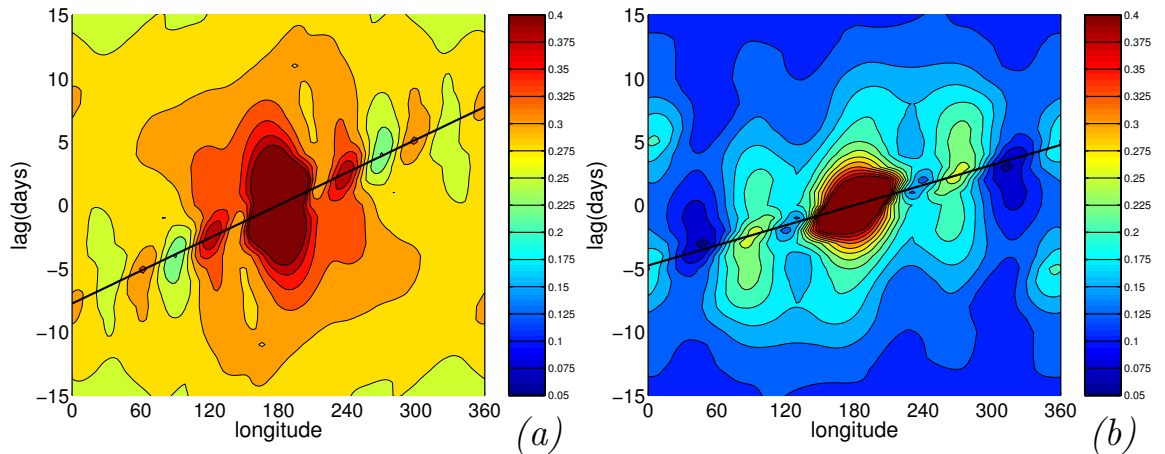


Figure 5.21: The same as Figure 5.20, but the range has been extended around the latitude circle. The color scale has been saturated at 0.4 to focus away from the local feature illustrated in Figure 5.20. The black contours mark a group velocity of  $23^\circ$  and  $38^\circ$  per day, respectively.

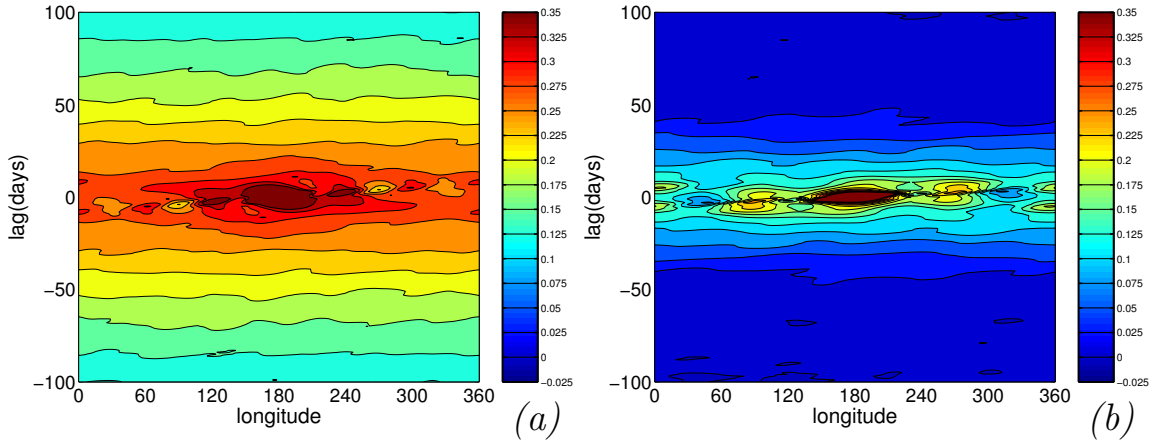


Figure 5.22: Same as Figure 5.20, but with extended ranges and color scale saturation at 0.35 to focus on the zonally uniform correlations at long lag.

much higher than that in Z80. We focus on this background in Figure 5.22. At lags beyond 10 days we begin to see a truly annular signal, where the correlation becomes independent of longitude. This is to say, the projection of the flow onto the dipole index at any given longitude, say,  $180^\circ$ , is equally correlated with the flow at *all* longitudes after 10 days. This suggest a hemispherically coherent signal – a physically annular mode. We can estimate the significance of the hemispheric correlation at zero lag by extrapolation. In Z80, the zonally uniform motion is perhaps 0.15 correlated with the local flow, while in Z40, this signal is over 0.3 correlated with the local flow. This zonally coherent signal represents a truly hemispheric pattern of variability.

This analysis helps explain why it is difficult to see an annular model in practice, as highlighted in Figure 7 of Cash et al. (2002). The zonal zonal index is generally dominated by local features seen in the Hövmöller diagrams in Figure 5.18, especially in simulations when the zonally coherent component of the annular mode is weak and not very persistence, as in simulation Z80. In these simulations, the zonal index signal is dominated by local events, to the point that the annular signal makes little difference to the zonal index except a longer lags. In simulation Z40, rather, there is a significant hemispheric signal that is masked, to some extent, by local events

riding on top the uniform movement of the jet. Synoptic variability will mask the hemispheric signal unless it is filtered in space or time.

We acknowledge that the decomposition into local and global structure is somewhat arbitrary. There is certainly local structure at long lags, but it has been smeared out to the point that the structure of individual eddies is lost. Rather, the key point that we wish to make is that the local structure of both Z40 and Z80 is relatively similar, despite the fact that the phase speed and group velocity of eddies in Z40 are weaker. The main difference between the two simulations is the dramatic difference in the importance of the slowly changing underlying structure. While much of the zonal index in Z80 is due to the projection of individual eddies onto the dipole pattern, there is a strong, long-lived, zonally symmetric signal in Z40 that makes a significant contribution to the annular mode at longer lags. The uniformity of this signal and the long timescales suggest non-local dynamics, and the potential for the interaction between the jet and synoptic forcing described Section 5.8. In Z80, the annular mode is more an expression of zonally uniform dynamics. Lacking a coherent movement of the jet, there is less opportunity for feedback involving wave propagation.

### **The Influence of Zonal Asymmetries on the Annular Mode Structure**

Lorenz and Hartmann (2003) performed analysis similar to LH on the zonal average zonal winds in the Northern Hemisphere. They found that baroclinic eddies were still most important in maintaining the eddy mean-flow feedback, also finding a role for quasi-stationary eddies in sustaining deviations of the mean flow. In our model, there is a significant drop in the persistence of the annular mode when zonal asymmetries are introduced, even a single mountain chain comparable in scale to the Andes. This suggest a fundamental change in the variability, so that even transient baroclinic eddies no longer couple to the large scale flow as they did in the zonally symmetric simulations.

Analysis of the local dipole index for the zonally asymmetric models suggest a substantial difference in the dynamics. Lag-longitude correlation maps of the local dipole index are shown from two base longitudes in Figure 5.23. In panel (a), the base longitude is in the peak baroclinic zone. Even with the color saturation at correlation 0.5, the map is dominated by the local phase behavior, which suggest eastward propagation of  $16^\circ$  per day. Outside the region immediately downstream the base point, the correlation with other longitudes is below 0.05 at all lags. Panel (b) illustrates the lag-correlation outside the storm track. While this point is located in the region of peak intraseasonal variability (as characterized by the first EOF of sea level pressure in Figure 4.8b) the pattern is characteristic of all points outside the baroclinic zone. The local structure suggest slower phase propagation and more extend correlations in time and in space. There is a notable block in the correlation in the baroclinic region between  $80$  and  $120^\circ$ , where the correlation at all lags drops below 0.05. A lull in the correlation is found in this region for other base points, too. We also note that the wavetrain associated with the base point changes between  $120$  and  $270^\circ$ ; in the storm track the wavenumber is higher and propagation is faster, consistent with higher zonal velocities in this region.

Figure 5.24 shows the equivalent lag-correlation structure for simulation RM60, which has the same topography as LSC+RM1-60, but lacks the heating anomaly. As noted in Section 4.3.2, the simulations with topography alone failed to generated a well localized storm track, but do have a pronounced drop in the persistence of the annular mode (and equivalently, the zonal index). We see the same features as in Figure 5.23, but the differences have been moderated. Of note is the same dip in correlation near the topography at  $90^\circ$ . The dip is found in lag-correlation maps from other longitudes as well.

The addition of zonal asymmetries, particularly topography, appears to inhibit the uniform correlation observed at in zonally symmetric simulations. That the to-

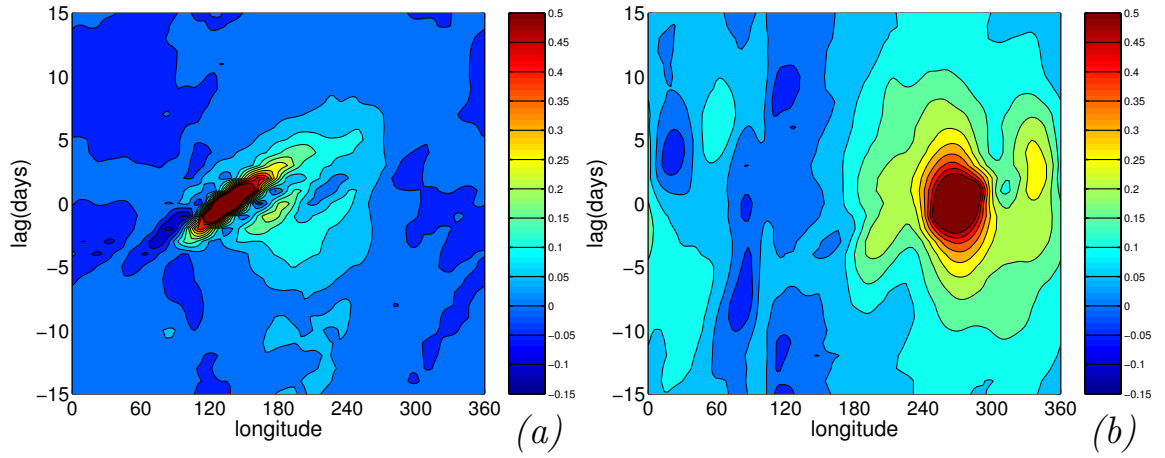


Figure 5.23: Lag-longitude correlation maps from simulation LSC+RM1-60. The color scale has been saturated at 0.5 to highlight the non-local correlations. In (a), the base point is located at  $120^{\circ}$  E, in the storm track. In (b), it at  $270^{\circ}$  E, in exit region of the storm track where the annular mode suggests a maximum in the intraseasonal variability.

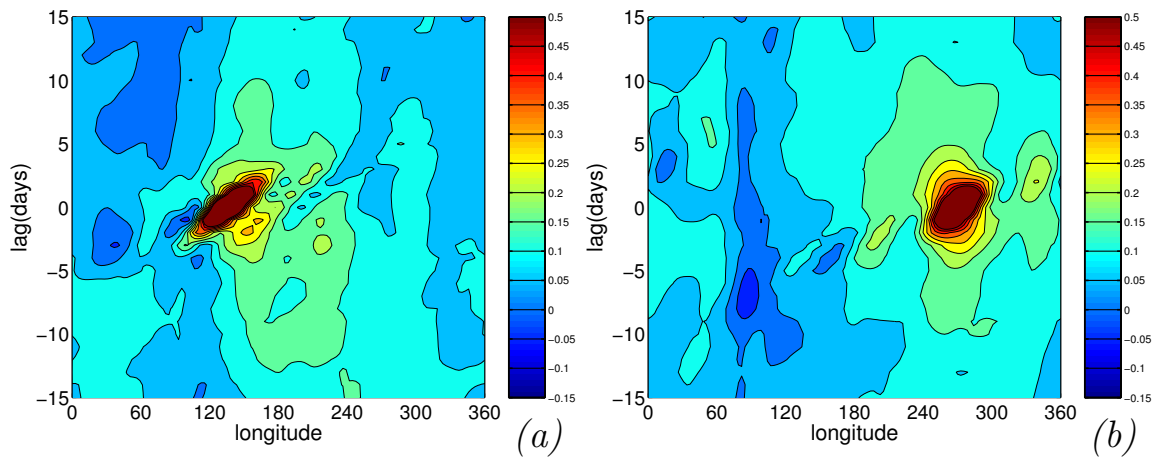


Figure 5.24: The same as in Figure 5.23, but for simulation RM60. The minimum in correlation over the topography at  $90^{\circ}$  E is present in lag-correlation maps from almost all longitudes, not just  $270^{\circ}$ .

pography also appears to shorten the timescales of the annular mode, and reduce (or even eliminate) the sensitivity to the equilibrium gradient, suggest a possible link between the two trends.

## 5.10 A Simple Model of the Feedback

We discussed a feedback of the zonal flow in Section 5.8, but the individual processes that make up the feedback can be localized in longitude, particularly the deposition of momentum by eddies, which involves nonlinear wave breaking. The localized spatial structure is accentuated in simulations with zonally asymmetric forcing. Eddy growth is focused in the baroclinic region at the entrance to the storm track, while eddy momentum fluxes peak at the exit region of the storm track. The interaction depends on both processes: momentum fluxes generate the low frequency anomaly, and the anomaly in turn shapes the stirring by limiting the reduction of shear in the jet core. If these two process do not occur at the same longitude, then the feedback is not direct; a lag in time and in space exist before the lower frequency anomaly can influence on the high frequency stirring.

We develop a model in the spirit of the one constructed in Section 3.3, but for the temporal evolution of the annular mode to account for the spatial separation involved in the large scale anomaly - eddy interactions. In particular, what occurs when there is a barrier in the flow that disrupts hemispherically coherent variability?

We divide the latitude circle into  $n$  sectors, and consider a string of coupled Ornstein-Uhlenbeck processes,  $x_i(t)$ ,  $i = 1, 2, \dots, n$ , that characterize the state of the local dipole index averaged over sector  $i$  as a function of time. We suppose that dipole index in each sector is randomly forced by white noise, meant to characterize the eddy forcing within that sector, damped with timescale  $\tau$ , and coupled to the state of the

dipole index in the sector – and other sectors – through a coupling function  $f$ ,

$$\frac{dx_i(t)}{dt} = \dot{W}_i - \frac{x_i}{\tau} + f(x_i(t)) \quad (5.10.1)$$

Here, the  $W_i$  are independent realizations of the Wiener Process.

To make the model tractable, we select a simple coupling function  $f$ . Following LH, we suppose a feedback linear with respect to the state of the dipole index. But to capture the zonal structure of the feedback, the fact that individual eddies propagate in longitude before depositing momentum into the flow, we separate the influence in longitude,

$$\begin{aligned} \frac{d}{dt}x_1 &= \dot{W}_1 - \frac{x_1}{\tau} + b x_n \\ \frac{d}{dt}x_i &= \dot{W}_i - \frac{x_i}{\tau} + b x_{i-1}, \quad i = 2, \dots, n \end{aligned} \quad (5.10.2)$$

Here, the dipole index at longitude  $i$  is influenced by the state of the index upstream, at  $i - 1$ , with intensity  $b$ . We have thus spread the feedback out in longitude, but have kept it zonally symmetric.

We are interested in the impact of the feedback on the local flow and on the zonal index,  $z = n^{-1} \sum_{i=1}^n x_i$ . Summing (5.10.2) over  $i$ , we find that the separation in longitude makes no difference to the zonally average flow.

$$\begin{aligned} \frac{d}{dt}z &= \frac{1}{n} \sum_{i=1}^n \dot{W}_i - \frac{z}{\tau} + b z \\ &= \frac{1}{\sqrt{n}} \dot{W} - \frac{z}{\tau} + b z \\ &= \frac{1}{\sqrt{n}} \dot{W} - \frac{z}{\tau_2} \end{aligned} \quad (5.10.3)$$

In the first step we apply a property of the Wiener process: the sum of  $n$  independent Wiener Processes behaves as one Wiener process with variance  $n$ . In the second, we

account for the influence of the feedback as a reduction of the effective damping time,  $\tau_2 = (\tau^{-1} - b)^{-1}$ . We conclude that a separation of the feedback in space has no effect on the zonal average flow when the statistics are zonally uniform. Even though the eddies do not feed back on the system at the longitude at which they originated, the aggregation of the localized feedback around the latitude circle gives the system the same effective feedback.

What happens, however, when the zonal symmetry is broken, as in simulations with zonal asymmetries, where a barrier in mechanism is created by the topography? Our model stays the same as (5.10.2), but we break the chain between index  $i=0$  and  $i=n$ ,

$$\frac{d}{dt}x_i = \begin{cases} \dot{W}_i - x_i/\tau & i = 1 \\ \dot{W}_i - x_i/\tau + b x_{i-1} & i = 2, 3, \dots, n \end{cases} \quad (5.10.4)$$

In this case, the equation governing the zonal index,  $z$  reduces to

$$\frac{d}{dt}z = \frac{1}{\sqrt{n}}\dot{W} - \frac{z}{\tau_2} + \frac{b}{n}(x_i - x_n) \quad (5.10.5)$$

For large  $n$ , the influence of the change becomes insignificant (as the new term on the right decays to zero), but for small  $n$ , the break in the feedback causes a substantial reduction in the persistence of the mode.

We simulated the  $x_i$  numerically with a forward Euler scheme. For the symmetric case, (5.10.2), the iteration equation is

$$x_i(t + \Delta t) = x_i(t) + \Delta t^{1/2} \phi_t - \tau^{-1} \Delta t x_i(t) + b \Delta t x_{i-1}(t). \quad (5.10.6)$$

where  $\Delta t$  is the time step and the  $\phi_t$  are identically and independently distributed Gaussian random variables sampled from the standard Normal distribution with mean zero and unit variance. For the broken chain case, the equation is the same for all  $x_i$  except  $x_0$ , which lacks the final term.

model conf.	$x_1$	$x_2$	$x_3$	$x_4$	$z$
b=0.5 symmetric	1.2	1.2	1.2	1.2	2.0
b=0.5 broken	1.0	1.1	1.1	1.2	1.5
b=0.9, symmetric	5.0	5.0	5.1	5.0	9.9
b=0.9, broken	1.0	1.3	1.5	1.6	2.2

Table 5.6: The e-folding timescales for the oscillators  $x_i$  and the “zonal average” signal  $z$  for the four simulations discussed in the text. Note that the decay function is perfectly exponential for  $z$  in the symmetric simulations and  $x_1$  in the broken chain simulations. Otherwise, these are best fit estimates.

As discussed in Section 3.3,  $n$  should not be thought of so much as the degrees of freedom in the system, but as an inverse length scale, as the simple feedback suggest a range of  $2\pi r/n$  for the feedback. Suggested by the separation between the peak eddy heat and momentum fluxes in simulation LSC+RM1, approximately  $90^\circ$ , we numerically simulate (5.10.4) with  $n = 4$  to see the effect of the break in the chain for varying  $b$ . We let  $\tau = 1$  set our nondimensional timescale. We consider a case with a moderate feedback,  $b = 0.5$ , which halves the effective drag  $\tau_2 = \tau/2$  of the symmetric model, and second case where a strong feedback,  $b = 0.9$  reduces the effective drag by a factor of 10,  $\tau_2 = \tau/10$ .

Results from the four simulations are shown in Table 5.6. The chief message is to be found in the final column, where we see the effect of the feedback break in the chain on the decorrelation timescale of the  $z$ , which represents the annular signal. When the feedback is uniform in longitude, the results confirm (to numeric precision) that the zonally averaged signal will feel the full feedback. When the chain is broken at one of the four links, however, the model becomes substantially less sensitive to the feedback.

We illustrate the autocorrelation functions for the  $x_i$  and  $z$  for the two simulations with strong feedback in Figure 5.25. In the symmetric case, panel (a), all of the individual oscillators have the same statistics. While the best fit decorrelation time is half that of the average signal, the autocorrelation functions have long tails; at short

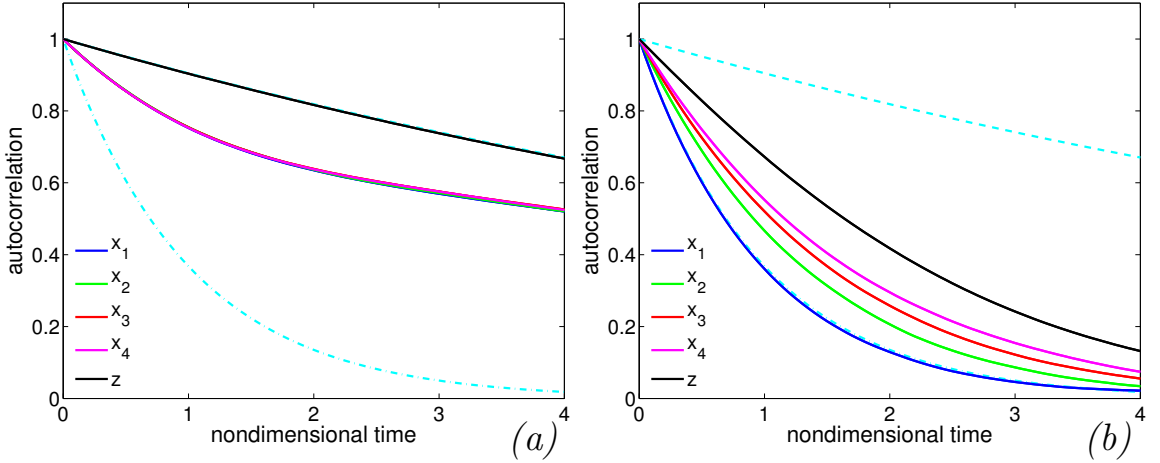


Figure 5.25: The autocorrelation functions of the oscillators  $x_i$  and the “zonal average” signal  $z$  for the model with  $n = 4$  and  $b = 0.9$ . Results from the symmetric model are shown in (a), and results from the model with the broken feedback chain are shown in (b). The light blue curves show exponential functions with e-folding timescale of 1 and 10 days, for reference.

lags, the random forcing leads to decorrelation, but at longer times, they appear to more influenced by the zonal signal. In the asymmetric case, the first oscillator will always decorrelate with the timescale set by  $\tau$ . As one moves downstream from it, the system starts to build up memory, but as we chose a short  $n$ , there is not sufficient space to build up a strong, coherent signal. The effect of the feedback is greatly reduced - the model’s annular signal persisting for only 2.2 days instead of 10.

While the simplicity of the model (and the arbitrary nature in which it was constructed) limit how much we can expect it to replicate the trends we observed, it does suggest an importance of zonal symmetry in sustaining an eddy-mean flow feedback when we account for the fact that the processes involved in the feedback are localized in space. The ability of the mean flow to influence the eddy forcing around the entire globe is important for building up a strong feedback. When processes are disrupted (or at least weakened) at a particular longitude, we can expect it to dramatically limit the effectiveness of the feedback. The model suggests that the zonal flow may

lose its memory in the baroclinic region, or in flowing over topography.

A possible physical mechanism for the breakdown of the feedback in longitude is suggested from observations by Ambaum et al. (2001). As the latitude of the zonal winds and of the annular mode vary as a function of longitude, the physical interpretation of the annular mode, or the zonal index, changes at different point around the globe. The observed NAM reflects a meridional “wobble” of the extratropical jet over the north Atlantic, but more of a “pulsing” of the subtropical jet over the north Pacific. As noted by LH, the feedback mechanism applies to anomaly patterns that characterizes a movement of the jet, and not patterns that reflect a change of intensity, as only the former shifts the critical latitudes. We observe a similar shift in the meaning of the zonal index and annular modes of the dynamical core with zonally asymmetric forcing. Thus, when eddies break downstream of the stirring region, the momentum fluxes are not aligned to shape the flow, which has changed from the longitude at which the eddies were generated.

## 5.11 Wave Breaking and Poleward Propagation

We have suggested that zonal asymmetries in the forcing limit the persistence of the intraseasonal variability by interfering with the coupling of eddies to the large-scale flow. But what controls the sensitivity in the zonally symmetric simulations? The arguments in Section 5.8 suggest that a genuine shift in the mean state is required to sustain the feedback. As shown in Section 5.9, the annular mode is not so annular when the temperature gradient is reduced, suggesting less opportunity for interaction. But this, and all our other analyses, serve more to diagnose the presence or lack of enhanced persistence of the eddy forcing than to explain it. When the interaction between the large scale flow and eddies is disabled, there is nothing left to organize the motions on large scales. In this final section we make a few conjectures to explain

the parameter sensitivities, with the hope of better understanding it in the future with further research.

The question is how can changes in the parameters short circuit coupling between the mean flow and eddies. As suggested by Robinson (1996), the surface friction plays a key role. The feedback depends on the fact that eddies in the jet core do not reduce the shear locally because of the redistribution of the momentum in upper layers. If surface friction does not damp the positive torque on the surface, however, the shear will be reduced in the jet core by the increase in the winds at the surface. In other words, without surface momentum damping, the shear is determined more by the surface circulation than the upper level circulation. Momentum redistribution in the upper levels will not be able to maintain the shear, and there is no means for the barotropic circulation to shape the stirring. Increasing the surface damping has the opposite effect, allowing the upper level flow more reign to control the baroclinicity, and the feedback is more effective.

This explanation is not easily related to the cases in which the equilibrium temperature gradient or thermal damping were modified. Here we change the thermal restoring force of the flow. It is possible that the weaker forcing on the mean flow allows the wave propagation feedback mechanism more control over the flow. It is also possible that the reasons are different in each case. For the simulations in which the equilibrium temperature gradient was varied, the reduction of the feedback might be due to the increase in the baroclinicity and eddy kinetic energy. Increasing the growth rate and magnitudes of the eddies increases the nonlinearity of the flow, and might limit the effectiveness of a mechanism that depends on linear wave propagation in the upper levels. As seen in the local dipole analysis in Section 5.9, the annular mode in Z80 was much more dominated by local projections onto the mean flow, associated with eastward propagating eddies. In varying  $k_a$ , there is less change in the baroclinicity and eddy kinetic energy, but the restoring forcing that rebuilds the

jet is also modified. The two effects could balance to give the same change in the feedback.

It is remarkable that in both cases, the mean climate and the variability responded in the same way as it did to changes in the surface damping. Enhanced persistence is consistently associated with weaker surface winds and an equatorward shift of the mean jet. This suggests that processes that set the position of the mean winds are related to processes controlling the variability.

Feldstein (1998) noted a tendency of anomalies of the zonally averaged zonal winds to propagate poleward. We have observed a similar tendency for poleward propagation in the dynamical core, as shown in Figure 5.26. The propagation, however, is quite sensitive to model configuration. In simulations where the annular mode was extremely persistent, the propagation speed was smaller, and it was in general much harder to find evidence of propagation. While it is visible in latitude-lag covariance plots based the flow at many different base points for simulations Z80, it was only visible when the base point was chosen near  $20^\circ$  N with simulation Z40. At all other latitudes the covariance maps were dominated by non-propagating anomalies associated with the position of the jet.

Poleward propagation can be understood in terms of a modification of the mechanism for extended persistence discussed in Section 5.8. The geometry of the sphere tends to refract eddy activity towards the equator. As shown in the cartoons in Figure 5.27, this modifies the response of the flow to eddy forcing. The picture is the same for eddies generated on the equatorward flank of the jet, in panel (a). There is limited propagation at height, and the response is a reduction of the shear. For eddies generated in the jet core, (b), the local response is the same – a mild reduction in the shear offset by meridional momentum fluxes at height. But all the momentum comes from the equatorward flank of the jet. Eddies generated on the poleward flank of the jet, (c), are more likely to generate upper level momentum fluxes, even though

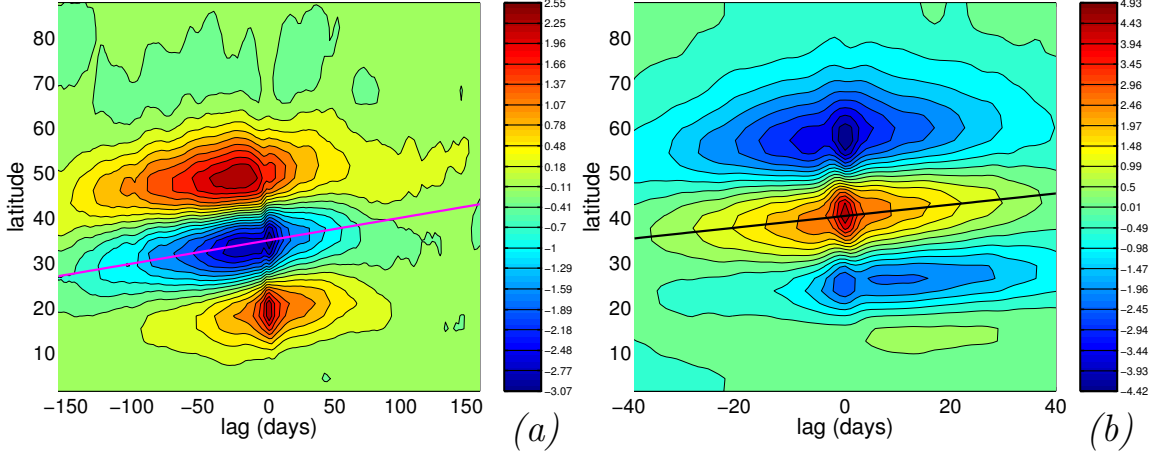


Figure 5.26: Evidence of poleward propagation in simulations Z40 and Z80. (a) The covariance of the .225  $\sigma$ -level zonal average zonal wind,  $\bar{u}$  at  $18^\circ$  N with the same wind as a function of lag and latitude. The magenta line shows propagation of  $0.05^\circ$  latitude per day. (b) The same as in (b), but the base point is at  $40^\circ$  N. Here, the black line shows propagation of  $0.125^\circ$  latitude per day.

the winds are weaker there. This provides a slight bias to move the upper level winds poleward.

In the limit that poleward propagation dominates the more stationary mechanism proposed in Section 5.8, one might expect the timescale of propagation to set the timescale of the annular mode; faster propagation would shorten the timescale of the variability. Indeed, the speed of poleward propagation in Z80 is faster than Z40. However, I think it is a little more complicated than that. The fact that it was much harder to find poleward propagation in Z40 suggests that it might be possible for the model to exist in different regimes, one in which poleward propagation dominates, the timescales of variability are short, and one in which a persistent feedback locks the position of the jet.

This explanation would help relate the latitude of the mean jet to the persistence. At lower latitudes, the effects of spherical geometry are weaker, and there is less a bias for eddy activity to refract towards the equator. I do not fully understand the geometric effects, and need to investigate this possibly further. In this scenario, the

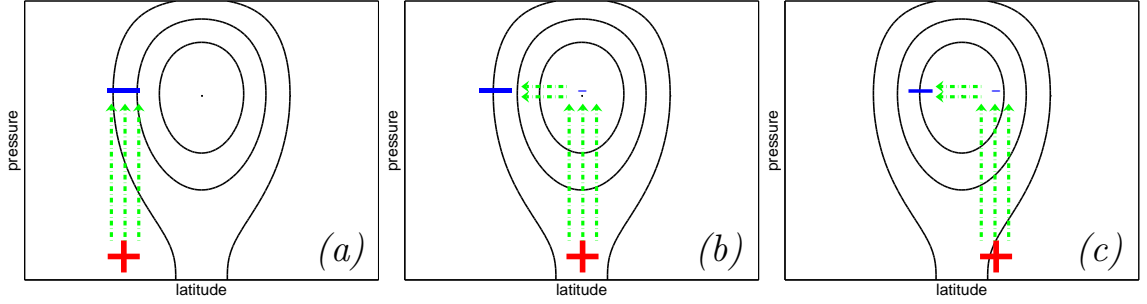


Figure 5.27: A cartoon illustration of the tendency of eddy-mean flow interactions to lead to poleward propagation of zonal anomalies. As in Figure 5.16, black contours mark the position of the zonal mean winds. Dashed green arrows denote the propagation of wave activity, or, equivalently, the direction of E-P fluxes. Plus and minus signs indicate divergence and convergence of the E-P fluxes, and so a torque on the mean flow.

variability stems from the latitude of the jet, and the key would be to understand what governs its position. If the mean jet is shifted further north, poleward propagation is favored, and variability reduced.

Alternatively, the latitude of the jet could be influenced by the strength of poleward propagation. A stronger tendency for the eddy driven jet to move poleward would shift the mean location of the jet. In this line of thought, the key would be to understand what sets the tendency of the jet to move poleward, and the mean state and variability would follow.

I have observed that there is a greater tendency for E-P fluxes to propagate poleward in simulations where the mean jet is further equatorward. But this does not indicate which came first. Are poleward E-P fluxes moving the jet equatorward, or is the southern location of the jet permitting poleward E-P fluxes? Experiments with a primitive equation model in a channel might help address this problem by removing the geometric effects.

## 5.12 Summary and Conclusions

We have sought to characterize the intraseasonal variability in a simplified GCM. After addressing issues of resolution (Section 5.4), we surveyed the response of the model to changes in three key model parameters (Section 5.5) and to the introduction of zonally asymmetric forcing (Section 5.6). We have found that the timescale of intraseasonal variability is quite sensitive to model configuration. The breadth of tests, however, have also shown that the timescale of variability is independent of many features, narrowing the potential mechanisms to explain the sensitivities. We summarize the key results below.

- The model responds similarly in direction and amplitude to changes of three parameters, the equilibrium temperature gradient ( $\Delta T_{eq}$ ), thermal damping coefficient ( $k_a$ ), and momentum damping coefficient ( $k_f$ ). A decrease in  $\Delta T_{eq}$  or  $k_a$ , or an increase of  $k_f$  shift the climatological jet equatorward, decrease the surface winds, and increase the persistence of the annular mode. The change in the timescale of variability and the mean state are uncomfortably similar to changes induced by modification of the vertical resolution at T42 horizontal resolution. This sensitivity to vertical resolution is not robust at T63 horizontal resolution, but the changes induced by parameters are robust at T63 resolution.
- Modulation of different parameters suggest that the timescales of interannual variability are not so sensitive to the baroclinicity of the flow, eddy kinetic energy, or eddy heat fluxes. The timescales do appear to be more sensitive to changes in eddy momentum fluxes, and so the processes regulating eddy decay and wave breaking. [This, however, is consistent with the fact that the barotropic circulation (as determined by the surface westerlies) is quite similar in simulations with equally persistent variability.]
- Zonal asymmetries in the flow, topography in particular, appear to dramatically

lower the timescales of intraseasonal variability, and limit its sensitivity to the model parameter  $\Delta T_{eq}$ .

The dramatic persistence of the annular mode (in some simulations it exhibited an e-fold timescale approaching 100 days) suggests a model configuration sensitive coupling between the large scale patterns of variability and the synoptic eddy forcing. In Section 5.7 we sought definitive evidence of a feedback and to rule out other possible explanations for the extended persistence. We determined that the long timescales of the annular mode were generated by remarkable coherence in the eddy forcing, as diagnosed by the Eliassen-Palm (E-P) flux divergence. For example in simulation Z40, positive E-P forcing of the annular mode leads *and lags* the annular mode index by over 100 days. (See Figure 5.12.) In other words, the annular mode index was propped up by eddy forcing on monthly timescales.

This contradicts the null hypothesis that the eddy forcing is independent of the state of the mean flow, (as we took in Chapter 2). Indeed, when we applied the analysis of LH, we found that natural damping timescale of the dipole anomaly of the jet to be about 8 days, and relatively independent of the equilibrium temperature gradient and topography. Absent coupling between the eddy forcing and zonal index, one would then expect the large scale variability to decay on timescales of 8 days or less. Rejection of the null hypothesis is not proof of a feedback between the eddy forcing and zonal flow. It is possible, for example, that the eddy forcing is somehow organizing itself on long timescales, independently of the mean flow.

In Section 5.8, however, we suggest a mechanism for coupling the eddies and the barotropic flow that can explain the organization of the eddy flux divergence on the long timescales observed. Eddy heat fluxes (associated with baroclinic growth in the lower troposphere) always act to reduce the vertical shear, thus breaking down the jet. Meridional propagation of wave activity in the upper troposphere, however, can spread out this effect, so that the shear is not necessarily reduced in the region where

the eddy was generated.

Linear theory suggest that wave activity is damped in regions where the zonal velocity is weaker. Waves can propagate meridionally until they near a critical layer, where nonlinear effects lead to wave breaking and irreversible mixing (Randel and Held 1991). This provides a pathway for barotropic circulation to interact with the stirring, as it increases the zonal wind, allowing for more meridional propagation of wave activity. The reduction of vertical shear by eddies generated in the jet core (defined by the position of the barotropic circulation) is smeared out by meridional propagation, so that the baroclinicity in the jet core is maintained. Eddies formed on the flanks of the jet core, however, lead to a pronounced drop in the vertical shear above them, as weaker upper level winds do not favor meridional propagation and the effect of the heat fluxes is felt locally. This provides a negative feedback on eddies that would move the jet, and so endow the jet with a certain degree of “stickiness,” or memory.

In terms of the persistence of the zonal anomaly, the negative feedback restricting movement of the jet expressed here is the same as a positive feedback reinforcing the position of the jet as expressed by Robinson (2000) and LH. We argue that the negative view is perhaps more true to the eddy dynamics. The eddy driven barotropic circulation does not increase the baroclinicity of the flow. Rather, it helps sustain the vertical shear in the jet core by reducing it on the flanks.

Reinforcement of the jet depends on wave propagation in the upper atmosphere, a fundamentally nonlocal process. As seen with the barotropic model in Chapter 2, it is possible to have annular patterns of variability where there is little zonal coherence in the dynamics, or any feedback between the high frequency variability – the stirring – and the large scale variability. Our simple stochastic models in Chapter 3 clarify how such patterns can arise naturally, demonstrating that the mass and angular momentum constraints favor the dipole pattern and spherical geometry

favors annular patterns. Here, the key is that the spatial (and temporal) spectrum is red, so that more variance is found at larger scales and lower frequencies. In the atmosphere, this reddening could be viewed as the outcome of an upscale cascade in energy. As seen from our random walk models the accumulation of small events also gives rise to a red spectrum – so that one need not ascribe this property to turbulence arguments. In either case, the existence of annular patterns of variability alone does not imply hemispherically coherent motions – and so a feedback involving nonlocal processes is not always possible.

We addressed this issue in Section 5.9, where we focus on the spatial and temporal characteristics of the dipole pattern projected onto the local flow. On shorter timescales, the annular mode is typically not very annular. Locally, the dynamics are dominated by the projection of individual eddies onto the annular mode pattern. The scale of these projections is consistent with synoptic events, and they propagate eastward with phase speed consistent with such eddies. If we shift the focus away from these individual eddies [in Figure 5.21 we did this by looking at weaker correlations away from the analysis longitude], but still at short timescales, we also see the projection of wave trains onto the annular mode pattern, which propagate eastward more rapidly. These strong, more short term projections are consistent with the annular mode that arises statistically, but does not exhibit a zonally coherent dynamics.

Shifting the focus to longer timescales, we find a significant annular signal in some simulations. This, we argue, is the presence of a physically annular mode where strong nonlocal interactions between the mean flow and eddies are possible. As seen in Figure 5.22, after 10-15 days the correlation of the local dipole projection becomes *independent* of longitude. This weaker, coherent signal is masked, to some extent by synoptic variability that dominates the projection at shorter timescales. This coherent signal is much more sensitive to model configuration, present when the baroclinic forcing of the jet is weak (small equator-to-pole temperature gradient) and

when there is little zonal asymmetry in the flow.

The addition of zonal asymmetries to the model, topography in particular, appears to limit the impact of the feedback, reducing the persistence of the annular mode and its sensitivity to changes of the equilibrium temperature gradient. The simple model in Section 5.10 is an extension of the LH feedback, but attempts to account for the fact that the eddy-mean flow interactions are separated in longitude. In particular, eddy decay through wave breaking is a local, nonlinear process. In the model, we suppose that the flow at a given longitude can only influence the forcing of the flow downstream. With zonal symmetry, the spread of the feedback in longitude does not affect the persistence of the zonal average signal. Figuratively, the memory of individual events propagates around the latitude circle, eventually influencing the longitude at which it originated, establishing the feedback as if it were direct. When the eddy-mean flow interactions are broken at one longitude (or more generally, just reduced) the feedback loop is short circuited. While memory builds up downstream of the event, it cannot cycle back around.

This may explain the decrease (and reduced sensitivity to parameters) of the timescales of variability in simulations with zonally asymmetric forcing. Shifts in the jet disrupt the feedback, as eddy momentum fluxes that would reinforce the baroclinicity in the jet core at the longitude where the eddy was created may increase it on the flanks at the longitude where it breaks. Zonal asymmetries also force eddies to break rather than flux energy forward, limiting their ability to influence the flow where they were generated. With zonally symmetric forcing, the dynamical core is generally much more persistent than the real atmosphere. While it is possible that the problem lies in the simplicity of the forcing, it is quite likely that zonal asymmetries are the key. When topography and diabatic forcing are added, the timescales of variability in the model match those of observations.

As noted in Section 5.11, we have not fully explained how changes in the parameters affect the timescales of variability. This is equivalent to the problem we had quantifying the proposed mechanism. The persistence of the annular mode appears to be correlated with the latitude of the mean jet. This suggests that geometry might play a role in the feedback, and the mechanism of poleward propagation proposed by Feldstein (1998) might provide a pathway for answering this question in the future. A increase in the tendency of poleward propagation could explain both the poleward shift in the mean state and decrease in the timescale of variability.

In either case, however, the atmosphere appears to be in a regime of limited feedback. As argued by LH, the feedback in the atmosphere extends the persistence of the annular mode by a few days, not months, as in certain simulations of the dynamical core. We have shown that zonal asymmetry, even a 1000 m ridge, significantly reduces the ability of the model to sustain low frequencies. Thus, the Andes in the Southern Hemisphere would be more than sufficient to disrupt such a sensitive feedback. It would be interesting to see if the jets on planets with more uniform forcing, such as Jupiter, exhibit more persistent variation of the jet position.

# Chapter 6

## Conclusions

We have gained a better understanding of the spatial and temporal structure of the NAO and annular modes through a study of three idealized models. Our first, the barotropic model discussed in Chapter 2, provides a simple context for understanding the basic features of the patterns. Both the NAO and annular modes are eddy driven phenomena whose spatial structure follows naturally from the zonal asymmetry of synoptic eddy statistics. To first order, their longer timescales emerge from a reddening of the eddy stirring by the equations of motion. The large scale flow integrates the eddy momentum fluxes, thus exhibiting more power at lower frequencies.

Despite the zonal symmetry of the top EOFs of streamfunction and zonal wind, the circulation in the barotropic model exhibits little coherence on hemispheric scales. The stochastic models in Chapter 3 make it clear that zonally coherent motion is not a necessary condition for a zonally uniform EOF. Rather, zonally uniform statistics are sufficient to produce annular patterns of variability. The stochastic model provide a baseline for interpreting EOF and single point correlation maps in the extratropics. Basic properties of the atmospheric circulation – chiefly the conservation of momentum and mass – and the symmetries and geometry of the sphere bias EOF analysis towards dipolar, annular modes of variability. This is not to say that the patterns

identified in the atmosphere or models are not dynamically interesting, but rather that their existence alone should not be taken as an indication of any dynamics beyond simple mass and momentum conservation.

To connect the results of these simple models to the atmosphere, we began work with a primitive equation model in Chapter 4. In particular, we were interested in how zonal asymmetries in the mean state give rise to zonal asymmetries in the synoptic variability – the storm tracks – and how they in turn shape the intraseasonal variability. We found that zonally localized variability like the NAO arises from the confluence of orographic and thermal effects. Thermal forcing was most effective in creating a storm track. The heating anomaly representing the effect of a warm wintertime ocean created a weak baroclinic zone, reducing eddy growth, and slowed the upper level winds, reducing the carrying capacity of the jet and so promoting wave breaking. Eddies transfer momentum to the mean flow in the decay process; hence intraseasonal variability is greatest in weak flow at the end of the storm track.

The standing waves established by topography, however, also appear instrumental in shaping the patterns of variability. Optimal alignment of topography and heating anomalies produced the most zonally localized EOF patterns – a nonlinear effect that could not be predicted from an overlap of the model’s response to topography or diabatic heating anomalies alone. In that a well localized storm track produces localized intraseasonal variability, results from the dynamical core confirm the conclusions of our barotropic study. But the dynamical core suggests there is another key difference between a pure annular pattern of variability and one with significant zonal asymmetry.

In the final chapter, 5, we investigated a coupling between the large scale variability patterns and the eddy stirring. In certain parameter regimes, the barotropic, eddy driven circulation appears to influence baroclinic processes by shaping the propagation of wave activity in the upper atmosphere. Eddy momentum fluxes in the upper

levels spread out the tendency of the eddy heat fluxes to reduce the shear, thus sustaining the baroclinicity of the flow in the jet core at the expense of baroclinicity on the flanks of the jet. This endows the jet with a “stickiness,” or memory, extending the persistence of anomalies in the zonal flow and leading to large-scale coherent motions at lower frequencies. In certain parameter regimes, the annular mode was not just a statistical feature, but a pattern characterizing a zonally coherent movement of the extratropical jet.

Zonal asymmetries, topography in particular, limit coupling between the large scale flow and the eddies. Disrupting it reduces the zonal coherence of the motions, making the dynamical core behave more like the barotropic or stochastic models, which lacked correlation of the flow on large scales. The transition from an annular pattern of variability to a NAO-like pattern in the dynamical core required both a localization of the eddy forcing (the storm tracks) and a weakening of the eddy mean flow coupling. The storm tracks led to greater variance of the jet in a zonally localized region, and the breakdown of coupling diminished hemispheric wide motions, preventing EOF analysis from weighting points all around the globe.

Looking back over the thesis, I feel that have come full circle in my understanding of the NAO and annular modes. The NAO and annular modes were first identified by comparing monthly and annual average statistics (e.g. Walker and Bliss 1932). From this filtered data, broad patterns of variability emerge, suggesting large-scale dynamics. As documented by Feldstein (2000a) and (2000b), however, the bulk of the power in these “oscillations” is found at shorter timescales, on the neighborhood of 10-15 days. This suggests that to understand the dynamics of the modes, one must understand the processes responsible for its variability at short timescales.

I entered the debate here, using the barotropic model to focus on the intraseasonal variability created by high frequency, stochastically forced eddies. I soon learned that on shorter timescales, the annular modes are not so annular. I feel this point is made

most clear by the local dipole analysis in Section 5.9. Even in simulation Z40, which does exhibit zonally coherent motions – a physically annular mode, so to speak – it is difficult to see the annular mode at any particular time. The zonal average flow is always dominated by local eddy motions. If one attempts to focus in on any particular annular mode or NAO event, one invariably finds the breaking of a single eddy or two. On these shorter timescales, the annular mode and NAO are best thought of as convenient statistical means of describing the flow. Wave breaking conserves momentum and so tends to move the jet, and the statistics of these events in longitude sets the zonal structure of the variability, as demonstrated with our stochastic models.

It was not until I began work with the dynamical core that I appreciated the potential importance of coupling between the eddy stirring and the large-scale flow. The ability of the eddy driven circulation to feed back on eddy processes makes possible the existence of a more physical annular mode and NAO. This is clearly the case in some of our simulations with the dynamical core, particularly when the thermal forcing is weak, or the surface drag increased. Here the large-scale dynamics clearly matter at lower frequencies, and the NAO and annular modes have more dynamical significance than simple mass and momentum conservation.

Thus, while much of the power in the annular mode and NAO is on shorter timescales, it is important not to focus in too closely. The interesting dynamics are in between the natural damping timescale of jet anomalies, about 7-9 days, and the timescale of the variability, about 10-20 days. The dynamics of the annular modes and NAO are found in the information left behind after one eddy breaks, which enables the large-scale motions to influence the next eddy.

Lastly, we briefly return to the question of nomenclature. The chief variation in the extratropical atmosphere is the movement of the eddy driven jet. This movement appears to be stochastically driven by chaotic eddy momentum and heat fluxes. The

dynamics of fluid motion, however, endow the jet with more persistence than would be expected from a purely stochastically driven system, and movement of the jet occurs on slower timescales and larger spatial scales. On shorter timescales, the NAO is more easily related to physical processes, such as wave breaking, and thus the most meaningful characterization. At very low frequencies, however, there is correlation between the North Atlantic and North Pacific storm tracks (Maarten Ambaum, personal communication), suggesting that the zonally uniform structure of the annular mode has meaning in this context.

The terms “oscillation” and “mode” however, imply an intrinsic pattern of variability, or a variation between two states, a positive phase jet, and a negative phase jet. I have not found any evidence of regimes in my models over a wide range in parameter space and number of zonal configurations. The NAO and annular modes are significant in that they track the position of the jet, one in the North Atlantic storm track, the other over both storm tracks. I think the older classification, the zonal index, is perhaps less apt to cause confusion. It provides the same information as the annular mode, and more directly implies that one is simply tracking the position of the eddy driven jet. A zonal index defined over the North Atlantic basin would provide the same information as the NAO, but also not imply the existence of regimes in the circulation.

The nomenclature is well entrenched, and I do not propose changing it. But it is important to be clear what is meant in classifying midlatitude variability in “modes,” as it can lead to confusion in the context of climate change. It is quite probable that climate change will project heavily onto the internal variability. In the extratropics, the jet and storm tracks are the least constrained feature, in that they are most variable. The effect of any perturbation is likely to be large in these elements. (Fluctuation-dissipation theory provides a scientific basis for this, as suggested by Leith (1975).) However, if a climate perturbation causes, say, the jet to move pole-

ward, how appropriate is it to say that this “projects heavily on the positive annular mode.” If the jet continues to wobble around its mean state in the new climate, it is probably more appropriate to think of this as a shift in both the climatology and the variability. In other words, are these “modes” fixed entities, independent of the mean state, or are they best thought of as an effective description of the variability with respect to the current mean.

In parting, we note that long ago David Crantz offered up this explanation for the unusual events in Greenland during the winter of 1739-40,

*The author ascribes both these effects to the warm and yet imperceptible exhalations, that were forced hither by the rigorous cold in the milder climates.*

Peering through the eighteenth century prose with a little poetic license, perhaps we may interpret this as an equatorward shift of the “rigorous” North Atlantic storm track, leading to anomalous southerly winds (i.e. imperceptible exhalations) over Greenland.

# Bibliography

- Ambaum, M. H. P., B. J. Hoskins, and D. B. Stephenson, 2001. Arctic Oscillation or North Atlantic Oscillation? *J. Climate*, **14**, 3495–3507.
- Barnston, A. G., and R. E. Livezey, 1987. Classification, seasonality, and persistence of low-frequency atmospheric circulation patterns. *Mon. Wea. Rev.*, **115**, 1083–1126.
- Batchelor, G. K., 1953. *The Theory of Homogeneous Turbulence*. Cambridge University Press, 197 pp.
- Branstator, G., 1990. Low-frequency patterns induced by stationary waves. *J. Atmos. Sci.*, **47**, 629–648.
- Branstator, G., 1992. The maintenance of low-frequency anomalies. *J. Atmos. Sci.*, **49**, 1924–1945.
- Branstator, G., 1995. Organization of the storm track anomalies by recurring low-frequency circulation anomalies. *J. Atmos. Sci.*, **52**, 207–226.
- Cash, B. A., P. Kushner, and G. K. Vallis, 2002. The structure and composition on the annular modes in an aquaplanet General Circulation Model. *J. Atmos. Sci.*, **59**, 3399–3414.
- Cash, B. A., P. Kushner, and G. K. Vallis, 2005. Zonal asymmetries, teleconnections, and annular patterns in a GCM. *J. Atmos. Sci.*, **62**, 207–219.

- Chang, E. K. M., and I. Orlanski, 1993. On the dynamics of a storm track. *J. Atmos. Sci.*, **50**, 999–1015.
- Cohen, J., and K. Saito., 2002. A test of annular modes. *J. Climate*, **15**, 2537–2546.
- DeWeaver, E., and S. Nigam, 2000. Zonal-eddy dynamics of the North Atlantic Oscillation. *J. Climate*, **13**, 3893–3914.
- Drower, G., 1989. When the Thames froze. *The Times of London*, Dec. 30.
- Duchon, C. E., 1979. Lanczos filtering in one and two dimensions. *J. Applied Meteor.*, **18**, 1016–1022.
- Edmon, H. J., B. J. Hoskins, and M. E. McIntyre, 1980. Eliassen-Palm cross sections for the troposphere. *J. Atmos. Sci.*, **37**, 2600–2616.
- Feldstein, S. B., 1998. The growth and decay of low-frequency anomalies in a GCM. *J. Atmos. Sci.*, **55**, 415–428.
- Feldstein, S. B., 2000a. Is interannual zonal mean flow variability simply climate noise? *J. Climate*, **13**, 2356–2362.
- Feldstein, S. B., 2000b. The timescale, power spectra and climate noise properties of teleconnection patterns. *J. Climate*, **13**, 4430–4440.
- Feldstein, S. B., and S. Lee, 1996. Mechanisms of zonal index variability in an aquaplanet GCM. *J. Atmos. Sci.*, **53**, 3541–3555.
- Feldstein, S. B., and S. Lee, 1998. Is the atmospheric zonal index driven by an eddy feedback? *J. Atmos. Sci.*, **55**, 3077–3086.
- Gerber, E. P., and G. K. Vallis, 2005. A stochastic model for the spatial structure of annular patterns of variability and the nao. *J. Climate*, **18**, 2102–2118.

- Held, I. M., 2000. *The General Circulation of the Atmosphere*. Proc. Woods Hole Summer School on GFD, 66 pp.
- Held, I. M., and P. J. Phillips, 1987. Linear and nonlinear barotropic decay on the sphere. *J. Atmos. Sci.*, **44**, 200–207.
- Held, I. M., and M. J. Suarez, 1994. A proposal for the intercomparison of the dynamical cores of Atmospheric General Circulation Models. *Bull. Am. Meteor. Soc.*, **75**, 1825–1830.
- Hoskins, B. J., and K. I. Hodges, 2002. New perspectives on the Northern Hemisphere winter storm tracks. *J. Atmos. Sci.*, **59**, 1041–1061.
- Hoskins, B. J., and P. J. Valdes, 1990. On the existence of storm-tracks. *J. Atmos. Sci.*, **47**, 1854–1864.
- James, I. N., and P. M. James, 1992. Spatial structure of ultra-low frequency variability of the flow in a simple atmospheric circulation model. *Quart. J. Roy. Meteor. Soc.*, **118**, 1211–1233.
- Kalnay et al., 1996. The NCEP/NCAR 40-year reanalysis project. *Bull. Am. Meteor. Soc.*, **77**, 437–471.
- Karatzas, I., and S. E. Shreve, 1991. *Brownian Motion and Stochastic Calculus*. Springer, 470 pp.
- Knight, F. B., 1981. *Essentials of Brownian motion and diffusion (Mathematical surveys; no. 18)*. American Mathematical Society, 201 pp.
- Kushner, P. J., and G. Lee, 2006. On the zonal structure of the Annular Modes. *J. Climate*, submitted.
- Lau, N.-C., 1988. Variability of the observed midlatitude storm tracks in relation to low-frequency changes in the circulation pattern. *J. Atmos. Sci.*, **45**, 2718–2743.

- Lee, S., 1997. Maintenance of multiple jets in a baroclinic flow. *J. Atmos. Sci.*, **54**, 1726–1738.
- Leith, C. E., 1975. Climate response and fluctuation dissipation. *J. Atmos. Sci.*, **32**, 2022–2026.
- Limpasuvan, V., and D. L. Hartmann, 2000. Wave-maintained annular modes of climate variability. *J. Climate*, **13**, 4414–4429.
- Lorenz, D. J., and D. L. Hartmann, 2001. Eddy-zonal flow feedback in the Southern Hemisphere. *J. Atmos. Sci.*, **58**, 3312–3327.
- Lorenz, D. J., and D. L. Hartmann, 2003. Eddy-zonal flow feedback in the Northern Hemisphere Winter. *J. Climate*, **16**, 1212–1227.
- Maltrud, M. E., and G. K. Vallis, 1991. Energy spectra and coherent structures in forced two-dimensional and beta-plane turbulence. *J. Fluid Mech.*, **228**, 321–342.
- North, G. R., T. L. Bell, R. F. Cahalan, and F. J. Moeng, 1982. Sampling errors in the estimation of Empirical Orthogonal Functions. *Mon. Wea. Rev.*, **110**, 699–706.
- North, G. R., and R. F. Cahalan, 1981. Predictability in a solvable stochastic climate model. *J. Atmos. Sci.*, **38**, 504–513.
- North, G. R., F. J. Moeng, T. L. Bell, and R. F. Cahalan, 1982. The latitude dependence of the variance of zonally averaged quantities. *Mon. Wea. Rev.*, **110**, 319–326.
- Obukhov, A. M., 1947. Statistically homogeneous fields on a sphere. *Uspekhi Matematicheskikh Nauk*, **2**, 196–198.
- Orlanski, I., 1998. On the poleward deflection of storm tracks. *J. Atmos. Sci.*, **55**, 128–154.

- Pierrehumbert, R. T., 1984. Local and global baroclinic instability of zonally varying flow. *J. Atmos. Sci.*, **41**, 2141–2162.
- Randel, W. J., and I. M. Held, 1991. Phase speed spectra of transient eddy fluxes and critical layer absorbtion. *J. Atmos. Sci.*, **48**, 688–697.
- Rhines, P. B., 1977. The dynamics of unsteady currents. In E. A. Goldberg, I. N. McCane, J. J. O'Brien, and J. H. Steele, Eds., *The Sea*, Vol. 6, pp. 189–318. J. Wiley and Sons.
- Robinson, W. A., 1994. Eddy feedbacks on the zonal index and eddy-zonal flow interactions induced by zonal flow transience. *J. Atmos. Sci.*, **51**, 2553–2562.
- Robinson, W. A., 1996. Does eddy feedback sustain variability in the zonal index. *J. Atmos. Sci.*, **53**, 3556–3569.
- Robinson, W. A., 2000. A baroclinic mechanism for eddy feedback on the zonal index. *J. Atmos. Sci.*, **57**, 415–422.
- Salmon, R., 1980. Baroclinic instability and geostrophic turbulence. *Geophys. Astrophys. Fluid Dyn.*, **10**, 25–52.
- Shepherd, T. G., and T. A. Shaw, 2004. The angular momentum constraint on climate sensitivity and downward influence in the middle atmosphere. *J. Atmos. Sci.*, **61**, 2899–2908.
- Simmons, A., and B. Hoskins, 1978. The life-cycles of some nonlinear baroclinic waves. *J. Atmos. Sci.*, **35**, 414–432.
- Smith, K. S., G. Boccaletti, C. Henning, I. Marinov, F. Tam, I. Held, and G. K. Vallis, 2002. Turbulent diffusion in the geostrophic inverse cascade. *J. Fluid Mech.*, **77**, 34–54.

- Stephenson, D. B., V. Pavan, and R. Bajariu, 2000. Is the North Atlantic Oscillation a random walk? *Int. J. Climatology*, **20**, 1–18.
- Stone, P. H., 1978. Baroclinic adjustment. *J. Atmos. Sci.*, **35**, 561–571.
- Thompson, D. W. J., and J. M. Wallace, 1998. The Arctic Oscillation signature in the wintertime geopotential height and temperature fields. *Geophys. Res. Lett.*, **25**, 1297–1300.
- Thompson, D. W. J., and J. M. Wallace, 2000. Annular modes in the extratropical circulation. Part I: Month-to-month variability. *J. Climate*, **13**, 1000–1016.
- Vallis, G. K., 2005. *Atmospheric and Oceanic Fluid Dynamics*. Available from [www.princeton.edu/~gkv/aofd](http://www.princeton.edu/~gkv/aofd). To be published by Cambridge University Press, 758 pp.
- Vallis, G. K., E. P. Gerber, P. J. Kushner, and B. A. Cash, 2004. A mechanism and simple dynamical model of the North Atlantic Oscillation and annular modes. *J. Atmos. Sci.*, **61**, 264–280.
- Vallis, G. K., and M. E. Maltrud, 1993. Generation of mean flows and jets on a beta plane and over topography. *J. Phys. Oceanogr.*, **23**, 1346–1362.
- van Loon, H., and J. C. Rogers, 1978. The seesaw in winter temperatures between Greenland and northern Europe. part I: General description. *Mon. Wea. Rev.*, **106**, 296–310.
- von Storch, H., and F. W. Zwiers, 1999. *Statistical Analysis in Climate Research*. Cambridge University Press, 484 pp.
- Walker, G. T., and E. W. Bliss, 1932. World weather V. *Memoirs of the R. M. S.*, **4**, 53–83.

- Wallace, J. M., 2000. North Atlantic Oscillation/Annular Mode: Two paradigms — one phenomenon. *Quart. J. Roy. Meteor. Soc.*, **126**, 791–805.
- Wallace, J. M., and D. S. Gutzler, 1981. Teleconnections in the geopotential height field during the Northern Hemisphere winter. *Mon. Wea. Rev.*, **109**, 784–812.
- Wanner, H., and J. Luterbacher, 2002. The LOTRED approach - A first step towards a “paleoreanalysis” for Europe. *PAGES News*, **10**, 9–11.
- Whitaker, J. S., and P. D. Sardeshmukh, 1998. A linear theory of extratropical eddy statistics. *J. Atmos. Sci.*, **55**, 237–258.